

**ADVANCED UV INSCRIBED FIBRE
GRATING STRUCTURES AND
APPLICATIONS
IN OPTICAL SENSING AND LASER
SYSTEMS**

**Pouneh Saffari
Doctor of Philosophy**

**ASTON UNIVERSITY
November 2010**

This copy of the thesis has been supplied on condition that anyone who consults it is understood to recognise that its copyright rests with its author and that no quotation from the thesis and no information derived from it may be published without proper acknowledgement.

ASTON UNIVERSITY
**ADVANCED UV INSCRIBED FIBRE GRATING
STRUCTURES AND APPLICATIONS IN OPTICAL
SENSING AND LASER SYSTEMS**

Pouneh Saffari
Doctor of Philosophy
November 2010

This thesis presents detailed investigation of UV inscribed fibre grating based devices and novel developments in the applications of such devices in optical sensing and fibre laser systems. The major contribution of this PhD programme includes the systematic study on fabrication, spectral characteristics and applications of different types of UV written in-fibre gratings such as Type I and IA Fibre Bragg Gratings (FBGs), Chirped Fibre Bragg Gratings (CFBGs) and Tilted Fibre Gratings (TFGs) with small, large and 45° tilted structures inscribed in normal silica fibre. Three fabrication techniques including holographic, phase-mask and blank beam exposure scanning, which were employed to fabricate a range of gratings in standard single mode fibre, are fully discussed.

The thesis reports the creation of smart structures with self-sensing capability by embedding FBG-array sensors in Al matrix composite. In another part of this study, we have demonstrated the particular significant improvements made in sensitising standard FBGs to the chemical surrounding medium by inducing microstructure to the grating by femtosecond (fs) patterning assisted chemical etching technique. Also, a major work is presented for the investigation on the structures, inscription methods and spectral Polarisation Dependent Loss (PDL) and thermal characteristics of different angle TFGs.

Finally, a very novel application in realising stable single polarisation and multiwavelength switchable Erbium Doped Fibre Lasers (EDFLs) using intracavity polarisation selective filters based on TFG devices with tilted structures at small, large and exact 45° angles forms another important contribution of this thesis.

Key words: fibre Bragg grating, chirped fibre Bragg grating, tilted fibre grating, optical fibre sensor.

*To my supportive mother and to
the loving memory of my dear father who was so looking forward to this moment but
could not quite live to celebrate it.*

*“Not everything that counts can be counted,
and not everything that can be counted counts”*

“Albert Einstein”

ACKNOWLEDGEMENTS

Although words are never enough to express my sincere gratitude to those who have helped me reach my goals, I would still like to thank my honorific supervisor, Professor Lin Zhang. It has been a great pleasure to be her PhD student. She has taught me, how good experimental physics is done and I do appreciate all her contributions of time and ideas to make my PhD experience productive and stimulating. The joy and enthusiasm she has for her research was contagious and motivational for me, even during tough times in my personal life. I am also thankful for the excellent example she has provided as a successful woman physicist and professor. I would like to extend my gratitude and appreciation to Professor Ian Bennion, for his tireless support and attention. Being part of his group was an absolute honour which I will cherish this memory for the rest of my life.

Special thanks are given to Dr Kaiming Zhou, who patiently offered me so much advice with no hesitation and always guided me in the right direction with his remarkable intelligence. I am also indebted to my dear friend Mr Chengbo Mou for the countless discussions and fruitful collaborations. He was the person who helped me to find the way around the laboratory at the first step.

Sincere appreciations are given to Mr Bert Biggs for providing such a well-organised laboratory environment. His remarkable skill as laboratory manager ensured that labs were running smoothly all the time. My thanks also go to Mrs Helen Yard for her kind support and beautiful attitude during my study in Aston University.

I gratefully acknowledge all the members of Photonics Research Group of Aston University who have contributed immensely to my personal and professional time at Aston University. The group has been a source of friendships as well as good advice and collaboration.

My time in Birmingham was made enjoyable in large part due to the many friends and groups that became a part of my life and in between I would like to convey my special heartfelt thanks to my first friend in Birmingham, Mr Reza Tohidi for being such a fantastic and supportive person.

Last but not the least, my great love and thanks go to my parents, Shirin and Kioumars Saffari, for creating an environment in which following this path seemed so natural. Their support forged my desire to achieve all that I could in life. I owe them everything and wish I could show them just how much I love and appreciate them.

CONTENTS

ACRONYMS	18
Chapter 1	20
Introduction and Thesis Structure	20
1.1. Introduction	21
1.2. Structure Of Thesis	22
Chapter 2	25
Theoretical Basis of Optical Fibre Gratings	25
2.1. Introduction	26
2.2. Photosensitivity in Optical Fibres	27
2.2.1. Photosensitivity Mechanisms	27
2.2.2. Photosensitivity Enhancement Techniques	31
2.2.3. Multi Photon Absorption Process	35
2.2.4. Stabilisation of UV-Induced Index Change	36
2.3. Couple Mode Theory	38
2.3.1. Backward Mode Coupling	41
2.3.2. Forward Mode Coupling	42
2.3.3. Phase Match Condition	44
2.3.4. Fibre Bragg Grating (FBG)	45
2.3.5. Long Period Grating (LPG)	45
2.3.6. Tilted Fibre Grating (TFG)	46
2.4. History of Grating Inscription	49
2.4.1. Original Hill Grating	49
2.4.2. Holographic Side Writing Technique	50
2.4.3. Phase Mask Inscription Technique	52
2.4.4. Point-By-Point Inscription Technique	54
2.5. Chapter Conclusion	56
Chapter 3	57
Inscription of Advanced Fibre Gratings Utilising UV Laser	57
3.1. Introduction	58
3.2. Fabrication Techniques of Optical Fibre Gratings	59
3.2.1. Two Beam Holographic Technique	59
3.2.2. Phase Mask Technique	64
3.3. Chirped Fibre Gratings	68
3.4.1. Design Principle of TFGs	73
3.4.2. TFGs with Small Tilted Structure	78
3.4.3. TCFGs with Small Tilting structure	81
3.4.4. Polarisation Characteristics of Small Angle Tilted Fibre Gratings	83
3.4.5. Thermal Responses of Gratings with Small Tilted Structures	85
3.4.6. Thermal Responses of Gratings with Large Tilted Structures	90
3.5. Type IA Gratings	92
3.5.1. Hydrogen Diffusion Effect In Type IA Gratings	99
3.5.2. Thermal Response Of Type I-IA Gratings	102
3.6. Chapter Conclusions	104
Chapter 4	106

Optical Sensing and Embedded Fibre Bragg Gratings in Aluminium Alloy Matrix Composite	106
4.1. Introduction.....	107
4.2. Fabrication of FBG arrays and their embedding in metal matrix composite structures	108
4.2.1. UV inscription of FBG array in optical fibre.....	109
4.2.2. Embedding FBG arrays in metal matrix by ultrasonic consolidation.....	111
4.3. Characterisation of Embedded FBG Metal Matrix Samples	115
4.3.1. Investigation of Polarisation Effect in Embedded Samples	118
4.3.2. Investigation of Temperature Effect in Embedded Samples	121
4.3.3. Investigation of Loading Effect in Embedded Samples	123
4.3.4. Investigation of Bending Curvature Effect in Embedded Samples	128
4.4. Chapter Conclusion.....	135
Chapter 5	137
Micro-structured Fibre Bragg Gratings and their Sensing Applications	137
5.1. Introduction.....	138
5.2. Fabrication of Microchannelled Chirped Fibre Bragg Grating.....	140
5.3. Spectral, Thermal and RI Sensing Characteristics of MCFBGs.....	142
5.3.1. 50 μm - MCFBG.....	144
5.3.2. 550 μm - MCFBG.....	148
5.3.3. 1000 μm - MCFBG	152
5.4. Summary on MCFBGs	157
5.5. Micro-slot in Fibre Bragg Grating	158
5.5.1. Fabrication of Micro-slot in Fibre Bragg Grating	159
5.5.2. Characteristics of Micro-slot FBG.....	164
5.6. Conclusion	176
Chapter 6	137
Fibre Lasers Using Intra-Cavity Tilted Fibre Gratings	179
6.1. Introduction.....	180
6.2. Single Polarisation and Multiwavelength Switchable Fibre Ring Lasers Using Intracavity TFGs with structures tilted at $\geq 45^\circ$	181
6.2.1. Dual Wavelength Oscillation Laser Cavity	182
6.2.2. Triple and Quadruple Wavelength Oscillation Laser Cavity.....	191
6.2.3. Tuning and Sensing Capability of Proposed Laser Cavities	203
6.3. Single Polarisation Fibre Ring Laser Using TFGs with small tilted structure ..	206
6.3.1. Polarisation characteristics of 9.3° -TFG.....	206
6.3.2. Single polarisation output of fibre ring laser by using 9.3° -TFG	209
6.4. Chapter Conclusion.....	214
Chapter 7	216
Conclusions and Future Works	216
7.1. Conclusions.....	217
7.2. Suggestion For Future Research	221
Chapter 8	225
Publications & References	225
8.1. Publications:.....	226
8.2. References:.....	227

LIST OF FIGURES

Figure 2. 1. Photoinduced refractive index change mechanism: Ge-Si wrong bonds breaks and release free electron to diffuse into the lattice network. The resulting molecular change alters the absorption characteristics and consequently the refractive index [30].....	30
Figure 2. 2. OH absorption band for a hydrogenated germanosilicate optical fibre [42]	34
Figure 2. 3. Schematic demonstration of multi-photon absorption.	35
Figure 2. 4. Schematic diagram of backward-mode coupling in FBG.	45
Figure 2. 5. Schematic diagram of forward mode coupling in LPG.	46
Figure 2. 6. Schematic diagram of backward mode coupling in TFG.	46
Figure 2. 7. Schematic diagram of forward mode coupling in TFG.	46
Figure 2. 8. Schematic diagram of TFG.	47
Figure 2. 9. Schematic diagram of the original setup for inscription of FBG set by Hill <i>et al</i> [17].	50
Figure 2. 10. The schematic diagram of the experimental setup by Meltz <i>et al</i> [63]..	51
Figure 2. 11. The schematic diagram of phase mask grating inscription technique[69].	53
Figure 2. 12. Schematic diagram of point by point grating fabrication technique.	54
Figure 3. 1. Two-beam holographic FBG inscription system in the Photonics Research Group laboratory at Aston University.....	60
Figure 3. 2. Schematic diagram of optical setup for fibre grating inscription using holographic technique.	61
Figure 3. 3. Transmission spectrum of an FBG fabricated by holographic technique.	63
Figure 3. 4. Schematic of diffraction of an incident beam at angle $\Phi_i = 0$ into various orders from a phase mask.	64
Figure 3. 5. Experimental arrangements in the Photonics Research Group of Aston University for the phase mask fabrication technique.....	66

Figure 3. 6. Microscope image of a uniform period UV inscribed FBG fabricated by phase mask technique.	67
Figure 3. 7. Schematic diagram of a CFBG showing longer wavelengths travel further in the grating than shorter ones.	68
Figure 3. 8. Transmission spectra of CFBGs fabricated by the phase mask technique.	70
Figure 3. 9. Transmission spectra of 5-mm CFBGs fabricated using different part of the mask.	71
Figure 3. 10. Schematic of the chirped phase mask and pointing different parts that were employed for inscription of each CFB.	72
Figure 3. 11. Phase mask technique for TFG fabrication. Note the mask has been tilted by angle α	73
Figure 3. 12. Two beam holographic technique for TFG fabrication while the fibre has been rotated by angle Φ	74
Figure 3. 13. Schematic diagram of a TFG structure exhibiting the difference between internal and external tilted angles.	75
Figure 3. 14. Phase matching conditions for TFGs with tilt angles, $\theta < =$ and $> 45^\circ$. <i>Note: Φ is the incident angle of the radiated light at the cladding boundary</i>	76
Figure 3. 15. Three coupling regimes for the phase matched light: (a) $\theta < \theta_{1c}$: Contrapropagating cladding mode coupling; (b) $\theta_{1c} < \theta < \theta_{2c}$: radiation mode coupling and (c) $\theta > \theta_{2c}$: forward cladding mode coupling.....	78
Figure 3. 16. Transmission-loss profiles of six TFGs with external tilt angles from 0° to 10° (note: the spectra were measured when the TFGs were submerged in index match gel to ensure the smooth profiles).	79
Figure 3. 17. Transmission spectra of 8° -TFG UV inscribed in B/Ge fibre using the phase-mask method. <i>Note: The resonance profile was obtained when the grating was surrounded by air and the smooth profile obtained when the grating was immersed in the index matching gel.</i>	80
Figure 3. 18. Transmission spectrum of UV inscribed externally 2° TFG in SMF 28 fibre employing the phase mask method.	81
Figure 3. 19. Transmission spectra of TCFGs with the external tilt angles from 0° to 10° . <i>Note: the spectra were measured when the TFGs were surrounded by air.</i>	82
Figure 3. 20. Schematic diagram of experimental setup for characterising the polarisation response of TFGs with small tilted structure.	83

Figure 3. 21. Transmission spectra of the UV induced TFGs with external angle $\theta =$ (a) 6° and (b) 10° in two polarisation states. <i>Note: the blue graph in figure. (b) is the transmission spectrum of the TFG when the probed light is not polarised.</i>	84
Figure 3. 22. Transmission spectra of the UV induced TCFGs with external angle $\theta =$ (a) 6° , (b) 8° and (c) 10° in two polarization states.	84
Figure 3. 23. Thermal response of normal FBG.	86
Figure 3. 24. Thermal responses of three selected dual peaks of 6° -TFG at 1500 nm, 1510 nm and 1520 nm.....	86
Figure 3. 25. Thermal responses of three selected dual peaks of 10° -TFG at 1499.6 nm, 1515.8 nm and 1543.2 nm.....	87
Figure 3. 26. Thermal responses of 0° -, 4° - and 6° -TCFGs.	88
Figure 3. 27. (a) Full transmission spectrum of 79.6° -TFG and (b) zoomed spectra of one paired polarisation loss peaks of 79.6° -TFG around 1550 nm measured with randomly (black line) and fully polarised input lights (red and blue lines).	89
Figure 3. 28. (a) Full transmission spectrum of 81.7° -TFG and (b) zoomed spectra of one paired polarisation loss peaks of 81.7° -TFG around 1550 nm measured with randomly (solid line) and fully polarised input lights (dashed lines).	89
Figure 3. 29. Thermal responses of the selected two pairs of dual peaks at 1341.1/ 1320.2 nm and 1672.2/1680.3 nm from 79.6° -TFG and two pairs of dual peaks at 1335.6/1340.8 nm and 1664.0/1671.6 nm from 81.7° -TFG spectrum.	91
Figure 3. 30. The transmission spectrum of a pair of Type I, IA gratings in PS1250/1500 fibre. <i>Note: the big absorption loss~ 14dB at 1400 nm that formed during the blank beam exposure process indicates the maturity of the fibre.</i>	95
Figure 3. 31. The transmission spectrum of a pair of Type I, IA gratings in SM1500 fibre.	97
Figure 3. 32. The transmission spectrum of a pair of Type I, IA gratings in SM1500 fibre.	98
Figure 3. 33. Transmission loss profiles of two identical samples made of SM1500 fibre type, one kept in the room temperature and the other was annealed at 103°C for 24 hours.....	100
Figure 3. 34. Transmission loss profiles of two identicalsamples made of B/Ge fibre type, one kept in the roomtemperature and the other was annealed at 103°C for 24 hours.....	100
Figure 3. 35. Bragg wavelength shift of (a) Type I and (b) Type IA grating inscribed in BG/e co-doped fibre over a period of one month at the room temperature.....	101

Figure 3. 36. Bragg wavelength shift of (a) Type I and (b) Type IA grating inscribed in SM1500 fibre over a period of one month at the room temperature.	101
Figure 3. 37. Thermal responses of Type I-IA gratings written in B/Ge co-doped fibre	102
Figure 3. 38. Thermal responses of Type I-IA gratings written in SM1500 fibre....	102
Figure 4. 1. Schematic diagram of the fabricated FBG array with three gratings at different wavelengths.....	110
Figure 4. 2. Alpha UC machine in the laboratory of Rapid Manufacturing Research Group of Loughborough University.	111
Figure 4. 3. Schematic diagram of the ultrasonic consolidation system used to embed FBG array fibres in metal matrix composite samples.....	114
Figure 4. 4. Cross section microstructures of the SM fibre (without jacket) embedded sample, a) bright field image, b) polarised light image after anodisation.....	114
Figure 4. 5. Measured transmission spectra of (a) sample S1, (b) sample S2 and (c) sample S3 before (blue graph) and after embedding	116
Figure 4. 6. Schematic diagram of the setup for polarisation measurement.....	118
Figure 4. 7. Polarisation measurements of (a) P1, (b) P2 and (c) P3, the three sub-gratings from sample S2.	119
Figure 4. 8. Polarisation measurements of (a) P1, (b) P2 and (c) P3 gratings from sample S1.....	120
Figure 4. 9. Schematic diagram of the temperature measurement set-up.....	121
Figure 4. 10. Transmission spectrum of S2, while it was subjected to a range of different temperatures from 0° C to 100° C.	122
Figure 4. 11. Temperature response of three embedded FBGs, P1, P2 and P3 in sample S2.....	122
Figure 4. 12. Temperature sensitivity of three embedded FBGs in S2.....	123
Figure 4. 13. Schematic diagram of experimental setup for loading measurement... Figure 4. 14. Transmission spectrum of the embedded sample under different loaded masses.	124
Figure 4. 15. Loading response of first embedded FBG, P1 in sample S2. The inset shows the loading sensitivity of the grating to the masses in the range of 0 kg – 1.5 kg	125

Figure 4. 16. Loading response of 2nd embedded FBG, P2 in sample S2. The inset shows the loading sensitivity of the grating to the masses in the range of 0 kg – 2 kg.	126
Figure 4. 17. Loading response of 3rd embedded FBG, P3 in sample S2.....	127
Figure 4. 18. Loading sensitivity of P3 to the masses in the range of 0 kg – 3 kg.	128
Figure 4. 19. Loading sensitivity of P3 in the range of 3 kg- 8 kg.	128
Figure 4. 20. Schematic diagram of the bending response measurement and presenting the maximised schematic diagram of the four-point bend system with a=120 mm, b=20 mm and bend depth h=0 to ~ 8 mm.....	128
Figure 4. 21. Curvature against bending depth using the four-point bending equipment.....	130
Figure 4. 22. Transmission spectral evolution of S2, while it was subjected to the bending measurement.	131
Figure 4. 23. Bending curvature sensitivities of three embedded gratings in sample S2.	131
Figure 4. 24. Transmission spectra of S2, while it was fully turned over and was subjected into the same bending measurement.	133
Figure 4. 25. Bending curvature sensitivities of three embedded gratings in sample S2 while the sample was fully turned at 180°.	134
Figure 5. 1. Schematic diagram of the proposed MCFBG consisting of a CFBG in the fibre core, and a microchannel (with the width of Lm) created in the middle region of the CFBG across the fibre.....	140
Figure 5. 2. UV inscribed 10-mm long CFBG in H ₂ loaded SMF-28 fibre.....	141
Figure 5. 3. RI response of a normal CFBG when it was immersed in a range of RI liquids.....	143
Figure 5. 4. Microscope image of 50 μm- MCFBG under a ×20 microscopic lens. .	144
Figure 5. 5. Transmission spectrum of 50 μm-MCFBG	145
Figure 5. 6. RI response of 50 μm-MCFBG when it was immersed in a set of RI oils	146
Figure 5. 7. Thermal response of 50 μm-MCFBG.....	147
Figure 5. 8. 550 μm- MCFBG microscope image under a ×10 microscopic lens. The inset shows the end image of the microchannel under a ×40 oil-immersion microscopic lens.....	148

Figure 5. 9. Transmission spectrum of 550 μm -MCFBG.....	149
Figure 5. 10. The wavelength shifts of the main (black squares) and the first sub transmission peak (red-circles) against refractive index of surrounding medium.....	150
Figure 5. 11. Thermal responses of main- and sub-transmission peaks of 550 μm -MCFBG.....	152
Figure 5. 12. Transmission spectrum of 1000 μm -MCFBG.....	153
Figure 5. 13. The zoomed spectrum of interference features from the stopband of 1000 μm -MCFBG.....	153
Figure 5. 14. Microscope image of the 1000 μm - MCFBG under a $\times 10$ microscopic lens.	153
Figure 5. 15. The wavelength shift of the main (red circles) and the first sub transmission peak (black squares) against refractive index of surrounding medium.	155
Figure 5. 16. Thermal responses of the main and sub-transmission peaks from the 1000 μm -MCFBG.	156
Figure 5. 17. The geometry of the proposed micro-slot along the grating and across the fibre.	159
Figure 5. 18. Transmission spectrum of UV inscribed 1mm-long FBG before induction of a micro-slot into its structure.	161
Figure 5. 19. RI response of 1mm-long FBG when it was immersed in a set of RI oils.....	162
Figure 5. 20. Thermal response of 1mm-long FBG.....	163
Figure 5. 21. Microscope image under a $\times 5$ microscopic lens showing the 1388.72 μm - micro-slot along a FBG and across the fibre. <i>Note: The insets are the microscope images of the same device observed by $\times 40$ oil-immersion microscopic lense.</i>	164
Figure 5. 22. Transmission loss profile of the micro-slot FBG when it was surrounded by air.	165
Figure 5. 23. Schematic diagram of the light distribution in micro-slot FBG when it is surrounded by air.	166
Figure 5. 24. The Transmission spectrum of the micro-slot FBG when it was immersed in 1.36 RI oil.	166
Figure 5. 25. The Transmission spectrum of the micro-slot FBG when it was immersed in 1.478 RI oil.	167

Figure 5. 26. RI characteristic of the proposed micro-slot FBG.....	169
Figure 5. 27. Thermal response of the 1mm-long micro-slot FBG when it was immersed in 1.448 RI oil. <i>Note: By increasing the temperature RI value of the oil decreases by rate of (-dn/dT=3.79×10⁻⁴/°C) and as indicated in the figure at 25°C and 60°C, the RI value of oil decreases from 1.448 to 1.442 and 1.429 respectivel .</i>	170
Figure 5. 28. Thermal response of micro-slot FBG when it as immersed in 1.456 RI oil	172
Figure 5. 29. PDL measurement of micro-slot FBG when it was immersed in air and RI oils.....	175
Figure 6. 1. The schematic setup of a single and dual wavelength switchable fibre laser cavity	183
Figure 6. 2. Schematic diagram of PDL measurement of 45°-TFG.	184
Figure 6. 3. PDL spectrum of 5 cm long 45°-TFG . <i>Note, the ripples are due to the residual reflection at the air-cladding boundary and the red line gives the spectrum when the grating immersed in index match gel.</i>	185
Figure 6. 4. (a) Transmission spectrum of the 77°-TFG over wavelength range of 1200 nm – 1700 nm; (b) Zoomed spectra of one paired polarisation loss peaks of 77 °-TFG around 1550 nm measured with randomly (solid line) and fully polarised input lights (black dotted line: fast-axis; red dotted line: slow-axis).	187
Figure 6. 5. Single-wavelength lasing oscillation of the proposed fibre ring laser using 45°-TFG and 77°-TFG lasing at two the seeding wavelengths (a) 1548 nm and (b) 1553.nm; (c) and (d) show the laser outputs at these two wavelengths for a 30min period.	188
Figure 6. 6. (a) Dual-wavelength lasing oscillation of the proposed fibre ring laser, (b) Stability of dual-wavelength oscillation (30 times repeated scan).	189
Figure 6. 7. Output power vs pump diode current for lasing at 1553 nm.....	191
Figure 6. 8. Schematic diagram of the tripe and quadruple wavelength fibre ring laser cavity.....	192
Figure 6. 9. (a) Transmission spectrum of the 79°-TFG over wavelength range of 1200 nm -1700 nm; (b) Zoomed spectra of one paired polarisation loss peaks of 79 °-TFG around 1550 nm measured with randomly (solid line) and fully polarised input lights (dashed lines).	193
Figure 6. 10. Single wavelength oscillation at (a) 1547.05 nm (b) 1553.27 nm and (c) 1563.07 nm.	194

Figure 6. 11. Demonstration of alternative dual wavelength lasing at (a) 1547.06 nm / 1553.27 nm (b) 1547.06 nm / 1563.07 nm and (c) 1553.27 nm / 1563.07 nm.....	195
Figure 6. 12. Triple wavelength oscillation for all three wavelengths.....	195
Figure 6. 13. Single wavelength lasing at (a) 1547 nm, (b) 1553 nm, (c) 1563 nm and (d) 1569 nm.....	196
Figure 6. 14. Output power against pump diode current for lasing at 1553nm.	198
Figure 6. 15. Output power against pump diode current for lasing at 1559nm.	198
Figure 6. 16. Demonstration of alternative dual-wavelength lasing at (a) 1547.06 nm/1553.27 nm (b) 1547.05 nm/1553.27 nm and (c) 1553.27 nm/1563.05 nm.....	199
Figure 6. 17. Triple wavelength oscillations at (a) 1546.94nm/1551.99nm/1562.63nm (b) 1546.94 nm/1551.99 nm/1568.89 nm (c) 1551.99 nm/1562.63 nm/1568.89 nm.	200
Figure 6. 18. The quadruple wavelength lasing of the proposed system.	201
Figure 6. 19. Stability measurement of (a) Single (b) Double, (c) Triple & (d) Quadruple lasing oscillations under the laboratory conditions & room temperature over 30 mins.....	202
Figure 6. 20. (a) Increasing temperature induced laser spectral evolution and (b) wavelength shift against temperature.....	204
Figure 6. 21. (a) Strain induced laser spectral evolution and (b) wavelength shift against strain.	204
Figure 6. 22. (a) Increasing temperature induced laser spectral evolution and (b) wavelength shift against temperature.....	205
Figure 6. 23. (a) Strain induced laser spectral evolution and (b) wavelength shift against strain.	206
Figure 6. 24.The transmission spectra of the 9.3°-TFG in air (multi-resonance) and immersed in index matching gel (solid line) and the inset shows the microscope image of 9.3°-TFG.	207
Figure 6. 25. PDL measurement for the 9.3° TFG while it was immersed in the index matching gel.....	208
Figure 6. 26. PDL measurement for the 9.3°-TFG while it was surrounded by air in (a) short- wavelength range, (b) medium wavelength range and (c) long wavelength range.....	209
Figure 6. 27. Schematic diagram of the single polarisation fibre ring laser system..	210
Figure 6. 28. Measured polarisation extinction ratio of the laser output oscillation at 1535 nm.	211

Figure 6. 29. Pumping efficiency of the proposed ring laser cavity.	212
Figure 6. 30. Stability measurement of the single polarised laser output.	213

LIST OF TABLES

Table 3. 1. Designed data for FBG fabrication by employing the holographic method	63
Table 3. 2. The measured blue shift of grating pairs in different fibre types.....	100
Table 4. 1. Parameter control ranges for the alpha UC machine.	112
Table 4. 2. Analysed data from three embedded samples.....	117
Table 6. 1. Summary of the measured technical values of the proposed TFG based fibre ring laser cavity.	202

ACRONYMS

BBS	Broadband Light Source
B/Ge	Boron/Germanium codoped
CFBG	Chirped Fibre Bragg Grating
CTE	Coefficient of Thermal Expansion
CW	Continuous Wavelength
DOP	Degree of Polarisation
EDF	Erbium Doped Fibre
EDFL	Erbium Doped Fibre Laser
EMI	Electromagnetic Interference
FBG	Fibre Bragg Grating
FS	Femtosecond
GODC	Germanium Oxygen Deficient Centre
HF	Hydrofluoric Acid
LPG	Long Period Grating
MCFBG	Mircorchanneled Chirped Fibre Bragg Grating
MCVD	Modified Chemical Vapour Deposition
OIS	Optical Isolator
OSA	Optical Spectrum Analyser
OSNR	Optical Signal to Noise Ratio
SMSR	Side Mode Suppression Ratio
PC	Polarisation Controller
PDL	Polarisation Dependent Loss
PER	Polarisation Extinction Ratio

PHB	Polarisation Hole Burning
PM	Polarisation Maintaining
RI	Refractive Index
SMF	Single Monomode Fibre
SRI	Surrounding-medium Refractive Index
TCFG	Tilted Chirped Fibre Grating
TFG	Tilted Fibre Grating
TIR	Total Internal Reflection
UC	Ultrasonic Consolidation
UV	Ultraviolet
WDM	Wavelength Division Multiplexing

Chapter 1

Introduction and Thesis Structure

1.1. Introduction

After the discovery of low loss optical waveguide in 1960 [1], fibre optics have been developed in such an extent that over last few decades, the use of optical fibres has revolutionised the way the world exchanges and processes information. The feasibility of handling over 25 trillion bits of data per second across oceans to different sectors of our society and providing high-speed communications that impacts all facets of modern life are consequences of optical fibres, substituting copper wires as the transmission medium.

Due to the advantages of non-electromagnetic interference, light weight, flexibility, low-loss and high temperature tolerance, optical fibres not only have developed and commercialised in optical communications but also underpinned the fast growing technology of sensing and metrology.

Optical fibre gratings have become one of the most important components in optical communication and sensing since their discovery in 1978 by Hill *et.al* at the Canadian Communications Research Centre (CRC) [2]. There are two major categories for fibre gratings named as FBGs and LPGs. The period of an FBG is approximately half a micrometer whereas the period of an LPG is typically several hundred micrometers. According to well known coupled-mode theory, in FBGs the guided mode will be coupled into the corresponding backward mode [2, 3] while LPGs induce codirectional coupling in which the guided mode will be coupled to the cladding modes. Further advances in UV-inscription technology and variety of novel fibres have led to the generation and development of fibre gratings with new and complicated structures that offer novel applications in communication and optical sensing.

Smart grating based sensors with functions superior to their conventional counterparts have a demonstrated capability of measuring and encoding a wide range of physical, chemical and biochemical data and being used for structure health monitoring across numerous industrial sectors including aerospace, civil, oil and gas, power and nuclear, etc. This thesis will review the smart functions of optical fibre gratings with different structures and illustrate their novel applications in optical sensing and laser systems. Predicted dramatic advances that will provide many, further social and economic benefits on one hand and the increasing demand for high function devices for a broad range of applications on the other hand are the motivations of this thesis.

1.2. Structure Of Thesis

This thesis describes the fundamentals, various fabrication techniques, versatile structures and different novel applications of fibre gratings. Chapters 1, 2 and 3 provide the introduction and a comprehensive discussion on fundamentals, inscription methods, spectral response and characteristics of different type gratings which assist the reader to understand the concept of fibre gratings and their applications in subsequent chapters. Chapters 4, 5 and 6 each describe individual novel applications for the advanced fabricated gratings and chapter 7 provides the thesis conclusion and suggests some research works for future. The contents of each chapter are as follows:

Chapter 1 explains the motivation and the structure of the thesis.

Chapter 2 gives a historical overview on the fundamentals and theoretical concept of fibre gratings with emphases on mode coupling theory and phase-matching conditions

for gratings of different structures. This chapter also covers the description of photosensitivity in optical fibre and a brief introduction to few popular photosensitising techniques.

Chapter 3 introduces the in-fibre grating inscription methods, fabrication and detailed characterisation of fibre gratings with novel structures including type I and IA, Chirped Fibre Bragg Gratings (CFBG) and Tilted CFBG (TCFG), Tilted Fibre Gratings (TFGs) with small, medium and large tilt angles. Comparative investigations of hydrogen diffusion and temperature characteristics of type I-IA gratings written in three different types of fibre, SM1500, B/Ge and PS 1250/1500 are presented.

Chapter 4 illustrates the application of optical fibre gratings in distributed sensing area employing embedded FBG arrays into metal composites. This chapter addresses the first time fabrication of embedded FBG array sensors in metal matrix composite employing the ultrasonic consolidation technique. The FBG embedded sandwich structure has been subjected to thermal, loading and bending measurements and performed the self-sensing capability, which is beneficial for a range of applications including monitoring the operation and health of engineering structures.

Chapter 5 forms one of the major contributions to this thesis on implementation of optical Refractive Index (RI) sensors utilising CFBGs and FBG with modified structures by fs laser inscription and chemical etching. The chapter gives a detailed explanation on RI sensing principle and fs aided hydrofluoric (HF) acid etching technique, which has been employed to enhance the RI sensitivity in the gratings, and

includes a systematic study of RI and temperature characteristics of the proposed devices.

Chapter 6 is also counted as another major part of this thesis and presents different novel techniques in realisation of fibre laser systems with single polarisation output being switchable at single and multi wavelengths by using TFGs with different tilt angles as intra-cavity polariser and polarisation loss dependent filters in the ring fibre laser cavity. The investigations on Degree Of Polarisation (DOP), stability, thermal and strain sensitivities of the proposed laser systems are also included to this chapter.

Chapter 7 concludes the work and provides some ideas for future research activities.

Chapter 2

Theoretical Basis of Optical Fibre Gratings

2.1. Introduction

This chapter contains an overview of the fundamental theory of in-fibre optical gratings. It begins with the review of the historical prospective of the photosensitivity mechanisms in optical fibres and a brief discussion on the reported photosensitisation techniques. The chapter also propose an introduction to the mode coupling theory for backward and forward coupled grating devices including FBGs, LPGs and TFGs. Finally we will give a brief introduction to different grating fabrication techniques, including two-beam holographic, phase mask scanning and point-by-point methods followed by a summary of the chapter.

2.2. Photosensitivity in Optical Fibres

Photosensitivity in optical fibres invariably refers to a permanent (or quasi-permanent) change in the RI of the fibre core following the exposure to light with characteristic wavelength and intensity depending on the core material. Photosensitivity of optical fibres was first discovered by Hill *et.al* in 1978 in germano-silicate fibres during the fabrication of the Hill grating [2] and since then, several published studies have explained the photosensitivity mechanisms. Regardless of the worldwide interest into the subject, there is still no single model to explain the photosensitivity in all cases, but it has been realised that the photosensitivity depends on a number of factors, including the core material and the wavelength and intensity of the radiating light. In the early research, it was believed that the photosensitivity only exists in germanium doped fibres [4], but later studies reported the photosensitivity in a wide range of different fibres containing other dopants such as europium [5], cerium [6], and erbium: germanium [7] that exhibit different degrees of sensitivity in silica host optical fibre. However, germanium doped fibres are still the most interesting photosensitive fibres due to their extensive applications in telecommunication and optical sensor area.

2.2.1. Photosensitivity Mechanisms

The photosensitivity mechanisms have been reported in several models including: colour-centre [8], compaction [9], stress relief [10], electron charge migration [11], permanent electric charge dipole [12], ionic migration model [13], and Soret effect [14].

In all mentioned models, the germanium oxygen vacancy defects such as twofold coordinated neutral germanium atom (GeO_2) or Ge-Si or the wrong bond (Ge-Ge) are the common responsible elements for the photoinduced refractive index changes in the germano-silicate fibre. In fibre drawing process, the gas phase oxidation process of the Modified Chemical Vapour Deposition (MCVD) technique occurs at such a high temperature that GeO_2 molecule breaks in to the more stable state of GeO molecule and itself becomes Ge^{2+} centre. When Ge^{2+} incorporates into the glass material, can form oxygen vacancy Ge-Si or wrong bonds Ge-Ge, which in both cases the created oxygen deficient matrix in the glass is linked to 240 nm absorption band. Here we only will briefly explain three main mechanisms regarding the photosensitivity characteristics of the most common germanium doped fibres: colour centre, compaction densification and stress relief models.

2.2.1.1. Colour Centre or Point Defect Model

Ionising radiation [15] and the fibre drawing process [16] can create defects centres, so called colour centres, which are very important for optical fibre due to their absorption bands. To understand the nature of colour centres, it is helpful to review the defects in germano-silicate fibres. Despite Si, Ge has two stable oxidation centres: +2 and +4, thus it can form either GeO_2 or GeO molecules in the glass. Thermodynamic rules imply a balance between GeO_2 and Germanium Oxygen Deficient Centres (GODCs) concentrations. Also as it has been explained before, at high temperature, GeO is more stable than GeO_2 and can exist as a discrete molecule but it is more likely to manifest itself in the form of wrong bonds, Ge-Si, in the glass. These wrong bonds are suspected defect precursors. Radiation studies on the

paramagnetic defect centres in the germano-silicate fibres indicate that Ge dopant of the core is directly related to damage centres which are labelled as Ge(n) [17]. Ge(n) centres can change to $\text{Ge}(n)^-$ centres by trapping an electron. Ge(0)/Ge(3) damage centres are also called GeE' centre which has the deepest electron trap depth.

The colour centre model was proposed by Hand and Russel [8] for the first time. As illustrated in Figure 2.1, in this model Ge-Si wrong bonds break under the UV exposure and form GeE' centres and release the electron into the glass matrix. The free electron will be recaptured elsewhere in the network and create a new form of defect centre such as $\text{Ge}(1)^-$ and $\text{Ge}(2)^-$. A later study by Atkins *et.al* performed that illuminating the fibre by a wavelength in coincidence with 240 nm band, results in bleaching of 241 nm band and creation of a new absorption band with the centre peak at 195 nm [19]. The new absorption bands will induce the RI change following Kramers - Kroning relationship [20]:

$$\Delta n_{\text{eff}}(\lambda) = \frac{1}{2\pi^2} P \int_0^\infty \frac{\Delta \alpha_{\text{eff}}(\lambda)}{1 - \left(\frac{\lambda}{\lambda'}\right)^2} d\lambda \quad (\text{eq:2.1})$$

Where P is the principal part of the integral, λ is the wavelength, and $\alpha_{\text{eff}}(\lambda)$ is the effective change in the absorption coefficient of the defect.

This relationship indicates that any photoinduced index change in the spectral range between infrared to visible is a consequence of a change in the absorption spectrum of the silica in the UV to far-UV spectrum [7, 21-23].

The colour centre model for the photosensitivity effect is supported by many researches and evidently the responsible mechanism for the original Hill grating was two photon beam absorption at 240 nm band [24, 25].

Although the model can explain the photosensitivity in both germanosilicate and hydrogen loaded geramnosilicate fibres up to a certain point, it is unable to fully explain the experimental investigations especially in higher value of RI changes [26-30].

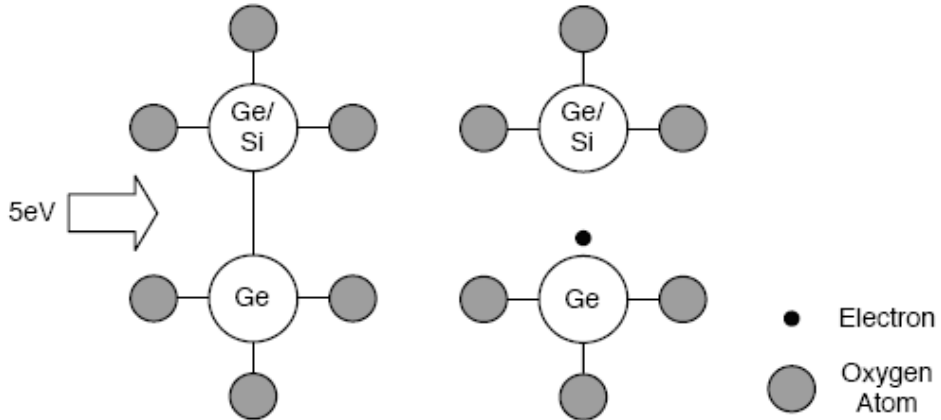


Figure 2. 1. Photoinduced refractive index change mechanism: Ge-Si wrong bonds breaks and release free electron to diffuse into the lattice network. The resulting molecular change alters the absorption characteristics and consequently the RI [30].

2.2.1.2. Compaction Densification Model

In the densification model, the RI of the glass is enhanced by the increase of laser irradiation induced density of the glass. Originally, Fiori and Devine [9] reported the experiment in which a thin film of amorphous silica grown on Si wafers was irradiated by a KrF excimer laser. After irradiation, 16% of the film's thickness was decreased while the RI was increased. Then they annealed the sample at 950°C in a vacuum for about 1 hour and discovered that the compaction disappeared and both refractive index and film's thickness returned to their original values. Further radiation resulted in compaction beyond the threshold and a permanent densification occurred. Malo *et.al* discovered [31] that annealing the sample at 1200°C fully removes the photosensitivity of the fibre, which is irreversible. It has been

experimentally proved that the photoinduced RI changes in non-hydrogen loaded fibres occur mainly due to the densification of the silica [32].

2.2.1.3. Stress Relief Model

During the high temperature fibre drawing process, the fibre core experiences an inner tension due to different thermal expansion of the core and cladding. At some point during the quick glass cooling process, the structure is frozen. According to the stress optic effect, thermal induced inner tension reduces the RI while the stress relief will increase the RI. The stress-relief model considers the RI change in germanosilicate fibre core due to the relaxation of built-in thermo-elastic stresses [33]. In 1995, Levy reported that the breakage of the wrong bonds over UV exposure will promote relaxation in the tensioned glass and reduce thermal stresses in the fibre core hence increase the RI of the core [34].

2.2.2. Photosensitivity Enhancement Techniques

Since simultaneous discovery of FBGs and fibre photosensitivity by Hill *et.al* considerable efforts have been made to increase the photosensitivity of the fibres as the intensity and UV exposure time affecting the grating property directly. The developed photosensitisation techniques, including co-doping in fibre core [35], hydrogen loading (hydrogenation) [36, 44] and flame brushing [37], are able to increase the photoinduced index modulations in the fibre core up to the order greater than 10^{-3} [37].

2.2.2.1. Co-doping Technique

The photosensitivity of germanosilicate fibre can be increased by adding various codopant such as boron (B) [35] and tin (Sn) [38, 39] into the fibre. In 1993, Williams *et.al* reported a systematic study on the corresponding photosensitivity to different fibre types including B doped fibres [40]. This report was addressing a saturated index change in B codoped fibre of about 4 times greater than that in pure germanosilicate fibre. In their experiment, three fibres: 1- standard telecom fibre (3 mol% GeO₂), 2- fibre with high Ge concentration (20 mol% GeO₂) and 3- B co-doping fibre (15 mol% GeO₂) were UV exposed until their index modulation became saturated. They achieved the saturated index modulation of approximately 7×10^{-4} for B co-doped fibre (15 mol% GeO₂) over about 10 minutes while for other two fibres, it took about 2 hours to reach the saturated index modulation of $\sim 3 \times 10^{-5}$ and $\sim 2.5 \times 10^{-4}$ respectively. Addition of boron oxide to silica results in a compound glass that has a lower RI than silica so B codoping reduces the RI of the core and makes it softer than before [17]. The absorption measurements suggest that in contrast to hydrogen loading and flame-brushing techniques, boron codoping does not enhance the fiber photosensitivity through production of GODCs. Instead, it is believed that stress relief is the photosensitivity mechanism of boron codoping technique. It seems likely that the RI of the core increases through photoinduced stress relaxation initiated by breaking of the wrong bonds by UV light. Although these investigations evidently indicate a much better photosensitivity response from B codoped fibre than the fibre with only equivalent Ge concentration, boron doping causes extra loss about 0.1 dB at 1550 nm range, which is not desirable.

In another approach to enhance the photosensitivity of the fibre, Sn was added to the fibre core as codopant. Dong *et.al* [38, 39] reported that Sn codoped fibre exhibits the saturated RI change of 3 times bigger than of the normal germanosilicate fibre. Undoubtedly this value can compete with what was investigated from B doped fibres. Sn codoped fibre also benefits from some advantages over B doped fibres including the grating survival at high temperature, as well as no induced loss induction in the 1500 nm window.

2.2.2.2. Hydrogen Loading or Hydrogenation Technique

Hydrogenation technique is a simple but highly effective approach to increase the UV induced photosensitivity in gremanosilicate fibres in which the fibres are pressurised in H₂ gas, at usually at room temperature, before the UV exposure process. The technique was introduced by Lemaire *et.al* for the first time in 1993 [37, 44] and is based on the interaction between Ge, Si and H₂ molecules in combination with UV exposure conditions. They soaked the fibre in H₂ gas at the temperature in the range of 20°C and 75°C and the pressure from approximately 20 atm to almost 750 atm. Then the fibre was exposed to the pulsed UV radiation. The result indicated the peak to peak index modulation of about 6×10^{-3} for hydrogen loaded fibre containing 3 mol% GeO₂ with 3.3 mol% H₂ and the enhanced average core index by 3.4×10^{-3} . The achieved increased photosensitivity in this process is due to the capability of hydrogen to create additional GODCs from germanium atoms in the lattice in the following fashion. In hydrogenation process, the fibre is housed in a high pressure hydrogen gas tube so H₂ molecules can diffuse into the fibre core via the cladding. UV exposure or any intense heat, including flame or CO₂ laser, will result in dissolving H₂ to thermally react with Si-O-Ge glass sites and subsequent formation of additional

GODCS, Si-OH and Ge-OH bonds which cause the large permanent index changes in the fibre core. As presented in Figure 2.2 the UV created OH band is centred about 1400 nm and contains two absorption peaks at 1390 nm and 1410 nm corresponding to Si-OH and Ge-OH bonds respectively. Canning *et.al* reported that the size of OH absorption band at 1400 nm is proportional to the hydrogen level in the fibre [41].

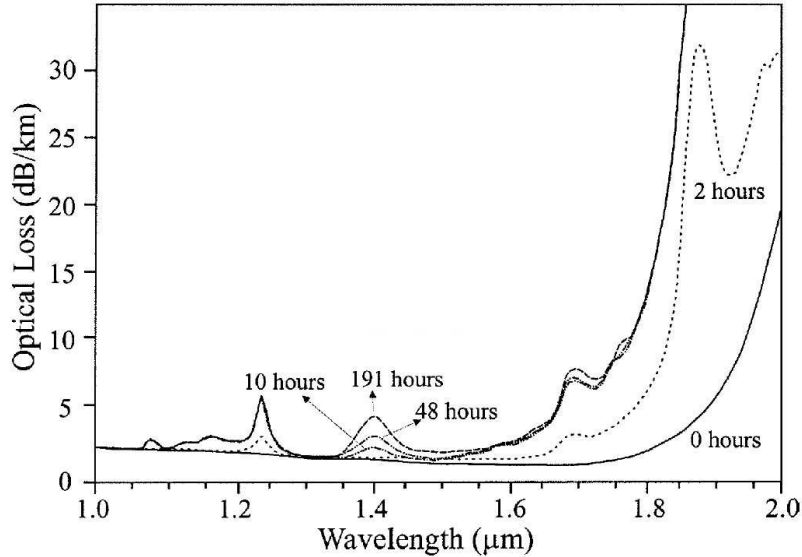


Figure 2. 2. OH absorption band for a hydrogenated germanosilicate optical fibre [42].

They also proved that it is possible to increase the photosensitivity of the fibre without creating a large OH band by employing the hydrogenation technique. To do so, first the fibre should be pre-sensitised during hydrogen loading and then goes through hydrogen outgassing process. However, this method is not applicable for type IA grating fabrication in which the presence of hydrogen is necessary.

2.2.2.3. Flame Brushing Technique

Flame brushing is an alternative technique to enhance the intrinsic photosensitivity of germanosilicate optical fibres. This technique is based on brushing the fibre repeatedly by a flame of a hydrogen and small amount of oxygen at a temperature of approximately 1700°C for almost 20 minutes [43]. Over the period of flame brushing process, diffused H₂ into the core quickly reacts with the glass lattice and forms GODCs and a strong absorption band at 240 nm UV range [17]. The effect only targets the fibre core while the cladding properties remain unaffected. It has been reported that by employing this technique, the photosensitivity of standard telecom fibres can be elevated by a factor of 10 and changes greater than 10⁻³ in the RI of the core at 1540 nm is achieved [43].

2.2.3. Multi Photon Absorption Process

It is extremely well known that the original Hill grating was 2-photon absorption process at 488 nm, which is shown schematically in Figure 2.3.

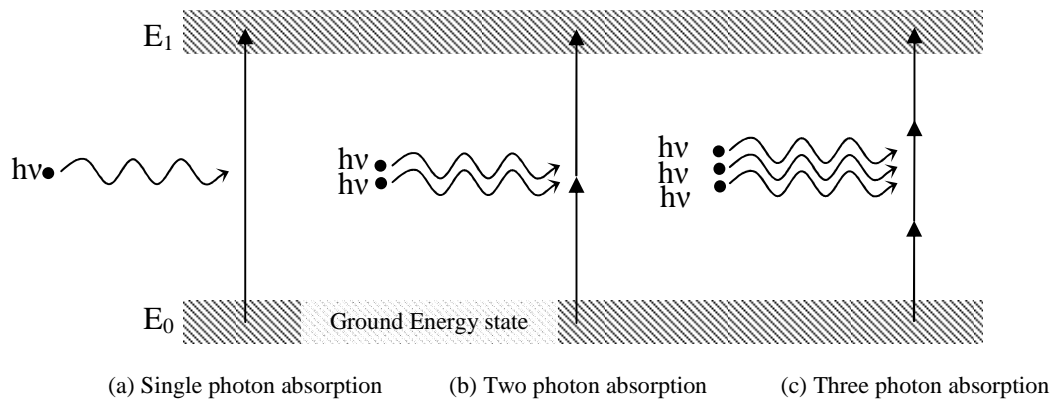


Figure 2. 3. Schematic demonstration of multi-photon absorption.

Niels Bohr defined the energy of a photon (E) proportional to its frequency by following equation:

$$E = hf = \frac{hc}{\lambda} \quad (\text{eq: 2.2})$$

Where h is Planck constant ($6.63 \times 10^{-34} \text{ J.s}^{-1}$), f is the frequency of the photon and c is the speed of light ($2.998 \times 10^8 \text{ m.s}^{-1}$). Bohr showed that in an atomic transition, when an electron from the excited energy band (E_1) returns to the ground state (E_0) to stabilise, a photon is emitted. The energy of this emitted photon is equal to the energy gap between excited and ground energy bands as follows:

$$hf = \frac{hc}{\lambda} = E_1 - E_0 \quad (\text{eq: 2.3})$$

Also, the same amount of energy, ($|E_1 - E_0|$), is required to excite an electron from E_0 to E_1 .

According to equation (2.2) the photon energy at 488 nm is 2.54 eV where 1 eV is defined as 1.60210^{-34} J . For a single photon absorption process, Figure 2.3 (a), the photon should have twice of that energy which is 5.08 eV. This energy corresponds to 244 nm wavelength of light and hence currently UV lasers operating at 244 nm are employed for grating fabrications. The frequency doubled Ar⁺ lasers operating at 244 nm which were also used for grating inscription in this thesis are good examples of this class of laser.

2.2.4. Stabilisation of UV-Induced Index Change

The UV induced index change in optical fibre is not a permanent phenomenon as after UV exposure, any dissolved or unreacted H₂ diffuses out of the fibre slowly.

Hydrogen diffusion leads to the wavelength shift of the Bragg resonance in a UV written FBG. As hydrogen diffusion rate increases with increasing temperature, the sensor gratings are often required to be annealed at elevated temperatures for long periods of time to out gas the residual H₂. It is thus necessary to study the thermal decay of FBGs for stabilisation and thermal sensing. In 1995, Williams *et.al* studied the thermal stability of in fibre gratings and reported that thermal annealing ensures the stability of the gratings for about 25 years at room temperature [40]. Later in 1997 the creditability of this work was further confirmed by Kannan *et.al* [45]. Ishikawa *et.al* introduced a model to calculate the accurate annealing time [46]. In another study by Patrick *et.al*, the grating stability written in hydrogenated and non-hydrogenated fibres were compared and the results indicated that gratings written in hydrogen-free fibre were noticeably more stable at high temperatures. They reported the UV-induced index modulation reduction by 40% and 5% in hydrogen-loaded and hydrogen-free fibres after 10 hours at 176°C, respectively [47]. However their data did not follow the proposed model based on “power law” by Erdogan *et.al* in which the thermal degradation of UV induced index for non-hydrogenated fibre was accurately explained [48]. Baker *et.al* confirmed that the power law thermal decay model is well fitted for non-hydrogenated fibres but does not apply for hydrogen loaded fibres [49]. They introduced a log-time model which could be used to predict the decay characteristics of UV written FBGs in hydrogenated fibres. Their proposed model holds well for other fibres in the need for thermally stable gratings including B-doped, Sn-doped and fluorine-doped fibres [50-52].

There are reports indicating the more stability for presensitised than hydrogenated fibres [53]. Niay *et.al* showed that employing CW or pulsed UV sources in grating

fabrication process does not make any difference in the grating's stability properties [29].

Practically, after the grating fabrication, a thermal annealing process (normally at 80°C for 48 hours) is implemented to accelerate the H₂ diffusion rate and to stabilise the grating properties effectively [54, 55]. Over the annealing process, the reflectivity of FBGs is normally decreased about 1-2% [40, 45]. Once the photo-induced index modulation has stabilised, temperature, strain, and external sources of radiation are the major factors to erase this index change. The most often crossed factor is thermal erasure, where the energy traps corresponding to defect centres are thermally excited and partially or totally remove the index modulation.

2.3. Coupled Mode Theory

Coupled-mode theory is a widely used technique to obtain an approximate solution for electromagnetic wave propagating in periodically layered medium and is capable of providing the quantitative information about the spectral response of fibre gratings. This theory is a simple and an accurate model employed to describe the characteristic and optical properties of most in-fibre gratings.

Detailed derivation of couple mode theory and description of its applications in guided mode and gratings was given by Yariv [56], Kogelnik [57] and Erdogan [3, 58]. Here a brief and abridged part of these reports is presented that is most related to the material of this thesis and the derivation in this section closely follows the proposed work by Erdogan.

We shall consider the ideal mode approximation to coupled mode theory in which the transverse components of the electric field are written as a superposition of the ideal modes. Modes should be considered in an ideal waveguide that does not experience a grating perturbation. If modes are labeled with index m , we will have:

$$\vec{E}^T(x, y, z, t) = \sum_m [A_m(z) \exp(i\beta_m z) + B_m(z) \exp(-i\beta_m z)] \vec{e}_m^T(x, y) \exp(-i\omega t) \quad (\text{eq: 2.4})$$

In above equation, $A_m(z)$ and $B_m(z)$ are slightly varying amplitudes of the m^{th} mode travelling in the $+z$ and $-z$ directions, respectively.

$\vec{e}_m^T(x, y)$ is the transverse mode field, which may describe a bound-core, cladding or radiation mode. β is the propagation constant and simply given by:

$$\beta = \frac{2\pi}{\lambda} n_{eff} \quad (\text{eq: 2.5})$$

Where n_{eff} represents the effective RI of m^{th} mode.

The mode coupling occurs in the presence of a dielectric perturbation and, as a result, the amplitudes A_m and B_m of the m^{th} mode evolve along the z direction based on the following equations:

(eq: 2.6 (a)):

$$\frac{dA_m}{dz} = i \sum_q A_q (C_{qm}^T + C_{qm}^L) \exp[i(\beta_q - \beta_m)z] + i \sum_q B_q (C_{qm}^T - C_{qm}^L) \exp[-i(\beta_q + \beta_m)z]$$

(eq: 2.6 (b)):

$$\frac{dB_m}{dz} = -i \sum_q A_q (C_{qm}^T - C_{qm}^L) \exp[i(\beta_q + \beta_m)z] - i \sum_q B_q (C_{qm}^T + C_{qm}^L) \exp[-i(\beta_q - \beta_m)z]$$

In above equations, C_{qm}^T and C_{qm}^L are the transverse and longitudinal coupling coefficients between q and m modes, respectively.

The longitudinal coupling coefficient, C_{qm}^L is analogous to transverse component, C_{qm}^T . However, for fibre, mode C_{qm}^L is usually neglected since it is half magnitude of the transverse components for fibre modes. The transverse coupling coefficient in the above equations is given by equation 2.7.

$$C_{qm}^T(z) = \frac{\omega}{4} \iint_{\infty} \Delta\epsilon(x, y, z) \cdot \vec{e}_q^T(x, y) \cdot \vec{e}_m^{T*}(x, y) dx dy \quad (\text{eq: 2.7})$$

$\Delta\epsilon(x, y, z)$ from the above equation is the permittivity perturbation and its value is approximately $2n\delta n$ where δn is the (effective) RI variation and small compared with the local index, n , in the idea fibre. Considering an ideal waveguide situation, ie no perturbation exists so $\Delta\epsilon = 0$, the coupling coefficient $C_{qm}^T(z) = 0$ and the transverse modes are orthogonal and do not exchange energy.

Exposure of photosensitive fibre to a spatially varying UV pattern produces the RI modulation of $\delta n_{eff}(z)$.

$$\delta n_{eff}(z) = \bar{\delta}n(z) \left[1 + s \cos\left(\frac{2\pi}{\Lambda}z + \phi(z)\right) \right] \quad (\text{eq: 2.8})$$

Where $\bar{\delta}n(z)$ is the “dc” index change spatially averaged over a grating period, s is the fringe visibility of the index change, Λ is the nominal period, and $\phi(z)$ describes grating chirp.

In most fibre gratings, the photo-induced index modulation is almost uniform across the core and negligible outside the core so the dc index change $\bar{\delta}n(z)$ can be replaced by $\bar{\delta}n_{co}(z)$ and based on what has already been explained $\Delta\epsilon(x, y, z)$ can be replaced by $2n_{co}\bar{\delta}n_{co}(z)$. By applying these substitutions, the general coupling coefficient, $C_{qm}^T(z)$, can be rewritten in the form of following equation:

$$C_{qm}^T(z) = \psi_{qm}(z) + 2k_{qm}(z)\cos\left(\frac{2\pi}{\Lambda}z + \phi(z)\right) \quad (\text{eq: 2.9})$$

$\psi_{qm}(z)$ and $k_{qm}(z)$ in the above equation are defined as “dc” and “ac” coupling coefficients respectively and can be calculated as:

$$\psi_{qm}(z) = \frac{\alpha n_{co}}{2} \bar{\delta n}_{co}(z) \iint_{core} \vec{e}_q^T(x, y) \cdot \vec{e}_m^{T*}(x, y) dx dy \quad (\text{eq: 2.10})$$

$$k_{qm}(z) = \frac{s}{2} \psi_{qm}(z) \quad (\text{eq: 2.11})$$

2.3.1. Backward Mode Coupling

In backward mode coupling, the dominant interaction is near the wavelength, at which reflection occurs from a mode with amplitude $A(z)$ coupled to an identical counter-propagating mode of amplitude $B(z)$. Under such conditions, equations (2.6 (a)) and (2.6 (b)) are simplified to the following equations [3].

$$\frac{dR}{dz} = i\psi'R(z) + ikS(z) \quad (\text{eq: 2.12})$$

$$\frac{dS}{dz} = -i\psi'R(z) - ik * R(z) \quad (\text{eq: 2.13})$$

In above equations, k is the “ac” coupling coefficient and ψ' is the general “dc” self-coupling coefficient which is defined as:

$$\psi' = \delta + \psi - \frac{1}{2} \frac{d\phi(z)}{dz} \quad (\text{eq: 2.14})$$

Where δ is the detuning and independent of z :

$$\delta = \beta - \frac{\pi}{\Lambda} = \beta - \beta_d = 2\pi n_{eff} \left[\frac{1}{\lambda} - \frac{1}{\lambda_d} \right] \quad (\text{eq: 2.15})$$

Here $\lambda_d = 2n_{eff}\Lambda$ is the “design wavelength” for Bragg scattering by an infinitesimally weak grating ($\delta n_{eff} \rightarrow 0$).

The amplitude R and S in equations (2.12 and 2.13) are defined as:

$$R(z) = A(z) \exp\left(i\delta z - \frac{\phi(z)}{2}\right) \quad (\text{eq: 2.16})$$

$$S(z) = B(z) \exp\left(-i\delta z + \frac{\phi(z)}{2}\right) \quad (\text{eq: 2.17})$$

For a single-mode Bragg grating, one may use the following simplified relations:

$$\psi = \frac{2\pi}{\lambda} \overline{\delta n} \quad (\text{eq: 2.18})$$

$$k = k^* = \frac{\pi}{\lambda} s \overline{\delta n} \quad (\text{eq: 2.19})$$

For the uniform grating along z direction $\overline{\delta n}$ is constant and $d\phi(z)/dz = 0$ indicating a non-chirped grating. Thus k , ψ and ψ' are constants. This simplifies equations (2.16) and (2.17) into coupled first-order ordinary differential equations with constant coefficients. The closed-form solutions may be found when appropriate boundary conditions are specified.

2.3.2. Forward Mode Coupling

Forward mode coupling is the condition in which a forward propagating mode with amplitude $A_1(z)$ is strongly coupled into a co-propagating mode of amplitude $A_2(z)$ close to the wavelength in which forward mode coupling occurs, then equations (2.6) and (2.7) can be rewritten in the form of the amplitudes of these two modes and making the usual synchronous approximation

$$\frac{dR}{dz} = i\psi'R(z) + ikS(z) \quad (\text{eq: 2.20})$$

$$\frac{dS}{dz} = -i\psi'R(z) + ik * R(z) \quad (\text{eq: 2.21})$$

And R and S are new amplitudes and defined as:

$$R(z) = A_1(z) \exp\left(i(\psi_{11} + \psi_{22})\frac{z}{2}\right) \exp\left(i\delta z - \frac{\phi}{2}\right) \quad (\text{eq: 2.22})$$

$$S(z) = A_2(z) \exp\left(-i(\psi_{11} + \psi_{22})\frac{z}{2}\right) \exp\left(-i\delta z + \frac{\phi}{2}\right) \quad (\text{eq: 2.23})$$

ψ_{11} and ψ_{12} are “dc” coupling coefficients as defined earlier in equation (2.10) and K is “ac” cross coupling coefficient defined in equation (2.11). Here $k = k_{21} = k^*_{12}$ and ψ' is the general “dc” self-coupling coefficient and is introduced as:

$$\psi' = \delta + \left(\frac{\psi_{11} - \psi_{12}}{2}\right) - \frac{1}{2} \frac{d\phi}{dz} \quad (\text{eq: 2.24})$$

If δ is considered constant along z direction then, will follow the below equation:

$$\delta = \frac{1}{2}(\beta_1 - \beta_2) - \frac{\pi}{\Lambda} = \pi \Delta n_{eff} \left[\frac{1}{\lambda} - \frac{1}{\lambda_d} \right] \quad (\text{eq: 2.25})$$

As it was introduced before, $\lambda_d = \Delta n_{eff} \Lambda$ is the design wavelength for a grating approaching zero index modulation and the correspondent grating condition for FBGs is $\lambda = \lambda_d$. In FBGs, the forward-coupling equations, equations (2.20) and (2.21) are first-order ordinary differential equations with constant coefficients. Thus when the appropriate boundary conditions are given, the closed form solutions can be found. However in the case of a uniform forward-coupled grating, ψ' and k are constants and in contrast to the FBG, here the coupling coefficient k may not be written as simple as defined in equation (2.19) and required the numerical evaluation.

2.3.3. Phase Match Condition

In the presence of the grating perturbation in the fibre core, the bound wave can be coupled to either backward or forward propagating modes. Fibre gratings can be categorised in two main types according to the direction of mode coupling.

One category contains the gratings which are backward-coupled including FBGs with uniform and chirped structures and TFG with small tilt angles, while the other group includes LPGs and TFGs with large tilt angle in which coupling occurs between forward propagating modes. So to transfer energy from one mode of amplitude $A_i(z)$ into a counter- or co- propagating mode of amplitude $B_j(z)$, the phase mismatch factor is defined as a detuning:

$$\Delta\beta = \beta_i \pm \beta_j - \frac{2\pi}{\Lambda_g} N \cos \theta \quad (\text{eq: 2.26})$$

β_i and β_j are the propagation constants for incident and diffracted modes respectively. Λ_g is the grating period and θ is the tilt angle of the grating where N indicates the diffraction order. Also “±” sign defines the propagation direction of “ $\mp(z)$ ”. To transfer a significant portion of energy the phase mismatch factor should be zero or phase matching condition satisfies $\Delta\beta = 0$, therefore:

$$\beta_i \pm \beta_j = \frac{2\pi}{\Lambda_g} N \cos \theta \quad (\text{eq: 2.27})$$

In backward propagation, β_i and β_j both have identical positive signs where for co-propagation β_i and β_j have opposite signs. In most cases, the first order diffraction is dominant and therefore, $N=1$. By substituting equation (2.5), the resonant wavelength this satisfied in the following relationship:

$$\lambda = (n_{eff}^i \pm n_{eff}^j) \frac{\Lambda_g}{\cos \theta} \quad (\text{eq: 2.28})$$

2.3.4. Fibre Bragg Grating (FBG)

Normal FBG represents a backward-mode coupling and the wavelength of the Bragg resonance from the core mode is given by:

$$\lambda_B = 2n_{eff} \Lambda \quad (\text{eq: 2.29})$$

Where n_{eff} represents the effective RI of the fibre core.

Figure 2.4 shows the schematic diagram of the backward mode coupling in an FBG.

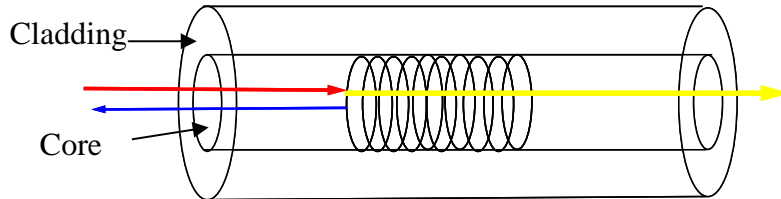


Figure 2. 4. Schematic diagram of backward-mode coupling in FBG.

2.3.5. Long Period Grating (LPG)

In a LPG, forward-mode coupling between the core and cladding modes occurs in which the resonant wavelength satisfies:

$$\lambda_{res} = (n_{co}^{eff} - n_{cl,m}^{eff}) \cdot \Lambda \quad (\text{eq: 2.30})$$

In the above equation, n_{co}^{eff} and $n_{cl,m}^{eff}$ are the effective indices of the core and m^{th} cladding mode, respectively. As the difference between core and cladding mode effective indices are far less than unity, the period of LPG is much larger than that of FBG. In fact, the investigated periods for LPGs are factors of hundred microns,

where the period of FBG is less than one micron [59, 60]. Figure 2.5 exhibits the schematic diagram of the forward mode coupling in an LPG.

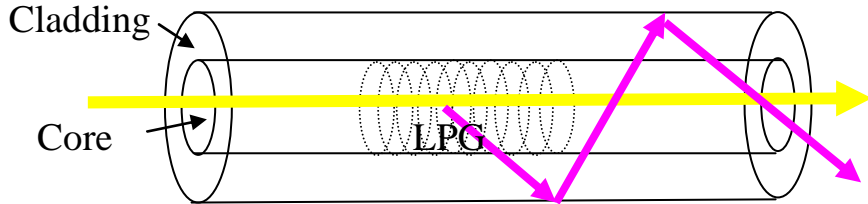


Figure 2. 5. Schematic diagram of forward mode coupling in LPG.

2.3.6. Tilted Fibre Grating (TFG)

TFGs are created when the grating structure is tilted by an angle θ . In such gratings, the mode coupling is not as simple as normal gratings. As illustrated in Figures 2.6 and 2.7 in TFGs mode coupling can occur in either forward or backward direction depending on the tilt angle.

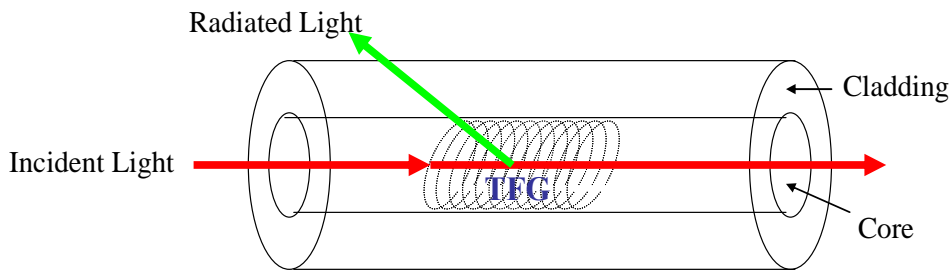


Figure 2. 6. Schematic diagram of backward mode coupling in TFG.

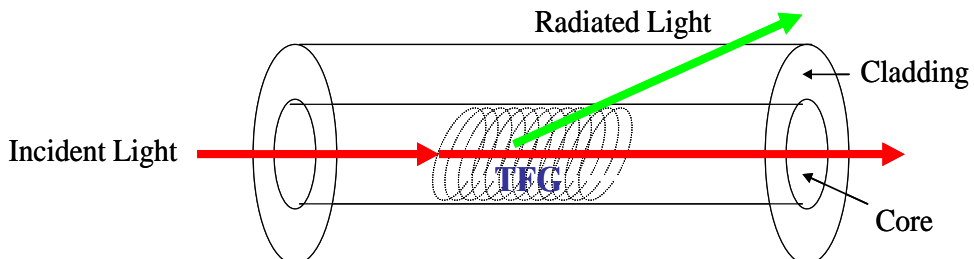


Figure 2. 7. Schematic diagram of forward mode coupling in TFG.

In the case of tilted gratings, the resonant wavelengths are [60, 61]:

$$\lambda_{co,cl} = (n_{co}^{eff} \pm n_{cl,m}^{eff}) \cdot \frac{\Lambda_g}{\cos \theta} \quad (\text{eq: 2.31})$$

The sign of “+” and “-” in the above equation indicate the direction of the mode propagation toward - z or + z direction respectively. As it is schematically presented in Figure 2.8, in TFGs, the grating period along the fibre axis is simply identified by the following relationship:

$$\Lambda = \frac{\Lambda_g}{\cos \theta} \quad (\text{eq: 2.32})$$

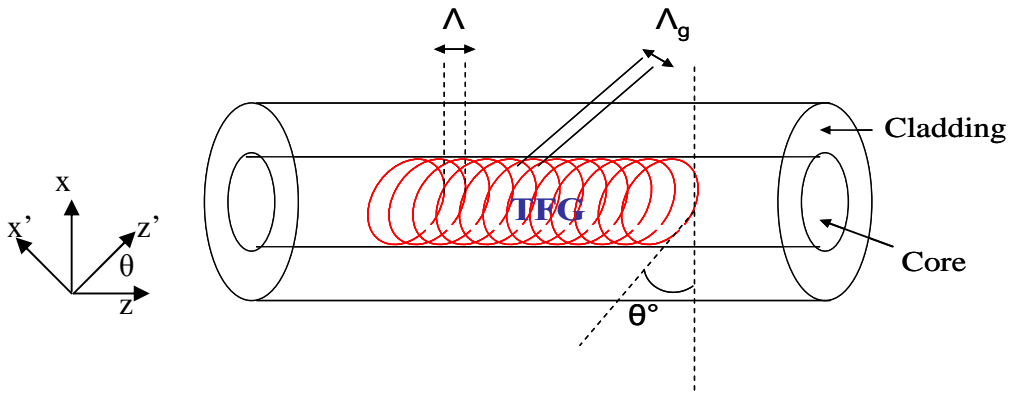


Figure 2. 8. Schematic diagram of TFG.

The photo-induced index change in the core of a single mode optical fibre, δn_{co} , follows the below relationship:

$$\delta n_{co}(x, z) = \overline{\delta n}_{co}(z') \left[1 + s \cos \left(\frac{2\pi}{\Lambda_g} z' + \phi(z') \right) \right] \quad (\text{eq: 2.33})$$

z' (illustrated in Figure 2.8) in equation (2.30) is defined as $z' = x \sin \theta + z \cos \theta$. But for slightly varying functions $\overline{\delta n}_{co}(z')$ and $\phi(z')$, it can be considered as $z' \cong z \cos \theta$. Then by taking the projectile of these functions along the fibre axis (z), the general

coupling coefficient (previously introduced in equation (2.9) can be rewritten in the following format:

$$C_{\mp\pm}^T(z) = \psi(z) + 2k_{\mp\pm}(z)\cos\left[\frac{2\pi}{\Lambda}z + \phi(z \cos \theta)\right] \quad (\text{eq: 2.34})$$

Where subscript “ m ” in equation (2.9) is associated with forward propagating mode (+ sign) and subscript “ q ” describes the backward propagating mode (– sign). The self coupling coefficient and cross coupling coefficient are modified in equations (2.32) and (2.33) respectively.

$$\psi(z) = \frac{\omega n_{co}}{2} \overline{\delta n}_{co}(z \cos \theta) \iint_{core} \vec{e}_\mp^T(x, y) \cdot \vec{e}_\pm^{T*}(x, y) dx dy \quad (\text{eq: 2.35})$$

and (eq: 2.36):

$$k_{\mp\pm}(z, \theta) = \frac{s}{2} \frac{\omega n_{co}}{2} \overline{\delta n}_{co}(z \cos \theta) \iint_{core} \exp\left(\pm i \frac{2\pi}{\Lambda} x \tan \theta\right) \cdot \vec{e}_\mp^T(x, y) \cdot \vec{e}_\pm^{T*}(x, y) dx dy$$

It is worthy to note that $k_\mp = k_\pm^*$.

The effect of tilting the structure of the grating is correspondent to “*effective fringe visibility*” defined as $s_{\mp\pm}(\theta)$ in the following relationship:

$$\frac{s_{\mp\pm}(\theta)}{s} = \frac{\iint_{core} \exp\left(\pm i \frac{2\pi}{\lambda} x \tan \theta\right) \cdot \vec{e}_\mp^T(x, y) \cdot \vec{e}_\pm^{T*}(x, y) dx dy}{\iint_{core} \vec{e}_\mp^T(x, y) \cdot \vec{e}_\pm^{T*}(x, y) dx dy} \quad (\text{eq: 2.37})$$

So equation 2.33 can be rewritten in:

$$k_{\mp\pm}(z, \theta) = \frac{s_{\mp\pm}(\theta)}{2} \psi(z) \quad (\text{eq: 2.38})$$

The result indicates that tilting the grating structure leads to reduction of the effective fringe visibility by amount presenting in equation (2.37). Also this result describes the effect of the grating perturbation in backward scattering.

Detailed discussion on fabrication and characterisation of TFGs are presented in chapter 3 of this thesis. Chapter 6 of this thesis also introduces one of the applications of TFGs with large tilted angles in a fibre ring laser cavity.

2.4. History of Grating Inscription

2.4.1. *Original Hill Grating*

In 1978, Ken Hill *et.al* from the Canadian Communication Research Centre (CRC), Ottawa, reported the simultaneous discovery of the photosensitivity of optical fibre and the formation of permanent FBG in an optical fibre [2]. They launched intense CW 488 nm (green) light from an Ar⁺ laser into a short section of a single mode germaniasilica optical fibre using the shown experimental set up in Figure 2.9. After few minutes they noticed an increase in the intensity of the reflected light which grew to the point that most of the probed light was reflected back from the fibre. Spectral measurement confirmed the formation of a narrow Bragg grating across the whole 1m long fibre. This achievement was named “*Hill Gratings*” or “*internally written gratings*” and explained the growth intensity of back reflected light by introducing the “*photosensitivity*” phenomenon which enables an index grating to be created. The Bragg grating with 90% reflectivity was written at the Argon laser wavelength and with the bandwidth of less than 200 MHz.



Figure 2. 9. Schematic diagram of the original setup for inscription of FBG set by Hill *et al* [17].

At that time it was realised that Hill gratings would have many applications in optic fibre communication and it was also presented that they can be employed as optical feed back in laser system or as strain sensor when strain is applied on the fibre.

A detailed study by Lam and Garside proved that the magnitude of the UV-induced refractive index change (grating's strength) increased as the square of the UV-power from the Ar⁺ laser source, operating at 488 nm [62]. This result indicated that the experiment was based on two photon beam absorption mechanism and also the possibility of grating fabrication by side-writing technique employing 244 nm UV radiation.

2.4.2. *Holographic Side Writing Technique*

It was discovered that unfortunately the functionality of Hill gratings is only limited by wavelength of the visible light and close to the writing wavelength and have normally a long length to achieve a useful reflectivity value. Ten years later, this limitation of photosensitivity was overcome in an experiment by Meltz *et.al.* In 1989,

Meltz *et.al* reported that the gratings could be written by much more efficient two-beam holographic exposure technique from the side of the fibre using UV radiation [63]. The schematic diagram of their experimental setup is presented in Figure 2.10. In their work, they successfully improved the inscription efficiency and also proposed a technique to design an arbitrary Bragg wavelength for the grating by simply adjusting the angle between two interference beams.

Figure 2. 10. The schematic diagram of the experimental setup by Meltz *et.al* [63].

As illustrated in the above figure, in Meltz's setup, the 244 nm UV beam was split into two equal intensity beams via a beam splitter and then recombined to create an interference pattern on the fibre. The optical fibre also was placed at the interference pattern area, and subsequently a RI modulation was induced in the core of the fibre. In such condition, the grating pitch is identical to the interference fringe pattern and depends on both the irradiation wavelength and the half angel φ between the two split UV beams. The grating pitch is defined as:

$$\Lambda = \frac{\lambda_{uv}}{2 \sin \varphi} \quad (\text{eq: 2.39})$$

And the Bragg condition is given by:

$$\lambda_B = 2n_{eff}\Lambda \quad (\text{eq: 2.40})$$

Where n_{eff} is defined as the effective index of the core. Considering equations (2.36) and (2.37) we can introduce the Bragg wavelength as follows:

$$\lambda_B = \frac{n_{eff}\lambda_{uv}}{\sin \varphi} \quad (\text{eq: 2.41})$$

So the Bragg wavelength can be easily tuned by changing φ or λ_{uv} . This proposed fabrication technique also suffers from some drawbacks. The main disadvantage of this technique is susceptibility to mechanical vibrations during the fabrication process and the requirement of an accurate laser source with good coherence. Since 1989, the holographic inscription technique has been developed and a number of different setups have been proposed and extended to different fibre types and the telecommunications wavelengths [64-68].

2.4.3. Phase Mask Inscription Technique

Phase mask technique is one of the most efficient approaches in FBG inscription and is considered as an alternative method for the tow beam holographic technique. As presented in Figure 2.11. This technique is based on near contact exposure through a phase mask and was first proposed by Hill *et.al* [69].

The phase mask itself is a one-dimensional periodic surface relief pattern with period Λ_{pm} etched into fused silica and is employed to spatially modulate the incident light in the following fashion:

When a UV light incident on the phase mask, it will almost entirely diffracted with little light transmitted in the zero-order beam. In fact, zero order is suppressed to less

than 5% of the transmitted light intensity while the transmitted light intensity in each of +1 and -1 diffracted orders is approximately 35%. In this technique a near-field fringe pattern is formed by the interference of the +1 and -1 diffracted orders. The period of the written grating by phase mask method is:

$$\Lambda = \Lambda_{pm}/2 \quad (\text{eq: 2.42})$$



Figure 2. 11. Schematic diagram of phase mask grating inscription technique [69].

This method benefits from the many advantages over other techniques including reproducibility and feasibility of high quality complex structure grating (eg: TFGs) fabrication. However for different wavelength separate phase masks, which are extremely expensive, are required. Both holographic and phase mask fabrication technique will be discussed in detail in chapter 3 of this thesis where we used to UV-inscribed different structure gratings.

2.4.4. Point-By-Point Incription Technique

Point-by-point fabrication method is usually employed to fabricate LPGs covering the period range of $10 \mu\text{m}$ to $660 \mu\text{m}$. The method was introduced by Malo, Hill and co-workers for the first time to fabricate FBGs in which the fibre was exposed through the image of a slit to the UV light coming from a KrF excimer pulse laser. The fibre was translated between pulses inducing one step index change at a time across the core. As the size of the focused spot light at 244 nm is about $0.25 \mu\text{m}$ and the period of the Bragg grating with $\lambda_B=1550 \text{ nm}$ is $\sim 0.5 \mu\text{m}$, it is a hard task to control the movement of the translation stage accurate enough to write FBGs by point-by-point technique. Figure 2.12 shows the schematic diagram of the experimental setup for point-by-point inscription technique.

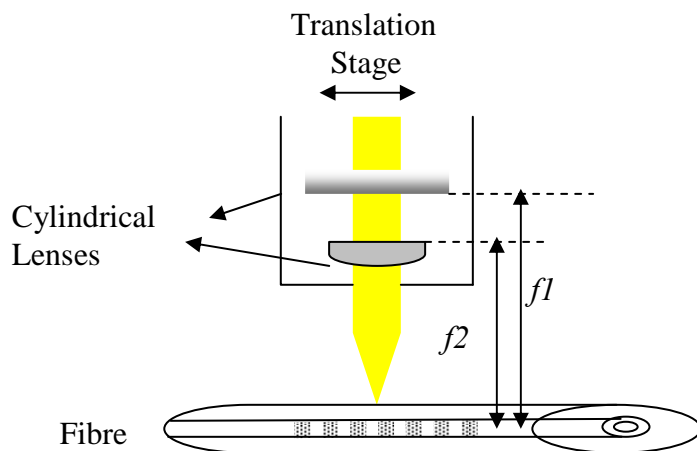


Figure 2. 12. Schematic diagram of point by point grating fabrication technique.

As presented in the above figure, this setup has an additional cylindrical lens comparing with the phase mask technique which is used to focus the UV beam to the fibre axis. The movement of the translation stage is computer controlled. The

parameters of the grating such as the grating pitch and length and duty cycle can be tuned by switching the shutter on and off depending on the system's design. Also in recent years, the direct point-by-point inscription to create fibre grating structures has been demonstrated, including both LPGs [70-72] and FBGs [73, 74]. By means of focusing the femtosecond pulses into the fibre core, point-by-point FBG inscription can be achieved without the need of a phase-mask. The high flexibility to alter the grating's parameter is counted as one of the main advantages of point-by-point fabrication technique.

2.5. Chapter Conclusion

This chapter has presented a comprehensive review on the photosensitivity concept of UV-inscribing fibre gratings, outlining aspects of three most common photosensitivity mechanisms: colour centre, compaction densification and stress relief model. Photosensitivity enhancement methods including co-doping, hydrogen loading and flame brushing techniques have also been discussed.

The systematic revision of mode coupling theory for three different types of grating FBG, TFG and LPG - was given and historical development on inscription technology of optical fibre gratings was also described. Using coupled mode theory, an insight into the principle of fibre gratings was presented and phase matching conditions for FBG, LPG and also TFG with different angles were explained. Fibre gratings inscription methods such as phase mask, holographic side writing and point-by-point techniques have been briefly introduced. Furthermore concerns about the device stability have been outlined and thermal stability studies have been reviewed with conclusion that such UV-induced fibre grating devices may possess lifetime as long as 25 years.

This chapter predominantly exhibits a clear outcome of theoretical study which is also helpful in practical aspects for experimentalists. The combination of current chapter with chapter 3 provides the basis for following experimental chapters in which novel applications for gratings with different structures are proposed and demonstrated.

Chapter 3

Inscription of Advanced Fibre Gratings Utilising UV Laser

3.1. Introduction

The significant discovery of photosensitivity in optical fibres led to the development of a new class of in-fibre components called fibre gratings. Photosensitivity refers to a permanent change of RI of the fibre core while expose to light with characteristic wavelength and intensity depending on the core material. In the recent years, owing to the numerous advantages of fibre gratings in a wide range of applications, they have attracted great attention over the other conventional fibre optic devices. Applications in which FBG structures are employed use the coupling between the forward and backward propagating core modes in the fibre while those using LPGs and TFGs utilise the other existent mode couplings, such as core-cladding and core-radiation mode coupling.

In this chapter, the two main in-fibre grating fabrication techniques including two beam holographic and phase-mask methods will be discussed in details. These techniques have been employed to fabricate all the different types of gratings described and used in this thesis. The chapter contains a full discussion of the properties of four types of fibre gratings which were designed and fabricated using the above mentioned techniques. The discussion includes a comparative investigation of the UV inscribed tilted fibre gratings at different tilt angles which are applicable for different purposes. The chapter also documents the detailed description of the fabrication method and the unique growth characteristics of type IA gratings. The comparative experimental study of formation type IA in different types of fibre and the H₂ diffusion effect in such samples are also addressed in this chapter.

3.2. Fabrication Techniques of Optical Fibre Gratings

Here we describe various techniques used to fabricate standard and complex in-fibre grating structures. The objective is to give a detailed outlook on the employed technology for inscribing grating structures. Depending on the fabrication method, fibre gratings may be classified as internally or externally written. However, as the internally inscribed gratings may not be considered very practical and also there are no employed internally written fibre gratings in this thesis, we only describe the externally fabricated gratings in which, the inscription techniques are one of the followings:

- 1- Two beam holographic technique (also named as interferometric technique)
- 2- Point-by-point technique
- 3- Phase mask scanning technique

Externally written gratings have overcome the limitations of internally inscribed gratings and are considered far more useful in a different range of applications including optical sensing.

3.2.1. Two Beam Holographic Technique

This fabrication technique is an external inscription approach for writing fibre grating in photosensitive fibres. Figure 3.1 shows the two beam holographic UV fabrication system in our laboratory. In this setup, an incident UV laser light is split into two beams with equivalent intensity while passing through a 50:50 amplitude splitter. After that, the two beams are reflected by two highly reflective mirrors, depicted as M_1 & M_2 in Figure 3.1, and subsequently recombined on the optical fibre. The

interfering beams are normally focused to enhance the intensity to the fibre core by employing two cylindrical lenses inserted into the two optical paths.

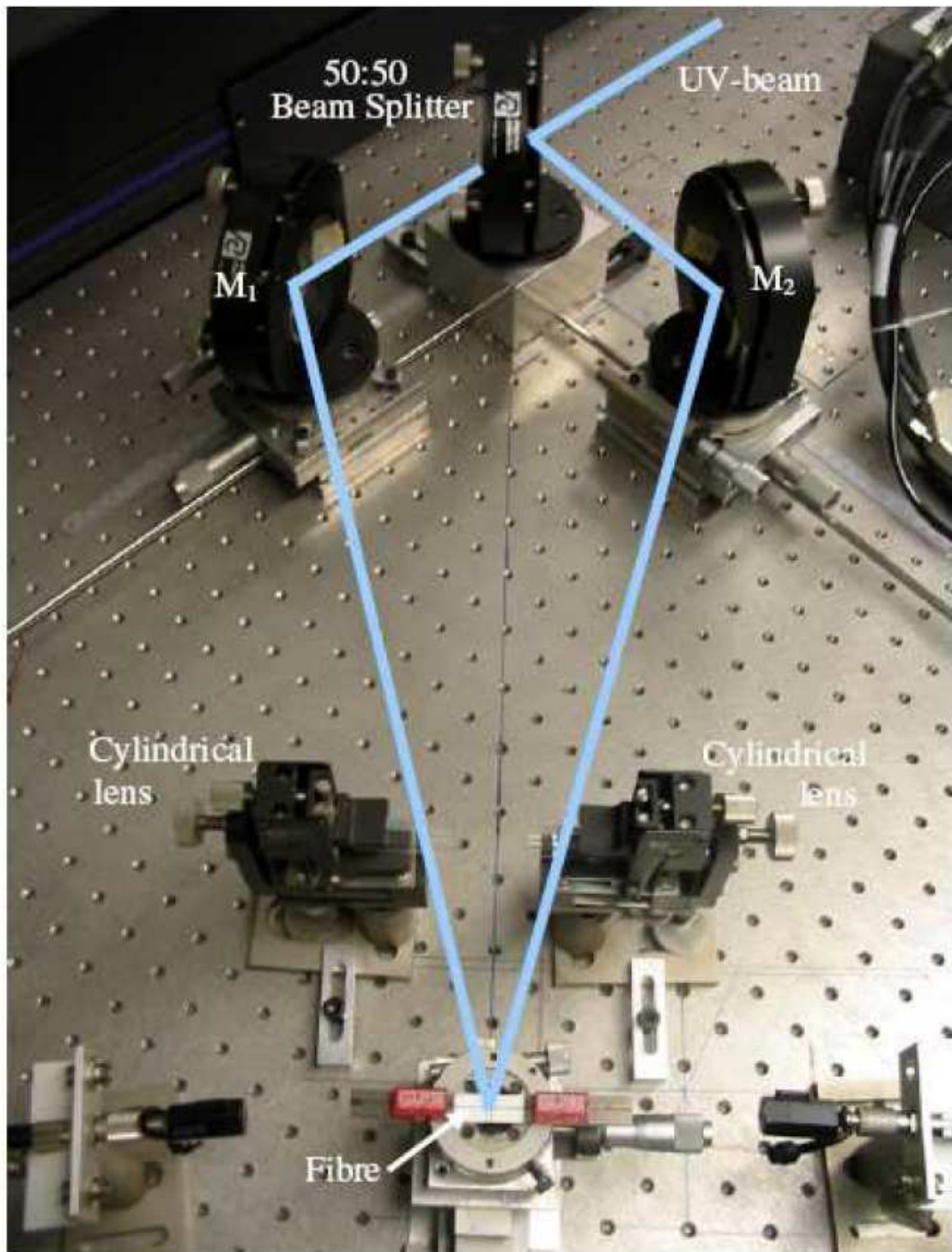


Figure 3. 1. Two-beam holographic FBG inscription system in the Photonics Research Group laboratory at Aston University.

Schematic diagram of the experimental setup for this technique is shown in Figure-3.2. As one may notice from this figure, a beam expanding telescope system consisting two cylindrical optical lenses (C & D), is inserted to the optical path due to expanding the width of UV Gaussian beam in X-Z plane and the length of the two interfering beam on the forthcoming meet at the point where the grating is fabricated.

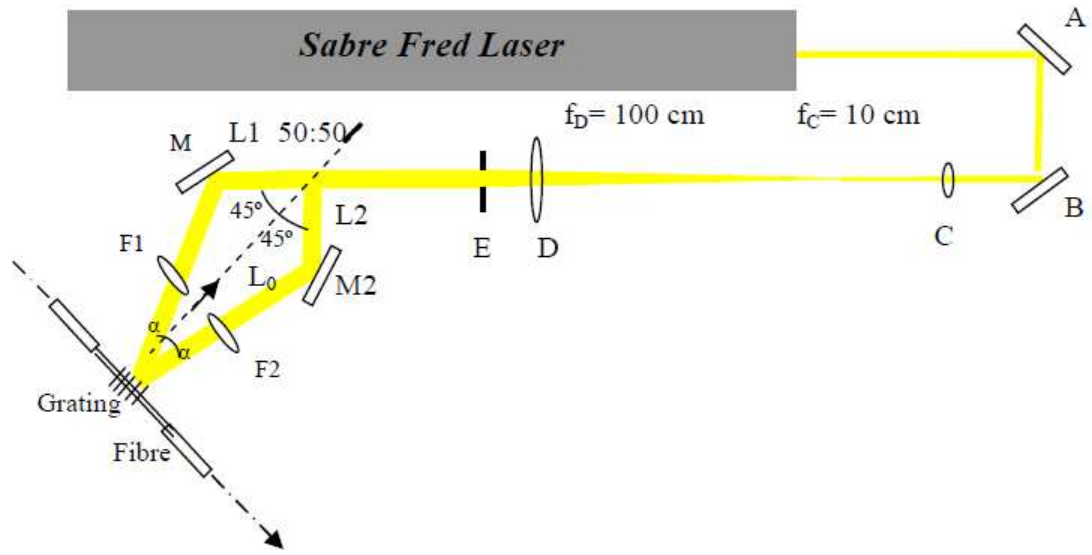


Figure 3. 2. Schematic diagram of optical setup for fibre grating inscription using holographic technique.

Aperture E in the above setup, which is usually placed after the beam expanding telescope and before the 50:50 amplitude splitter, selects the central portion for the expanded beam to achieve a uniform intensity profile. The maximum length of the written grating employing this setup is about 12 mm. F1 and F2, two cylindrical optical lenses, are used to focus the beams to the fibre core with enhanced intensity in y dimension. The driven mathematical relationship between the Bragg wavelength and the system parameters is [75].

$$\lambda_B = \frac{n_{eff} * \lambda_{uv}}{\sin \left[\arctan \left(\frac{L_1 \sin 45^\circ}{L_0 - L_1 \cos 45^\circ} \right) \right]} \quad (\text{eq:3.1})$$

For a fixed L_0 (distance between the beam splitter & the fibre), the grating wavelength, (λ_B), can easily be tuned by adjusting the arm length, L_1 , in the setup shown in Figure 3.2. It should be mentioned that in this setup both arm lengths are equal, ie $L_1=L_2$. L_1 and L_2 can be adjusted by moving the reflective mirrors, M_1 and M_2 , to different positions by tuning the micrometer drivers attached to the mirrors. This all means that grating with desirable wavelength may be fabricated by simply changing the arm lengths in this system.

The ability of grating fabrication with arbitrarily selected wavelengths by simply adjusting the angle between the two interfering beams is counted as the major advantage of this technique. Depending on the range of the employed Optical Spectrum Analyser (OSA) and the light source, holographically written FBGs, are normally in the range of 750 nm to 1650 nm. This inscription technique also has the main disadvantage of susceptibility to mechanical vibrations. In fact during a relative long time exposure, submicron displacements in the position of any optics in the fabrication system will cause poor fringe pattern, and consequently the poor quality grating. A number of solutions including prism interferometer [64, 67] and the Lloyd interferometer [76] based fabrication systems, have been reported. In these systems the optical setup is simplified by employing only one optical component so the sensitivity to mechanical vibrations is reduced. However the disadvantages are the limitation on the grating length and Bragg wavelength tuneability.

In this thesis, most of gratings were fabricated using phase mask technique which is discussed in the following section. However, at some specific wavelengths where there were no available phase masks, the holographic technique was used. Table 3.1 lists holographically written FBGs with the fabrication conditions for five gratings

with Bragg reflections in 1450 nm to 1475 nm range for telecom-supercontinuum laser system.

Designed λ_B (nm)	α (°)	L_1 & L_2 (mm)	Achieved λ_B (nm)
1450	16.01°	145.03	1450.10
1455	16.07°	145.48	1455.02
1460	16.13°	145.92	1460.08
1465	16.19°	146.35	1465.11
1475	16.3°	147.22	1470.04

Table 3. 1. Designed data for FBG fabrication by employing the holographic method.

Apart from these five gratings, two FBGs at 1568.44 nm and 1562.68 nm were also fabricated by the two beam holographic technique to be employed as wavelength seeders for a fibre ring laser cavity [chapter 6]. Figure 3.3 depicts a typical spectrum of a holographically written FBG at 1568.44 nm wavelength and strength of only 2.28 dB due to the specific application of this FBG.

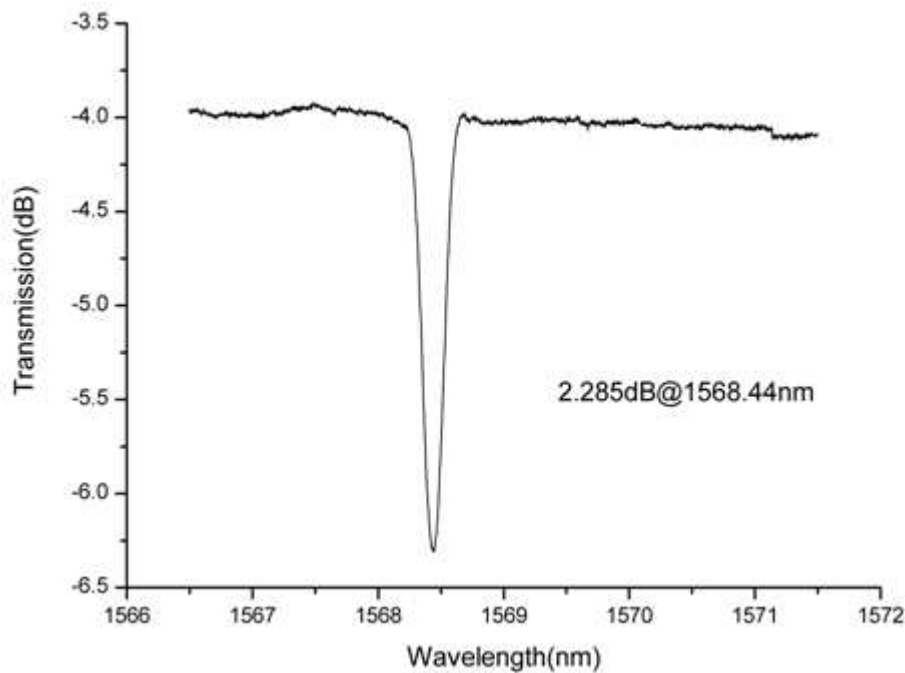


Figure 3. 3. Transmission spectrum of a FBG fabricated by holographic technique.

3.2.2. Phase Mask Technique

One of the most effective methods for reproducible fibre grating inscription is the phase mask technique, which is based on near-contact UV-exposure through a phase mask to the fibre. In this technique, the phase mask is employed as a diffractive optical element that is responsible for spatially modulating the incident UV writing beam. The phase mask is a one dimensional periodic surface relief pattern, with period Λ_{pm} etched into fused silica which can diffract the incident light into several orders named as $m = 0, +/- 1, +/- 2, \dots$ where $m = 0$ representing the transmitted light. Figure 3.4 presents the schematic of the beam diffraction from a phase mask while the incident angle (Φ_i) is zero. In such a situation, the diffraction angles of incident light are equal for negative and positive orders and the interference formed between different orders beam can be used to generate the fringe pattern to write a grating into the optical fibre.

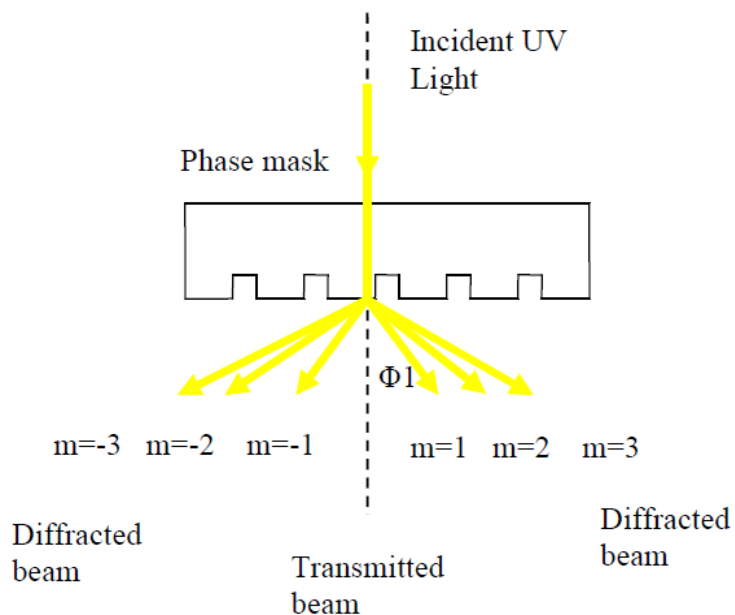


Figure 3. 4. Schematic of diffraction of an incident beam at angle $\Phi_i = 0$ into various orders from a phase mask.

As in most cases, orders $m= +/- 1$ are employed for grating fabrication, it is necessary

to suppress all other orders to increase the visibility of the interference pattern. This issue has been considered in the structure of the phase mask; the profile of the periodic surface relief gratings is generated such that:

1. The zero order diffracted beam is suppressed to less than few percent (typically less than 3%) of the transmitted light when the light is incident on the mask.
2. The diffracted ± 1 orders are maximised and each order typically contains more than 35% of the transmitted light.

As a result, a near field fringe pattern will be generated by interference of the first orders diffracted beams with a good visibility and a period equal to one-half of the mask. ie $\Lambda_{\text{Grating}} = 1/2(\Lambda_{\text{pm}})$. The Bragg wavelength is then given by [3]

$$\lambda_B = 2n_{\text{eff}} \Lambda = n_{\text{eff}} \Lambda_{\text{pm}} \quad (\text{eq: 3.2})$$

Over the years, the phase mask technique has developed to a level that the fabrication of almost 100% reflective gratings is now routine. The technique noticeably reduces the complexity of the grating inscription process. The experimental arrangement in our laboratory is presented in Figure 3.5.

A 244 nm, CW frequency doubled Ar⁺ laser is used as the source of UV light. The translating mirror C and a cylindrical lens are mounted on a computer-controlled air translation stage. The stage can be moved relative to the fibre, permitting phase shifts to be incorporated into the fibre grating during UV-beam scanning across a phase mask which is located in a close proximity to the fibre. Thus it is capable of introducing a profiled coupling coefficient into a grating for inscription of complex grating structures. The cylindrical lens here is employed to focus the UV beam into the fibre core and increases the intensity of the beam irradiation in one dimension in the beam fibre plane.

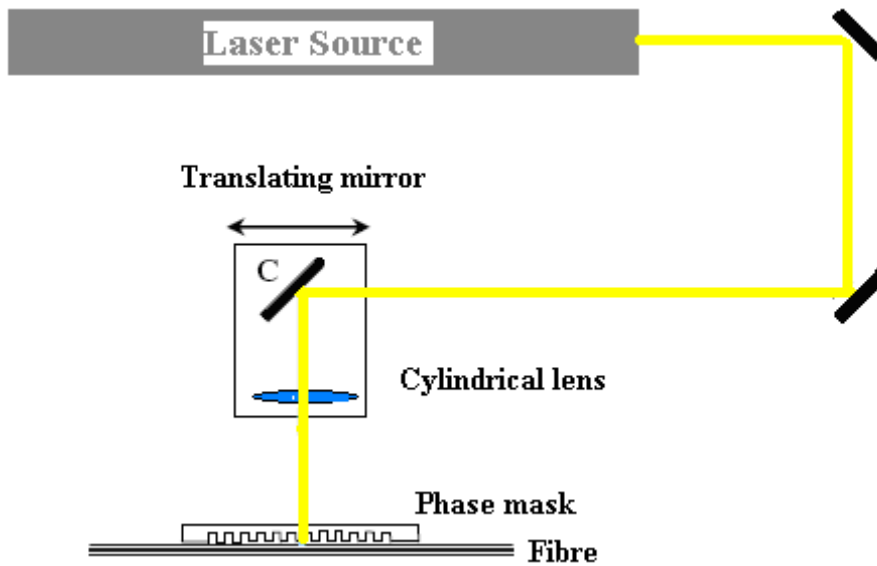


Figure 3. 5. Experimental arrangements in the Photonics Research Group of Aston University for the phase mask fabrication technique.

Spatial coherence of the UV source plays an important role in the phase mask technique [72], so the separation between the fibre and mask is a critical parameter during grating fabrication process. One may notice that if the fibre is placed in contact with the phase mask, it can cause damage to fine grating corrugation on the mask, so the stripped fibre in general is kept very close to but not touch the phase mask. In comparison with the two beam holographic method, employing phase mask provides a robust and stable method of reproducing highly reflective fibre gratings. Figure 3.6 presents the microscope image of the fringe structure inscribed in the fibre core employing the phase mask technique. The image was examined and measured by use of the Axioskop 2 mot plus microscope (Carl Zeiss) in conjunction with AxioVision Cameras and Frame Grabbers system with high magnification.

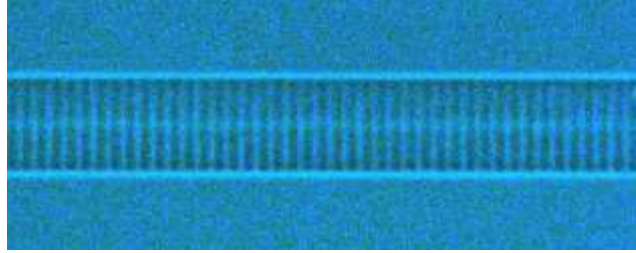


Figure 3. 6. Microscope image of a uniform period UV inscribed FBG fabricated by phase mask technique.

This technique enabled the author to fabricate the high quality complex grating structures, including, FBG arrays [application: chapter 4], CFBG [application: chapter 5], TFGs and TCFGs with different tilt angles [application: chapter 6] and type IA gratings for different novel applications which will be discussed in details in the referenced chapters.

Similar to other techniques, phase mask inscription method also suffers from some drawback including the limitation of Bragg wavelength variation, as an individual mask is required for each wavelength. To overcome this problem, Prohaska *et.al* presented experimentally that by adding a converging lens before the mask it is possible to shift the Bragg wavelength to shorter wavelengths [78]. In another report by Zhang *et.al* the Bragg wavelength shift for a fixed mask periodicity was achieved by applying strain to the fibre during the UV illumination [79]. However in both mentioned technique the wavelength tuning is possible for over a small range and toward the shorter wavelengths. In addition, the high price of the phase mask is another disadvantage that makes this technique an expensive approach to the fibre grating fabrication.

3.3. Chirped Fibre Gratings

The majority of sensing techniques are based on most basic grating structures, i.e. FBGs. However, more novel sensors based on chirped or other tailored grating structures also have been reported in literatures for sensing and laser applications. There are many applications for which the reflection bandwidth of a uniform grating, typically < 0.2 to 0.5 nm, is too narrow. Strong uniform gratings can provide wider bandwidth but are then inevitably accompanied by substantial, unavoidable losses on the short-wavelength side of Bragg wavelength and a significant overall UV-induced loss. Fabrication of CFBGs is an alternative approach to realising wider reflection bandwidths [80].

In a CFBG, the Bragg condition varies continuously or quasi-continuously along the length of the grating. Here the Bragg condition (equation 3.2.) varies with position z along the grating length by changing the amount of n_{eff} or Λ along the grating length.

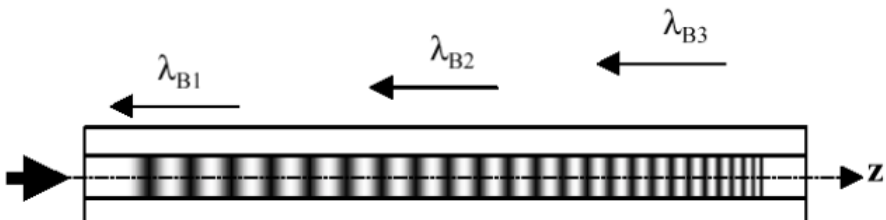


Figure 3. 7. Schematic diagram of a CFBG showing longer wavelengths travel further in the grating than shorter ones.

Clearly, different wavelengths reflected from different positions will correspond to different time delays, as shown in Figure 3.7; this property is widely used to compensate for standard fibre dispersion in high-bit-rate optical communication systems and in laser cavities [74]. Although interest in CFBGs focused originally on their mentioned potential application in telecommunication system, they have found other applications in different areas. In fibre optic sensing, they can be used for

wavelength encoding of measurands and demodulation, as well as wavelength selective devices in fibre lasers and spectrally broad band pass and band stop filters [80]. Chapter 5 of this thesis contains the detailed explanation of a novel application of the CFBGs with modified structures in which the gratings are employed for simultaneous measurement of temperature and RI of the surrounding medium.

Since a chirp is achieved simply by varying the grating period, the average index or both along the length of the grating, the method chosen for making the grating must target one or both of these parameters. In my research work, a chirped phase mask has been used to fabricate CFBGs. The fabrication method is exactly the same as the phase mask scanning method explained in the last section but utilising a chirped phase mask instead of a uniform phase mask. The employed phase mask in this experiment was in a circular shape with the radius of 20 mm, a central pitch of 1070.6 nm and the chirp rate of about 1.11 nm/mm. In order to characterise the employed phase mask, two sets of CFBG were fabricated:

1. CFBGs with different lengths (5 mm, 20 mm and 48 mm) and the same central wavelength of \sim 1542 nm. The transmission loss profiles of this set are presented in Figure 3.8.
2. CFBGs with the same length of 5mm, fabricated by employing different parts of the phase mask. Figure 3.9 exhibits the spectra of these CFBGs.

All CFBGs were fabricated while the laser source was running at 100 mW with the driven current set at 36.9 mA. The scan velocity was set at 0.05 mm/s during the fabrication process of 5 mm and 20 mm long CFBGs while it was increased to 0.07

mm/s for 48 mm long CFBG. Due to the large size of 48 mm CFBG, the fibre experienced a longer UV exposure time during the fabrication process so the scan velocity of 0.07 mm/s was considered to be sufficient for achieving a comparable profile from this CFBG.

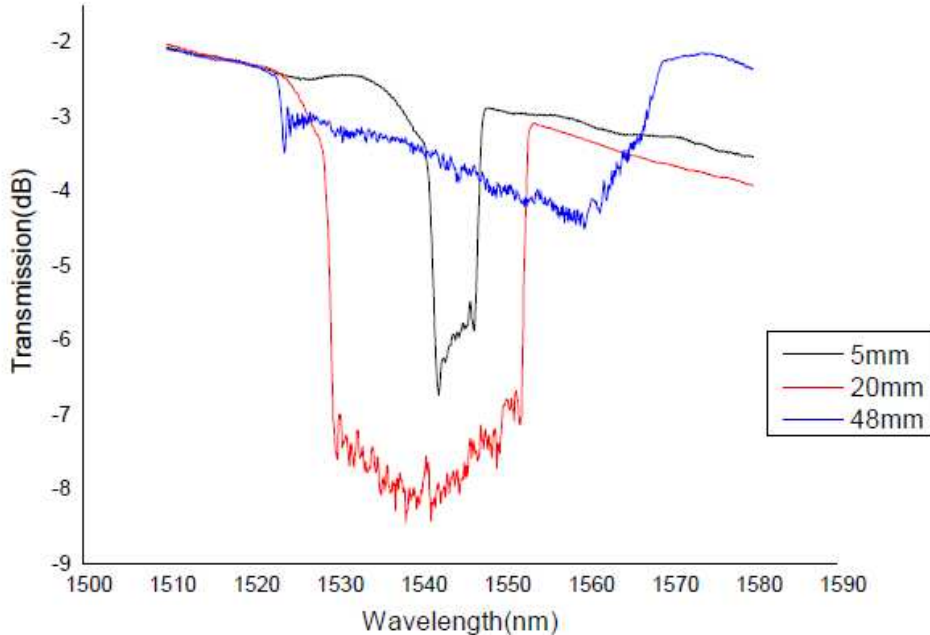


Figure 3. 8. Transmission spectra of CFBGs fabricated by the phase mask technique.

The above figure shows the transmission loss profiles of three UV written CFBGs with the fabrication lengths of 5 mm, 20 mm and 48 mm employing the same phase mask. During the fabrication process, the central wavelength of these gratings was set to be the same. However, as the mask period varies continuously along its length the central wavelengths of three gratings are slightly apart from each other. Regardless of the same fabrication condition of 20 mm- and 5 mm- CFBG, Figure 3.8 evidently shows a stronger loss profile for 20 mm- CFBG. This can be explained by considering the fact that for the same scan velocity, the fibre has experienced more UV exposure during the fabrication of the longer grating than the shorter one. The same figure also presents, 48 mm- CFBG as the weakest grating in this set due to a faster scan speed

(0.7 mm/s) over the inscription process. Figure 3.9 exhibits the transmission spectra of two 5 mm- CFBGs (C_1 and C_2) written by employing different parts of the chirped phase mask. The figure clearly indicates that fabricated CFBGs corresponding to different parts of the mask have different central wavelength. The measured bandwidth for C_1 (CFBG located at shorter wavelength side) and C_2 (CFBG located at longer wavelength side) was 5.81 nm and 6.23 nm respectively. This indicates that the phase mask is positively chirped having smaller period in the shorter wavelengths and a gradual increase in period toward the longer wavelength side. To clarify the argument, the schematic diagram of the employed chirped phase mask is demonstrated in Figure 3.10. This figure addresses the schematic of employed corresponding parts of the mask to fabricate C_1 and C_2 .

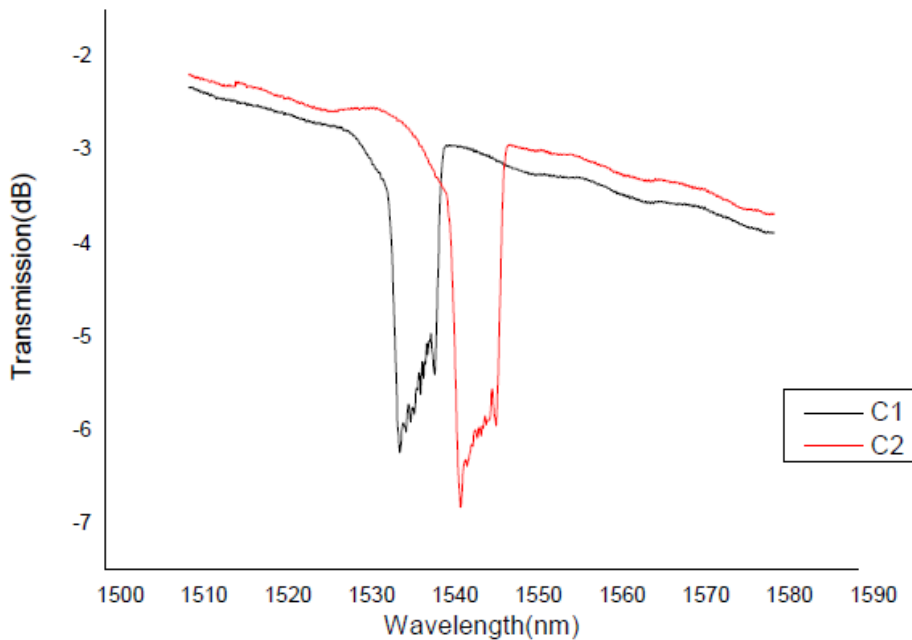


Figure 3. 9. Transmission spectra of 5 mm CFBGs fabricated using different part of the mask.

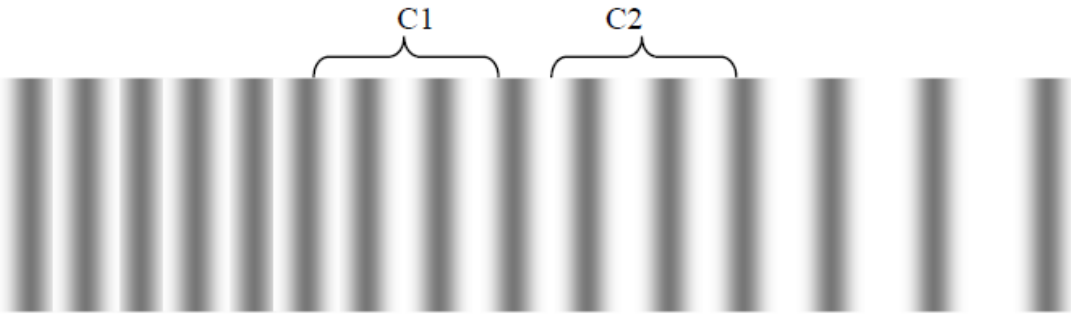


Figure 3. 10. Schematic of the chirped phase mask and pointing different parts that were employed for inscription of each CFB.

3.4. Fibre Gratings with Tilted Structures

In 1990, TFGs were demonstrated by Meltz *et.al* for the first time [81]. Later in 1996 theoretical study on TFG structures and simulation spectra of small angle tilted gratings were revealed by Erdogan and Sipe [61]. The simulation spectra of small angle TFG based on this theory were in good agreement with the experimental data. Advanced UV inscription technology has led to development and study of TFGs with different angles recently. Depending on their tilting angles, TFGs have their unique device functionalities for a range of applications including in-fibre spectrometer [82], EDFA gain flatter [83] and optical sensor interrogation system [84-86]. Also due to the special polarisation property of TFGs, which is discussed later in this thesis, they have been implemented as in-line polarimeters [87, 88], high extinction ratio in-fibre polarisers [chapter 6] and Polarisation Dependent Loss (PDL) equalisers [89-91]. Many of the mentioned reports are based on employing TFGs with small tilt angles or maximum at 45° , where the light is only coupled from the forward propagating core mode to the contra-propagating cladding modes or to the radiation modes. Recently, the theoretical and experimental investigations of large angle ($>45^\circ$) TFGs and a detailed study of the characteristics of forward mode coupling were reported by Zhou

et.al [92]. He performed the investigation showing advantages of TFGs with large tilt angles in temperature, twist, RI and strain sensing [93-95]. Also his theoretical simulation of transmission loss profiles of TFGs with different angles for mode coupling with two orthogonal polarisation states proved that 45°-TFG exhibits the maximum PDL.

3.4.1. Design Principle of TFGs

There are two inscription methods to achieve a tilted structure for a fibre grating:

1. In the phase mask inscription system: tilting the phase mask with respect to the fibre as it is illustrated in Figure 3.11.

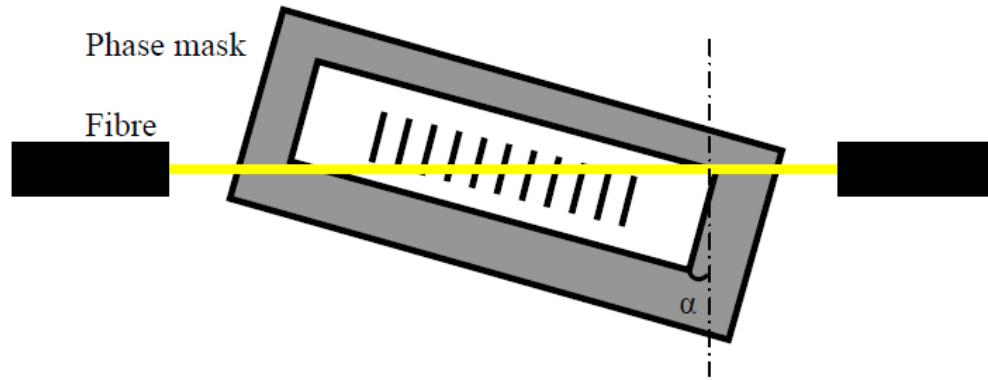


Figure 3. 11. Phase mask technique for TFG fabrication. Note the mask has been tilted by angle α .

2. In the holographic system: rotating the fibre about the axis normal to the plane introduced by two interfering UV beams. Figure 3.12 shows the inscription of TFGs employing holographic technique.

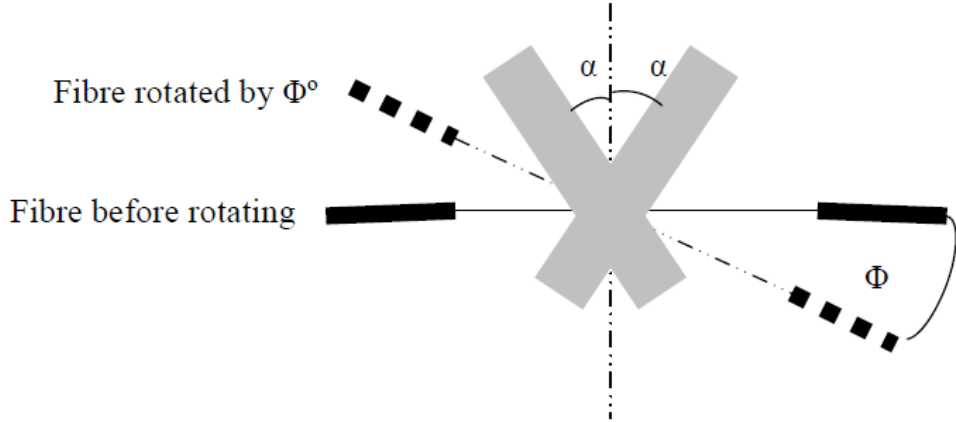


Figure 3. 12. Two beam holographic technique for TFG fabrication while the fibre has been rotated by angle Φ .

However, since by rotating the fibre the interference area is reduced the stability concerns become more important. In fact even a submicrometer displacement in the positions of the beam splitter, mirrors or any other optics mounted in the interferometer during UV exposure results in drifting the fringe pattern and washing out the grating from the fibre.

On the other hand, as it has been mentioned in section 3.2, for a specific wavelength, high quality gratings can be easily fabricated employing phase mask inscription technique. Therefore, all TFGs in this thesis were UV inscribed by using the first method.

Due to the cylindrical geometry of the fibre, the internal grating tilted angle θ_{int} is different with the external phase mask angle in the phase mask technique or the angle of fibre rotation in holographic system θ_{ext} .

In the phase mask technique, the internal angle of the grating, θ_{int} , has the following relationship with the external phase mask tilting angle, θ_{ext} [93]:

$$\theta_{int} = \frac{\pi}{2} - \tan^{-1} \left[\frac{1}{n \tan \theta_{ext}} \right] \quad (\text{eq: 3.3})$$

Where, n is the RI of the fibre.

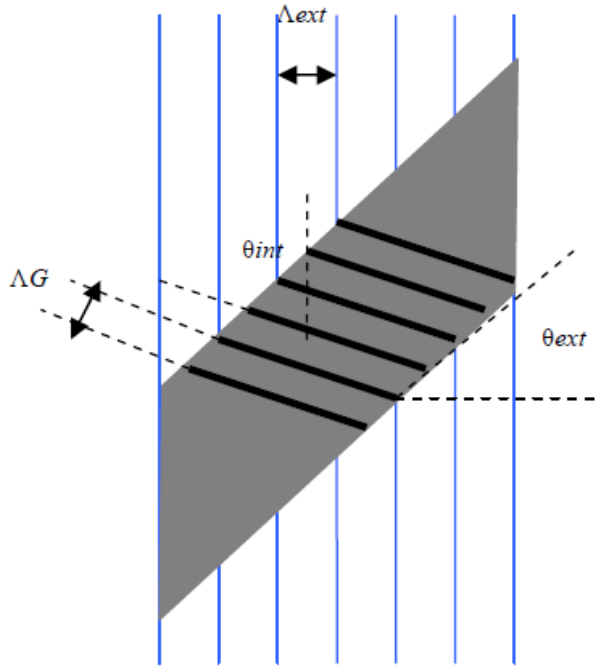


Figure 3.13. Schematic diagram of a TFG structure exhibiting the difference between internal and external tilt angles.

As illustrated in Figure 3.13, the internal grating period of a TFG, ΔG , is depending on the UV interference fringe period, Λ_{ext} by the following relationship:

$$\Delta G = \frac{\Lambda_{ext} \cos \theta_{int}}{\cos \theta_{ext}} \quad (\text{eq: 3.4})$$

The UV interference fringe period, Λ_{ext} can be considered as $\Lambda_{ext} = \Lambda_{pm}/2$ where Λ is the pitch of the phase mask. When the light composed of a range of different wavelength probed into the core of the host optical fibre and meets a TFG, two main processes occur: firstly the light will be diffracted out from the core of the fibre by TFG and secondly it will travel to the cladding until it reaches the boundary of the fibre cladding. Figure 3.14 graphically presents the phase matching conditions for TFGs with tilt angles (θ) <, = and > 45°.

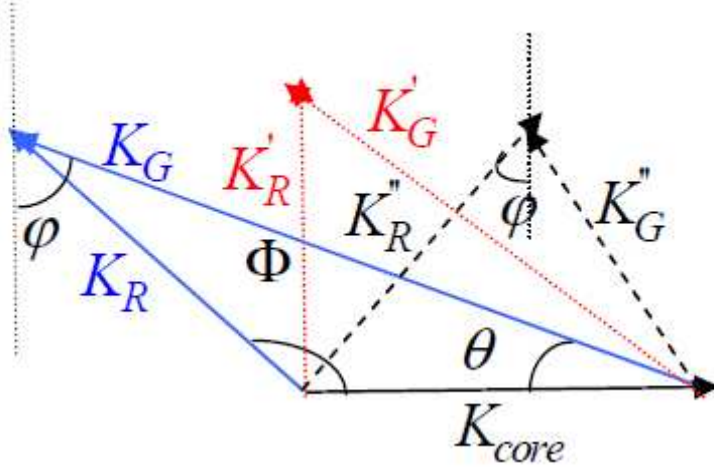


Figure 3.14. Phase matching conditions for TFGs with tilt angles, $\theta <$, $=$ and $> 45^\circ$. Note: φ is the incident angle of the radiated light at the cladding boundary.

The strongest mode coupling only happens when the below phase matching condition is satisfied [88]:

$$\vec{K}_R = \vec{K}_G + \vec{K}_{core} \quad (\text{eq: 3.5})$$

In the above equation, \vec{K}_R , \vec{K}_G and \vec{K}_{core} are the wave vectors of the radiated light, tilted grating and core mode, respectively. Due to the negligible difference of the refractive indices of cladding and core, we may ignore the amplitude difference between \vec{K}_R and \vec{K}_{core} . As shown in Figure 3.14, the coupled light will be directed to different optical paths depending on the tilt angle of the grating (θ). This figure indicates that for $\theta < 45^\circ$, the radiation angle Φ is an obtuse angle and the core mode will be coupled to the backward propagation direction, but for $\theta > 45^\circ$ while the radiation angle Φ is an acute angle, the core mode will be coupled to the forward propagating direction. At $\theta = 45^\circ$ and the radiation angle $\Phi = 90^\circ$, all the phase matched light will be radiated out from the side of the fibre. The Total Internal Reflection (TIR) effect at the cladding boundary is also another important factor that

should be carefully noticed. Due to TIR when the coupled light is radiated out of the core, it either is confined and propagates into the cladding or is not bound by the cladding and tapped out from the side of the fibre. The range for radiation mode coupling can be defined by the critical angle α_c :

$$\alpha_c = \arcsin \frac{n_1}{n_2} \quad (\text{eq: 3.6})$$

Where in the above equation, n_1 and n_2 are refractive indices of the surrounding medium and cladding, respectively. If air is the surrounding medium of the fibre ($n_1 \sim 1$), by employing equation 3.6 the critical angle can be calculated as $\alpha_c = 43.8^\circ$.

Using the same equation, $\alpha_c = 67^\circ$ will be achieved if we change the surrounding medium from air to the water with the RI of about 1.33. As presented in Figure 3.16, φ is the incident angle of the phase matched light that has been radiated out from the core to the cladding / surrounding medium boundary. This angle is related to the internal tilt angle of grating, θ , by:

$$\varphi = \left| 2\theta - \frac{\pi}{2} \right| \quad (\text{eq: 3.7})$$

Now if $\varphi < \alpha_c$, the range of the radiation mode out coupling will be defined as

$\theta_{lc} < \theta < \theta_{2c}$ when θ_{lc} and θ_{2c} are introduced by the following equations:

$$\theta_{lc} = \frac{1}{2} \left(\frac{\pi}{2} - \alpha_c \right) \quad (\text{eq: 3.8}) \quad ; \quad \theta_{2c} = \frac{1}{2} \left(\frac{\pi}{2} + \alpha_c \right) \quad (\text{eq: 3.9})$$

Figure 3.15 illustrates this concept and addresses the calculated value for this range which is 23.1° to 66.9° when air is the surrounding medium and 11.5° to 78.5° in water surrounding medium. As it is also presented in the figure, the light will be radiated out from the fibre as it can not be confined by the cladding in this range.

However, beyond or below this range, all the light will be bound to the fibre, as it will coupled to the contra- or co-propagating cladding modes, respectively.

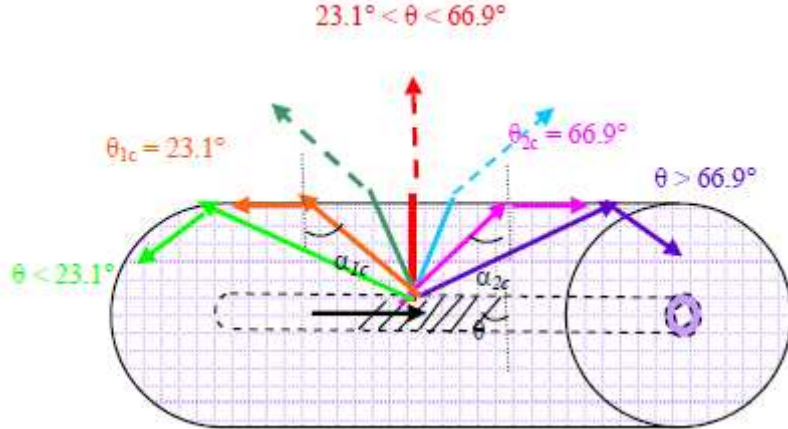


Figure 3. 15. Three coupling regimes for the phase matched light: (a) $\theta < \theta_{1c}$: Contra-propagating cladding mode coupling (b) $\theta_{1c} < \theta < \theta_{2c}$: radiation mode coupling and (c) $\theta > \theta_{2c}$: forward cladding mode coupling.

3.4.2. TFGs with Small Tilted Structure

A comparative study of the characteristics of radiation-mode out-coupling in TFGs, including the fabrication and characterisation of several TFGs and TCFGs was carried out. A set of six 10 mm-long TFGs with the external tilt angles of 0° , 2° , 4° , 6° , 8° and 10° , were fabricated in SMF-28. In this fabrication process, we employed the near field interference pattern of a uniform phase mask with the pitch, length and width of 1083 nm, 30 mm and 13 mm respectively. Prior to the fabrication, the photosensitivity of the fibre samples was enhanced by pressurising them in hydrogen for a period of 48 hours at 150 bars and 80°C . The phase mask was illuminated with a 244 nm UV beam with an average power of 100 Mw. Figure 3.16 presents the transmission spectra of these TFGs.

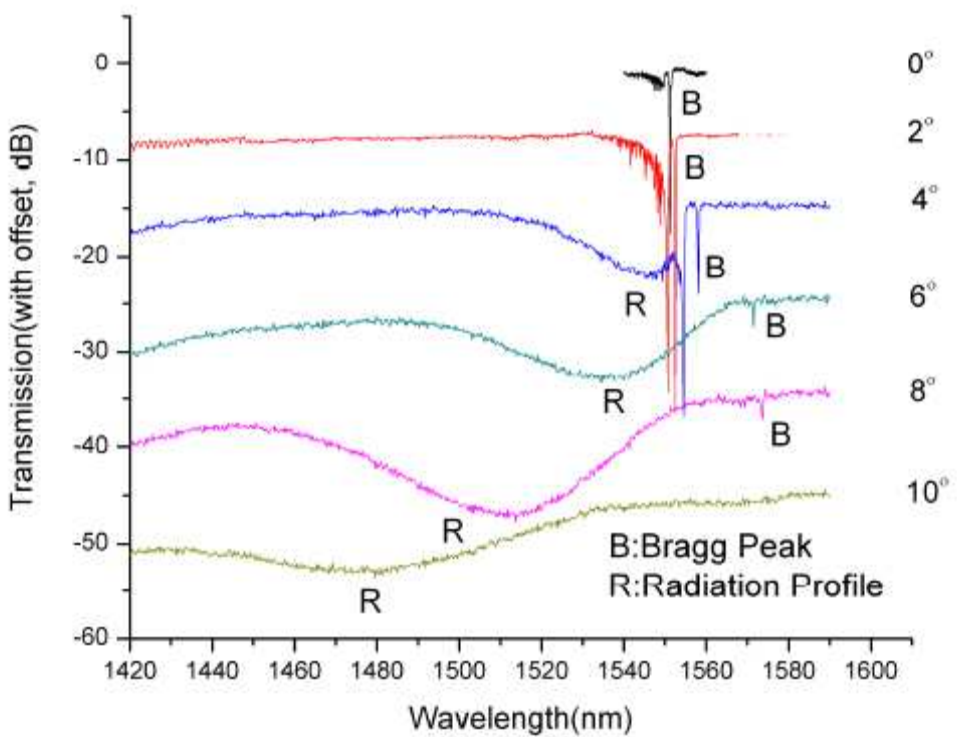


Figure 3.16. Transmission-loss profiles of six TFGs with external tilt angles from 0° to 10° . Note: the spectra were measured when the TFGs were submerged in index match gel to ensure the smooth profiles.

TFGs consist of a RI modulation that is purposely tilted relative to the fibre axis in order to increase coupling between the forward propagating core mode and the contra-propagating cladding modes. As shown in Figure 3.16 the transmission loss profiles of the TFGs are strongly dependent on their tilt angles. With increasing tilt angle, the Bragg peak shifts toward the longer wavelengths whilst its strength decreases until it fully disappears from the profile of 10° -TFG where all light is coupled to the cladding modes. This figure also indicates that the radiation mode out coupling changes gradually with the change in the tilt angle. With increasing tilt angle, the strength of the radiation mode coupling reduces and the central wavelength shifts toward the shorter wavelength side. The dynamic range of the radiation mode out coupling is also increased when the fringes are more tilted. Over the fabrication process, it was noticed that for the same laser power, longer exposure time is required to obtain a high quality

radiation profile of a TFG with larger tilt angle. This is due to the reduction of the interference area after the phase mask being more tilted. As a solution for fabrication of stronger TFGs with tilt angles larger than 4° , we have used the hydrogen loaded B/Ge fibre which benefits from much higher intrinsic photosensitivity comparing with SM-28 fibre.

In order to obtain smooth transmission profiles of tilted gratings, the TFGs were immersed in index gel while measuring their transmission spectra. Figure 3.17 exhibits an example of the transmission profile of 8° TFG, before and after being immersed in index gel. The dense resonances cover 1400 nm – 1500 nm range are caused by the core-cladding coupling and the reflection at the cladding-air boundary. So the multiple resonances can be removed by immersing the grating in index matching gel to generate an infinite cladding layer. In this case, the light is coupled from the core mode to radiation modes, thus the dense resonances evolve to a smooth transmission loss profile.

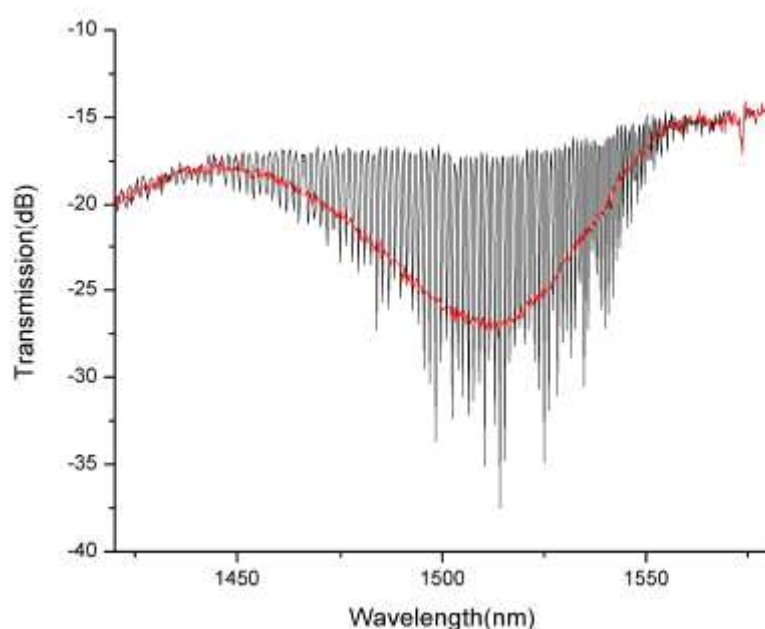


Figure 3. 17. Transmission spectra of 8° -TFG UV inscribed in B/Ge fibre using the phase-mask method. Note: The resonance profile was obtained when the grating was surrounded by air and the smooth profile obtained when the grating was immersed in the index matching gel.

For a small tilt angle, for example 2° , it is possible to produce a well defined single loss band that is blue-shifted with respect to the main Bragg feature as shown in Figure 3.18. This loss band is called ghost dip as it is comparable in size to the Bragg reflection dip [96].

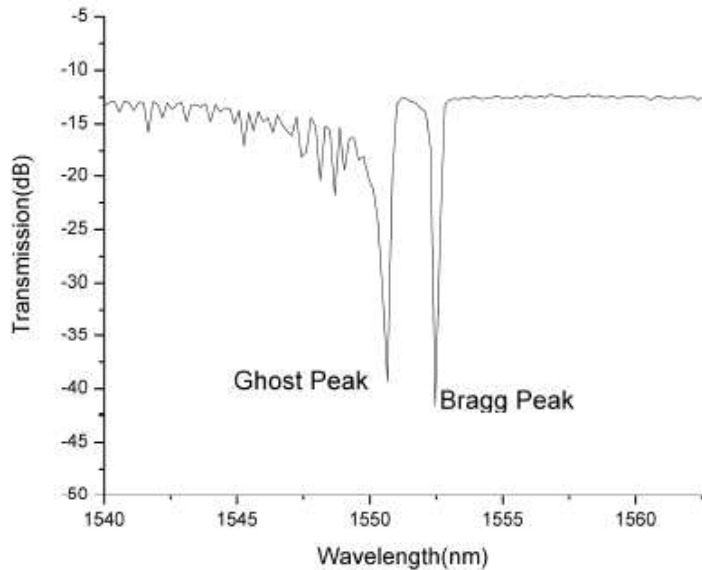


Figure 3. 18. Transmission spectrum of UV inscribed externally 2° TFG in SMF 28 fibre employing the phase mask method.

3.4.3. TCFGs with Small Tilting structure

We used the earlier mentioned chirped phase mask to fabricate TCFGs with small tilted structures by rotating the mask at angles of 0° , 2° , 4° , 6° , 8° and 10° . These six TCFGs with the length of 10 mm were all fabricated in hydrogen loaded B/Ge codoped optical fibre. Transmission loss profiles of the fabricated TCFGs are illustrated in Figure 3.19.

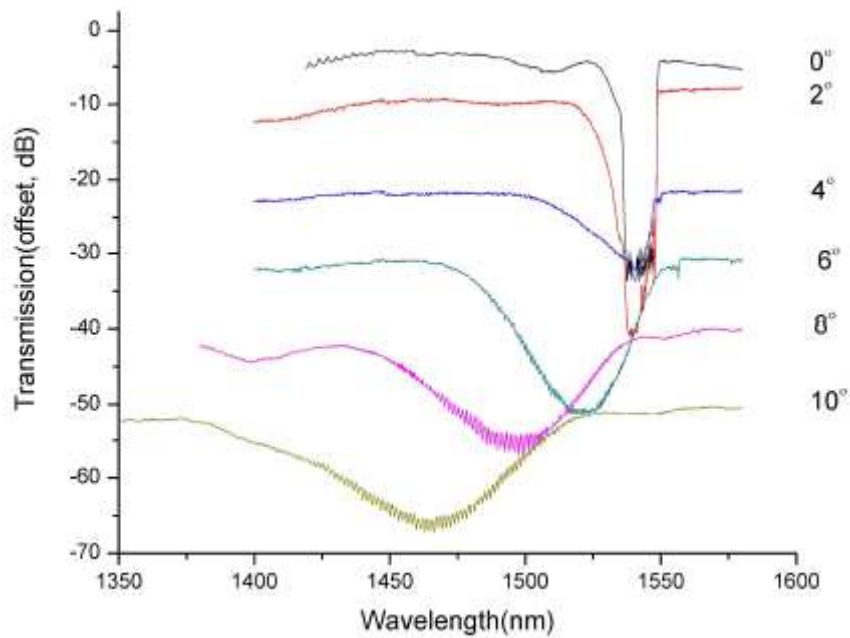


Figure 3.19. Transmission spectra of TCFGs with the external tilt angles from 0° to 10° . Note: the spectra were measured when the TFGs were surrounded by air.

Similar to TFG coupling mechanism, in TCFGs also the coupling takes place between the guided light in the fibre core and the radiation mode field in a contra-propagating direction, but much more stronger than in TFGs with similar tilted structures. In the case of a broadly tilted chirped grating as we can see from Figure 3.19, the loss peaks induced from the radiation mode out-coupling for different wavelengths are spectrally superimposed, resulting in one broad and almost smooth transmission loss peak, and this radiation loss band becomes broader and shifting to the shorter wavelength side with increasing tilt angle. The investigated results clearly show that in general, the spectral response of the loss peak in TCFG depends on the number of factors such as tilting angle, chirp rate and the coupling strength.

3.4.4. Polarisation Characteristics of Small Angle Tilted Fibre Gratings

Experiments were carried out to investigate the spectral response of tilted gratings to different polarisation states. The experimental setup is shown in Figure 3.20.

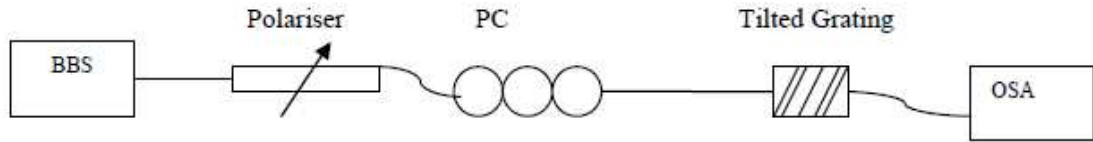


Figure 3. 20. Schematic diagram of experimental setup for characterising the polarisation response of TFGs with small tilted structure.

Light emitted from a broad band source, BBS, was guided into a polariser and a polarisation controller (PC) through a pigtail. The PC was used to adjust the polarisation state of incident light to a TFG or a TCFG. The transmitted light was directed into OSA in which the transmission spectrum was displayed and recorded. In order to obtain the high quality experimental results, the resolution of OSA was set as 0.06 nm. Figures 3.21 (a, b) and 3.22 (a-c) present the polarisation responses of TFGs and TCFGs, respectively. We have realised that there is no noticeable polarisation dependency for gratings with the external tilt angles of 2° and 4° in both standard and chirped tilted gratings and the polarisation effect only start to show for the TFGs / TCFGs with external tilted angles larger than 6° .

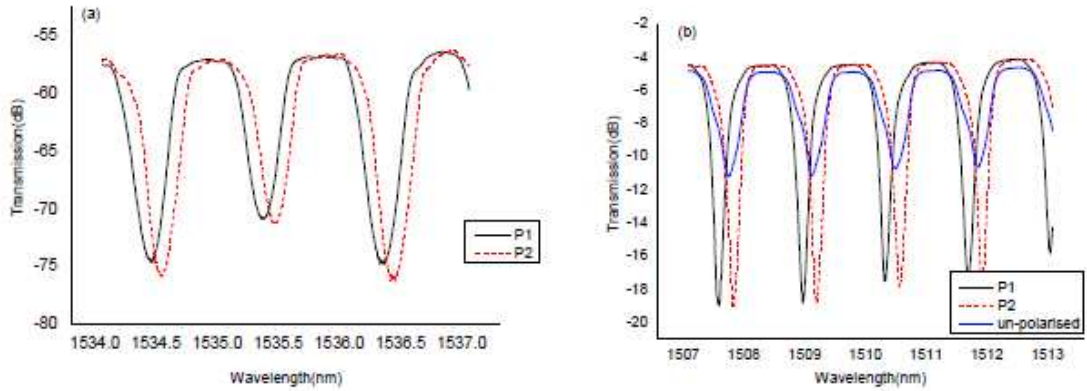


Figure 3.21. Transmission spectra of the UV induced TFGs with external angle θ = (a) 6° and (b) 10° in two polarisation states. Note: the blue graph in figure. (b) is the transmission spectrum of the TFG when the probed light is not polarised.

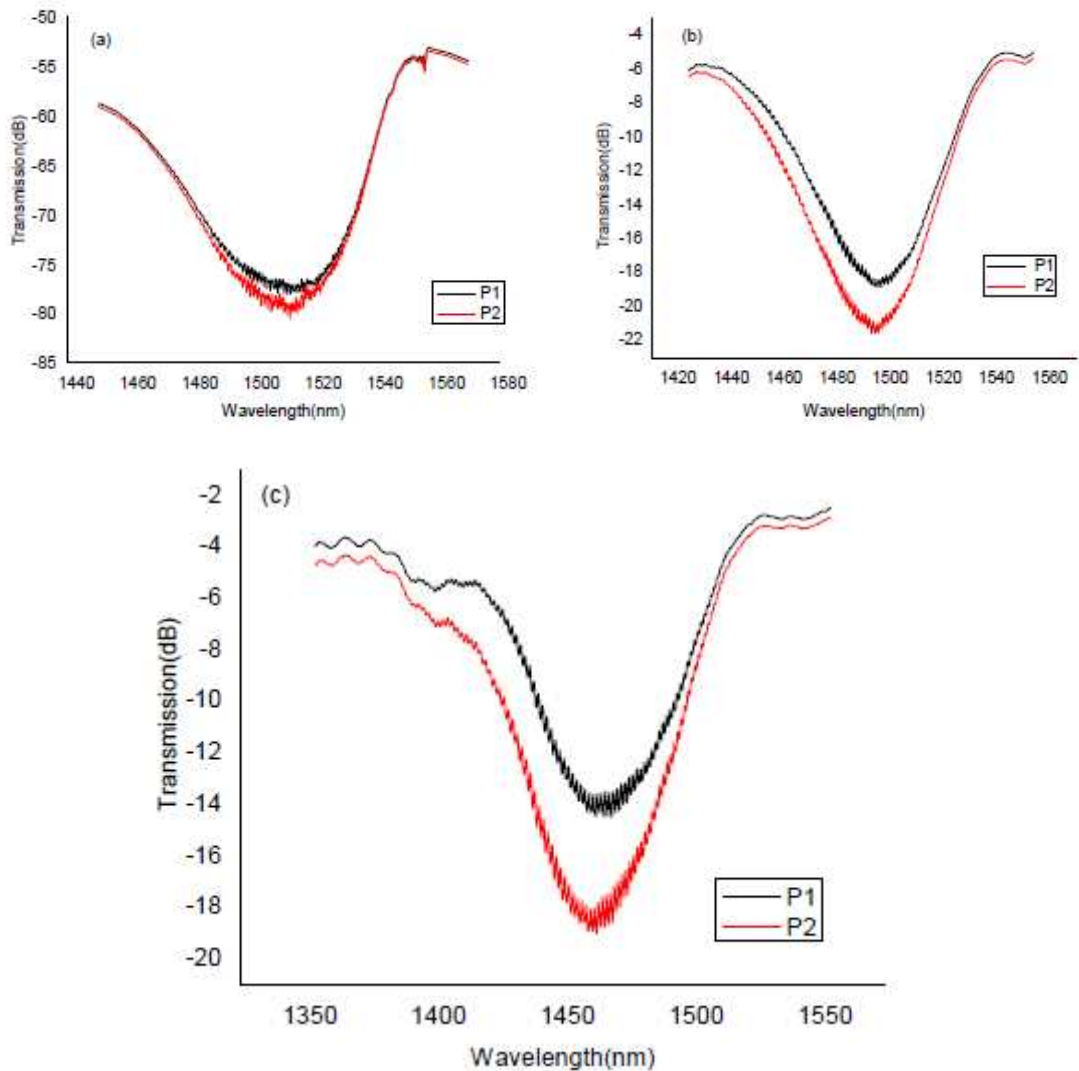


Figure 3.22. Transmission spectra of the UV induced TCFGs with external angle θ = (a) 6° , (b) 8° and (c) 10° in two polarisation states.

In both figures the red and black curves show the radiation mode profiles of tilted gratings for probed light with two orthogonal polarisation states that have been achieved by adjusting the polarisation controller. From Figure 3.21 we can see that for 6°- and 10°-TFG, when the polarisation of the probe light changes, the central wavelength of the coupled cladding mode shifts noticeably but hardly affecting the loss peak strength. Especially for the 10°-TFG, we can see when the grating is excited with un-polarised light, all coupled cladding modes give ~5dB broader loss peaks as shown by blue trace in Figure 3.21 (b), and when the grating is probed by the polarised lights, two sets of narrower and stronger (~12dB) polarisation slit peaks generated. However, we see a quite different picture for TCFGs.

From Figures 3.22 (a-c), it is evident that the polarisation induced shift in central wavelength of the radiation loss profile is almost negligible in TCFGs. However the strength change in transmission profiles of the TCFGs with switching the polarisation state from one to another is much more significant and the strength change becomes more noticeable with the increase in the tilt angle of TCFG from 6° to 10°. This indicates that the PDL value increases with the tilt angle of TCFG. As we will see in chapter 6 of this thesis, the observed polarisation dependency of small angle tilted gratings will present themselves as a good candidate of polarisation loss filter and being employed as infibre polariser in a fibre ring laser cavity to enable single polarisation output.

3.4.5. Thermal Responses of Gratings with Small Tilted Structures

In order to investigate the thermal responses of small angle tilted gratings, the 0°-, 6°-, 10°- TFGs and 0°-, 4°- and 6°- TCFGs were subjected to the thermal condition by increasing the temperature from 10° to 80°C with an increment of 10°C and the

spectra were recorded for each temperature. Figure 3.23 presents the thermal response of a normal FBG (0°-TFG) which was measured ~ 11.5 pm/ $^{\circ}$ C. Figure 3.24 exhibits the wavelength shift of three selected dual peaks of 6°-TFG at around 1500 nm, 1510 nm and 1520 nm against temperature variations. From this figure the thermal sensitivities of 9.82, 9.91, 10.21, 10.29, 10.52 and 10.63 pm/ $^{\circ}$ C were measured for the three sets of dual peaks at 1500 / 1500.1 nm, 1510.4 / 1510.5 nm, and 1520.3 / 1520.4 nm, respectively.

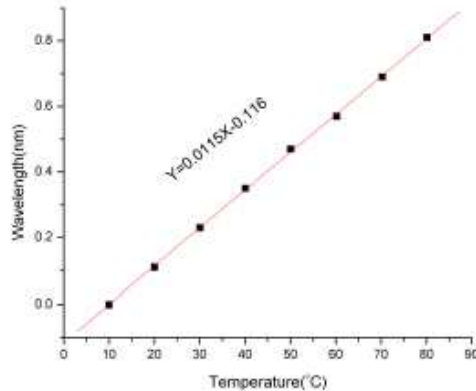


Figure 3. 23. Thermal response of normal FBG.

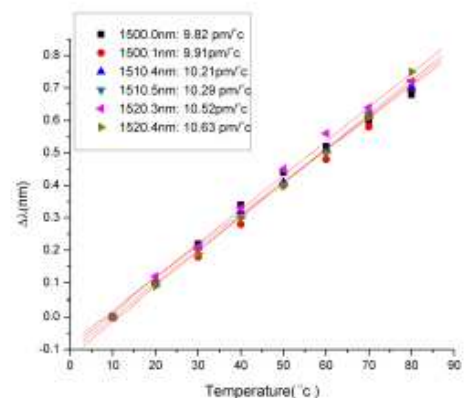


Figure 3. 24. Thermal responses of three selected dual peaks of 6°TFG at 1500 nm, 1510 nm and 1520 nm.

Figure 3. 25 also presents the thermal responses of the three selected polarisation dual peaks of the 10°-TFG and gives the measured thermal sensitivities of 9.12, 9.2, 10.0, 10.1, 10.31 and 10.43 pm/ $^{\circ}$ C for resonances at 1499.6, 1499.7, 1515.8, 1515.9, 1543.2 and 1543.3 nm respectively.

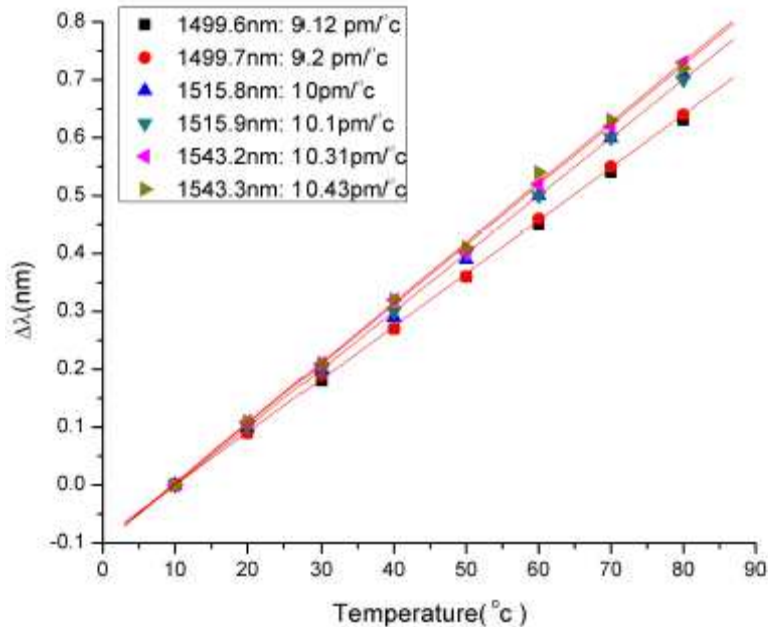


Figure 3.25. Thermal responses of three selected dual peaks of 10°TFG at 1499.6 nm, 1515.8 nm and 1543.2 nm.

Our investigations show the correspondent thermal sensitivities of 6°- and 10°- TFGs are similar and increase slightly for coupled cladding modes with lower orders (longer wavelengths) in the range of ~ 1500 nm to 1550 nm and slightly less than the thermal sensitivity of normal FBG as presented in Figure 3.23.

The measured temperature responses of 0°-, 4°- and 6°-TCFGs are also presented in Figure 3.26. The experimental results indicate the similar value of thermal sensitivities of ~ 11 pm/°C for 4°- and 6°-TCFGs. This response is also quite close to the measured temperature sensitivity of a normal CFBG which is 10.7 pm/°C. Our observations present the tilting angle in TCFGs has a negligible effect on the thermal response of this class of gratings.

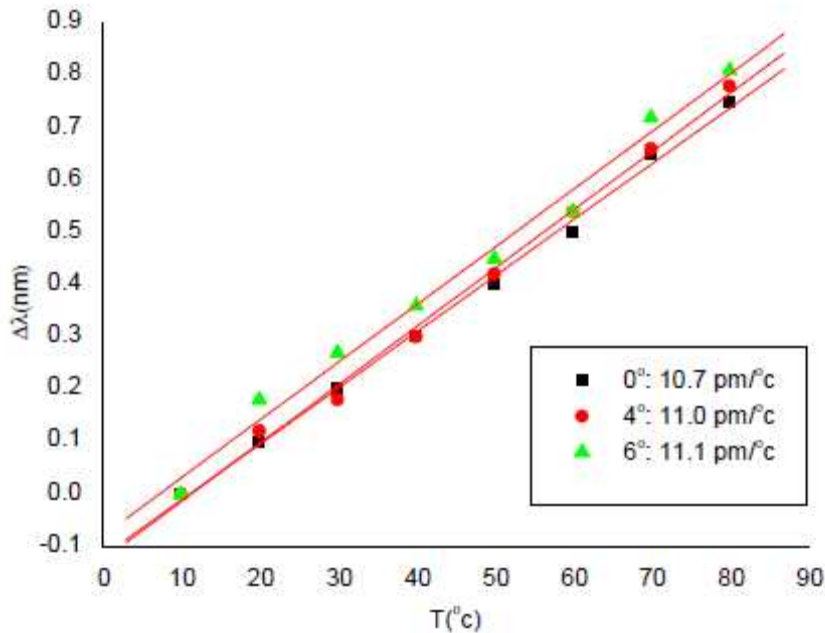


Figure 3. 26. Thermal responses of 0° -, 4° - and 6° - TCFGs.

Two TFGs with the internal tilt angle of 79.6° and 81.7° were UV inscribed in H_2 loaded SMF-28 optical fibre employing a custom designed amplitude mask with the pitch of $6.6 \mu\text{m}$. Considering the relationship between internal and external tilt angles of a TFG, equation (3.3), to fabricate 79.6° and 81.7° the mask was rotated at 75° and 78° respecting to the fibre axis respectively. The grating lengths were 12 mm limited by the size of the amplitude mask. Due to the large pitch size of the mask, there will be less index fringes created in the fibre core, resulting in weaker grating, so multiple scanning was employed during the fabrication. Figures 3.27 (a) and 3.28 (a) exhibit the transmission spectra of 79.6° - and 81.7° - TFG when the randomly polarised light was probing the gratings. Here the tilt angle $\theta(79.6^\circ \text{ and } 81.7^\circ) > \theta_{2c}(66.9^\circ)$ so the light is coupled to the forward propagating cladding modes and series of dual polarisation peak resonances will appear in the transmission spectra. The strength of these dual peaks is about 3 dB when the randomly polarised light is probed in. Figures 3.27 (b) and 3.28 (b) present the zoomed spectra of one paired polarisation loss peaks of

79.6° and 81.7° - TFG around 1550 nm measured with randomly and fully orthogonal polarised states (P and S) of input light, respectively. When the light is switched to one of the polarisation states, one of the dual peaks grows to its maximum where the other one is almost vanished from the spectrum.

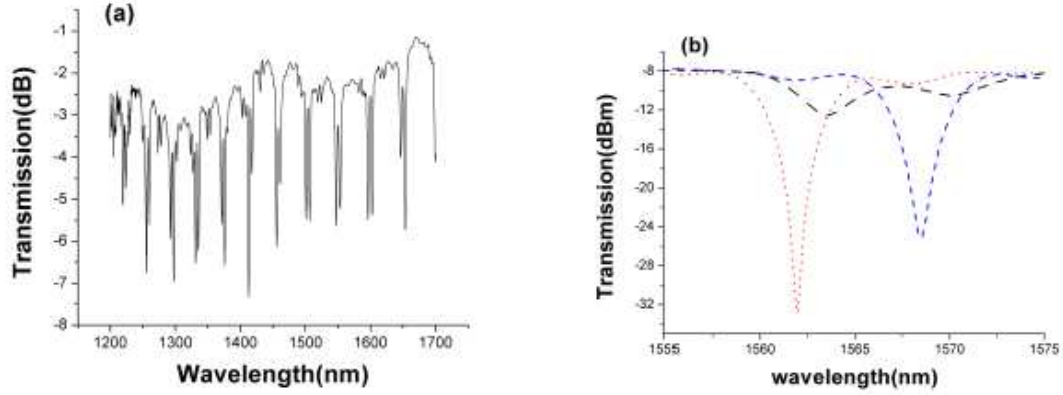


Figure 3. 27. (a) Full transmission spectrum of 79.6° -TFG and (b) zoomed spectra of one paired polarisation loss peaks of 79.6° -TFG around 1550 nm measured with randomly (black line) and fully polarised input lights (red and blue lines).

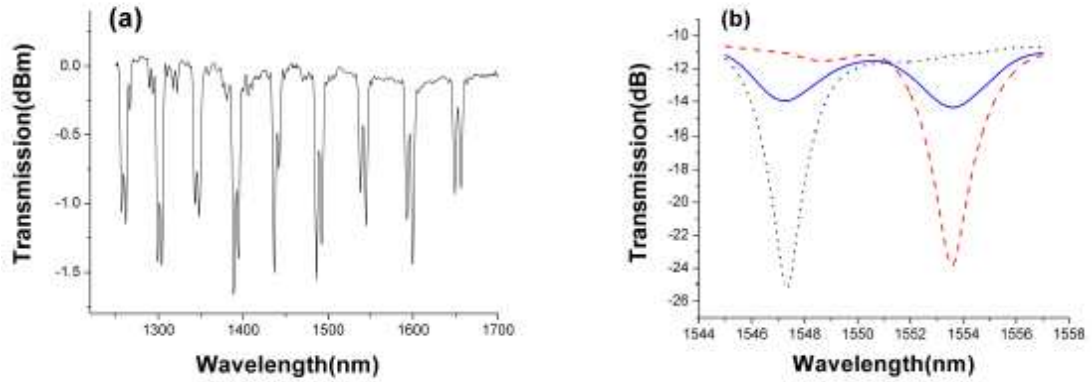


Figure 3. 28. (a) Full transmission spectrum of 81.7° -TFG and (b) zoomed spectra of one paired polarisation loss peaks of 81.7° -TFG around 1550 nm measured with randomly (solid line) and fully polarised input lights (dashed lines).

As it is clearly seen from Figures 3.27 (b) and 3.28 (b), the mode separation between two orthogonally polarised modes in these two TFGs is quite large (~ 6 nm) comparing with small angle TFGs. This might happen as a result of the high

birefringence induced by the highly asymmetric structure of TFGs with largely tilted structure. As it will be discussed in chapter 6, we used the large angle TFGs as PDL filters in fibre ring laser for multiwavelength switchable operation.

3.4.6. Thermal Responses of Gratings with Large Tilted Structures

The two large angle TFGs were characterised in term of their thermal responses. However as their transmission loss profiles were covering a very broad range, from almost 1300 nm to about 1700 nm, only two pairs of dual peak, one at the lower and the other at the longer wavelength side were selected from the transmission spectra of the two TFGs for a comparative study. We chose two pairs of dual peaks one at 1314.1 / 1320.2 nm and the other at 1672.2 / 1680.3 nm from the loss profile of 79.6°-TFG. From the transmission spectrum of 81.7°-TFG, also two pairs of dual peak at 1335.6 / 1340.8 nm and 1664.0 / 1671.6 nm were selected. The TFGs were subjected to the temperature measurement while the temperature was rising gradually in the range of 10°C to 60°C with the increment of 5°C and the thermal sensitivity of the selected dual peaks was measured as presented in Figure 3.29.

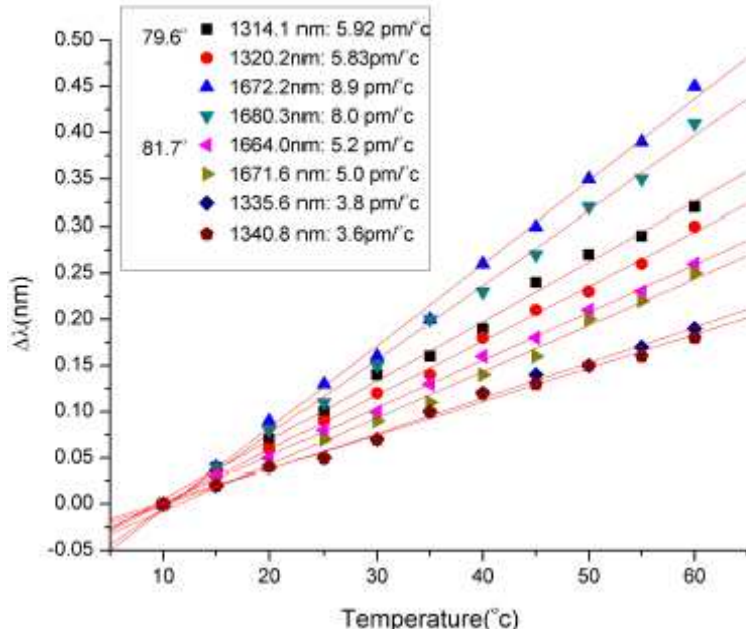


Figure 3.29. Thermal responses of the selected two pairs of dual peaks at 1341.1 / 1320.2 nm and 1672.2 / 1680.3 nm from 79.6°-TFG and two pairs of dual peaks at 1335.6 / 1340.8 nm and 1664.0 / 1671.6 nm from 81.7°-TFG spectrum.

The measured thermal sensitivities for two sets of dual peaks from 79.6°-TFG at 1314.1 nm, 1320.2 nm, 1672.2 nm and 1680.3 nm are 5.92, 5.83, 8.9 and 8.0 pm/°C respectively and those for 81.7°-TFG at 1335.6 nm, 1340.8 nm, 1664.0 nm and 1671.6 nm are investigated as 3.8, 3.6, 5.2 and 5.0 pm/°C respectively. These data indicate that although the thermal response of dual peak with two orthogonal polarisation states are similar, the peak appeared at the longer wavelength has exhibited a bigger temperature sensitivity in all four selected peaks of each TFG. By comparing the selected pair of dual peaks in 79.6°- and 81.7°-TFGs, it is noted that in general 79.6°-TFG is more temperature sensitive than and 81.7°-TFG. Overall, the investigated values are evidently much lower than the typical value of the temperature sensitivities of normal FBGs and TFGs / TCFGs with small tilted structures. This result can be explained by considering the fact that thermal response of a fibre grating is based on thermal expansion coefficient of the fibre corresponding to the variation of the grating's period and thermo-optic coefficient of the grating that is related to the

change in the modal index. It is well-known that, the latter effect is the dominant responsible process for the grating's wavelength shift due to the temperature variations and in large angle TFGs, the thermo-optic coefficient of the grating is less than normal FBGs or small angle TFGs. The low thermal sensitivity of large angle TFGs introduces a new advantage of overcoming the thermal cross-sensitivity in applications.

3.5. Type IA Gratings

Considering the concept of photosensitivity and based on different growth mechanisms, FBGs can be categorised into four classes: Type I, Type II, Type IA and Type IIA. Fabrication of Type I gratings does not require necessarily hydrogenated fibres as they can be written in both hydrogenated and non-hydrogenated fibres and by relatively short exposure time [97-99]. However, in hydrogenated fibre by increasing the inscription exposure time, the index modulation depth reduces resulting in disappearance of Type I grating and formation of Type IA and Type IIA grating in association with different photosensitivity mechanisms. Type IA gratings first discovered by Liu *et.al* in hydrogen loaded fibres and a long exposure time [100-102]. Type IA gratings have a distinct growth profile from other grating types. This class of grating starts to form on the longer wavelength side of the initial Type I grating while still the initial grating is being erased. With the extended exposure time, a large increase in the mean index of the fibre core occurs which is identified from continuous red-shifting of the regenerated grating. This red-shifting depends on a number of factors including the hydrogenation condition and fibre type. There are four reported methods for fabrication of regenerated gratings:

- 1) Long time exposure in holographic inscription setup.
- 2) Static beam exposure through a phase mask.
- 3) Repeated scanning beam in phase mask fabrication technique.
- 4) Blank beam pre-exposure technique.

The main in common disadvantage of the first three techniques is the requirement of the micron scale interference pattern for the full duration of long time exposure; presence of the fringe pattern over the long time exposure, that can take from 20 mins to about 5 hours, would cause the stability concerns.

In the first method in which the holographic fabrication system is used, an extra care must be taken to assemble the component such that any vibrations affecting the interference fringes are minimised. The stable operation of this technique demands good quality devices such as optical lens mounts carefully fixed to an optical bench and an air bearing stage system to isolate the optical bench from ground vibrations. Even with a perfect setup, the quality will be degraded due to the large mechanical distance between the beam splitter and the interference fringes. Also the unavoidable vibrations within the system will increase with the distance, resulting in a degraded quality of the extended exposure.

In static beam phase mask exposure method, FBG inscription demands the minimum of equipment but the high quality flexure stages are essential. The technique is one of the best for simple grating design; however, it suffers from the high cost of the phase mask itself and its wavelength limitation. This system has the same drawbacks as the holographic method in terms of the reduced quality of the fringes visibility due to the stability concerns. A uniform exposure over the grating length and eliminating the system vibrations is hard to achieve, however, owing to the small distance between

phase mask and the interference fringes, (roughly 100 μm), in general this method is more reliable and also more stable than the first one.

Scanning beam phase mask fabrication is also a well known method of grating fabrication. The technique is similar to the static beam phase mask technique but here a small UV-beam is scanned across the optical fibre to induce index modulation. This system again seems straightforward in principle, however, it is very difficult to perfect. In this method a mirror (usually a very complicated and expensive piece of equipment) is placed on a translation stage that scans the beam along the length of the phase mask thus inscribing a grating within the fibre core. In this system an aperture card is used to ensure a uniform exposure of the grating.

Under the perfect conditions when the system is well equipped with an extremely high quality translation stage and other required devices, this technique exhibits some advantages over the static beam phase mask method. Scanning beam phase mask technique is capable of writing the gratings as long as the employed phase mask or even longer while still ensures a uniform intensity profile utilising an aperture card.

In blank beam pre-exposure technique, the fibre properties will change prior to grating fabrication. The principle of this technique is similar to the standard scanning beam inscription setup but here the phase mask is removed so that the UV-beam will pass through a section with no phase relief pattern and the fibre will be pre-exposed to the UV radiation till becomes preconditioned and the index change will be saturated to a certain degree over several scanning process. At this stage, the phase mask will be reintroduced to the system and the Type IA grating will be written in a standard way. This method was introduced in OFS 2003 for the first time [103] where the

association between the maturity level of fibre and the absorption band at 1400 nm was presented. We used this method to fabricate several samples containing a pair of type I - IA gratings in different types of fibre.

Three types of fibre: PS 1250/1500, SM1500 and B/Ge co-doped fibres, were hydrogen loaded at 200 bar and 80°C for 48 hours and stored for a short period at -40°C till they have been used. A phase mask with the length, width and the period of 50 mm, 3.0 mm and 1060.85 nm respectively was employed for the fabrication of a pair of Type I - IA gratings in all three different fibres. It should be noted that the following given experimental parameters for fabrication of gratings in different fibre types are achieved by experimentally examining of different setup parameters. So the reported parameters for each fibre type have been experimentally proved to be the best. The transmission loss profile of a standard FBG and a Type IA grating inscribed in PS1250/1500 fibre is presented in Figure 3.30.

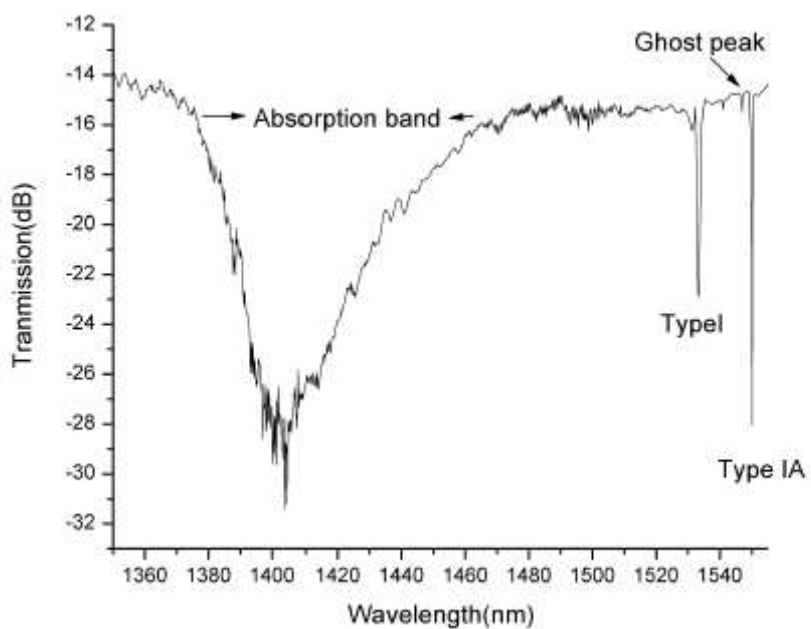


Figure 3. 30. The transmission spectrum of a pair of Type I- IA gratings in PS1250/1500 fibre. Note: the big absorption loss ≈ 14 dB at 1400 nm that formed during the blank beam exposure process indicates the maturity of the fibre.

In order to write the Type IA grating in PS 1250/1500 fibre, 5 mm length of the fibre was pre-exposed to UV radiation from a Sabre FreD laser at 244 nm running at 200 mW over 20 times scanning with the scan velocity of 0.05 mm/s while the phase mask had been removed. The transmission spectrum of the fibre was monitored using a BBS and an OSA during the blank beam exposure process in order to indentify the maturity of the fibre by monitoring the absorption band at 1400 nm. As this absorption band is due to the formation of OH ions in the fibre and not depending on the modulated index change needed for FBG fabrication, therefore monitoring the transmission loss at 1400 nm gives an accurate feedback about the maturity of the fibre. When this loss saturates the fibre is fully mature and ready for the fabrication of the Type IA grating. As depicted in Figure 3.30 the transmission loss at 1400 nm of about 14 dB was achieved during 20 scans of blank beam exposure so the phase mask was reintroduced and type IA grating was formed by UV scanning of 3 mm long piece of the pre-exposed area with the scan velocity 0.01mm/s. Then we inscribed a 5 mm long standard FBG located 3 mm apart from the pre-exposed region of the fibre by employing the same setup and a single scan at 0.1 mm/s velocity. As it was expected, Figure 3.30 evidently shows the appearance of Type IA grating on the longer wavelength with the red-shift of 16.8nm respecting to the normal FBG (Type I) due to large increase in the mean RI of the fibre core caused by the growth of Type IA grating. The observed ghost mode at 1546.98 nm in the same figure also can be referred to the same reason; the increase in the mean refractive index of the core was sufficient for the fibre to become few moded in the pre-exposed section of its length.

In order to investigate the characteristics of Type IA gratings written in different types

of fibre, the same setup and technique was used to fabricate a pair of Type I - IA gratings in SM1500 fibre. Figure 3.31 shows the loss profile of this sample.

7 mm length of the fibre was pre-exposed during three times scanning with the velocity of 0.05 mm/s at the laser power of 300 mW. The fibre became mature while the transmission loss of absorption band at 1400 nm saturated with the strength of ~ 7dB. Then, 3 mm long Type IA grating was UV inscribed by a single scan at 0.05 mm/s velocity in the pre-exposed region of fibre core. A standard 3 mm long FBG was written 3 mm apart from the pre-exposed area of the fibre core during one scan with 5mm/s scan velocity. Figure 3.31 also shows the red-shift of 12.42 nm of Type IA grating which is different from the observed red-shift value in PS 1250/1500.

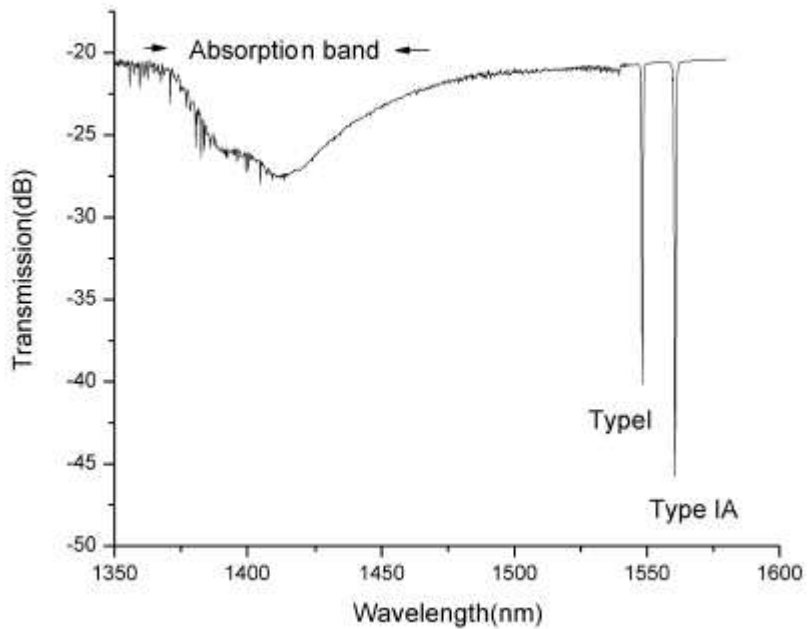


Figure 3. 31. The transmission spectrum of a pair of Type I, IA gratings in SM1500 fibre.

The further study was carried out with the same experimental setup for B/Ge co-doped fibre. Again 7 mm length of fibre was blank pre-exposed to the UV radiation while the laser was running at 180 mW during 5 scans at the velocity of 0.5 mm/s. The maturity of the fibre was realised while the transmission loss of absorption band

at 1400 nm saturated at about 7 dB. Then 2 mm long Type IA grating was fabricated in the pre-exposed area by one scan at 5 mm/s. 3mm apart from the blank exposed part of the core, a 5 mm long FBG was written over a single scan at 12 mm/s. The transmission spectra of these gratings are exhibited in Figure 3.32. The figure indicates a red-shift of 12.04 nm for Type IA. This value is similar to the measured red-shift value of Type IA grating in SM1500 but still different by 0.38 nm. In overall we can see that the observed red-shift values of Type IA gratings fabricated in three different types of fibre are different, indicating that the change in the mean RI of core depends on the fibre type.

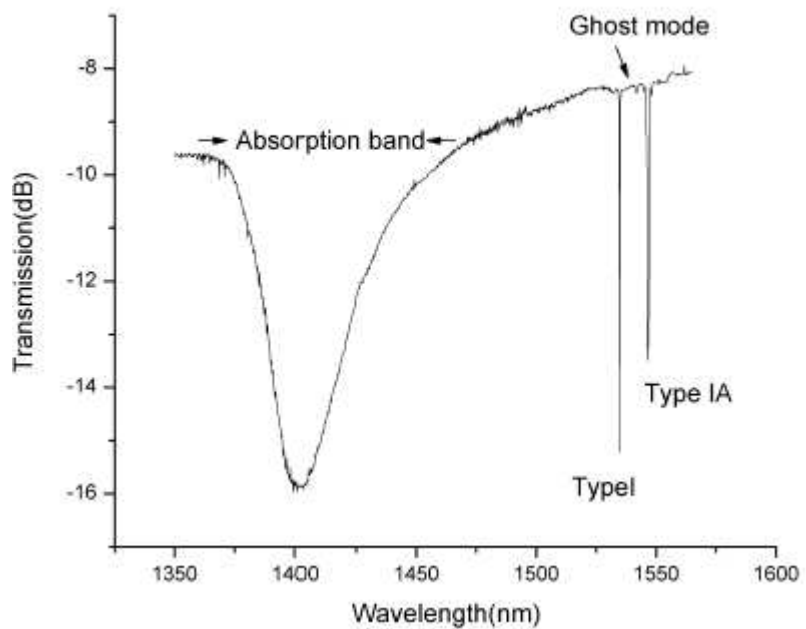


Figure 3. 32. The transmission spectrum of a pair of Type I, IA gratings in SM1500 fibre.

During fabrication of several Type IA gratings over a large period of time and using three different types of hydrogenated fibre, it was noticed that the concentration of H₂ is one of the most important key issues in the quality of written gratings and the maturity level of the fibre, which will be further examined in the following section.

3.5.1. Hydrogen Diffusion Effect In Type I- IA Gratings

During the grating inscription, a portion of UV light is absorbed by the fibre seeing as a slight blue spot at the point where the laser is incident. This absorption causes a significant temperature increase at that point which remains localised due to the very small thermal mass of fibre core and immediately cools down when the UV radiation is removed. If the UV induced absorbed energy is sufficiently large, the temperature increase will be large enough to cause the hydrogen diffusion over the fabrication time resulting in the grating self-annealing process. The hydrogen diffusion effect during the fabrication process results in the shift of Bragg wavelength to such that the grating forms quickly but it will blue-shift up of few nm depending on the fibre type before the end of inscription process. A further study of hydrogen diffusion effect in Type I and IA gratings was carried out by fabricating two identical samples made in two different fibre types: PS1250/1500 and SM1500. One sample from each fibre type was annealed at 103°C for 24 hours immediately after fabrication and the other one was kept in the room temperature where its transmission spectrum was continuously monitored with different time intervals, starting from 5 minutes to 4 days, over 1 month period when it became stabilised. Figures 3.33 and 3.34 show the transmission spectra of these paired Type I and IA samples made in SM1500 and B/Ge co-doped fibres respectively.

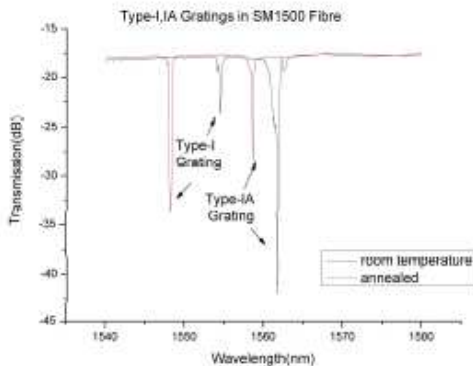


Figure 3.33. Transmission loss profiles of two identical samples made of SM1500 fibre type, one kept in the room temperature and the other was annealed at 103°C for 24 hours.

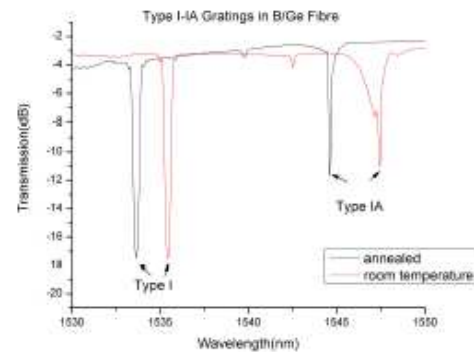


Figure 3.34. Transmission loss profiles of two identical samples made of B/Ge fibre type, one kept in the room temperature and the other was annealed at 103°C for 24 hours.

The above figures evident the blue-shift of both Type I and IA gratings in two fibre types as a result of hydrogen out-gassing. The measured wavelength shifts of these gratings have been summarised and presented in table 3.2.

Fibre Type	Type I / $\Delta\lambda$ (nm)	Type IA / $\Delta\lambda$ (nm)
B/Ge	1.81	2.87
SM 1500	3.4	3.08

Table 3.2. The measured blue shift of grating pairs in different fibre types.

The different wavelength-shifts for different gratings in different fibres are a clear consequence of different hydrogen concentrations in the fibre core and various rates of H₂ out-gassing. The transmission spectra of two samples that were kept in room temperature were continually monitored employing a BBS and an OSA. Figures 3.35 (a, b) and 3.36 (a, b) present the Bragg wavelength shifts of Type I and Type IA gratings made in B/Ge co-doped and SM1500 fibre respectively.

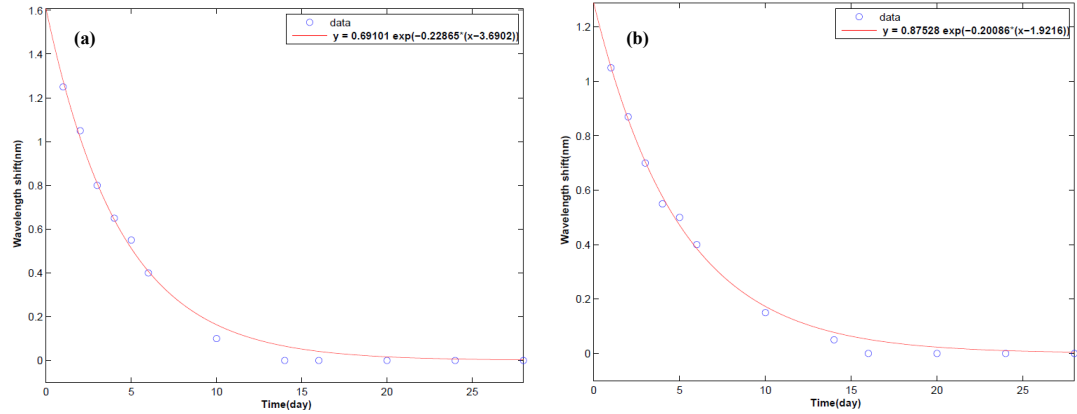


Figure 3.35. Bragg wavelength shift of (a) Type I and (b) Type IA grating inscribed in BG/e co-doped fibre over a period of one month at the room temperature.

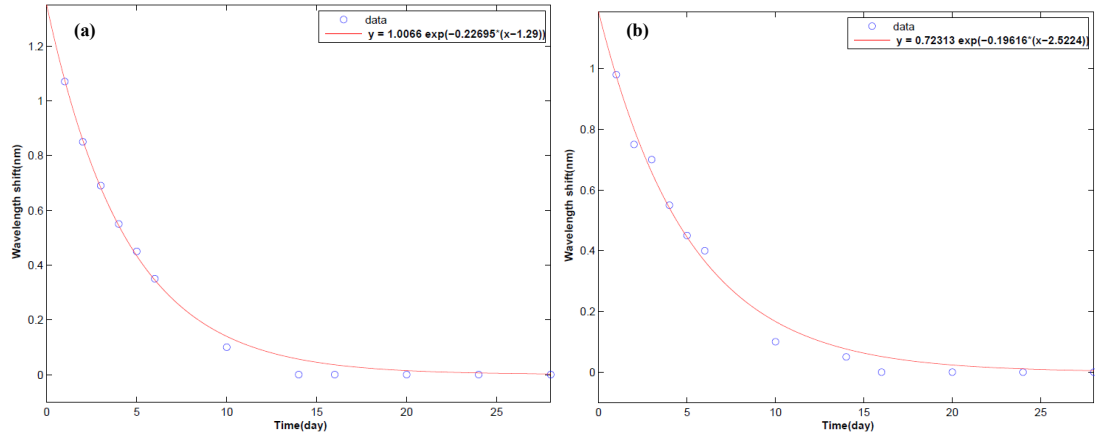


Figure 3.36. Bragg wavelength shift of (a) Type I and (b) Type IA grating inscribed in SM1500 fibre over a period of one month at the room temperature.

The above figures present an exponential trend of the Bragg wavelength shift in all gratings. As it is seen in the figures Type I gratings reached to the stability after 14 days in both fibre types while Type IA gratings carried with the decay trend till 16 days at the room temperature. Over one month period, the measured blue shifts of Type I and IA gratings inscribed in B/Ge co-doped fibre at room temperature were 1.07 nm and 0.98 nm respectively. The wavelength shift values over the same period and at room temperature for Type I and IA gratings written in SM1500 fibre were 1.25 nm and 1.05 nm respectively which are slightly more than what have been realised from the B/Ge fibre. Our experimental data shows a larger wavelength shift

for Type I than Type IA grating written in the same fibre type under the same conditions and over the same period of time.

3.5.2. Thermal Response Of Type I-IA Gratings

The temperature responsivities of Type I-IA gratings inscribed in both SM1500 and B/Ge co-doped fibres were also examined. For this measurement, the sample was placed in a Peltier device in connection with a temperature controller. Then the sample was connected to a broad band light source from one end and to an OSA from another end and the transmission spectra of the gratings were monitored. The temperature was gradually increased from 30°C to 90°C with the increment of 10°C. The temperature response of Type I-IA gratings fabricated in B/Ge co-doped and SM1500 fibre are presented in Figures 3.37 and 3.38, respectively.

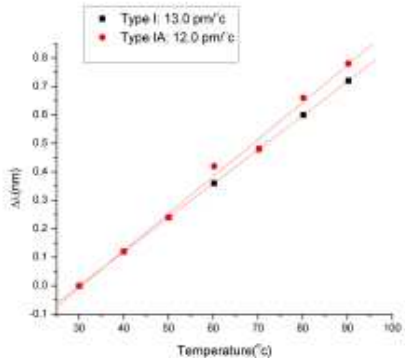


Figure 3. 37. Thermal responses of Type I-IA gratings written in B/Ge co-doped fibre.

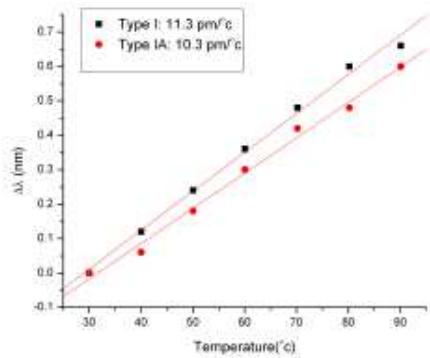


Figure 3. 38. Thermal responses of Type I-IA gratings written in SM1500 fibre

The investigated thermal sensitivities for Type I gratings in BG/e co-doped and SM1500 fibres were 11.3 and 13.0 pm/°C, respectively, while the thermal responses of Type IA gratings in both fibres were measured 10.3 and 12.0 pm/°C, respectively. The result indicates that Type IA gratings were less sensitive to the temperature than type I gratings by 1 pm/°C in both fibre types. Also from the above figures it is

observed that the gratings inscribed in SM1500 fibre exhibited slightly higher thermal sensitivity. The difference between the temperature sensitivities of Type I and Type IA gratings written in the same fibre over a relatively simple fabrication process introduces an efficient approach in fabrication of a dual sensor capable of decoupling of strain and temperature [103].

3.6. Chapter Conclusions

This chapter contains a full discussion of two main fibre grating inscription techniques, holographic and phase mask, which have been employed to fabricate all gratings in this thesis. The holographic inscription method has been employed to fabricate FBGs with arbitrary wavelengths in the range of 1450 nm; these gratings have been employed for telecommunication applications.

The phase mask fabrication technique, as the preferred method to inscribe the high quality gratings, has been chosen to inscribe almost all different structures gratings mentioned in this thesis employed for sensing applications and tuneable ring laser systems.

The chapter also demonstrated the systematic investigation of the structure, fabrication method, spectral response, polarisation dependency and thermal response of various UV written fibre gratings with novel structures, including chirped gratings, small angle TFGs and TCFGs and TFGs with large tilted structure. All these novel fibre gratings exhibited unique properties and desirable advantages which may offer potential use for a range of applications.

Finally in this chapter, we have discussed the grating growth characteristics for two different photosensitivity types of grating: Type I and Type IA. The detailed description for each type of grating written in three different fibre types and their distinct spectral evolution during UV-exposure was performed. Blank beam exposure fabrication technique as the most efficient approach of Type IA grating inscription was employed.

A detailed investigation of H₂ out-gassing effect on a pair of Type I-IA gratings written in two different fibre types was carried out. Thermal characteristics of these

gratings were also investigated and the comparison study between the thermal responses of Type I-IA gratings inscribed in different fibre types was performed. The paired Type I-IA gratings may be used for optical sensing applications with dual parameter sensing capability.

Chapter 4

Optical Sensing and Embedded Fibre Bragg Gratings in Aluminium Alloy Matrix Composite

4.1. Introduction

The concept behind fibre optic sensing can be simply explained by an optical fibre carrying light to an area where it is encoded in response to a change of the measurand or condition (for example, strain, temperature) and the encoded light signal reflects back or transmits through the fibre to be processed thereby extracting the sensing information. In transit, this optical signal is completely immune to the Electro-Magnetic Interference (EMI), so the fibre sensor can be located in a region of high electric potential or in a hazardous area without the need for any sort of special precautions. In general, fibre sensors offer important advantages like electrically passive operation, EMI immunity and high sensitivity.

FBGs are good examples of fibre sensors, which provide all above mentioned advantages plus additional capability of inherent self referencing and multiplexing in a serial fashion along a single fibre. Their sensing functions are derived from the sensitivity of both RI and the grating period to the externally applied mechanical or thermal changes. FBG-based sensors have appeared to be useful for many applications particularly in the area of distributed sensing where the FBG arrays can be embedded in materials for creating smart structures to allow for measurements of parameters such as load, temperature, and strain from which the health condition of the structure can be monitored and assessed on a real-time basis. However, the choice of embedding material has always been limited to the glass and carbon fibre reinforced composite materials and structures and there has not been any work reporting of embedding grating arrays into metal matrix composite.

Via a collaboration project between the Photonics Research Group at Aston University and the Rapid Manufacturing Research Group of Loughborough University, we for the first time have embedded FBG array sensors into Aluminium alloy matrix composites using Ultrasonic Consolidation (UC) technique and investigated the possibility of using FBG sensors to monitor metal matrix structures. Experimental investigation is presented on characterisation of transmission spectra of embedded FBGs under different conditions. These spectra indicate optical responses of the embedded samples to the induced bending, loading and temperature changes. Additionally, the polarisation effect of the embedded samples has been studied. The results from the investigation have clearly demonstrated the self-sensing capability of the FBGs embedded in metal matrix composite. We envisage that metal matrix based engineering tools and structures made by advanced solid-state rapid manufacturing UC technique may incorporate with FBG sensor arrays thereby becoming smart structures, which would be beneficial to a range of applications such as civil structure monitoring, bridges, rail monitoring and vehicles.

4.2. Fabrication of FBG arrays and their embedding in metal matrix composite structures

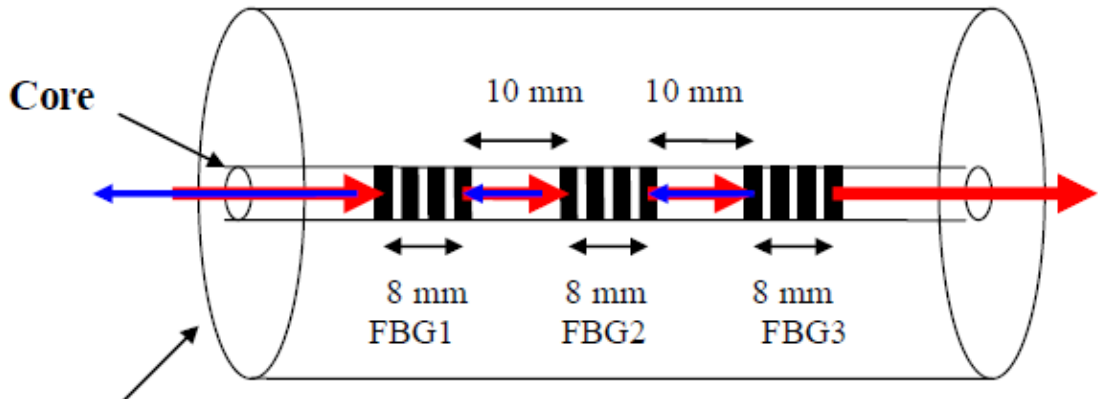
The fabrication process of the proposed sensors contains two major steps:

- 1- UV- inscription of the FBG array in a single mode optical fibre.
- 2- Embedding FBG array into layers of metal composite by UC technique.

In total, four fibres containing the array of three FBGs at different wavelengths were fabricated and then subjected to the embedding process. Three out four FBG array fibres were survived the embedding process, indicating a reasonable creditability of the embedding procedure in terms of high survival rate.

4.2.1. UV inscription of FBG array in optical fibre

The FBG arrays were UV-inscribed in SMF-28 fibres using a scanning phase mask technique with CW frequency doubled Argon ion laser operating at 244 nm. Prior to the UV-inscription, the photosensitivity of SMF-28 fibres were enhanced by pressurising them in hydrogen tube for a period of 48 hours at a pressure of 150 bars and 80°C. The integrated phase mask used in the experiment contains three 8 mm - long mask patterns with different pitch sizes along one dimension separating by 10 mm, thus three FBGs of different wavelengths could be written in a single fibre during one UV beam scan. The schematic profile of the fabricated FBG array is presented in Figure 4.1.



Cladding

Figure 4. 1. Schematic diagram of the fabricated FBG array with three gratings at different wavelengths.

According to the design from the Rapid Manufacturing Research Group of Loughborough University, the fibre length containing the FBG array should be about 70 mm to accommodate the size of the metal matrix sample. Thus, 60 mm length of the middle part of the host fibre was chemically stripped off using a normal chemical paint remover for grating array inscription. The chemical stripping of the fibre could help the device to experience less damage in the stripping process providing a more survival chance for the sample during the embedding process where the fibre would be subjected to the pressure and load. The length of each FBG was about 8 mm and the separation distance between adjacent gratings is 10 mm, as defined by the phase mask pattern. The UV laser power of 100 mW was used and the focused laser beam was scanned across the fibre through the mask at a velocity of 0.5 mm/s. After the UV-inscription, all FBG array samples were annealed at 80°C for 24 hours to stabilise their properties.

4.2.2. Embedding FBG arrays in metal matrix by ultrasonic consolidation

UC is a solid-state rapid manufacturing process which may be employed to fabricate metal structures in layer-by-layer style and finish the final profile by contour milling [104]. This fabrication process involves transducer passing through a sonotrode to samples in the form of ultrasonic oscillations. It has been reported that these oscillations cause friction at the consolidation interface, which breaks up oxides and contaminants at interfaces and brings clean surfaces into contact to bond together [104].

The alpha UC machine used in this work was modified from a 3.3 kW seam welding apparatus and supplied by Solidica Inc., USA. The machine works at a constant 20 kHz frequency with a 50 mm diameter sonotrode. It consists of a power supply, ultrasonic transducer-booster-sonotrode stack, a motor drive system and a pneumatic pressure system for applying a clamping force to a work piece as shown in Figure 4.2.

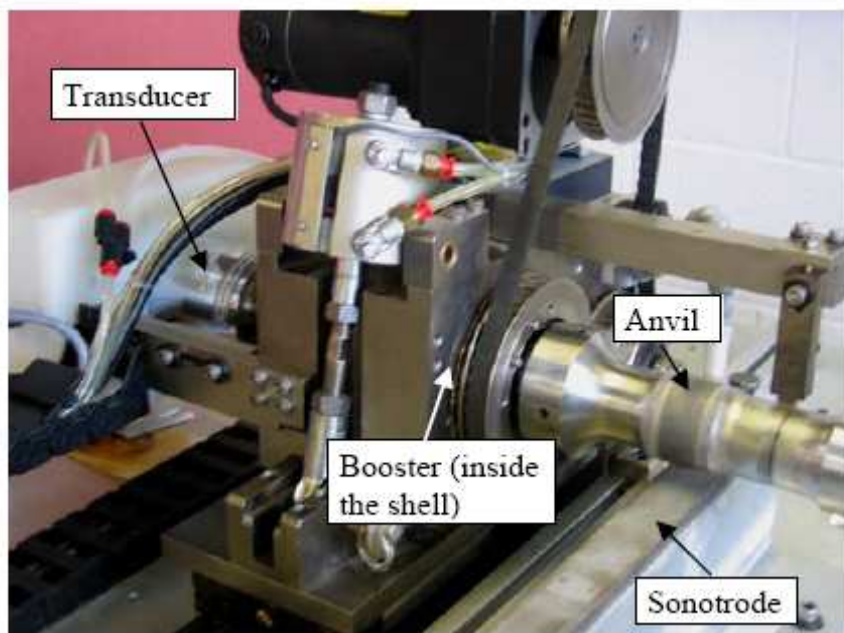


Figure 4. 2. Alpha UC machine in the laboratory of Rapid Manufacturing Research Group of Loughborough University.

Three process parameters can be controlled in this machine, i.e. amplitude of oscillation, contact pressure and traverse speed, and their control ranges are shown in table 4.1.

Oscillation amplitude, μm	Contact pressure*, MPa	Transverse speed, mm/s
6.5 – 14.5	72.5 -264	0 -77

Table 4. 1. Parameter control ranges for the alpha UC machine.

* Contact pressures on work pieces are controlled by a pneumatic cylinder with pressure ranging from 0 to 690 kPa.

In order to shape the embedding structure, two types of Aluminium Alloy, Al 3003 H18 (which is fully strain hardened) and 3003 O (which is annealed and soft) - with a width of 25 μm and a thickness of 100 μm, were employed. If SMF-28 fibres were embedded between two 100 μm metal foils, they would be easily damaged by the sonotrode as the large plastic flows may occur around the fibre during the consolidation process and also due to the relatively fragile property of the fibre [105]. Therefore, two foils were monolithically pre-bonded by the UC machine to form a layer with the thickness of 200 μm. Pre-bonding process took place at a pressure of 114 MPa, amplitude of ultrasonic oscillation of 6.5 μm and consolidation speed of 34.5 mm/s but for embedding process, the pressure was increased to 155.8 MPa and the amplitude of ultrasonic oscillation was 10.4 μm but the transverse speed was kept the same as in pre-bonding process.

After testing the four different structure arrangements, the matrix arrangement was chosen to be plate/H18/O/FBG and SiC/O/H18. In this arrangement an Al 1050 support plate with the thickness of 1.2 mm was introduced into sandwich structure. During the UC, foils tended to distort along the consolidation direction into a ‘U’ shape due to plastic flow. Although this has not been a serious problem for monolithic

consolidation, it can damage the fibres due to the large deformations that may occur during embedding process. This problem is generally solved with the increase in the structure's thickness. By introducing a support plate, distortion of foils can be minimised to avoid large bending deformations.

To accommodate the support plate into an embedding process, an Al 3003 H18 foil was first consolidated onto the support plate using the embedding parameters, and an Al 3003 O foil was then bonded on the top of H18 foil using the pre-bonding parameters. After that, the fibre containing FBG array was placed between the two pre-bonded layers, this sandwiched structure was clamped at one end and the other end was free for consolidation. To keep the balance, two SiC fibres were placed on each side of the fibre containing FBG sensors between the two pre-bonded metal foils. It should be mentioned that for UC embedding, all fibres were fully stripped in the embedding region to ensure a high interfacial strength due to the distribution of the fibre's jacket along the interface.

As shown in Figure 4.3 the sonotrode was laid down to contact with the sample where the pressure is applied and ultrasonic oscillation takes place. After the sonotrode travelled from the clamped to the free end, the fibre containing FBG sensors and four SiC fibres were embedded in the metal matrix composite in solid state. Three out of Four embedded samples were survived from the UC embedding process.

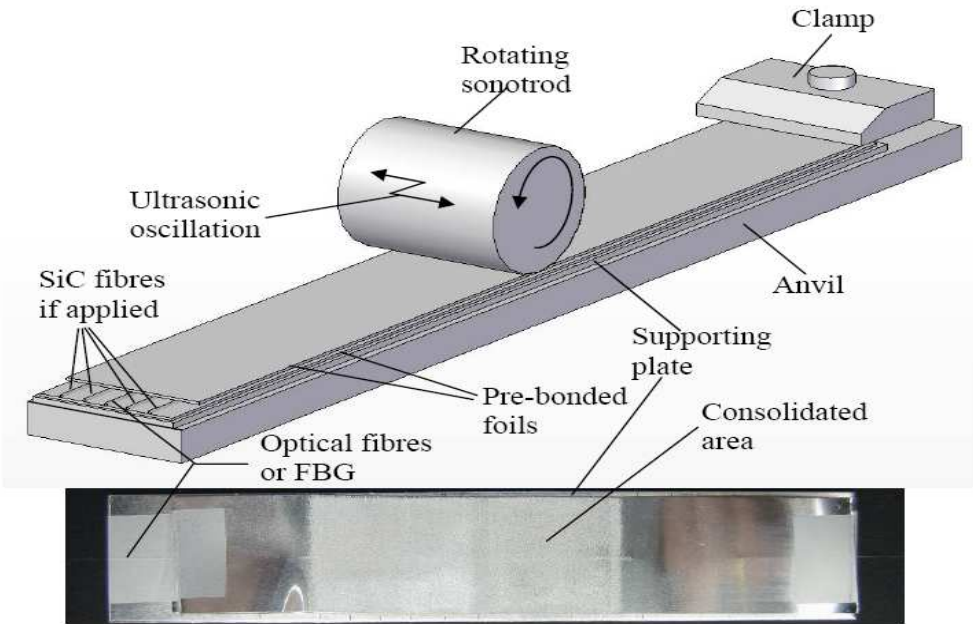


Figure 4. 3. Schematic diagram of the UC system used to embed FBG array fibres in metal matrix composite samples.

The microscope image of the cross section of the embedded fibres was examined in both bright field and the polarised light image as presented in Figures 4.4 (a, b). These figures indicate the survival of the fibre under the embedding process since no sign of crack or damage in the cross section of the fibre is observed.

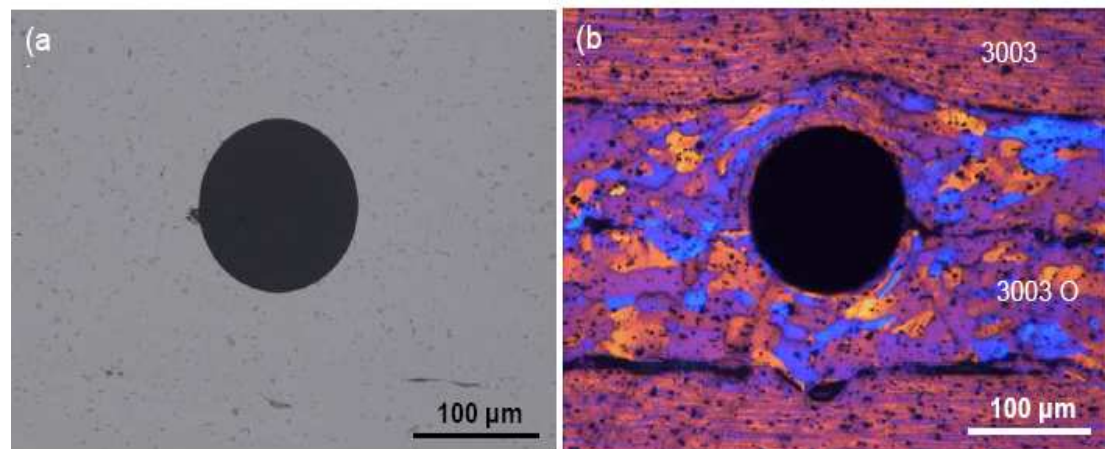


Figure 4. 4. Cross section microstructures of the SMF-28 fibre (without jacket) embedded sample, a) bright field image, b) polarised light image after anodisation.

The UV inscribed FBG array sensors were embedded into such layer-consolidation formed metal structures. The further experimental investigations, which will be explained in details in the later sections of this chapter, indicate that these FBG embedded metal composite structures are possessing smart structure function with the self-referencing and sensing capabilities.

Comparing with other fibre embedding techniques, UC has several advantages. Firstly UC is an additive manufacturing process and can produce components with complicated geometry [104]. Secondly, UC is a low temperature process; in this method fibres can be embedded at temperatures around 30% - 50% of the matrix absolute melting point [105, 106], so stress caused by a mismatch in Coefficients of Thermal Expansion (CTE) between matrix and fibre is reduced. Furthermore, UC process is able to break up the oxide film and contaminant on the foil surface to make metal to metal contact and as a consequence no pre-treatment and atmosphere control are required in this method [107-109].

4.3. Characterisation of Embedded FBG Metal Matrix Samples [P5, P7]

Characterisation of FBG sensor arrays was carried out before and after embedding process in order to reveal the embedding induced effects. Transmission spectra of the three survived FBG embedded metal matrix samples, S1, S2 and S3, were analysed using a BBS and an OSA (HP86142A) and the comparative spectra before and after the embedding are shown in Figures 4.5 (a-c).

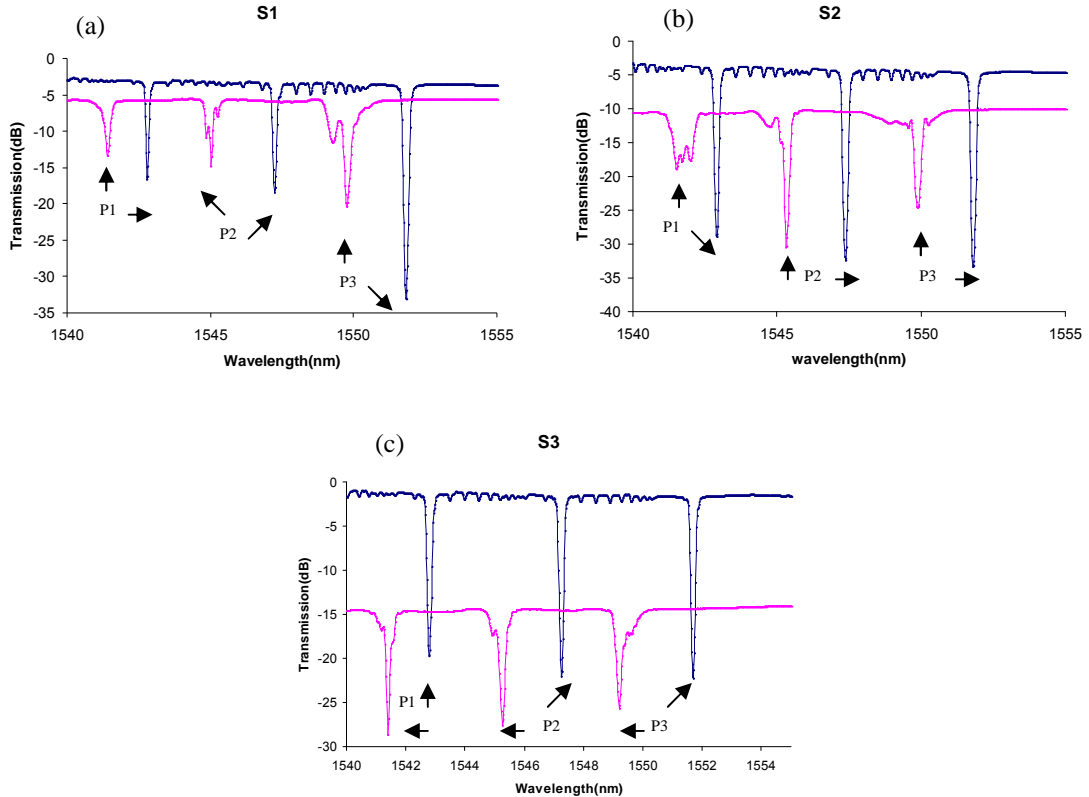


Figure 4.5. Measured transmission spectra of (a) sample S1, (b) sample S2 and (c) sample S3 before (blue graph) and after (pink graph) embedding.

The blue plots in Figures 4.4 (a-c) are presenting the transmission spectra of the embedded samples measured in their freeform, showing three Bragg peaks situated around 1542.8 nm, 1547.30 nm and 1551.80 nm, whereas the pink plots in the same figures show the measured transmission spectra of the same samples after being embedded into the Aluminium matrix composite.

From these figures it can be seen that after embedding process, three embedded gratings (shown as P1, P2 and P3 in the figures) in all three samples have experienced a wavelength shift toward the shorter wavelength side but by different amounts. Considering that UC is a low temperature process, the blue shift of the Bragg resonances can only be the result of the mechanical compression induced by the UC to the embedded fibres. The extracted data from the above figures have been

summarised in table 4.2. The different amounts of the wavelength shift by three Bragg resonances indicate a non-uniform embedding process experienced by the samples. The localised non uniformity is also evident by the observed peak splitting effect shown on P2 and P3 from sample S1. For sample S2, we also see the broadening effect on P1 indicating that the sample has experienced more strain in that area during the embedding process compared to the other two peaks almost kept the same shape as before embedding.

In despite of the other two embedded samples have shown different degrees of non-uniformity, there is no evident splitting or broadening effect on sample S3, suggesting a much more uniform embedding process experienced by sample S3.

	Peak	Wavelength Blue-shift (nm)	Strain ($\mu\epsilon$)	3dB Band-width increased (nm)	Strain Distribution ($\mu\epsilon$)	Reflectivity Decreased
S1	P1	1.38	1380	0.06	60	5.71
	P2	2.23	2230	-0.04	-40	6.53
	P3	2.08	2080	0.08	80	15.53
S2	P1	1.19	1190	0.58	580	17.28
	P2	2.05	2050	0.08	80	9.37
	P3	1.92	1920	0.06	60	16.26
S3	P1	1.40	1400	0.00	0	4.43
	P2	2.00	2000	0.06	60	7.79
	P3	2.48	2480	0.00	0	10.25

Table 4. 2. Analysed data from three embedded samples.

The strain values assumed experienced by the nine FBGs in the three samples are estimated based on the fact that around 1550 nm region, 1 μm wavelength shift of FBG made in silica fibre corresponding to $\sim 1 \mu\epsilon$. From table 4.2 it can be seen that the strain distribution is most non-uniform on sample S2, as one can notice the average compression strains experienced by the three FBGs vary from 1190 $\mu\epsilon$ to 2050 $\mu\epsilon$ and the localised field change from 60 $\mu\epsilon$ to 580 $\mu\epsilon$. However, with the FBG array embedded in these metal matrix composite samples, it is possible to monitor the conditions they will be subjected to, such as loading, bending and temperature variation.

4.3.1. Investigation of Polarisation Effect in Embedded Samples

As the embedding induces local non-uniformity, such as noticeable splitting and broadening effect, it is the concern if these non-uniformities will induce polarisation effect on the embedded FBG sensor arrays. To clarify, we have conducted the polarisation measurement on two embedded FBG array samples S1 and S2. The experiment was performed by employing a polariser and a PC, placed between the BBS and the embedded sample, as shown in Figure 4.6.

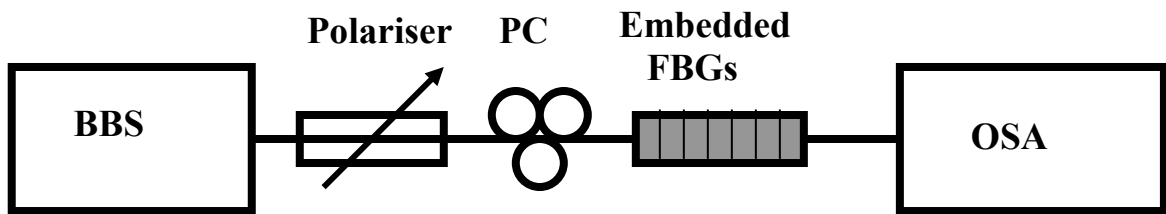


Figure 4. 6. Schematic diagram of the setup for polarisation measurement.

By adjusting the PC, the polarisation state of the probing light was changed and we examined the spectral change of the embedded FBG array samples. The results of this experiment are plotted in Figures 4.7 (a-c) and 4.8 (a-c) for each Bragg resonance of the two samples, respectively.

As one may notice from Figures 4.6 (a-c), there is no noticeable shift in the wavelength for the three sub-gratings in sample S2 when changing the polarisation state of the incident light, confirming the polarisation independency of this sample. This confirmation made S2 a good candidate to study for its sensing capabilities, which will be discussed in section 4.3.2.

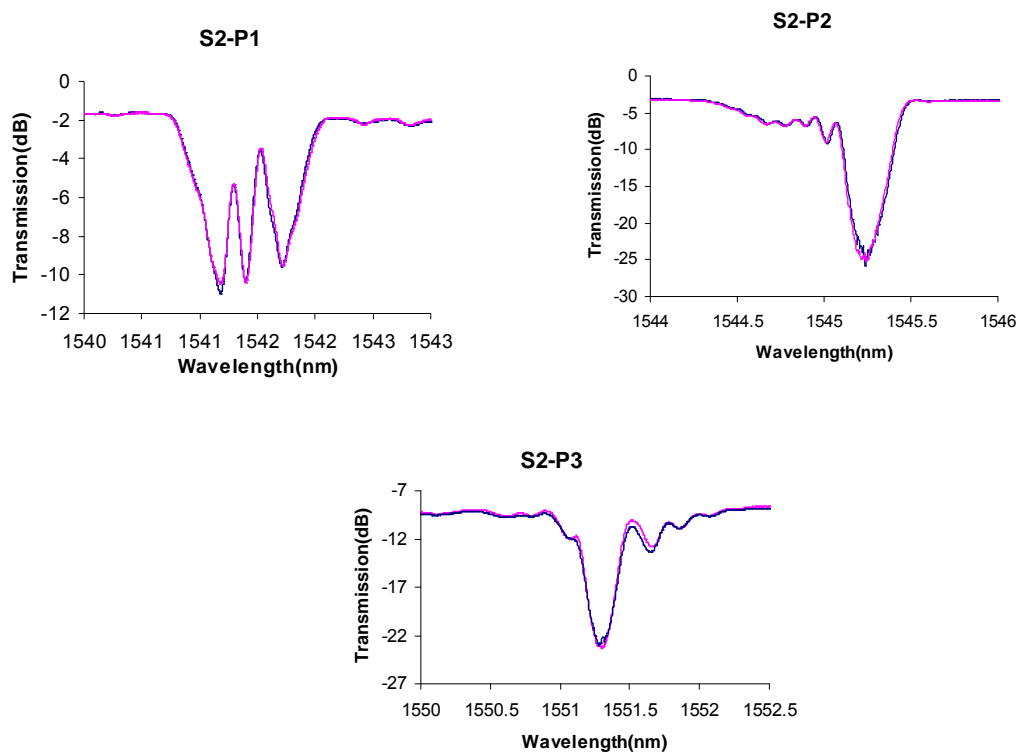


Figure 4.7. Polarisation measurements of (a) P1, (b) P2 and (c) P3, the three sub- gratings from sample S2.

The same experiment was conducted on sample S1 and the measured spectra for probing light with different polarisation states are depicted in Figures 4.8 (a-c). As

we can clearly see that there is no wavelength shift for the sub-gratings P1 and P2, but a noticeable shift of 0.07 nm (measured from the OSA) for P3. This small amount of shift indicates the embedded third sub-grating P3 has become slightly birefringent as its fibre geometry may be deformed slightly and also some stress induced in the fibre by the embedding process. A 0.07 nm shift is still in significantly small and may not cause measurement error for those applications not requiring very high resolution.

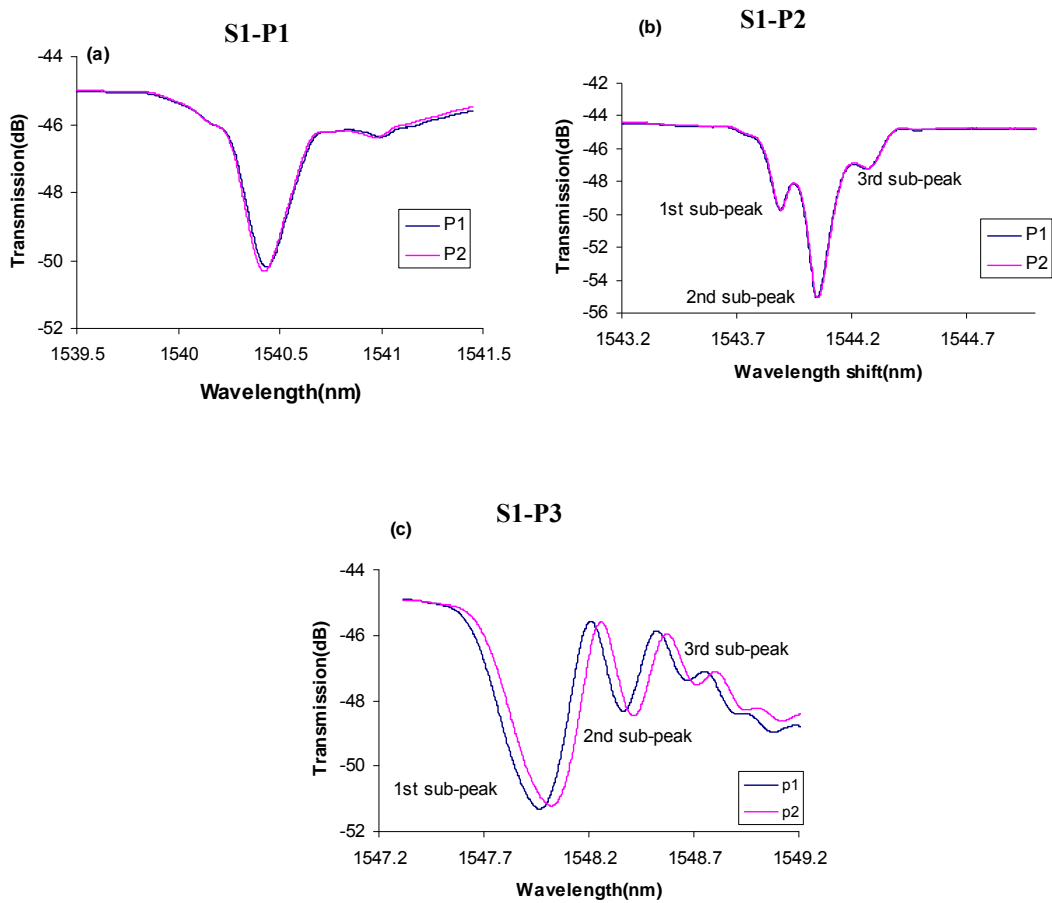


Figure 4.8. Polarisation measurements of (a) P1, (b) P2 and (c) P3 gratings from sample S1.

It then can conclude that the embedding FBG array in metal matrix samples by UC process would induce un-uniformity in the sample thus causing splitting and

broadening of the FBG spectrum, and it does not induce significant birefringence to the grating fibres.

4.3.2. Investigation of Temperature Effect in Embedded Samples

FBGs as optical sensors are based on the RI and period change by external environmental conditions, such as temperature and strain. When the fibre grating embedded in metal matrix composite, the temperature response may differ from what it is in its freeform. For this reason, we have evaluated the thermal response of the embedded FBG arrays. In the thermal response evaluation experiment, each sample was placed on an electrically controlled heater, as shown in Figure 4.9 and the transmission spectra were measured and recorded for the temperature elevation from 0°C to 100°C with an increment of 10°C.

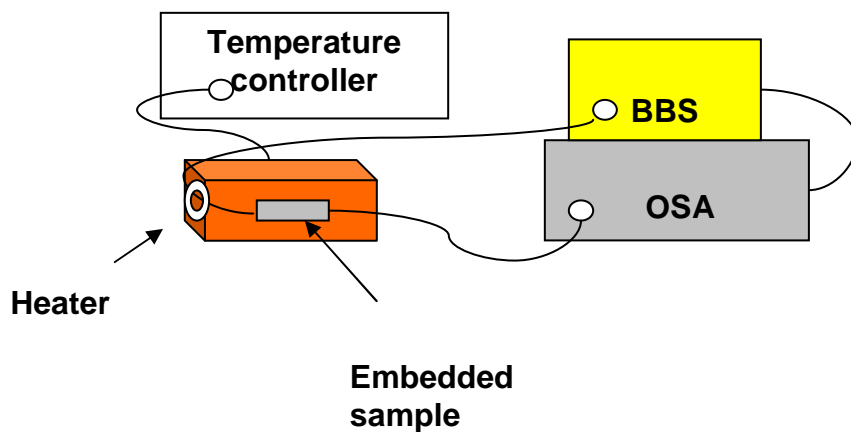


Figure 4. 9. Schematic diagram of the temperature measurement set-up.

The spectral analysis of all three embedded samples showed a similar response to the temperature changes. Showing as typical results, here we only present the measurement results for sample S2.

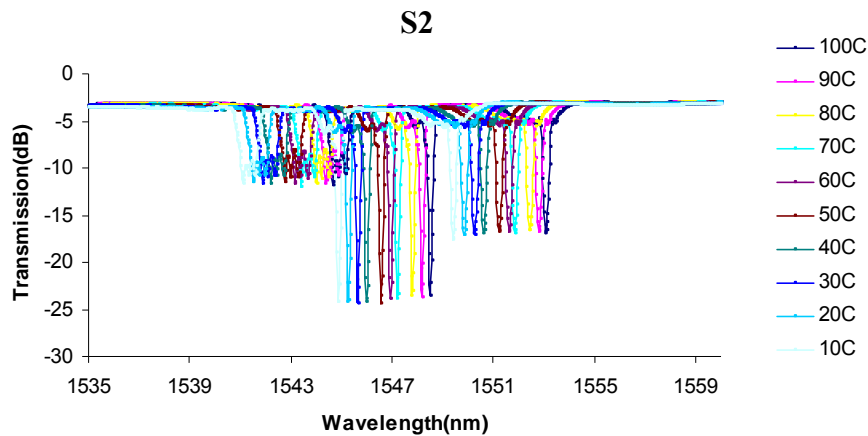


Figure 4.10. Transmission spectrum of S2, while it was subjected to a range of different temperatures from 0°C to 100°C.

As the temperature changed from 0°C to 100°C, the three FBG spectra shifted towards longer wavelength side as shown in Figure 4.10. Figure 4.11 plot the Bragg wavelength shift against temperature for the three sub-gratings of sample S2.

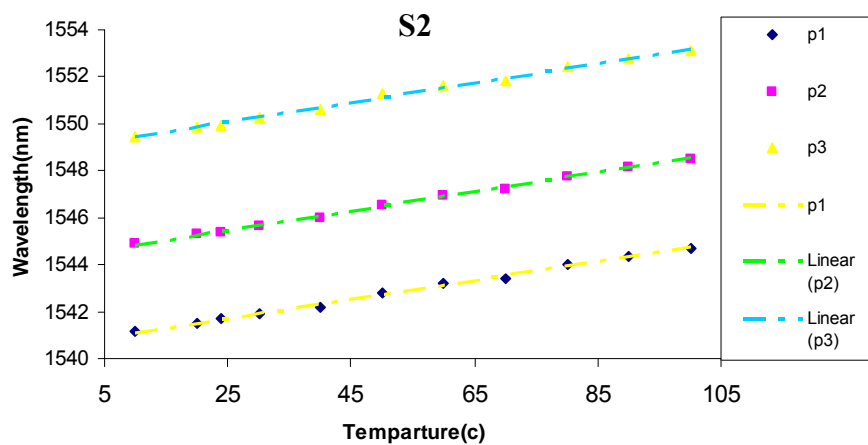


Figure 4.11. Temperature response of three embedded FBGs, P1, P2 and P3 in sample S2.

Figure 4.12 gives the superimposed temperature responses of the three sub-gratings by removing the wavelength off-sets. As clearly seen from Figure 4.12, the three sub-gratings exhibit a near-linear and similar temperature response.

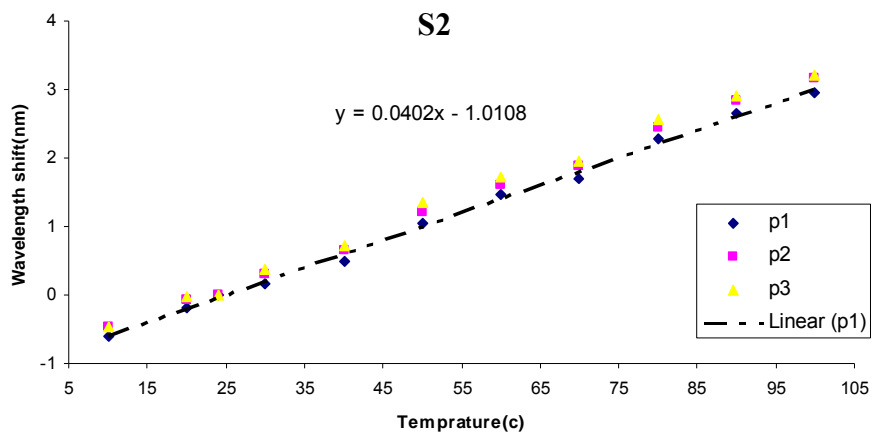


Figure 4.12. Temperature sensitivity of three embedded FBGs in S2.

The best fit to the three linear plots in Figure 4.12 gives an average thermal sensitivity ($\Delta\lambda / \Delta T$) of ~ 40 pm/ $^{\circ}\text{C}$. It was initially quite surprising to see this value, as it is almost four times of the typical temperature sensitivity value of a freeform FBG in this wavelength range. This large value can be explained considering the fact that FBG arrays have been embedded between the metal matrix composite layers and the thermal coefficients are different for Al and Si. Around room temperature 20° C, the reported thermal expansion coefficients for Al alloy 3003 and Si are $46 \times 10^{-6} / ^{\circ}\text{C}$ and $6 \times 10^{-6} / ^{\circ}\text{C}$ respectively. Therefore, the increased thermal sensitivity is simply caused by the combination effect on thermal expansion of aluminium and silica glass materials.

4.3.3. Investigation of Loading Effect in Embedded Samples

The embedded FBG array sample S2 was also subjected to the loading experiment. Figure 4.13 shows the experimental set-up for this study. In order to make sure the loading will be distributed uniformly across sample S2, a balance plate was placed on

the top of the sample and the mass was then loaded to the top of the plate. In the measurement, the one end of the FBG array fibre in sample S2 was launched with light from a BBS and the other end was connected to the OSA and a set of masses from 0 kg to 8 kg were gradually loaded on the top of the embedded FBG array sample. Also, because the fibre grating array was embedded in the middle area of the Al alloy sample, the grating response may different if the load is placed on the different positions on the sample. To clarify this, the load was placed in several positions on the sample, but we did not see noticeable change on the spectrum.

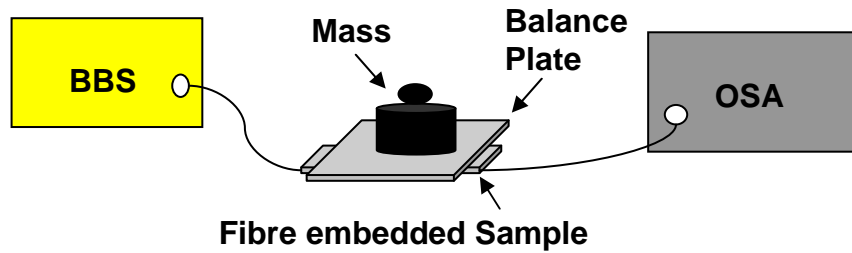


Figure 4.13. Schematic diagram of experimental setup for loading measurement.

Figure 4.14 shows the spectral evolution of sample S2 under loading from 0 kg to 8 kg. We can immediately see that all three Bragg peaks shift to longer wavelength side with increasing loading.

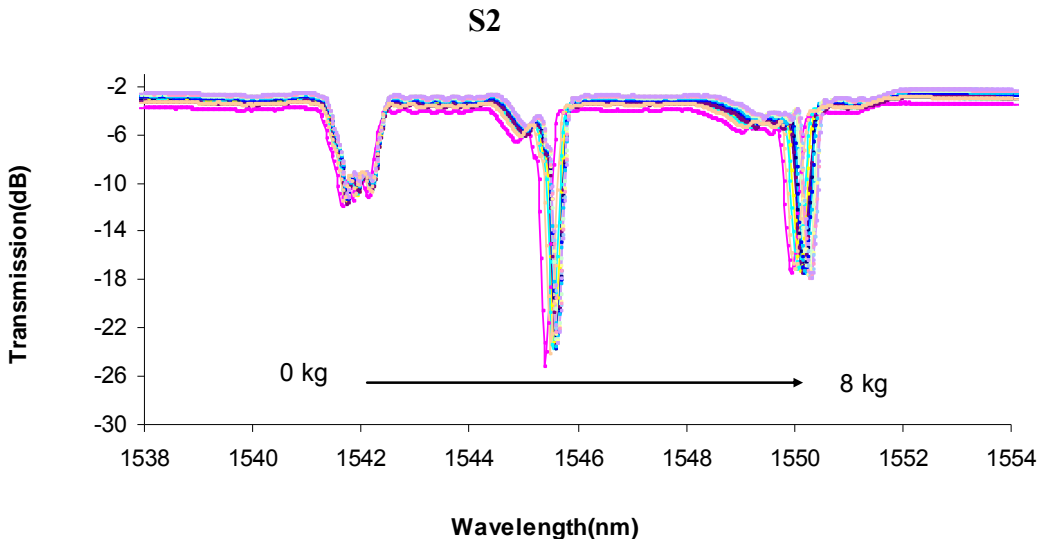


Figure 4. 14. Transmission spectrum of the embedded sample under different loaded masses.

By plotting the wavelength shift against loading we can see a much clear picture that how each grating responses to the loading. Analysed data from this measurement indicates the different responses from the three FBGs to the loading effect. The wavelength shifts of the embedded FBGs are plotted against the corresponding loaded mass in Figures 4.15, 4.16. and 4.17, respectively.

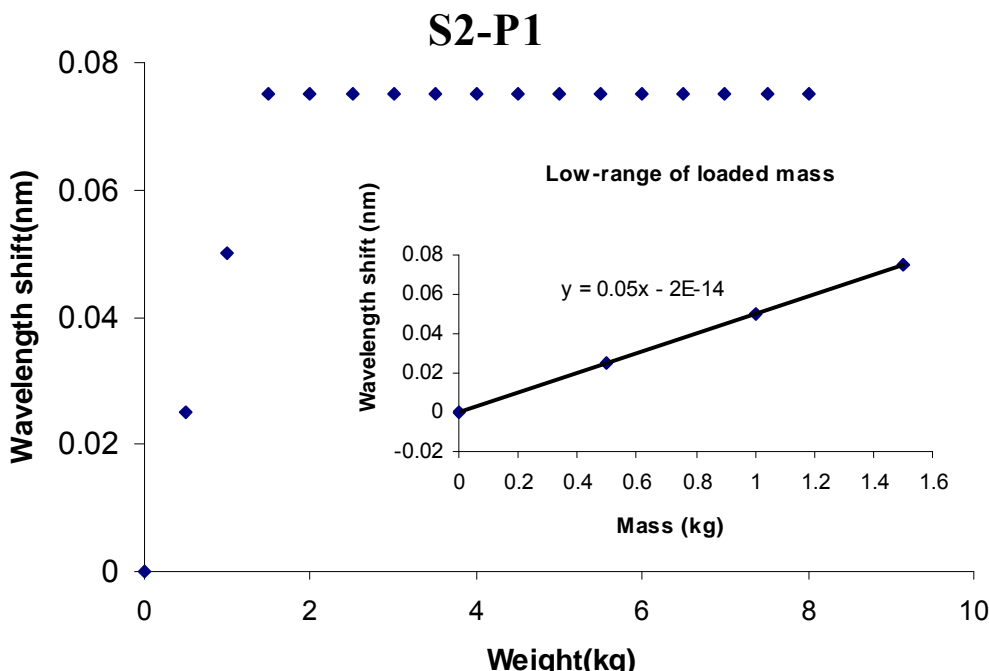


Figure 4. 15. Loading response of first embedded FBG, P1 in sample S2. The inset shows the loading sensitivity of the grating to the masses in the range of 0 kg – 1.5 kg.

As it is presented in Figure 4.15 for P1, there are two response regions corresponding to low and high loading range. In the low weight range up to 1.5 kg, the response of P1 is linear with a load responsivity of 0.05 nm/kg, as shown by well fitted plot in the inset of figure 4.15, when the applied load exceeds the threshold of 1.5 kg, the Bragg peak does not shift any more. In fact after 1.5 kg, its response to the loading is saturated and the peak becomes insensitive to the loading effect.

Similar behaviour was observed from the 2nd embedded grating P2, as shown in Figure 4.16. The P2 linearly responded to the loading just a little over 1.5 kg to 2 kg with a loading responsivity of 0.09 nm/kg. After the threshold point 2 kg, the grating response becomes static and insensitive to any further loading.

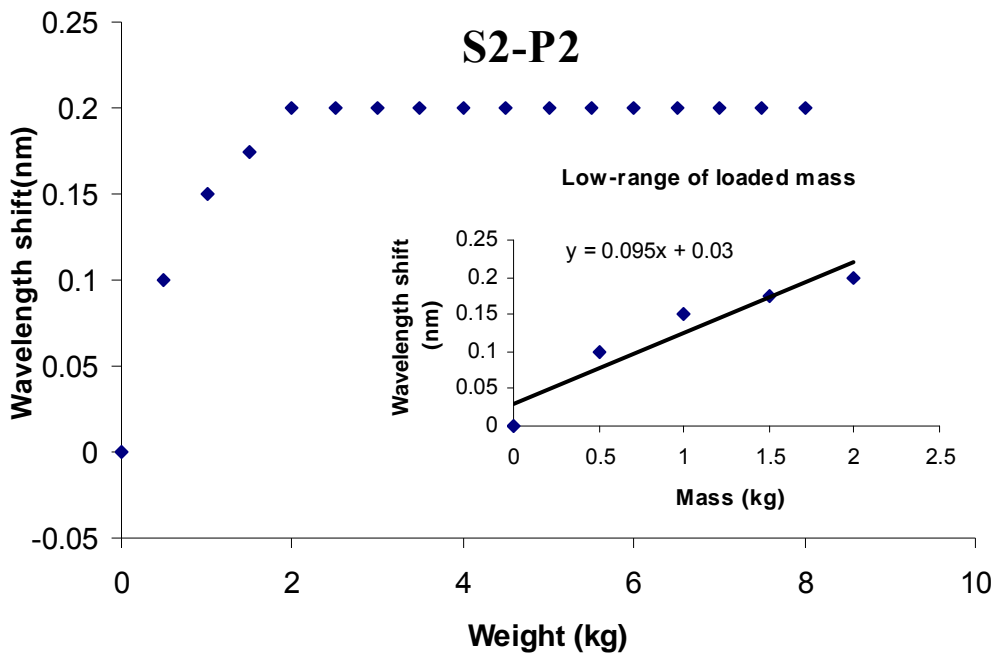


Figure 4.16. Loading response of 2nd embedded FBG, P2 in sample S2. The inset shows the loading sensitivity of the grating to the masses in the range of 0 kg – 2 kg.

Although all three sub-gratings were embedded in the same metal matrix sample, the third grating P3 responses to the loading quite differently from P1 and P2. As shown in Figure 4.17, there are clearly two loading response ranges for P3, but the grating

response in the second range is not static and the first linear responding range extends to 3 kg. These two ranges are re-plotted separately in Figures 4.17 and 4.18. From the figures we can see that in the first range, the linear loading responsivity is ~ 0.08 nm/kg and the grating still respond to the loading change beyond 3 kg but with a much smaller sensitivity, i.e. only 0.02 nm/kg and also the loading response in high loading range is not perfectly linear. At this stage, it is difficult to explain why the three gratings embedded in the same sample behave so differently to the loading. However, this is not conclusive and the response could be unique for this sample. More experiment should be conducted over a large number of samples in order to see more universal pattern on FBG loading response to embedded metal matrix structures.

However, we may conclude from this experiment that the FBG array in the metal matrix composite could be used to monitor loading or loading induced structure change, but only to a small load range up to 1.5-2 kg.

S2-P3

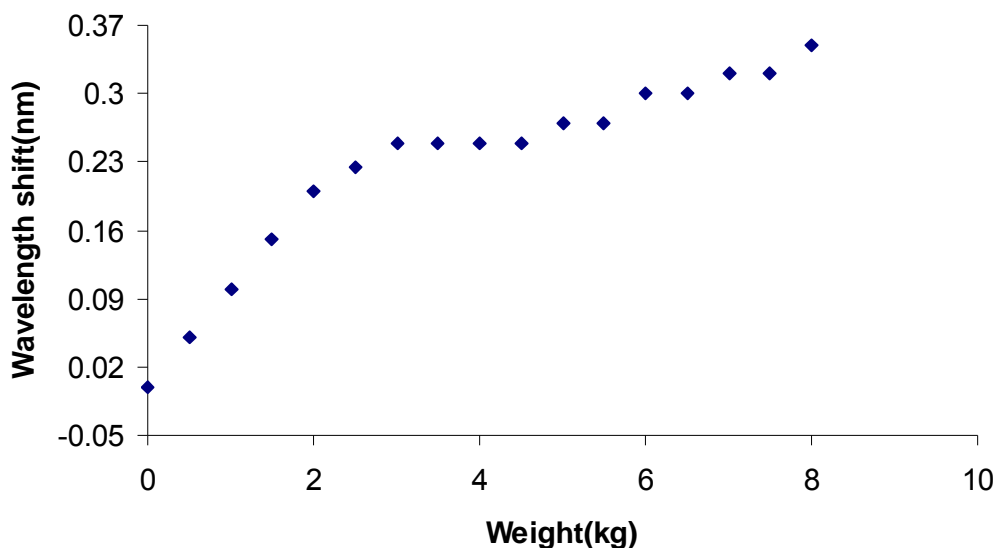


Figure 4. 17. Loading response of 3rd embedded FBG, P3 in sample S2.

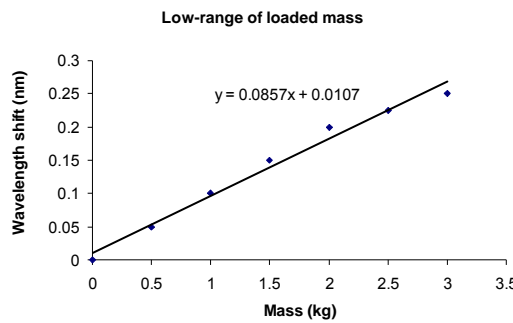


Figure 4. 18. Loading sensitivity of P3 to the masses in the range of 0 kg – 3 kg.

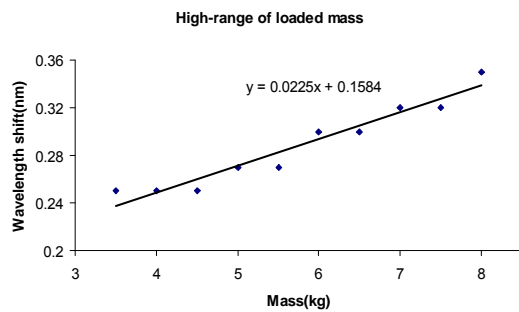


Figure 4. 19. Loading sensitivity of P3 in the range of 3kg- 8kg.

4.3.4. Investigation of Bending Curvature Effect in Embedded Samples

The embedded FBG array sample has also been subjected to the bending experiment to assess if it would response to bending induced structure shape deformation. Figure 4.20 shows the experimental setup for this investigation and indicates the geometric configuration of a four-point bending system that was designed for implementing a curvature measurement experiment.

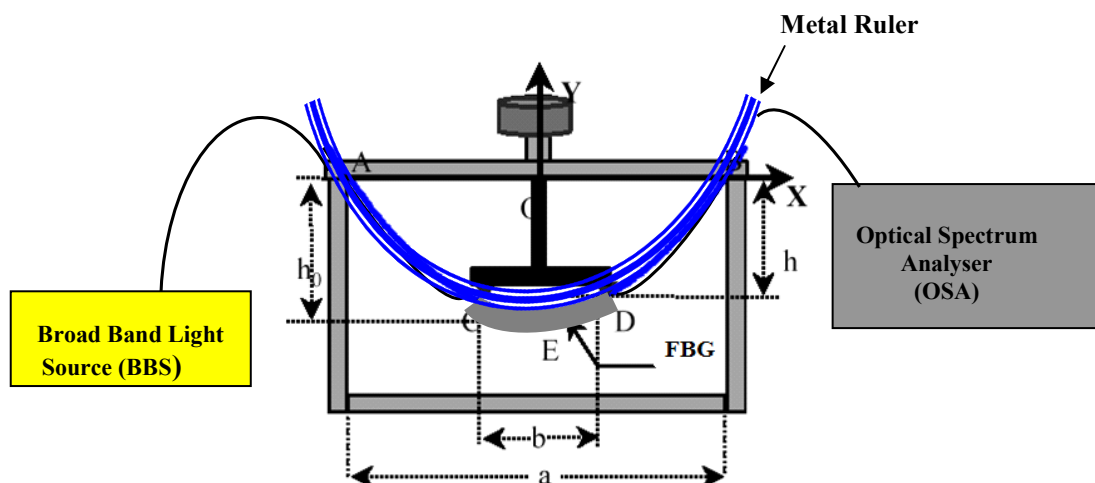


Figure 4. 20. Schematic diagram of the bending response measurement and presenting the maximised schematic diagram of the four-point bend system with $a=120\text{mm}$, $b=20\text{mm}$ and bend depth $h=0$ to $\sim 8\text{mm}$.

To prevent the breakage along the embedded fibre sample containing the three FBGs, a thin metal plate was attached on the top of the sample and across its whole length. As illustrated in Figure 4.20, by depressing the central micrometer driver with a depth (h), the sample was bent. The bend curvature ($1/R$) has a near linear relationship with the depressing depth (h) as the analysis shown below.

According to the geometric configuration, the bend curvature of the fibre follows [110]:

$$\begin{cases} R^2 = (R - h_0)^2 + \left(\frac{a}{2}\right)^2 \\ \left(\frac{b}{2}\right)^2 + [-h - (R - h)] = R^2 \end{cases} \quad (\text{eq: 4.1})$$

Where R is the bend radius, h is the bend depth which can be accurately read from the micrometer driver, a and b are spacing of the two sets of forced points as shown in Figure 4.20.

Simplifying equation 4.1 yields

$$\left(\frac{a}{2}\right)^2 - 2R\left[R + h - \sqrt{R^2 - \left(\frac{b}{2}\right)^2}\right]^2 + \left[R + h - \sqrt{R^2 - \left(\frac{b}{2}\right)^2}\right]^2 = 0 \quad (\text{eq: 4.2})$$

For $R \gg a, b$ and h and also $a \gg b$ and h , as an approximation, equation (4.2) reduces to

$$\frac{1}{R} = \frac{8h}{a^2 - b^2} \quad (\text{eq: 4.3})$$

Clearly, equation (4.3) exhibits a linear relationship between the bend curvature and the bend depth. This fact is also evident in Figure 4.21, where the applied bend curvature ($1/R$) on the embedded sample using our four-point bending system was plotted against the depressing depth (h) and exhibit a linear relationship with the depressing depth (h).

In the employed bending kit we used, the measured values are for $a = 109\text{ mm}$ and $b = 40\text{ mm}$.

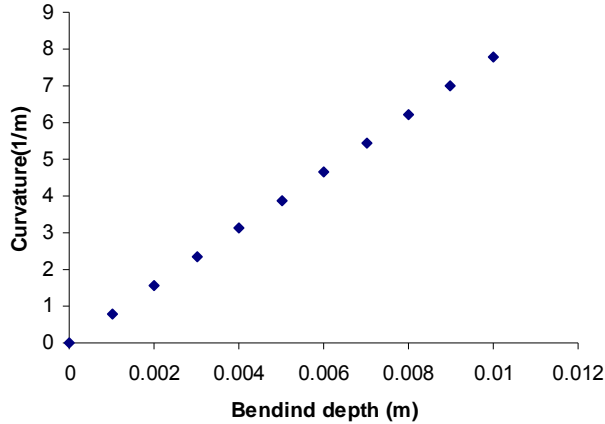


Figure 4. 21. Curvature against bending depth using the four-point bending equipment.

The sensitivity of all three embedded gratings, P1, P2 and P3, in sample S2 was investigated under bending tests for two opposite bend directions. In the measurement, the micro-meter of the bending equipment gradually travelled down from 0 mm to 8 mm inducing different curvatures in the sample. We recorded the transmission spectrum for each bending and all spectra are plotted in Figure 4.22. As clearly seen from Figure 4.22, all three FBG peaks shift to longer wavelength side with increasing bending.

Despite usual bending curvature measurements in which the fibre containing FBGs is fixed from one end while the other end is left free to move with increase in the bending amount, here the fibre containing FBG array has been embedded into metal composite across its whole length and as a consequence it is fixed and the observed red-shifting in FBGs' spectra is not purely due to the bending curvature itself. The

investigated wavelength shift in this measurement indicates that the bend also induces a longitudinal strain to the fibre sample.

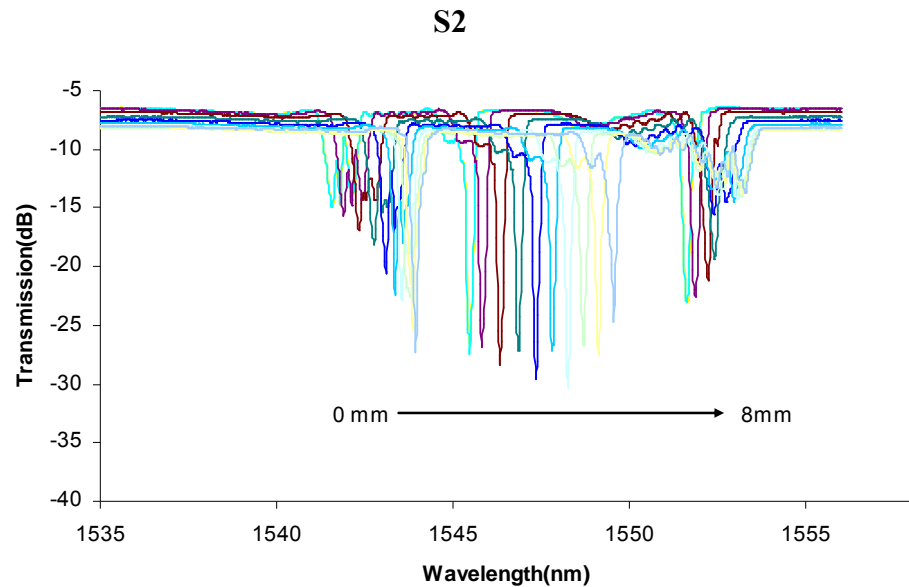


Figure 4.22. Transmission spectral evolution of S2, while it was subjected to the bending measurement.

The wavelength shift of each grating is plotted against the corresponded bending curvature individually in Figure 4.23.

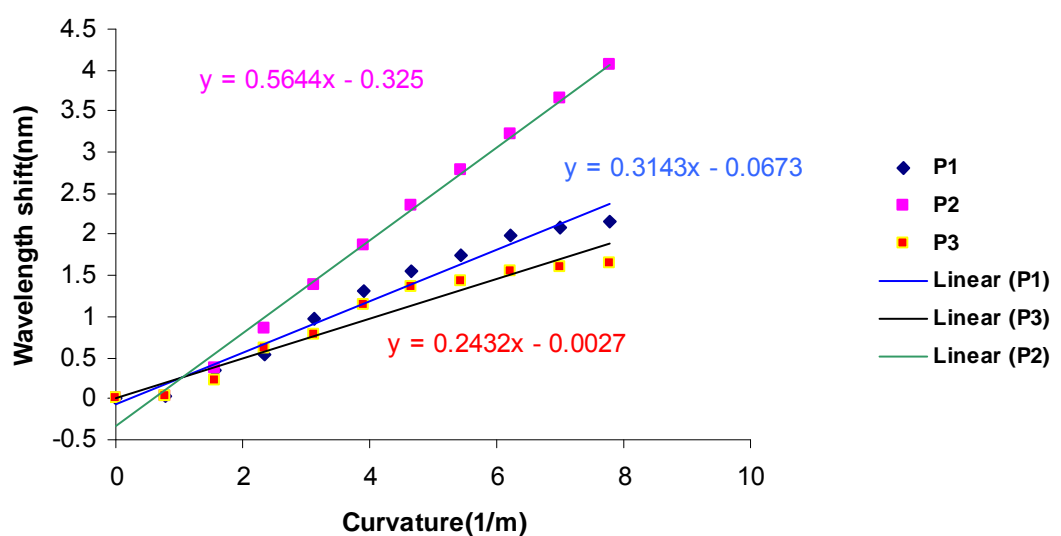


Figure 4.23. Bending curvature sensitivities of three embedded gratings in sample S2.

As shown in the figure, three FBGs showed similar behaviours in terms of a linear upward response to the curvature increase process. However different bending sensitivity values of 0.24 (nm)/(1/m), 0.31 (nm)/(1/m) and 0.56 (nm)/(1/m) were obtained for three gratings P3, P1 and P2, respectively. The maximum bending sensitivity of 0.56 (nm)/(1/m) corresponding to the grating P2 which was located in the middle of the other two FBGs (P1 and P3), indicates more axial strain in the middle part of embedded sample due to the bending process while the less bending sensitivity values of the side FBGs, as they experiencing less strain in those regions.

After that measurement, to reveal the bending characteristics of the embedded gratings when the bending is applied on the opposite side of the sample, the embedded sample was fully turned over and placed in the bending system. Again the same plate was attached on the top of the sample to facilitating the application of the bending. The same experimental procedure was made for this measurement. The recorded spectra of the embedded sample, shown in Figure 4.24, indicate the wavelength shift of three FBGs toward the shorter wavelengths, i.e. blue-shifting. The observed blue-shift indicates the applied bending induces compression but not axial strain over the fibre sample.

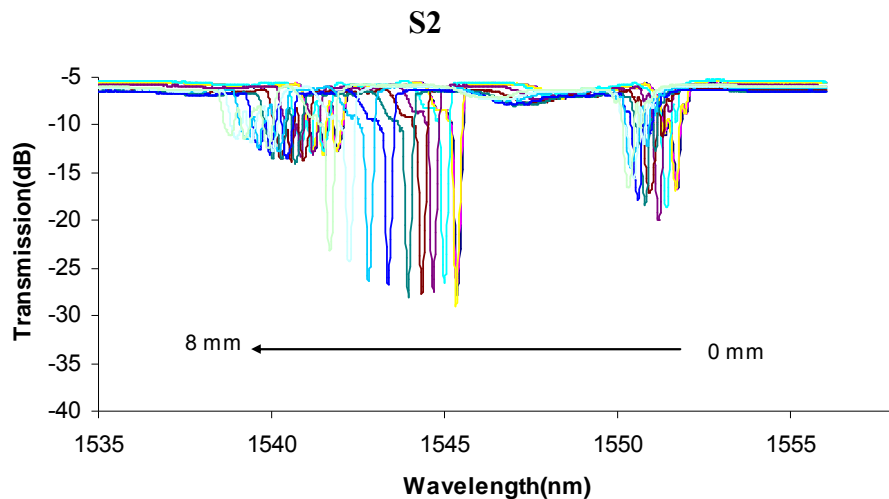


Figure 4. 24. Transmission spectra of S2, while it was fully turned over and was subjected into the same bending measurement.

The behaviour of the three embedded FBGs in these two experiments indicates the wavelength shift toward different directions depending on the bending direction applied to the sample. This interesting character of the embedded FBGs may be explained as a result of induced asymmetric geometry of the embedded sample, as there is an extra Al 1050 supporting plate (with the thickness of 1.2mm) placed on the one side of the sandwich structure of the metal matrix composite. To reveal the bending sensitivities of three Bragg peaks in this measurement, the wavelength shift of these gratings was plotted versus the applied curvature in Figure 4.25. Similar to the previous experiment, here also the bending induced wavelength shift exhibits a linear response in all three embedded FBGs; however the trend of the shift is downward. The measured bending sensitivity of the middle grating, P2, is about 0.49 (nm)/(1/m) and again the highest value comparing with the side gratings, P1 and P3 whose bending sensitivities of about 0.35 (nm)/(1/m) and 0.21 (nm)/(1/m), respectively, indicates the most compression occurred in the middle part of the embedded sample.

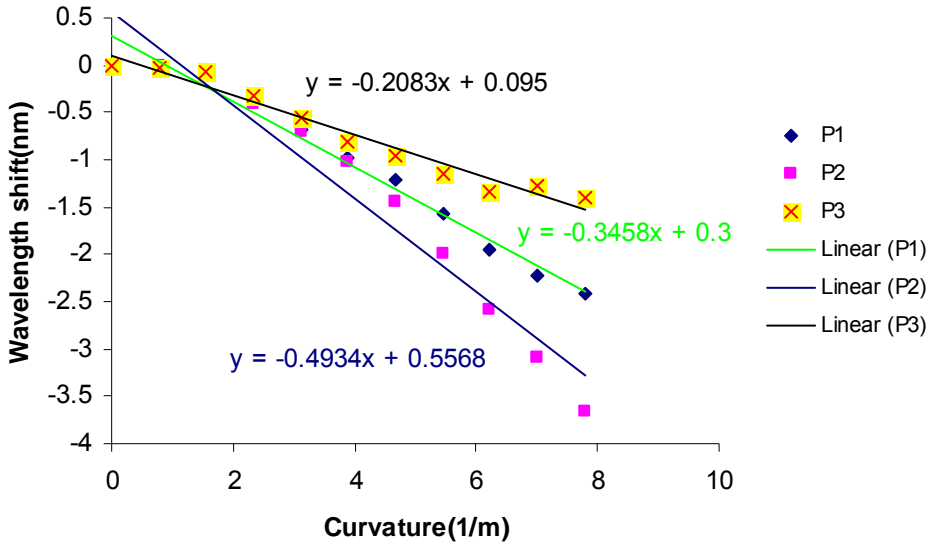


Figure 4. 25. Bending curvature sensitivities of three embedded gratings in sample S2 while the sample was fully turned at 180°.

Comparative results from the mentioned two bending experiments show the similar first digit number in the value of bending sensitivity of the three FBGs in both experiments. However the measured bending sensitivity for each grating in one experiment is not exactly the same as its corresponded value in the other measurement. In fact as one may notice in the second experiment, the bending sensitivity for all three embedded FBGs were measured to be smaller than their measured when the bending was applied to the opposite direction. This may be explained as a result of the slight deformation of the embedded sample after first bending experiment. As the sample was taking the shape of bending during the measurement, in order to repeat the measurement we had to manually reshape the sample to take it to its flat form. However, the direction assignment with asymmetric embedded structure may provide a method to recognise the bending direction, so in this case, vector sensor concept may be realised and would be useful for some applications.

4.4. Chapter Conclusion

In this chapter, the first time fabrication of embedded FBG array sensors in metal matrix composite by ultrasonic consolidation technique is reported. Three FBGs have been embedded in Al alloy matrix composite and have been investigated for their thermal, loading and bending responses.

As a result of the combination effect on the thermal expansion of aluminium and silica glass materials in the embedded samples, the investigated values of average thermal sensitivity, ($\tan \alpha = \Delta\lambda / \Delta T$), for three embedded FBGs were similar and about 40 pm/ $^{\circ}\text{C}$ which is almost three times higher than the typical temperature sensitivity of a free form FBG.

In contrast with the temperature measurement, three embedded FBGs showed different responses to the loading and bending curvature measurement. For loading measurement, there were two different response regions for the gratings corresponding to the low and high weight region. All three gratings showed the higher sensitivity and a linear upward response to the loading effect in their low weight region response. The maximum value of loading sensitivity was measured \sim 0.09 nm/kg corresponded to the 3rd embedded FBG (P3) in its low weight region response (0kg- 3kg). The first grating, P1, performed the least value of loading sensitivity of \sim 0.05 nm/kg in its low weight response region which was up to 1.5 kg. During the loading measurement 1st and 2nd gratings, P1and P2, after exceeding 1.5 kg and 2 kg respectively, became insensitive to the applied loads while the 3rd grating (P3) was still presenting the wavelength shift but with a lower sensitivity showing a wavelength shift rate of 0.02 nm/kg after exceeding 3 kg.

The embedded sample was subjected to two bending curvature measurements in which bending was applied to different sides of the embedded sample each time. In these measurements, the embedded FBGs have not been experiencing a pure bending curvature effect, As the three FBGs were embedded into metal composite material so the host fibre was fixed into this composite across its whole length, therefore, the bending process applied some longitudinal strain to the gratings as well. In two bending experiments, three embedded FBGs showed linear response to applied bending but with the shift in opposite directions for each experiment owing to the asymmetric sandwich structure of the embedded sample. The experimental data presents the vector bending sensing capability of the embedded sample with the bending sensitivity in the range of 0.24 (nm)/(1/m) to 0.56 (nm)/(1/m) . In both measurements, the maximum bending sensitivity was corresponded to the FBG (P2) embedded in the middle part, so the FBG has experienced the most expansion when bent in one direction and the compression in the other direction.

Overall, the performed experiments and obtained results have clearly demonstrated the self-sensing capability of the FBG embedded metal matrix composite. We envisage that metal matrix based engineering tools and structures made by advanced solid-state rapid manufacturing UC technique may be embedded with FBG sensor arrays becoming smart structures, which would be beneficial to a range of applications such as monitoring the operation and health of engineering structures.

Chapter 5

Micro-structured Fibre Bragg Gratings and their Sensing Applications

5.1. Introduction

Optical fibre sensors offer unique solutions over conventional techniques for applications where an advanced multifunctional sensing system is required to monitor the physical, chemical, and biological parameters in natural environments, industrial processes or structural health. Specifically the enormous advantages of in FBGs over conventional electrical strain gauges such as linearity in response over many orders of magnitude, compactness, low insertion loss, narrow band wavelength reflection, multi-parameter measurement, miniaturisation, high sensitivity and remote sensing capability have generated increasing interests in optical sensing over last two decades.

This class of sensors can be employed for a wide range of measurements, including strain, temperature, pressure, bending and many others. One of particular interests is to utilise FBGs as chemical sensors while changing the chemical composition of the surrounding medium will cause the shift in the Bragg wavelength. However, since in normal FBGs, the mode coupling occurs between the well bounded core modes, they are intrinsically insensitive to the surrounding medium and consequently are not capable of RI sensing. To measure small changes in chemical/biological solution, it is necessary for the optical mode to penetrate evanescently into the surrounding medium solution.

Recently with the advances in micro-photonic devices for modern biomedical, chemistry and sensing applications, microfluidic components have attracted huge attentions due to the importance of the RI measurements in a wide range of environmental and chemical applications. By employing microstructuring techniques, modified FBG structures have also been proposed to implement RI sensors. For instance thinned and microstructured FBGs fabricated by chemical etching have been

employed to induce RI sensitivity to the grating structures [111, 112]. Nonuniform thinned FBGs were also presented as RI sensors with the self temperature referencing functionality [113]. In all mentioned techniques, the strength of the device is significantly degraded as the fibre cladding is completely removed over the chemical etching process.

In recent years, the laser inscription technique in transparent dielectrics by employing the tightly focused fs laser irradiation has attracted much research interest. Owing to the high peak power and spatial resolution of fs laser, this technique has been introduced as one of the most efficient approaches to the microstructure inscription into silica materials / fibers. Zhou *et al*, employed fs laser to fabricate microchannels in to the optical fiber [114]. Later he reported the inscription of a micro-slot superimposed on a FBG employing the same technique [115]. Also in another research from the same group, Hantovsky *et al* reported that fs modified regions have much higher etching rate than the pristine material; they reported the contrast ratio as high as 100:1 [116].

In this chapter, the efficient and low-cost fs-inscription/chemical-etching combined approach microstructured FBGs will be discussed. The fabrication and characterisation of three MCFBGs with different channel sizes (50 μm , 550 μm and 1000 μm) and one micro-slot FBG with the slot size of 1.388 μm by using fs laser assisted chemical etching will be presented in details. This chapter contains a systematic study of spectral characteristics of these devices to the surrounding medium refractive index and the temperature changes. For the appropriate channel or slot size, the proposed devices exhibit the enhanced RI sensitivity with non-degrading mechanical strength, making them ideal candidates for implementation of in-fiber bio-chemical sensors for a range of potential applications.

5.2. Fabrication of Microchannelled Chirped Fibre Bragg Grating

Three MCFBG samples with the channel width of 50 μm , 550 μm and 1000 μm were fabricated by introducing the channels in the middle of CFBGs and across the whole length of the host fibre. The geometric configuration of the proposed devices is exhibited in Figure 5.1. In all three samples, the height and length of the channels are the same and about 1 to 2 μm and 125 μm , respectively.

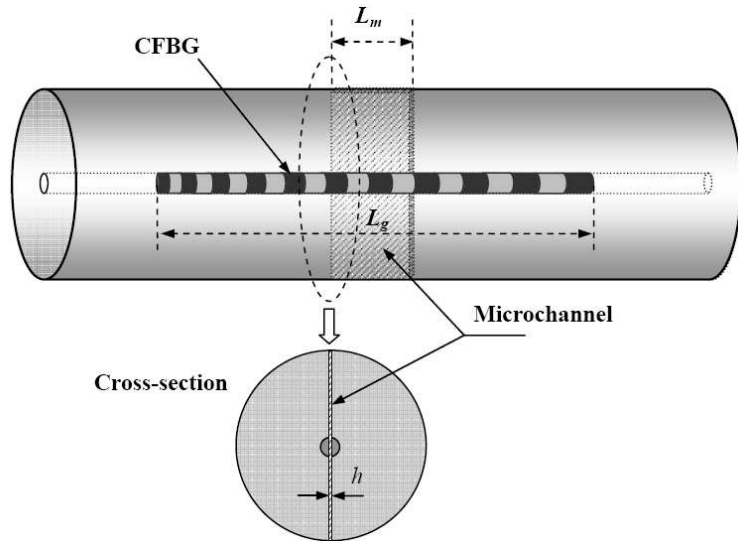


Figure 5. 1. Schematic diagram of the proposed MCFBG consisting of a CFBG in the fibre core, and a microchannel (with the width of L_m) created in the middle region of the CFBG across the fibre.

In Figure 5.1, the proposed MCFBG consists of a CFBG in the core of the fibre and a microchannel has been introduced in the middle of the CFBG across the whole fiber. In this figure, the length, pitch and the chirp rate of the CFBG are presented as L_g , Λ , and C respectively, where L_m is the width and h is height of the microchannel structure.

The fabrication process of such MCFBG samples included three main steps. Firstly, CFBGs were UV written in the core of SMF-28 fibres using a scanning phase mask technique and a CW frequency doubled Argon -ion laser operating at 244 nm. To

fabricate the chirped gratings, a circular shaped chirped phase mask with the radius of 20 mm, a central period of 1070.6 nm and the chirp rate of about 1.11 nm/mm was employed. The photosensitivity of SMF-28 fibres were enhanced by pressurising them in hydrogen for a period of 48 hours under pressure of 150 bars and the temperature of 80°C prior to the UV-inscription. Each host fibre is about 60 mm length and the middle part of ~ 2 cm was stripped off for grating inscription. A UV power of 100 mW and a scanning speed of 0.025 mm/s were used to inscribe CFBG structures in the host fibres. A number of CFBGs with 10nm chirp bandwidth but at different centre wavelengths were fabricated for inducing microchannels of different sizes. Figure 5.2 shows the typical transmission spectrum of these chirped gratings, giving a reflectivity of 8 dB across a bandwidth of ~10nm.

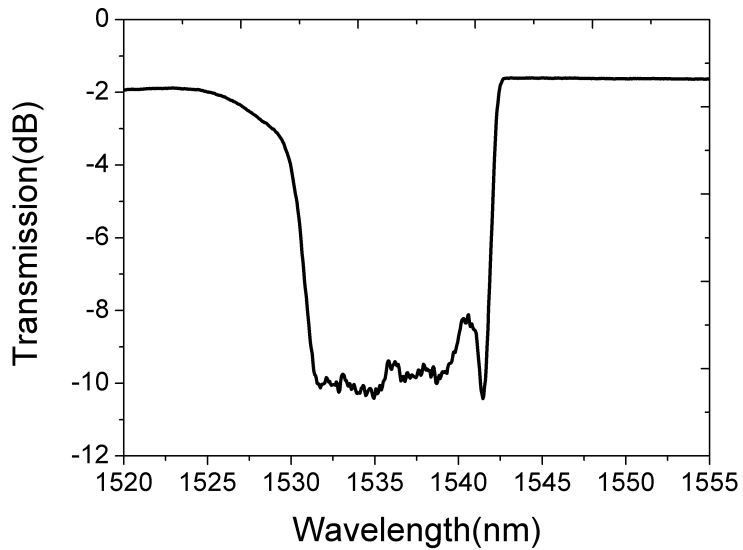


Figure 5. 2. UV inscribed 10-mm long CFBG in H₂ loaded SMF-28 fibre.

The second step of fabrication process was microchannel patterning process which was done by Dr Kaiming Zhou from our group. At this stage, the designed microchannel was patterned in the middle of CFBGs and across the whole length of the fibre by employing the tightly focused fs laser beam. A ×100 objective lens with an N.A. of 0.55 and a working distance of 13 mm was utilised to focus the fs pulses

of 800 nm on the fibre. The pulse width of employed fs laser beam was measured to be about 150 fs, and the repetition rate was at 1 kHz. The fibre containing CFBG was carefully placed on a dual-axis air-bearing translation stage, and the microchannel pattern with the desired dimensions was written by moving the stage along the cross-section of the fibre and around the middle of the CFBG region. In order to study three different microstructured CFBGs, fs patterning microchannels with width of 50 μm , 550 μm and 1000 μm in three CFBGs were carried out, resulting in three MCFBGs with different channel sizes.

The last part of the fabrication process was chemical etching, where the fs modified regions of CFBG fibres were chemically etched off by submerging the fibre samples in a 5% HF solution. The samples were left in a container where they were surrounded by HF solution and in order to enhance the penetration of HF solution into the fs laser pre-treated areas, the container was placed in an ultrasonic bath. The etching time for samples with different channel sizes was chosen to be different depending on the size of the channel. The etching process for 550 μm MCFBG was only about 8 mins while for another samples with 1000 μm and 50 μm patterned microchannels, etching time was about 15 mins and 12 mins respectively. We used a high-resolution optical microscope to inspect the MCFBGs after the chemical etching process and some photos are shown in Figures 5.5 and 5.9 in the following sections.

5.3. Spectral, Thermal and RI Sensing Characteristics of MCFBGs

FBGs with uniform and chirped structures have been extensively used in a wide range of optical sensing applications including, temperature, loading, strain and pressure, etc. However, as it is presented in Figure 5.3 FBGs are intrinsically insensitive to the

surrounding RI and can not be directly employed as RI sensors to detect chemical and biological properties. This characteristic of FBGs is due to the fact that mode coupling is taking place between the well-bounded forward and backward propagating core modes while the influence of the RI of surrounding medium is normally affecting the cladding modes.

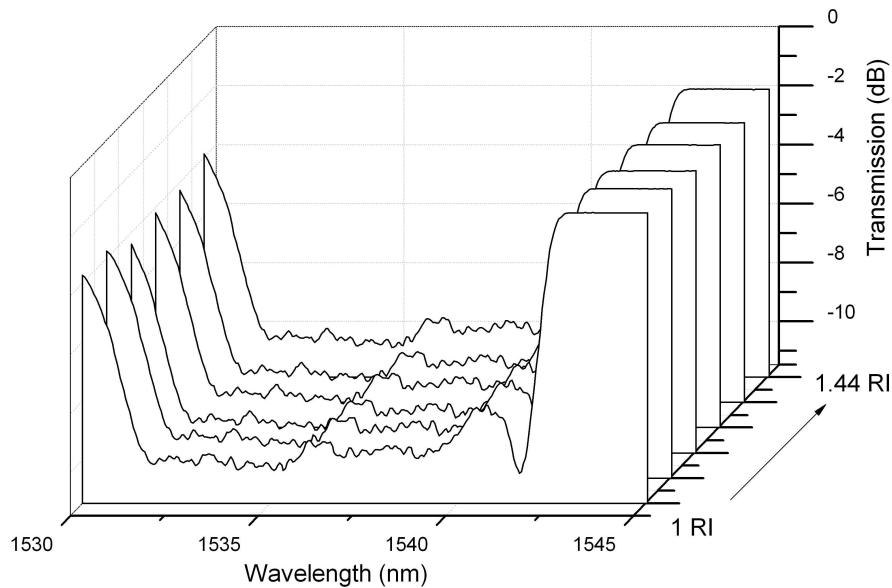


Figure 5. 3. RI response of a normal CFBG when it was immersed in a range of RI oils.

By fs laser patterning and chemical etching of the fibre, microchannel can be created on the CFBG fibre and the grating structure then would be sensitive to the surrounding medium RI change, thus the MCFBG can be used as a chemical and biological sensor. In the following sections, the spectral, thermal and RI sensing characteristics for three MCFBGs with three different microchannel sizes will be discussed.

5.3.1. 50 μm - MCFBG

Figure 5.4 shows the microscope image of the MCFBG with a 51.74 μm long microchannel created in the middle of the CFBG and we can see that the channel has gone through the whole cross-section of the fibre. This photo was taken by employing a $\times 20$ microscopic lens and the measured microchannel size is in a good agreement with the designed length of 50 μm .

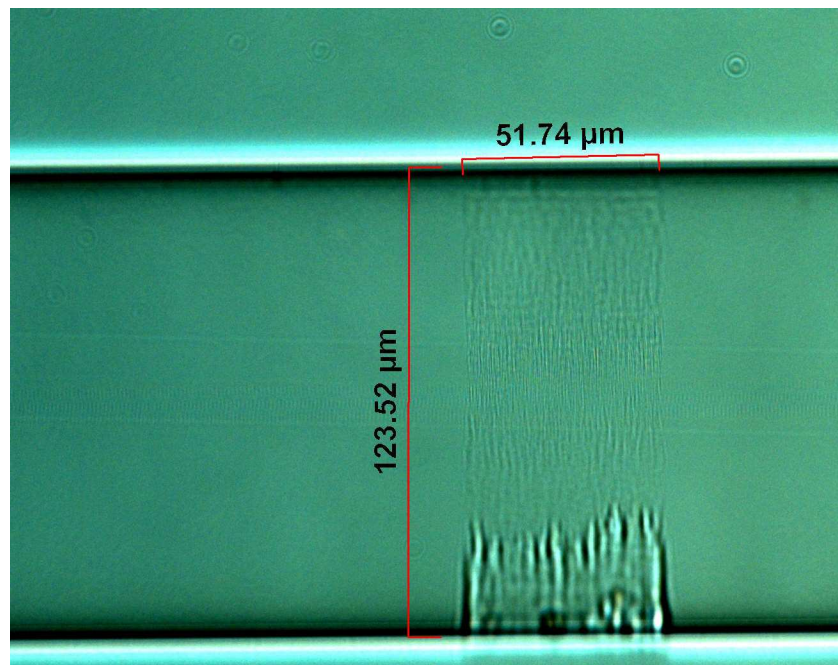


Figure 5.4. Microscope image of 50 μm - MCFBG under a $\times 20$ microscopic lens.

We then examined the transmission spectrum of this device and the measured profile is presented in Figure 5.5.

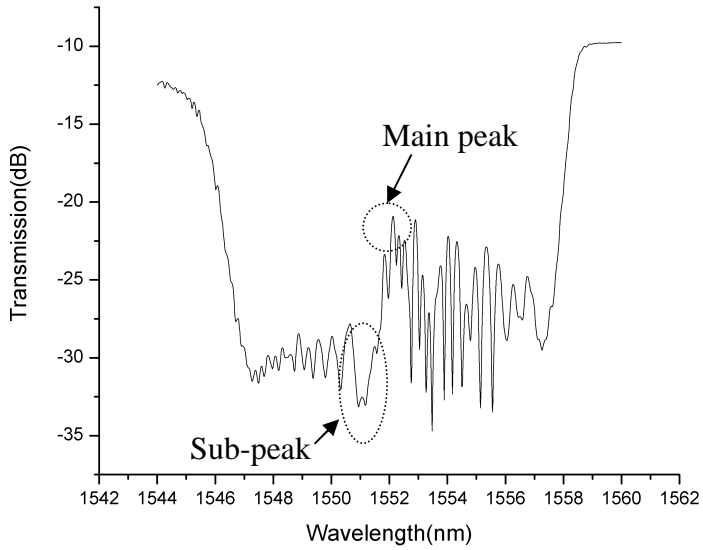


Figure 5. 5. Transmission spectrum of 50 μm -MCFBG.

From this figure we can see some type of phase shift feature – a transmission peak around 1552 nm superimposed with a series of resonances occurred inside of the stopband which well-agreed with simulated spectrum of such a device [P8]. The resultant spectrum can be explained by the combining effect from three sub-gratings; two with the length of about 5 mm separated by a tiny grating of 50 μm length containing the microchannel. Since in the microchannel region, the fibre material is substituted by air so the RI of the short grating is reduced resulting in blue shifting of its reflection band to the shorter wavelength side, thus generating a main transmission peak at ~ 1552 nm. The interference feature within the stopband partially due to the reflection band of the 50 μm grating slightly overlaps with the sub-FBG on the shorter wavelength side. However, due to a very narrow size of the short grating, it has a broad reflection spectrum, which may shift less toward the short wavelength side and more overlaps with the sub-FBG on the longer wavelength side resulting in the appearance of more interferences in the longer wavelength stopband.

5.3.1.1. RI Characteristic of 50 μm - MCFBG

The device was subjected to the RI measurement using a series of index matching gels from Cargille Laboratories by immersing the device in the oil and the transmission spectrum was monitored with an OSA. In this experiment, the 50 μm -MCFBG was fixed in a V-grooved aluminium plate to ensure the measurement was taken free from other effects including strain, bend and temperature. To ensure no residue RI oil left in the microchannel, after each RI oil measurement, the transmission spectrum of the sample was recorded and then the sample was rinsed with acetone, methanol and water several times until the original spectrum was restored. The transmission spectra of 50 μm -MCFBG, while it was immersed to a set of RI oils are presented in Figure 5.6.

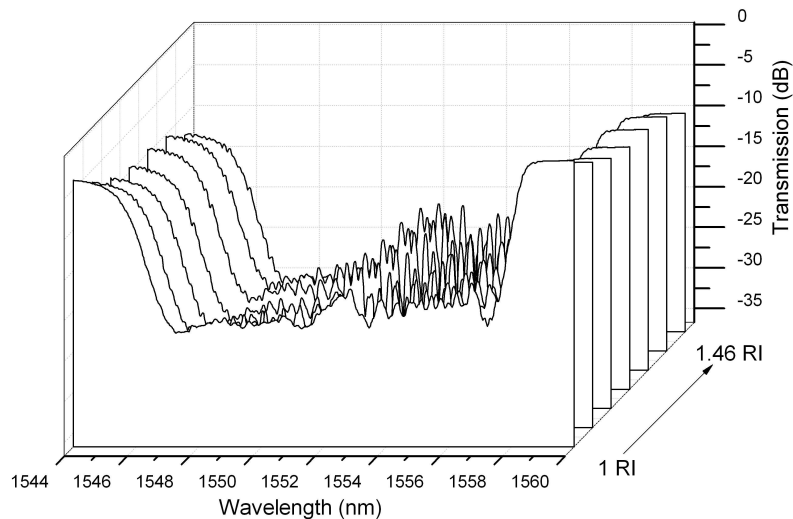


Figure 5. 6. RI response of 50 μm -MCFBG when it was immersed in a set of RI oils.

As we can see in Figure 5.6, no significant response to the surrounding RI medium was achieved from this sample. The creation of a microchannel in the CFBG structure should change the effective index due to the infusion of the surrounding RI

medium in that region. However, it seems that in this sample the channel size is too small in such an extent that the oil with different RI could not fill in the microchannel or the channel was not fully induced through the whole cross section of the fibre and consequently no changes in the spectrum of the proposed MCFBG was detected.

5.3.1.2. Thermal Characteristic of 50 μm - MCFBG

To investigate the thermal property of the device, the sample was housed on a heating base which was connected to a temperature controller. The temperature was increased from 10°C to 60°C by increments of 5°C and the transmission profile of 50 μm -MCFBG was monitored by employing an OSA. The temperature induced wavelength shifts of this device are plotted in Figure 5.7.

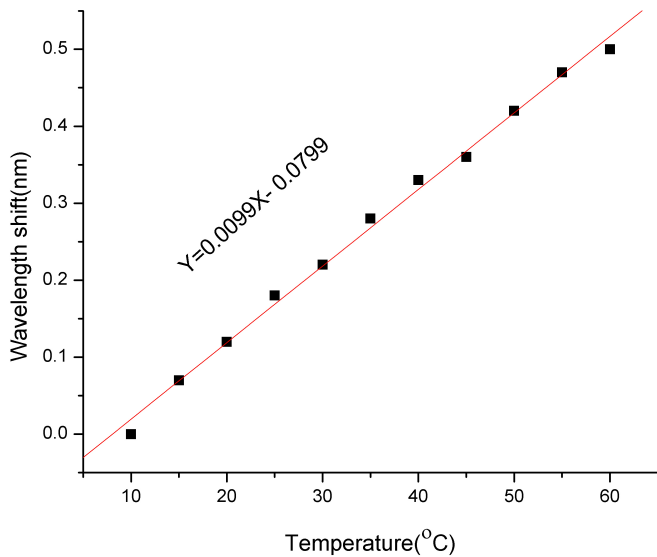


Figure 5. 7. Thermal response of 50 μm -MCFBG.

This figure indicates a thermal sensitivity of about 10 pm/°C for the fabricated MCFBG which is very similar to the thermal response of CFBG without the microchannel. In this situation, the thermal response of the device is mainly determined by the thermo-optic coefficient of the fibre so the whole fibre experienced

the same temperature effect as a normal CFBG with no induced microchannel in its structure.

5.3.2. 550 μm - MCFBG [P8, P9]

We have continued our studying on MCFBG with much larger microchannel size - 550 μm . The microscopic view of this 550 μm -MCFBG is shown in Figure 5.8 where the actual microchannel size was measured as 557.03 μm under a $\times 10$ microscopic lens, which is also in a good agreement with the designed length of 550 μm . The inset in this figure also presents the microscope image of the same MCFBG under the $\times 40$ oil immersion microscopic lens, showing more clearly the edge of the microchannel.

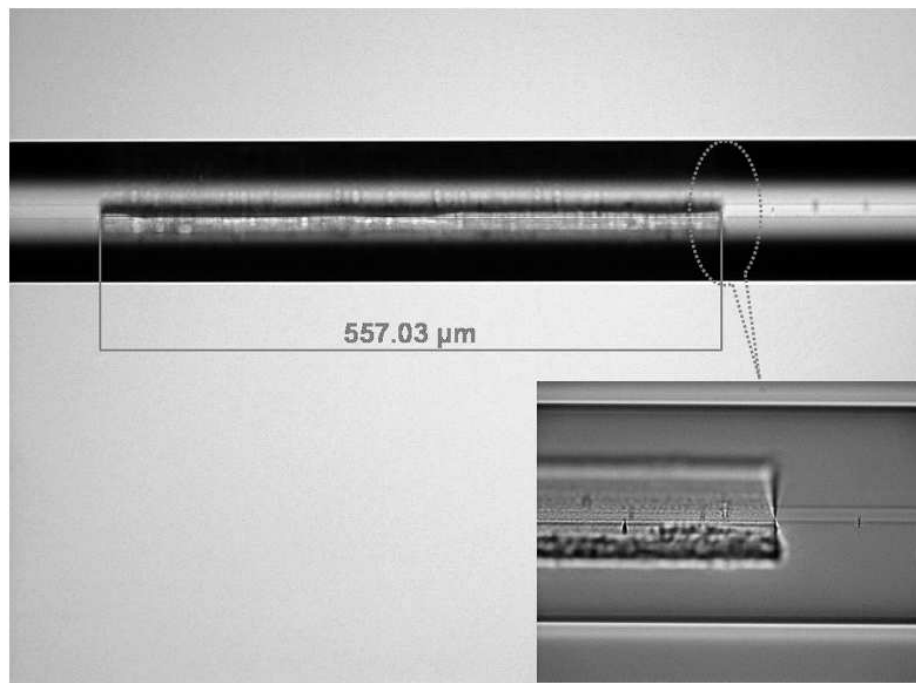


Figure 5.8. 550 μm - MCFBG microscope image under a $\times 10$ microscopic lens. The inset shows the end image of the microchannel under a $\times 40$ oil-immersion microscopic lens.

Figure 5.9 shows the transmission profile of the 550 μm -MCFBG, where we can clearly see a typical phase shift feature which is much clearer than the 50 μm -

MCFBG. From the figure one may notice that from random interference features within the stopband, there are several clear sub-transmission peaks situated on the shorter wavelength side of the main transmission peak, which agree well with simulated spectrum of such a device [P8].

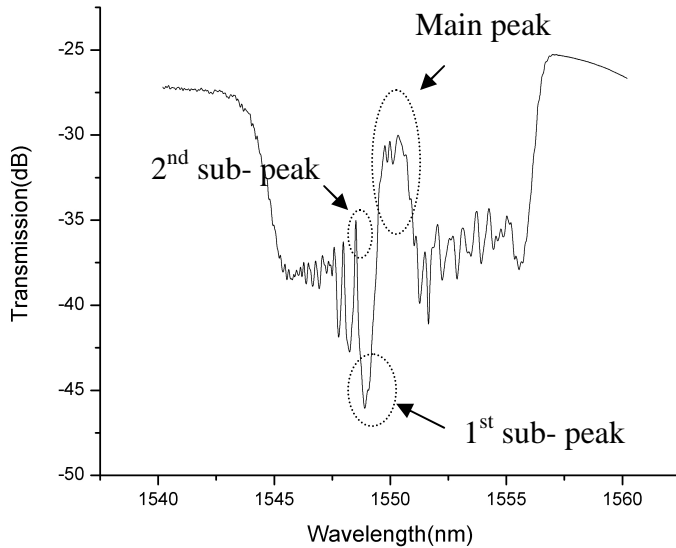


Figure 5. 9. Transmission spectrum of $550 \mu\text{m}$ -MCFBG.

We may consider the resultant spectrum of this $550 \mu\text{m}$ -MCFBG is a combination of three sub-CFBGs arranged as two sub-CFBGs of length $\sim 4725 \mu\text{m}$ separated by a very short ($550 \mu\text{m}$) grating in the middle. However, in this sample as the channel size is far bigger than the previous device, so the reduced effective RI of the short grating will shift its reflection band to the shorter wavelength side, thus resulting in the generation of the main transmission peak in the middle of the original spectrum. The shifted reflection spectrum of the middle sub-CFBG is partially overlapping with the sub-CFBG located in the shorter wavelength side and causes the strong interferences on the shorter wavelength side of the main peak. Also due to the further blue-shifting of the middle sub-CFBG, there is less overlap in the middle part,

so the main transmission peak is well defined and clearer comparing with 50 μm -MCFBG.

5.3.2.1. RI Sensitivity Characteristics of 550 μm - MCFBG

In order to identify the RI response of 550 μm -MCFBG, the measurement was taken employing the same technique as for 50 μm -MCFBG sample. In this sample, since the shifted reflection of the short grating partially overlapped with the sub-CFBG on the shorter wavelength side and generated the strong interferences (sub transmission peaks) in the overlap spectral region (Figure 5.10), we evaluated the RI response of both the main and the first sub transmission peaks against the surrounding medium RI by monitoring their wavelength shifts against the applied RI liquids. The result of this measurement is exhibited in Figure 5.10.

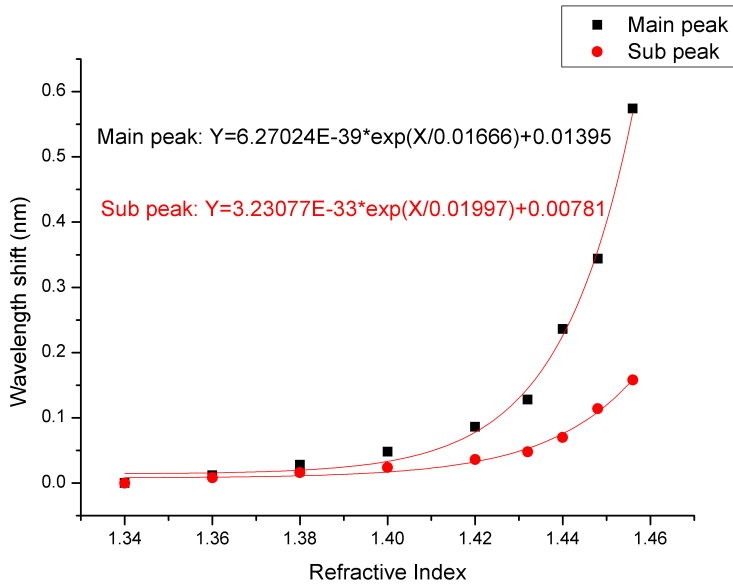


Figure 5. 10. The wavelength shifts of the main (black squares) and the first sub transmission peak (red-circles) against refractive index of surrounding medium.

As it was expected, both peaks red-shifted with changes of RI value but exhibiting a non-linear characteristic trend. To quantitatively estimate the RI sensitivity, we can

introduce two response regions for these peaks corresponding to the low and high RI values. From Figure 5.10 we see for the main transmission peak, the RI sensitivity is about 1nm/RI in the low RI region from 1.34 to 1.42 and 10 nm/RI in the high RI region from 1.42 to 1.46, However, the obtained RI sensitivity values for the first sub peak are much less than that of the main-peak, as only about 0.1 nm/RI and 1nm/RI in the low and high RI regions, respectively. In the low RI region since the RI value of the oil is smaller than the glass core of the fibre, most of the light is confined in to the glass than the oil while in high RI range, when the RI value of the oil is greater than the glass, the light is mostly guided by the oil than glass and we observe a higher RI response from the device. The main peak exhibited more RI sensitivity than the sub-peak since it is corresponding to the middle sub-grating that contains the microchannel is in this sample. The different RI sensitivities of the main and the sub peaks may provide a mechanism for multi-parameter sensing for some applications.

5.3.2.2. Thermal Characteristic of 550 μm - MCFBG

The 550 μm -MCFBG sample was also subjected to the temperature changes. The sample was housed on a heating base which was connected to a temperature controller. The temperature was increased from 10°C to 70°C by an increment of 5°C. The measured wavelength shifts of main and sub transmission peaks were plotted against the temperature changes as shown in Figure 5.11.

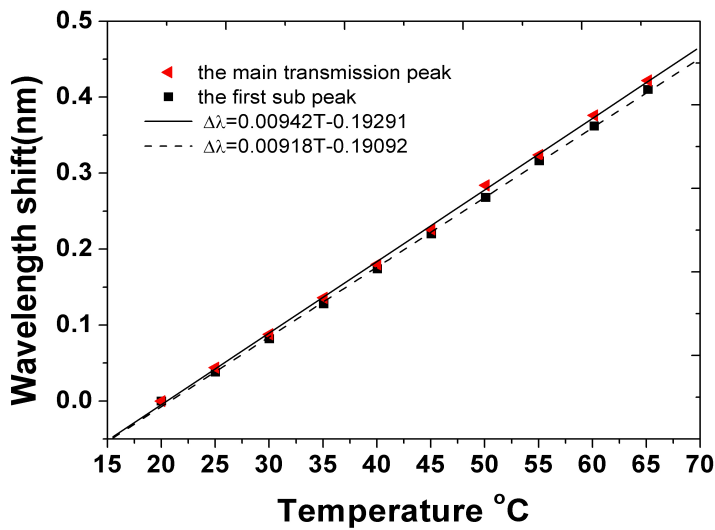


Figure 5.11. Thermal responses of main- and sub-transmission peaks of $550\mu\text{m}$ -MCFBG.

As it is seen in the figure, the main- and sub-transmission peaks exhibit similar thermal responses with the values of about $9.4 \text{ pm}^{\circ}\text{C}$ and $9.2 \text{ pm}^{\circ}\text{C}$ when the sample was surrounded by air. In this situation, the thermal response of the peaks is mainly determined by the thermo-optic coefficient of the fibre, so the whole fibre experiences the same temperature effect.

5.3.3. $1000 \mu\text{m}$ - MCFBG [P2]

The study on MCFBG went further by fabricating another MCFBG containing a $1000\mu\text{m}$ long channel in the middle of a CFBG. The transmission spectrum of this device is presented in Figure 5.12. Also the zoomed spectrum of the fine interference pattern and microscope image of the $1000 \mu\text{m}$ -MCFBG are shown in Figures 5.13 and 5.14, respectively.

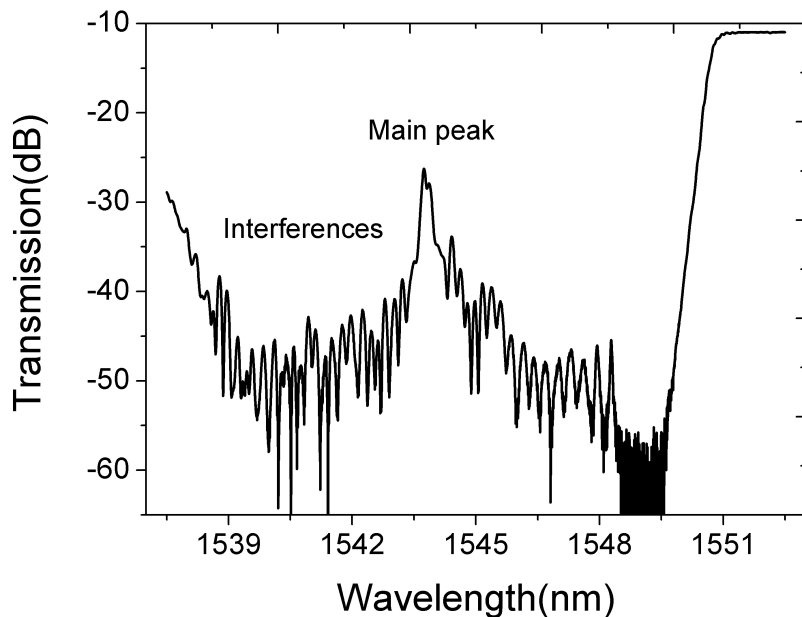


Figure 5. 12. Transmission spectrum of 1000 μm -MCFBG.

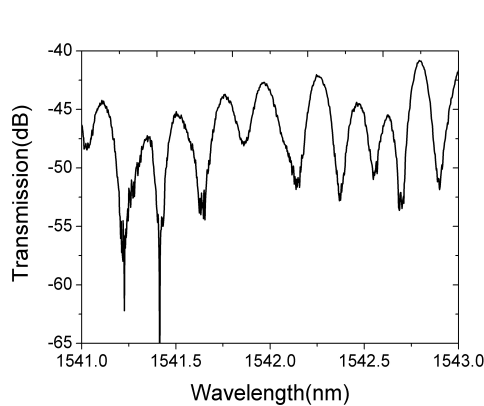


Figure 5. 13. The zoomed spectrum of interference features from the stopband of 1000 μm -MCFBG.

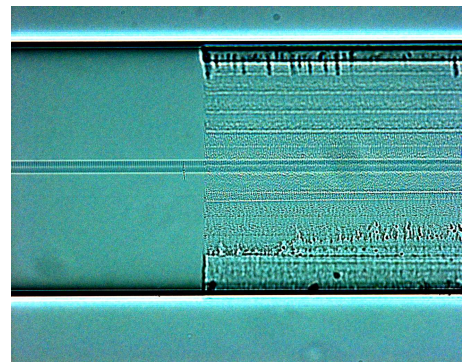


Figure 5. 14. Microscope image of the 1000 μm - MCFBG under a $\times 10$ microscopic lens.

As it is well indicated in Figure 5.12, a slightly narrower main transmission peak appeared in the centre of stopband due to the induction of 1000 μm long channel comparing with the other two proposed devices. Again here we can consider that the whole structure of original CFBG has been divided in three sub-gratings; two 4500 μm long sub-CFBGs separated by a 1000 μm long CFBG which contains a 1 mm

long microchannel. The induction of the microchannel with almost double length of the 550 μm -MCFBG decreased the RI of the middle-sub grating and resulted in the blue shift of the middle sub-grating. In this case since the channel size is broader than the other two MCFBGs, its reflection band is narrower and it may move further toward the shorter wavelength side and totally overlaps with the sub-grating in the shorter wavelength side resulting in more fine interference features and absence of the sub-grating in the middle part of the stopband

5.3.3.1. RI Characteristic of 1000 μm - MCFBG

This 1000 μm -MCFBG sample was also subjected to the RI measurement in the same fashion as the other two MCFBGs. The wavelength shifts of the main transmission peak and one of the sub-peaks from the shorter wavelength side were measured while a set of index liquids with different refractive indices were applied on the sample in turn. As presented in Figure 5.15, in this sample only the interference sub-peak responds to the RI change while the main transmission peak remains insensitive to the surrounding medium RI.

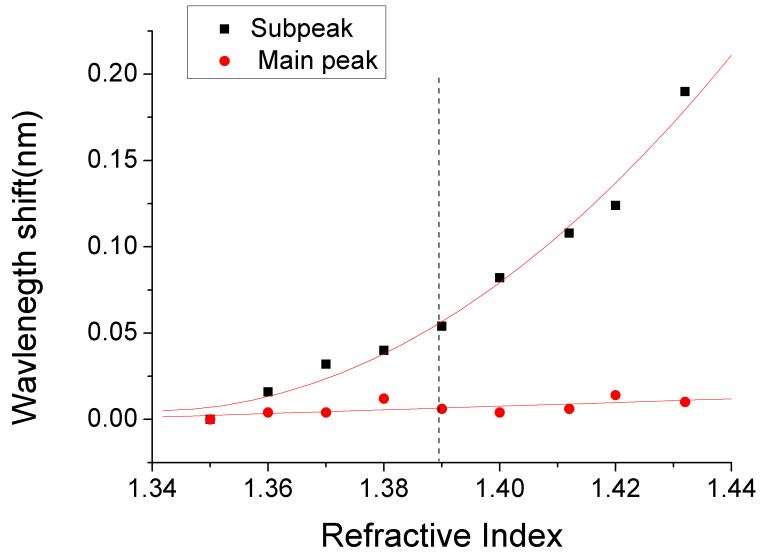


Figure 5.15. The wavelength shift of the main (red circles) and the first sub transmission peak (black squares) against RI of surrounding medium.

This result is in contrast with 550 μm -MCFBG in which both main and sub transmission peaks were sensitive to the RI changes. In this sample as the channel size is almost double of that in the 550 μm -MCFBG sample, we can assume that due to the narrower reflection band of the middle sub-grating, it has fully moved to the short wavelength side and left the absence of FBG in the centre of stopband and introduced the main transmission peak. This means in the middle part of the stopband where the main peak has been formed, there is no grating to respond to the applied RI changes. Thus, the main peak will not be affected by the RI changes. From Figure 5.15, one may notice that the RI response of the sub-peak of this device is also non-linear which is in a good agreement with the results from 550 μm -MCFBG sample. Here also two response regions corresponding to the low and high RI values can be introduced for the sub-peak. In the low RI range which is from 1.34 to 1.39, the average sensitivity of 1.32 nm/RI was measured for the sub-peak. The investigated RI sensitivity for this sub-peak in the high RI range from 1.39 to 1.43 is 3.29 nm/RI. Comparing these results to what we have observed in 550 μm -MCFBG, one can see

that the sub-peak from 1000 μm -MCFBG is more sensitive to RI changes than the sub-peak from 550 μm -MCFBG, but still noticeably lower than that of the main peak in 550 μm -MCFBG sample.

5.3.3.2. Thermal Characteristic of 1000 μm - MCFBG

The thermal characteristic of the 1000 μm -MCFBG sample was also studied by placing the sample on the heat plate while it was surrounded by air. Then we increased the temperature from 10°C to 80°C by increments of 5°C employing a temperature controller which was connected to the heater. The result of this measurement is presented in Figure 5.16.

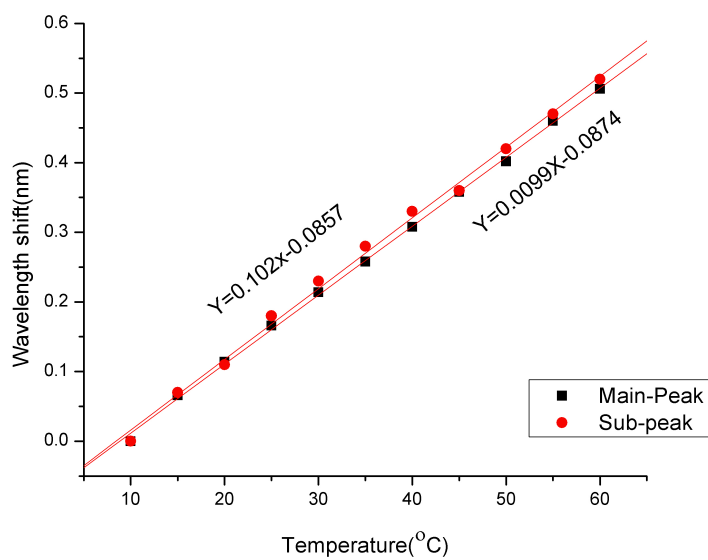


Figure 5. 16. Thermal responses of the main and sub-transmission peaks from the 1000 μm -MCFBG.

The figure indicates that the thermal sensitivities are of 9.9 pm/ $^{\circ}\text{C}$ and 10.2 pm/ $^{\circ}\text{C}$ for the main and sub-transmission peaks, respectively. Evidently in this device also the thermal sensitivities of the main and sub-transmission peak are similar to the measured temperature sensitivities of 50 and 550 μm -MCFBGs, as they were all

measured when surrounded by air, so it is expected well matched with the thermal characteristic of the normal CFBGs.

Since only the interference peak is sensitive to the RI changes and the main peak is fully insensitive to the surrounding refractive index medium and comparison with 550 μm -MCFBG, this device with slightly broader microchannel size exhibited more advantages as an RI sensor. In this structure, the main peak can offer the temperature reference function, thus eliminating the temperature cross sensitivity problem on RI measurement from the sub-transmission peak. So the proposed device has shown the capability of simultaneous measurement of temperature and RI changes.

5.4. Summary on MCFBGs

In general, the aim of the creation of microchannels in CFBGs was to enable the gratings to be penetrated by the surrounding medium, presenting the RI response for chemical and biological sensing. Although, MCFBG sensors exhibit lower sensitivity in respect to LPG [117-118] and thinned FBG [111] sensors their performances in terms of RI measurements, they are still comparable with relatively lower cost instrumentation. In fact, for FBG demodulation, several low-cost FBG interrogation units with high performances (1-pm resolution around 1550 nm) have been proposed in the past decade [119] while for the demodulation of LPG sensors, only spectral analysis with lower resolution and higher costs have been reported. Furthermore, The small size of the induced microchannel will not only help the grating to access to the RI solution but also maintain the robustness of the device making the proposed devices more desirable candidates comparing to those FBGs with the fully or largely etched off cladding layers. However, our first experiment in which a 50 μm -MCFBG

was proposed and fabricated indicates that in the case of microchannel with too small size, the device can not offer any RI response as either the RI liquid will not be able to pass through the channel or the channel has not been induced properly through the whole cross section of the fibre. The other advantage the MCFBG can offer is the simultaneous measurement of RI and temperature as the main and sub resonance peaks exhibit different RI and temperature sensitivities.

5.5. Micro-slot in Fibre Bragg Grating [P10, P12]

The modified fiber Bragg gratings can also be employed as refractometers for a range of applications like in-situ monitoring or sensor miniaturisation. The employed mode coupling in a FBG based refractometer can be one of the following approaches: (a) forward mode coupling in TFGs with large tilting angles [94] and LPGs [117, 118], (b) backward cladding mode coupling generated by TFGs with small tilt angles [119], or (c) backward core mode coupling in FBGs with modified structures in which the fiber's cladding has been fully removed [111]. Between the mentioned categories, LPGs and TFGs with large angle are the most RI sensitive devices but they are limited in respect of miniaturization because of their long size and use of transmission profiles. In small angle TFGs, the RI sensitivity is relatively low with typical value $\sim 10^{-4}/\text{pm}$ [115] and the gratings with removed cladding are extremely fragile.

In all three categories, since only a small portion of the propagating light in the fibre, which can only exist in the cladding, interacts with the material under test the proposed devices suffer from the limited sensitivity and an operational range below the RI of fibre core. Another reported technique to enhance the RI sensitivity is to

employ a liquid as the core of the waveguide instead of its cladding to guide the light in applications such as spectroscopy [119] and fluorescence [120]. For the first time a fibre based liquid core device employing a refractive grating was reported by Zhou *et.al* from our research group to interrogate the surrounding medium RI [114]. He employed the fs assisted chemical etching technique to engrave a micro-slot of $1.2 \times 125 \times 500 \mu\text{m}$ along a UV inscribed FBG in a standard optical fibre. His proposed device benefits from being more robust and highly sensitive in both low and high RI ranges. Here we report the development of the mentioned study by inscribing a micro-slot across the whole length of a 1 mm-long FBG and study the characteristics of the fabricated device in terms of RI and temperature sensitivities.

5.5.1. Fabrication of Micro-slot in Fibre Bragg Grating

Figure 5.17 presents the geometry of the proposed micro-slot engraved in the core of the fibre and along a FBG.

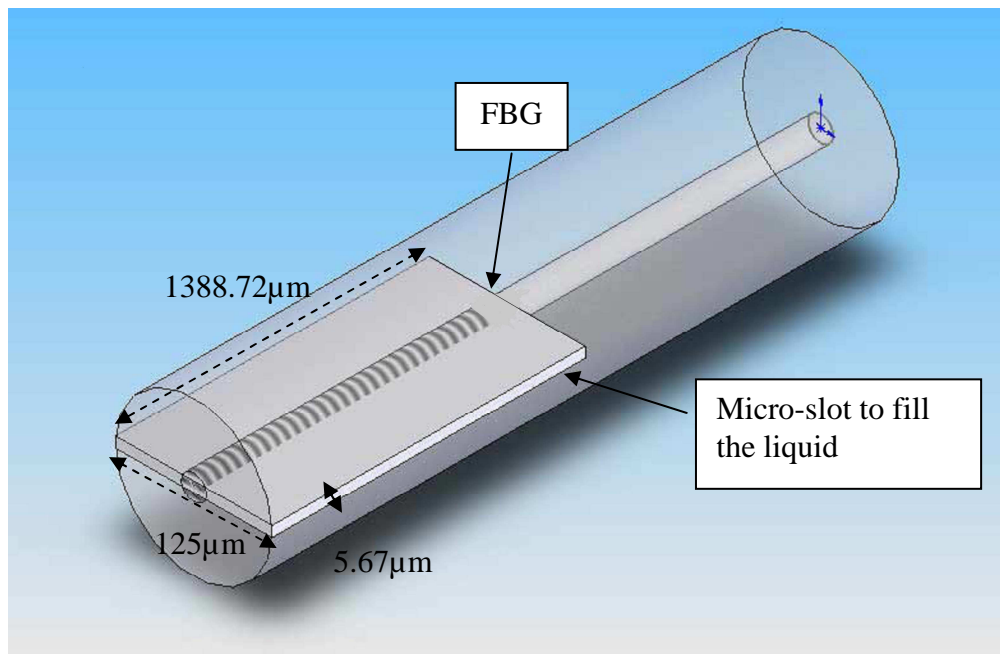


Figure 5. 17. The geometry of the proposed micro-slot along the grating and across the fibre.

Fabrication process of the proposed micro-slot in FBG includes three main steps:

1. Fabricating FBG into the core of a hydrogen-loaded standard telecom single-mode fibre by UV light using the phase mask inscription technique;
2. Patterning the micro-slot of the desired dimension along the full length of FBG and across the whole fibre using tightly focused fs laser beam;
3. Etching the fs-modified FBG in a 5% HF solution for selective removal of the fs-modified region.

1 mm-long FBG was UV inscribed in a SMF-28 optical fibre employing the scanning phase mask technique and a CW frequency doubled Ar ion laser operating at 244nm. Prior to the UV-inscription, the photosensitivity of SMF-28 fibre was enhanced by pressurising in hydrogen for a period of 48 hours at a pressure of 150 bars and the temperature of 80°C. The uniform integrated phase mask used in the experiment has the dimensions of 50 mm × 3 mm and the period of 1071.92 nm.

A 50 mm length of the host fibre was stripped for the middle part of ~1mm for grating inscription. The FBG was fabricated by a single scan through the phase mask at scan velocity of 0.05 mm/s. During the fabrication process, the UV laser was running at 100mW under a current of 38 mA. Figure 5.18 shows the transmission spectrum of the fabricated 1mm-long grating with the central wavelength of 1552.25 nm and reflectivity of ~ 9 dB.

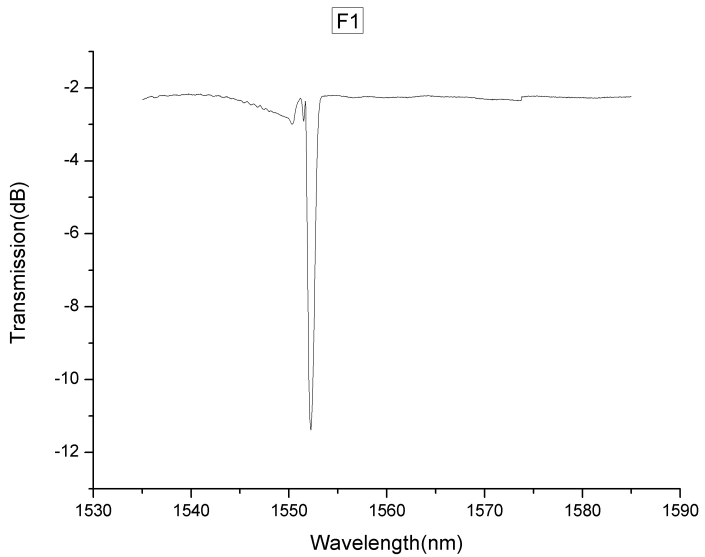


Figure 5. 18. Transmission spectrum of UV inscribed 1mm-long FBG before induction of a micro-slot into its structure.

The fabricated 1 mm-long FBG was annealed for 48 hours and at 103°C to become stabilised. The 1 mm-long FBG was first subjected to RI measurement. For this measurement, the sample was housed in a V-groove plate where a set of oils with different RI values were applied on the grating. The transmission spectrum of the grating was recorded after each measurement. The result of this experiment is presented in Figure 5.19.

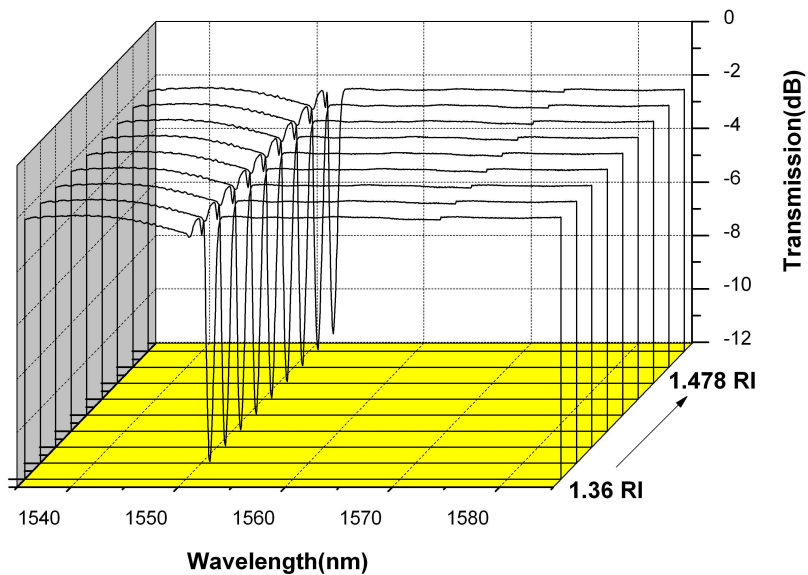


Figure 5. 19. RI response of 1mm-long FBG when it was immersed in a set of RI oils.

As it was expected the FBG exhibited no sensitivity to the surrounding medium RI so it requires some structure modification to become RI sensitive.

The thermal response of the sample was also investigated by locating the FBG on a heater plate which was connected to the temperature controller. The temperature was increased gradually from 10°C to 80°C by increment of 10°C while the spectrum of the FBG was recording after each measurement employing an OSA. The result is presented in Figure 5.20. This figure indicates the temperature sensitivity of 11.5 pm/°C for the fabricated FBG, which is standard for a normal FBG in SM-28 fibre.

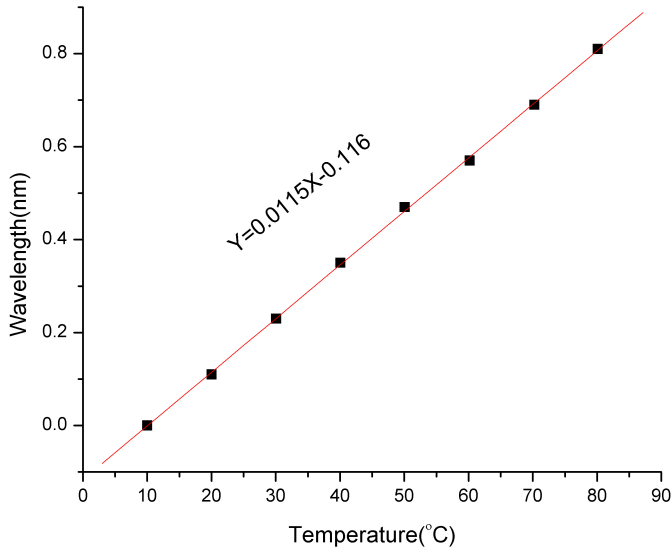


Figure 5. 20. Thermal response of 1mm-long FBG.

At this stage of sample preparation, a 125 (width) \times 5.74 (height) \times 1388.72 (length) μm micro-slot was patterned across the whole fibre and along the FBG by employing the fs-laser machining technique. fs-laser pulses of $\lambda= 800\text{nm}$ were tightly focused on the fibre by a $\times 100$ objective lens with N.A. of 0.55 while the working distance was set at 13 mm. The pulse width of the laser was ~ 150 fs with 1 kHz repetition rate. The fibre was mounted on a dual-axis air-bearing translation stage to write the desire pattern simply by translating the fibre with respect to the fs-laser beam. It is worth to mention that the cylindrical geometry of the fibre would cause the distortion to the focus volume if the inscription was performing with fibre in air [115].

Following this step, the fibre with the micro-slot pattern was chemically etched in 5% HF acid solution and an ultrasonic bath was employed to increase the penetration of HF acid into the patterned region of the fibre. During the etching process, the transmission spectrum of the sample was monitored using a broadband light source and an OSA. The spectrum exhibited the loss after 9 mins since the start of etching process and then the rapid growth of the loss was observed. This fast loss growth rate

indicated that the region close to the core was being etched. The fs-laser patterning caused a very high etching rate which was approximately 100 times higher than in pristine materials. After approximately 15 minutes of chemical etching, a micro-slot with a height of 5.74 μm was generated along the FBG and across the fibre. A high-resolution optical microscope was employed to inspect the micro-slot structure in FBG after the chemical etching process. Microscope images of the proposed device under $\times 5$ and $\times 40$ microscopic lenses are presented in Figure 5.21.

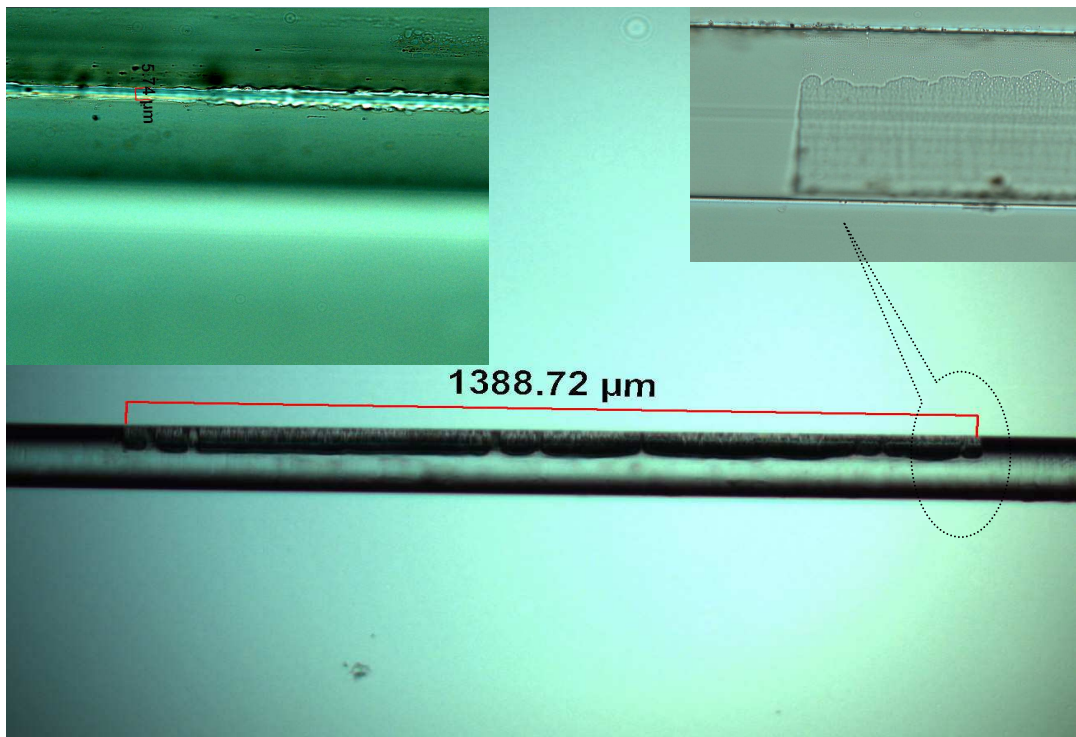


Figure 5. 21. Microscope image under a $\times 5$ microscopic lens showing the 1388.72 μm - micro-slot along a FBG and across the fibre. Note: The insets are the microscope images of the same device observed by $\times 40$ oil-immersion microscopic lense.

5.5.2. Characteristics of Micro-slot FBG

Transmission loss profile of the device was recorded when it was surrounded by air and different RI oils. A tuneable laser light source (Agilent 8164A) which was

connected to an optical vector analyser EL from LUNA Technologies was employed to carry out these measurements. Three transmission loss spectra of the sample have been selected to present. Figure 5.22 shows the transmission profile of the device, when it was surrounded by air.

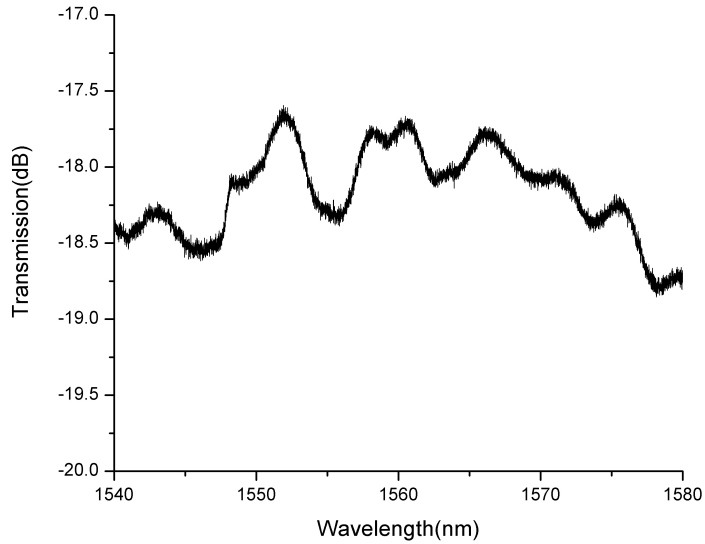


Figure 5. 22. Transmission loss profile of the micro-slot FBG when it was surrounded by air.

As it is expected due to the large size of the induced micro-slot, Fabry Perot resonances spread all over the spectrum and the original Bragg peak is not observed in this figure. This effect might happen due to the change in the light distribution in this sample as a result of the induced air-filled micro-slot in a relatively large area of the central part of the fibre core where the grating is located. Figure 5.23 shows the schematic diagram of the light distribution in the proposed device under this condition. In this case the high intensity wavefront of the incident light mainly does not enter the micro-slot and will be confined in the remaining glass part of the fibre, where the remaining tiny portion of the grating is located. After some distance from the other end of the micro-slot once again light is confined in the fibre core. In such

condition, two edges of the micro-slot will act as reflecting mirrors resulting in Fabry-Perot resonances in the transmission spectrum of the device.

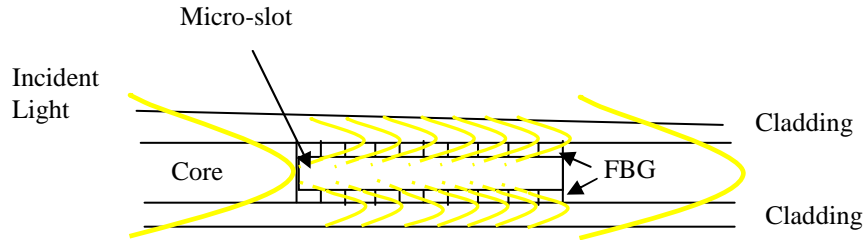


Figure 5. 23. Schematic diagram of the light distribution in micro-slot FBG when it is surrounded by air.

Then we have applied 1.36 RI oil on the sample and recorded the transmission spectrum of the device and the spectrum is exhibited in Figure 5.24.

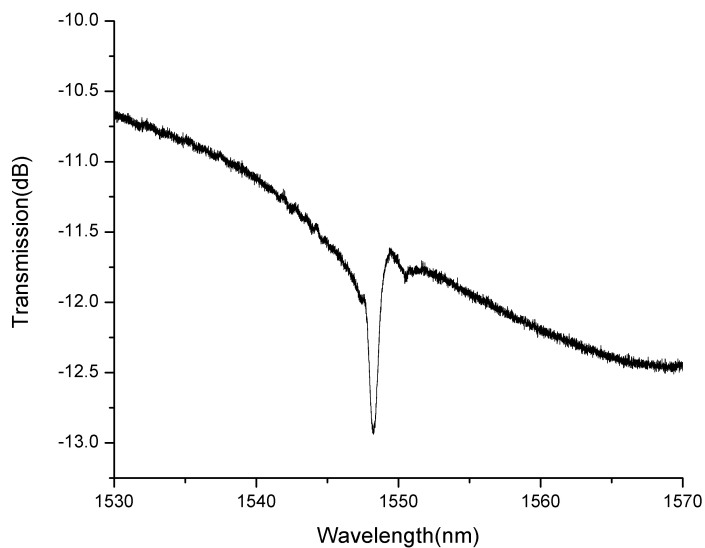


Figure 5. 24. The Transmission spectrum of the micro-slot FBG when it was immersed in 1.36 RI oil.

As we can clearly see in this figure, with filling the micro-slot by the index oil the Bragg peak appears in the spectrum but at lower wavelength than the original FBG. Here the Bragg peak is located at 1548.39 nm with 1 dB transmission while in the original FBG without the micro-slot the Bragg peak was at 1552.25 nm and exhibiting

9 dB transmission. This data evidently presents the induced loss of creating a big micro-slot across the fibre. Also by introducing a big micro-slot across the fibre and along whole grating, the total effective index of the fibre will be decreased. Here the micro-slot has been filled with the oil having less RI value than fibre material so the value of total effective index has been reduced and resulted in the blue-shift of the Bragg peak.

After this measurement, the sample was subjected to another experiment when 1.478 RI oil was applied on the sample. Figure 5.25 presents the transmission loss profile of the proposed micro-slot FBG when it was immersed in 1.478 RI oil.

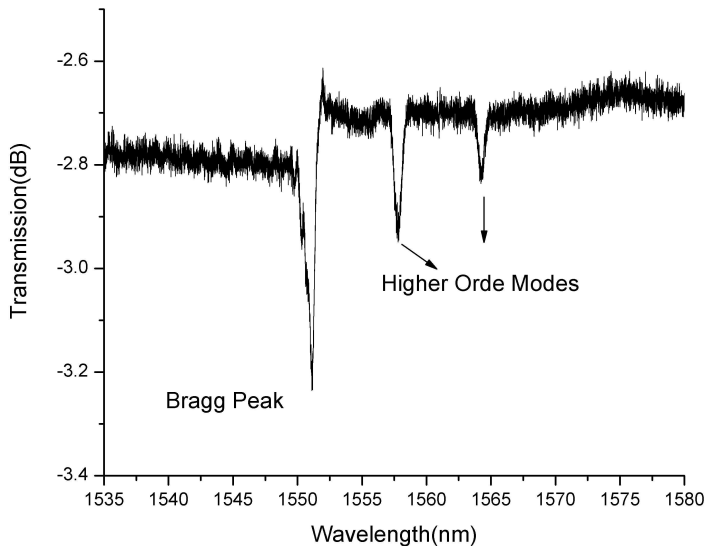


Figure 5. 25. The transmission spectrum of the micro-slot FBG when it was immersed in 1.478 RI oil.

Figure 5.25 evidents the appearance of the Bragg peak in its original wavelength of 1551.21 nm and two more reflection peaks located in higher wavelength range in the transmission profile of the proposed device. This can be explained by considering the fact that when the oil with higher RI value of 1.478 is applied, the device becomes a liquid refractometer in which the oil takes the role of leading the light. The high RI value of the penetrated oil in the sample results in increase in the mean effective index

of the fibre to such an extent that it becomes few-moded and the grating couples the light to higher order modes.

5.5.2.1. RI Characteristic of Micro-slot FBG

The response of the proposed and fabricated 1mm-long micro-slot FBG device to the RI of surrounding medium was investigated by applying a set of index oils from Cargille Laboratories on the sample and the transmission spectrum of the device for each individual RI oil was measured employing a Lunar tuneable laser source.

In this experiment, similarly the device was fixed in a V-grooved aluminium plate to ensure the measurement is taken free from other effects including strain, bend and temperature. Considering the relatively big size of the micro-slot to ensure no residue RI oil left in the micro-slot, after applying each RI oil and recording the transmission spectrum of the sample, it was rinsed with acetone, methanol and water. This process repeated for several times until the original spectrum of the device when it was surrounded by air was restored, and the sample was ready for the next RI measurement. Figure 5.26 indicates the RI response of the proposed device in a range from 1.36 to 1.496.

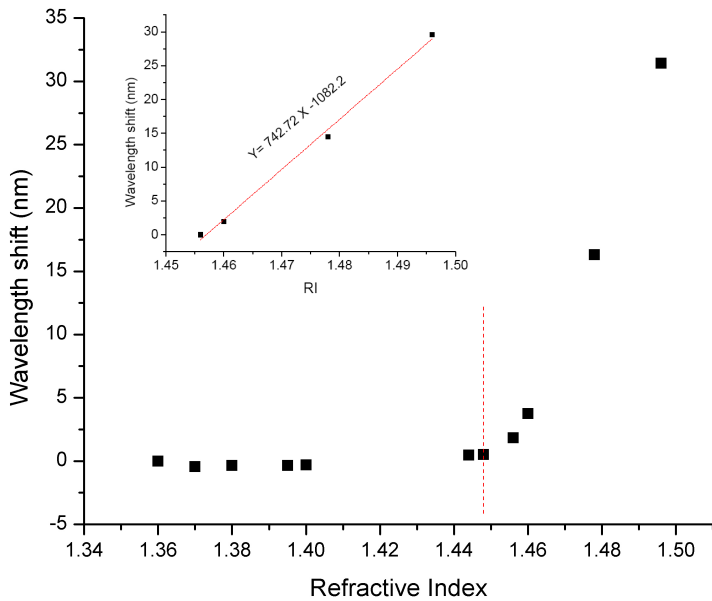


Figure 5. 26. RI characteristic of the proposed micro-slot FBG. *Note: The inset presents the response of the device in high RI range.*

As it is indicated in Figure 5.26 there are two very different response regions for this sample corresponding to the low (1.36 to 1.448) and high (1.456 to 1.496) RI values. In the low RI region, the proposed device is almost insensitive to the applied RI while for the high RI values, it exhibits the RI sensitivity of about 742.73 nm/RI. It seems that in the low RI region, the launched light is still confined with the glass and guided by the fibre material so still only evanescent wave penetrates into the oil in this region. In high RI region, the oil will take over the light guiding and the light will mainly remains in the gel filled part, so the effective index is decided by the index oil. This result is in a good agreement with the reported simulation and experimental results in Zhou *et.al* paper [115].

5.5.2.2. Temperature Characteristic of Micro-slot FBG

We also investigated the thermal characteristic of 1mm-long micro-slot FBG sample by placing the sample on the heat plate and increasing the temperature from 10°C to 60°C by increments of 5°C employing a temperature controller which was connected to the heater. The transmission spectrum of this device was recorded using a tuneable laser. The measurement was carried out twice for the sample while it was surrounded by 1.448- and 1.456 –RI oils, respectively.

We examined the temperature sensitivity of the device when it was subjected to 1.448 RI oil and the result is presented in Figure 5.27.

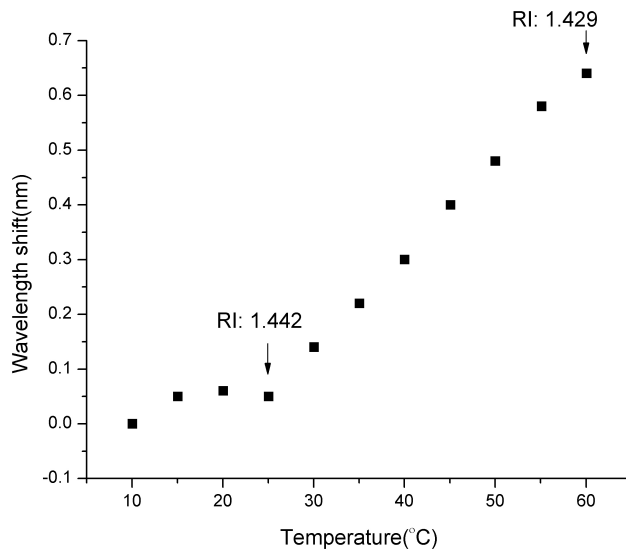


Figure 5. 27. Thermal response of 1mm-long micro-slot FBG when it was immersed in 1.448 RI oil.
Note: By increasing the temperature RI value of the oil decreases by rate of $-dn/dT=3.79 \times 10^{-4} / ^\circ C$ and as indicated in the figure at 25°C and 60°C, the RI value of the oil decreases from 1.448 to 1.442 and 1.429 respectively.

The figure indicates two thermal response regions for the device when is immersed in 1.448 RI oil. In low temperature region from 10°C to 25°C, there is a certain degree of random wavelength shift for the device while by increasing the temperature and entering to the higher temperature range from 25°C to 60°C, a rapid upward

wavelength shift is realised. The measured temperature sensitivity in this region is about 17.1 pm/°C which is much higher than the thermal response of the primary FBG. This result can be explained by considering the fact that by increasing the temperature, the RI of the 1.448 RI oil will decrease by the factor of $-\frac{dn}{dT} = 3.79 \times 10^{-4}$ (the value provided by Cargille Laboratories), so as it is indicated in the figure, at 25°C, the RI of the oil decreases not significantly from 1.448 to about 1.442 and with further increase of the applied temperature to 60°C, the RI value of the oil reaches to almost 1.429. In this region, the RI value of the oil decreases in such a level that the light will be confined in the glass rather than in the oil and the Bragg peak starts red-shifting with increasing temperature. The high temperature sensitivity in this region is due to the combination of the rapid reduction of RI value of the oil at high temperature and increase in RI value of the glass by heating the sample.

In the low thermal region, while the RI is still high, the temperature sensitivity is driven by the oil and due to the negative thermo-optic coefficient of the oil, there is no noticeable red-shift trend in the Bragg resonance. This argument is in a good agreement with the observed results from the other measurement in which the sample was immersed in 1.456 RI oil and was subjected to the temperature experiment. Figure 5.28 presents the thermal response of the 1mm-long micro-slot FBG when it was surrounded by 1.456 RI oil.

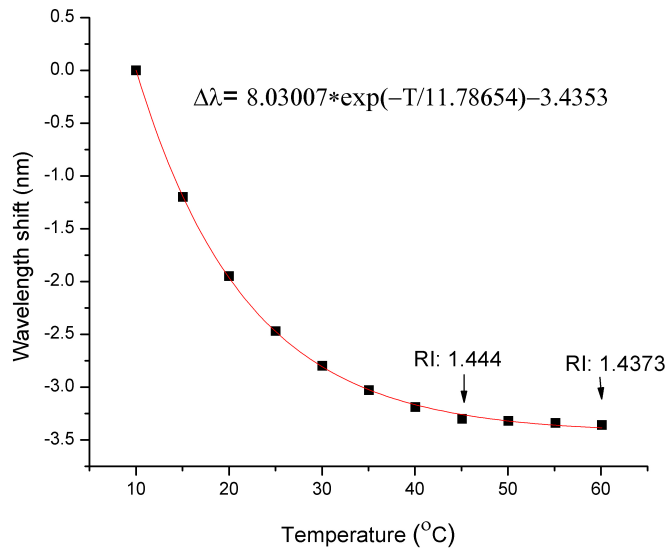


Figure 5. 28. Thermal response of micro-slot FBG when it as immersed in 1.456 RI oil.

The figure clearly indicates an exponentially decaying thermal response of the device, which is opposite to that shown in Figure 5.27. We may also divide two well separated response regions corresponding to the low (from 10°C to 45°C) and high (45°C to 60°C) temperature values for this measurement. In this case also the RI of the oil is reducing by enhancing the temperature. The decrease rate of 1.456 RI oil is determined by the value of $-\frac{dn}{dT} = 3.74 \times 10^{-4} \text{ } \textcircled{C}$. The calculation based on this factor presents that by increasing the temperature to 45°C, the RI value of the oil reduces to 1.444 and when the temperature is set at 60°C, this value further reduces to 1.4373, as marked in the figure.

Based on the fact the effective RI, n_{eff} , of the proposed device is a function of combination between RI of the silica glass and the RI oil, we can write the following equation:

$$n_{eff} = C_1 n_{Glass} + C_2 n_{Oil} \quad (\text{eq: 5.1})$$

Where C_1 and C_2 are representing the portion of light distributing into the glass and oil respectively. Also n_{Glass} and n_{Oil} are RI of the glass and consequently the portion of light travelling into the glass part will increase by Δn_{Glass} and ΔC_1 while the RI of the oil and the portion of light confining into the liquid part decrease by Δn_{Oil} and ΔC_2 due to the negative thermo-optic coefficient effect of the liquid as shown in equation 5.2.

$$n_{eff} = (C_1 + \Delta C_1)(n_{Glass} + \Delta n_{Glass}) + (C_2 - \Delta C_2)(n_{Oil} - \Delta n_{Oil}) \quad (\text{eq: 5.2})$$

Simplifying the above equation results in equation 5.3.

$$n_{eff} = C_1 n_{Glass} + C_2 n_{oil} + \Delta C_1 (n_{Glass} + \Delta n_{Glass}) - \Delta C_2 (n_{Oil} - \Delta n_{Oil}) \quad (\text{eq: 5.3})$$

When oils with higher RI values than glass are applied on the device, by increasing the temperature the negative term in equation 5.3 becomes the dominant part and results in decreasing of the effective RI and consequently wavelength blue shifting. This wavelength shift trend continues with the temperature until the RI value of the oil reduced to a value close to the index of the fibre glass. So, in the low temperature response and when the RI of the oil is in the range of 1.456- and 1.444, similar to the given explanation in the previous experiment , the oil is a predominating factor and based on the negative thermo-optic coefficient of the oil, the Bragg peak shifts to the shorter wavelength. When the temperature further increases to 45°C, the RI value of oil becomes close to the glass so the downward trend of the wavelength shift stops. At this point since the sample is about to start behaving based on glass character, it is predicted that by further increase in the temperature, we should observe a linear red-shift of the Bragg peak.

5.5.2.3. PDL Measurement of Micro-slot FBG

The induction of a large micro-slot into the grating structure can induce some PDL in to the device since the geometry of the fibre is changed. However, if the micro-slot is inscribed symmetrically into the fibre the polarisation effect will be negligible and an ideal sensing performance from the device will be achieved. The polarisation characteristic of the proposed device was investigated by employing a tuneable laser light source (Agilent 8164A) which was connected to an optical vector analyser EL from LUNA Technologies. The optical vector analyser is capable of characterising polarisation effects such as PDL by scanning a tuneable laser only once. This is achieved by conditioning the optical signal in the fibre before it propagates through the device under test. The single scan nature of the technique leads to greatly enhanced measurement speeds and higher levels of accuracy and repeatability.

The result of this experiment is presented in Figure 5.26. It should be noticed that for a clear comparison, the measured PDLs for each index oil are displayed with offsets in this figure. As we can see from Figure 5.29 there is no noticeable PDL value for the 1mm-long micro-slot FBG. The largest observed PDL is about 0.55 dB seeing from the measurement in which the sample was immersed in 1.40 RI oil. As one may observe from this figure, for the measurements in which the sample was surrounded by index oils with the high RI value, the device shows a non polarisation dependent characteristic.

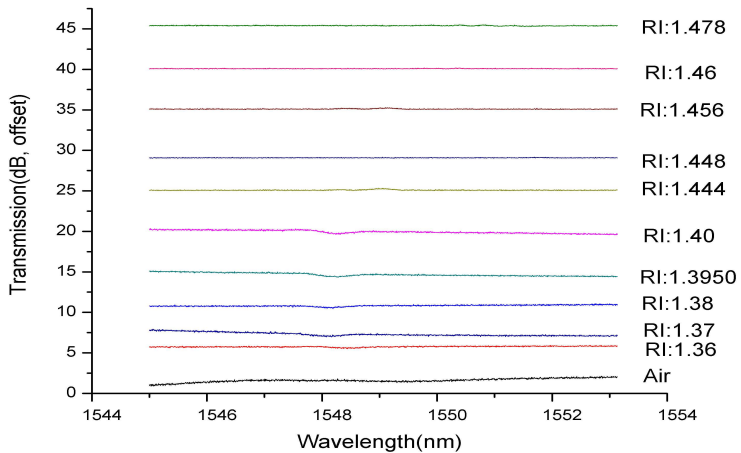


Figure 5.29. PDL measurement of micro-slot FBG when it was immersed in air and RI oils.
Note, the PDLs are plotted with offsets.

In summary, we have investigated a micro-slot FBG with the capability of temperature and RI measurement. The result was in a good agreement with the previous theoretical and experimental published data. Comparing with the earlier discussed MCFBGs, the proposed micro-slot FBG has expressed more sensitivity to the surrounding medium. This device benefits from the low cost and relatively simple and efficient approach in fabrication technique.

5.6. Conclusion

In this chapter the systematic study of fabrication and characterisation of three MCFBGs with different channel sizes of 50 μm , 550 μm and 1000 μm and one micro-slot FBG with the slot size of 1388 μm were proposed, fabricated and experimentally characterised. All the proposed devices were fabricated by employing the fs-laser patterning aided chemical etching technique. In standard glass optical fibre, effective RI is not influenced by the surrounding medium and also as the mode coupling takes place between well bounded forward and backward propagating core modes, FBGs are normally RI insensitive. In the demonstrated micro-structured FBG devices, the Bragg wavelength shift associated in the etched part is directly related to the dependence of the effective RI of the fundamental mode on the surrounding medium RI. Due to the interaction of the evanescent field with the surrounding medium, when RI increases the evanescent field in the surrounding medium also increases and causes the maximum sensitivity of the device while the value of surrounding RI medium is close to the cladding one. In this case, only measurand changes will influence the RI and the grating period is practically unchanged.

In 550- and 1000- μm MCFBGs, the reduced effective index of the microchannel region results in generation of transmission bands inside the CFBG stopbands and the devices become sensitive to the RI variation. The spectral responses of the fabricated MCFBGs are in a good agreement with each other. The RI sensitivity of these MCFBGs is evaluated by measuring the wavelength shifts of the main and sub transmission peaks against the surrounding medium RI, showing a nonlinearly increased RI sensitivity.

For 550 μm -MCFBG, the main transmission peak shows the RI sensitivity up to about 10^{-4} RI/pm where the sub transmission peaks are less sensitive to the RI changes. However due to their narrow line-width feature they are capable of providing a higher sensing resolution. In 1000 μm -MCFBG, the main peak exhibits no RI response while the sub-peaks are sensitive to the RI changes. In the case of 50 μm -MCFBG, the fibre core could not be penetrated by RI oils so no RI response was detected from this sample; There are two assumptions for this result: 1- the channel might has not been induced fully over the whole cross section of the fibre and 2- due to the very tiny size of the channel the oil could not penetrate to the fibre's core.

Furthermore this chapter reported the investigation on the temperature characteristics of MCFBGs; in all three MCFBGs the main and sub transmission peaks exhibit similar thermal responsivities of about 10 pm/ $^{\circ}\text{C}$ while they were surrounded by air. This value is similar to the measure temperature sensitivity of normal CFBG and indicates that the thermal response of the proposed devices is influenced by the thermo-optic coefficient property of the fibre. Furthermore, since the main peak from the spectrum of the 1000 μm - MCFBG is only sensitive to temperature changes, it can be employed as a temperature reference sensor and the device can be employed for simultaneous measurements of RI and temperature, thus represents an ideal structure for implementation of in-fibre bio-chemical sensors.

In this chapter we also report the engraving of a micro-slot with 5.67 (H)×125 (W) ×1388 (L) μm along a 1mm-long FBG using the same fs-laser patterning and chemical etch technique. The micro-slot FBG was also subjected to the RI and temperature test and the results indicate that the device is effective in a broad RI

range. The micro-slot FBG exhibits the RI sensitivity of about 742.72 nm/RI in the RI range from 1.456 to 1.496.

The thermal response of the micro-slot FBG was measured when it was immersed in two different RI oils and the results were fully discussed. It was clearly observed that if the device is immersed in oil with higher RI value than the glass, by increasing the temperature, the thermal response of the micro-slot FBG immersed will exponentially decrease due to the negative thermo-optic effect of the oil.

The PDL characteristic of the micro-slot FBG was also studied and no noticeable PDL was observed from this sample surrounded by air or a set of RI oils. Overall, all the proposed and fabricated micro-structure gratings show not only the enhanced sensitivity to the external RI, but also a better mechanical strength than other chemically etched FBG sensing devices, thus represent a more ideal structure for implementation of in-fiber bio-chemical sensors.

Chapter 6

Fibre Lasers Using Intra-Cavity Tilted Fibre Gratings

6.1. Introduction

Optical fibre lasers with single polarisation and switchable multiwavelength output are useful devices for many applications, such as WDM in optical fibre communication systems, fibre sensors, optical instruments, and system diagnostics. FBGs are ideal wavelength selective components for fibre lasers due to their advantages of intrinsic fibre compatibility, ease of use, and low cost fabrication. Erbium-Doped Fibre (EDF) has been developed and widely used for commercial fibre lasers and amplifiers owing to its high optical gain and low noise figure in the 1550 nm region. However, because of its relatively broad homogeneous excitation, it is difficult to obtain the stable and relatively close wavelength spacing oscillations in EDF Lasers (EDFLs) at room temperature. Various techniques have been developed to suppress the mode competition induced by the homogeneous broadening of EDF, such as cooling down EDF in liquid nitrogen [122], incorporating a frequency shifter in the cavity [123], employing a hybrid gain medium [124], and utilising spatial hole burning by inserting a multiphase shift FBG in a linear cavity fibre laser [125]. Special laser cavity configurations for multiwavelength operation by incorporating a segment of highly nonlinear photonic crystal fibre or dispersion shifted fibre have also been reported [126-128]. In the recent years, multiwavelength fibre lasers operating at room temperature utilising the Polarisation Hole Burning (PHB) effect have also been studied extensively and various setups have been demonstrated [129–131]. However, in all these reports, the PHB effect has only been studied with the Polarisation Maintaining (PM) fibre-based devices.

Based on spectral characteristics of TFGs discussed in chapter 3, this chapter will report the stable, single polarisation and multiwavelength switchable EDFL using

intracavity polarisation selective filters based on TFG devices with tilted structures at small and large angles. The proposed cavities do not contain any PM fibre based device. Depending on the angle size of the tilted structure, different TFGs are employed as an in-fibre polariser or a fibre PDL filter in the cavity. The combined effect of these TFGs induces the PHB effect in the cavity for switching the laser operating at single, double, triple and quadruple wavelengths. The proposed laser systems have demonstrated a good stability under room temperature condition and also achieved a high DOP(~30 dB), high Optical Signal to Noise Ratio (OSNR) up to 63 dB, and high Side Mode Suppression Ratio (SMSR) about 50 dB. The proposed cavities have also been investigated for their capability of the temperature and strain sensing by subjecting the seeding FBGs to the temperature and strain variations. The fibre ring laser systems have shown the good self-referencing and sensing responses to the temperature and strain variations, providing sensitivities of approximately 11.7 pm/ $^{\circ}\text{C}$ and 0.85 pm/ μe respectively.

6.2. Single Polarisation and Multiwavelength Switchable Fibre Ring Lasers Using Intracavity TFGs with structures tilted at $\geq 45^{\circ}$

We have constructed two EDF fibre ring laser systems to demonstrate single polarisation outputs with single, double, triple and quadruple wavelengths by employing a 45° -TFG as an in-fibre polariser and one/two tilted $> 45^{\circ}$ TFGs as polarisation selective filters in the cavities.

In contrast to the reported single polarisation switchable wavelength fibre lasers in which almost all the employed fibre gratings were inscribed in special fibres, like PM and multimode fibres, our proposed systems are based on all standard single mode fibres, possessing advantages of low splicing and insertion loss.

6.2.1. Dual Wavelength Oscillation Laser Cavity [P4]

The configuration of the proposed double-wavelength switchable fibre ring laser system is shown schematically in Figure 6.1. In this configuration, the gain medium is a 10 m section of a highly erbium doped fibre, which is pumped by a 1480 nm laser diode through a 1480/1550 WDM coupler. An Optical Isolator (OIS) ensures an anticlockwise ring cavity. The 10% arm of the 10/90 coupler is used as the output port of the laser. As shown in the figure, a 45°-TFG is used as an in-fibre polariser while the other large angle tilted grating, 77°-TFG, is employed as polarisation loss selective filters in the system. A PC is placed between the two TFGs to select/optimise the polarisation of the cavity. In order to achieve single and dual wavelength operation, two normal structure FBGs (G1 and G2) with a reflectivity of ~ 97% and wavelengths at 1547 nm and 1553 nm, which match the polarisation bands of the 77°-TFG, are used as two wavelength seeders incorporated in the cavity through an optical circulator. The output of the fibre laser is measured either through an OSA or a system marked in the dotted box for measurement of polarisation.

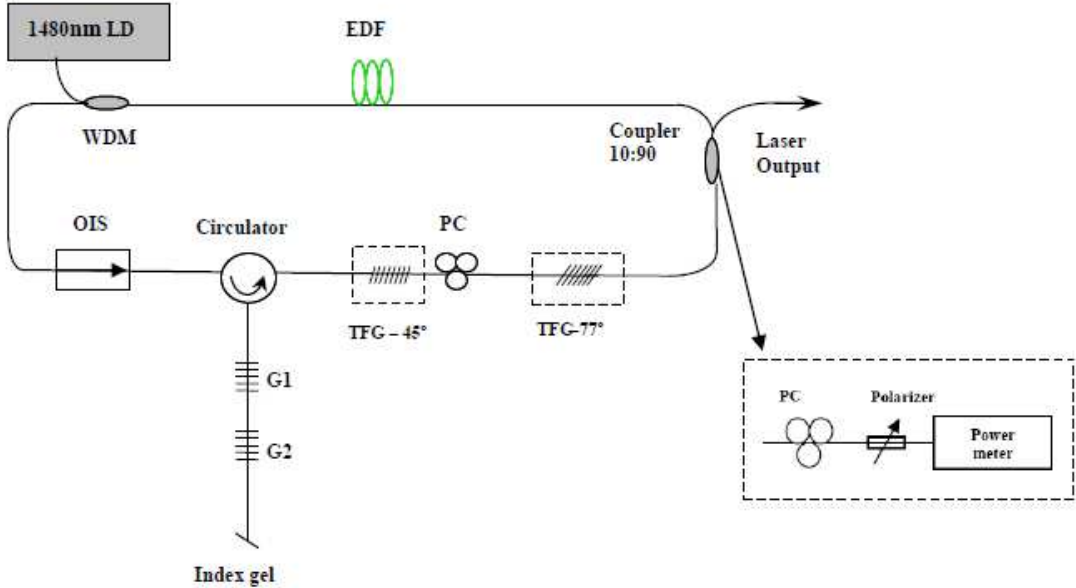


Figure 6. 1. The schematic setup of a single and dual wavelength switchable fibre laser cavity.

According to the previous work of our group [132], a TFG with structure tilted at 45° will couple S-polarised light out and leave P-polarised light transmitting in the fibre. This behavior may be explained by Brewster's law; if we consider the grating's periodic structure comprising of two layers material with slightly different refractive indices, n_1 & n_2 , the Brewster's angle (α_c) for the interface is determined by:

$\tan \alpha_c = n_1/n_2$ and due to the almost identical value of n_1 & n_2 , with the difference of less than 0.01, α_c is $\sim 45^\circ$. This unique characteristic of the 45°-TFG, provides a mechanism through which it can be implemented as an ideal in-fibre polariser. Also in the same work, it was investigated that the Polarisation Extinction Ratio (PER) increases linearly with the length of the grating but varies more significantly with the grating's strength. It was reported that a 5cm long 45°-TFG exhibits a strong PDL \sim 30 dB over nearly 80 nm bandwidth in the 1550 nm region.

In order to realise single polarisation output, the 45° -TFG was used in our fibre ring laser system as an intra-cavity polariser. The grating was inscribed in the hydrogen loaded B/Ge single mode fibre using scanning phase mask technique and a 244 nm, CW doubled frequency Ar⁺ UV laser. The period of the employed phase mask was 1800- nm. To achieve the tilted fringes at 45° in the fibre core and induce the radiation response around the 1550 nm region, the phase mask was rotated at 33.7° respecting to the fibre axis in the UV-inscription. Limited by the size of the phase mask, concatenation method was used in the fabrication to obtain a 5 cm long 45° -TFG. The 5 cm long, 45° -TFG was characterised for its PDL using the scheme illustrated in Figure 6.2.

In this measurement, light from a BBS was first polarised by a polariser prior to launching in to the 45° -TFG. A PC was also employed to change the polarisation state of the probed light in the grating. By changing the polarisation states, the maximum and minimum transmission spectra were measured, employing an OSA.

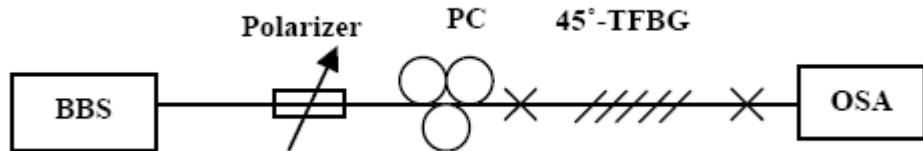


Figure 6. 2. Schematic diagram of PDL measurement of 45° -TFG.

PDL spectrum was then obtained by subtracting the minimal transmission from the maximal transmission. As the light of different wavelengths from the BBS is polarised at different degrees, the measured PDL is an average effect over the measured

wavelength range. The PDL spectrum measured using the above mentioned scheme for the 45° -TFG, is presented in Figure 6.3.

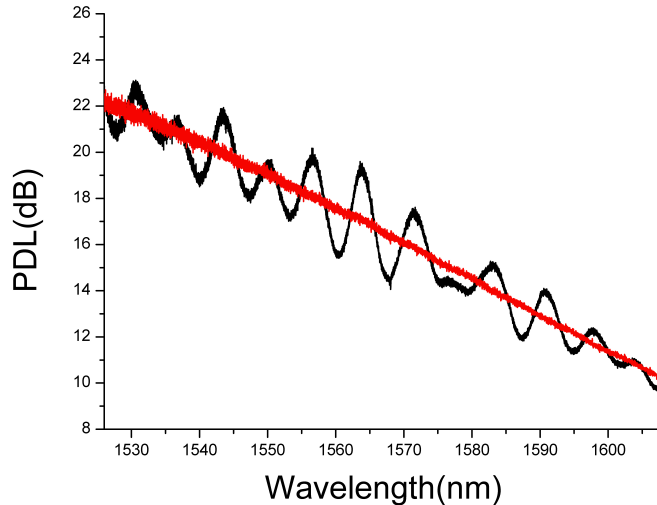


Figure 6. 3. PDL spectrum of 5cm long 45° -TFG . Note, the ripples are due to the residual reflection at the air-cladding boundary and the red line gives the spectrum when the grating immersed in index match gel.

From the Figure 6.3 one may notice that the PDL decreases from 20 dB to 10 dB with wavelength increasing from 1530 nm to 1600 nm. The ripples appeared in the black line spectrum were caused by the residual reflection at the air-cladding boundary. While the grating was immersed in index matching gel, they were disappeared and the smooth spectrum was obtained, as shown by the red line in Figure 6.3.

The large angle TFG used as PDL filter in the laser system was fabricated using the system inscription system with designed tilted angle at 77° to match the wavelengths of the two seeding FBGs in 1550 nm region. The 77° -TFG was UV-inscribed in the hydrogen loaded SMF-28 fibre using a custom-design amplitude mask with a $6.6 \mu\text{m}$ period. The mask was carefully rotated at 73° in the inscription system to obtain the desired TFG structures.

Figure 6.4 (a) depicts the transmission spectrum of the 77°-TFG measured in the wavelength region from 1200 nm to 1700 nm. From the figure we can clearly see that there is pronounced peak splitting on the spectrum and all the peaks are relatively weak giving strength around 2-3dB. This spectrum was measured using unpolarised light. When a polariser and a polarisation controller were inserted between the BBS and the TFG, either split peak was excited depending on the polarisation of the probe light. As clearly shown in Figure 6.4 (b), which gives zoomed one pair of split-peaks for the 77°-TFG, when the light was switched from the equivalent fast-axis polarisation to the equivalent slow-axis polarisation, the peak at the shorter wavelength side vanishes while the peak at the longer wavelength side grows to the maximum and vice versa. This evidently indicates that the 77°-TFG can act as a strong PDL filter and this property can be utilised to induce wavelength selective PHB effect to realise a multi-wavelength switchable function in the proposed fibre ring laser system.

As shown in Figure 6.1 a PC, placed between 45°-TFG and 77°-TFG, is employed in the system to adjust the polarisation state of the cavity. As mentioned before, two normal structure FBGs (G1, G2) were used as the wavelength selective seeding devices and fed to the ring cavity via an optical circulator. This circulator also acts as an isolator to maintain the single direction oscillation. The two FBGs were fabricated in hydrogen loaded SMF-28 fibre using standard UV-inscription and the phase mask technique. The Bragg wavelengths and reflectivities for the two FBGs were 1547 nm /2.5 dB and 1553 nm /2.2 dB, respectively. These two wavelengths were chosen to match the two polarisation loss bands of the 77°-TFG in 1550 nm region. The end of

the FBG array is terminated by index matching gel in order to eliminate the background ASE noise. It must be mentioned that all tilted and normal structure gratings were thermally annealed at 80°C for a period of 48 hours after the fabrication to stabilise their spectral properties.

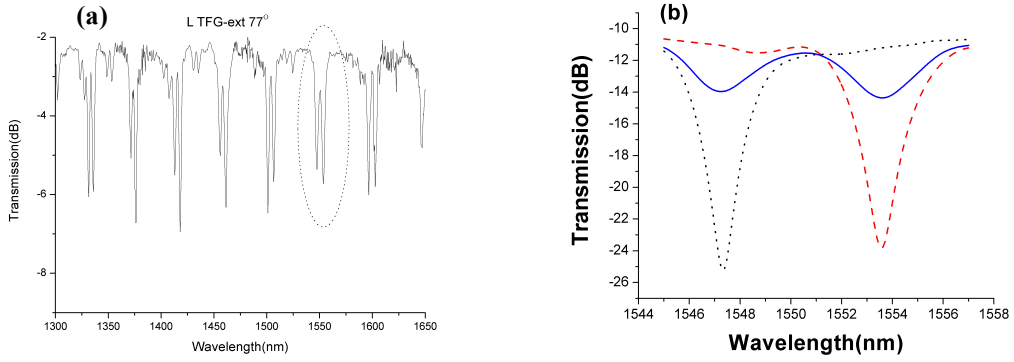


Figure 6.4. (a) Transmission spectrum of the 77°-TFG over wavelength range of 1200nm – 1700nm; (b) Zoomed spectra of one paired polarisation loss peaks of 77 ° -TFG around 1550 nm measured with randomly (solid line) and fully polarised input lights (black dotted line: fast-axis; red dotted line: slow-axis).

The operation principle of this EDL is described as follows. The intracavity 45°-TFG has a high PER, which can guarantee that the fibre ring laser will oscillate in a single-polarisation regime [90].

The 77° TFG will induce PDL to the ring cavity around its paired attenuation band region, thus imposing PHB effect to the gain medium in this region. The amplitude of the loss depends on the polarisation state of the light travelling in the 77°-TFG. By adjusting the PC to control the polarisation state of the light entering the 77°-TFG, i.e., polarised in the equivalent fast- or slow-axis of the 77° -TFG, single-polarisation and single-wavelength lasing at either 1548 nm or 1553 nm can be realised. Figures 6.5 (a, b) represent the single wavelength oscillation of the proposed laser at the mentioned wavelengths.

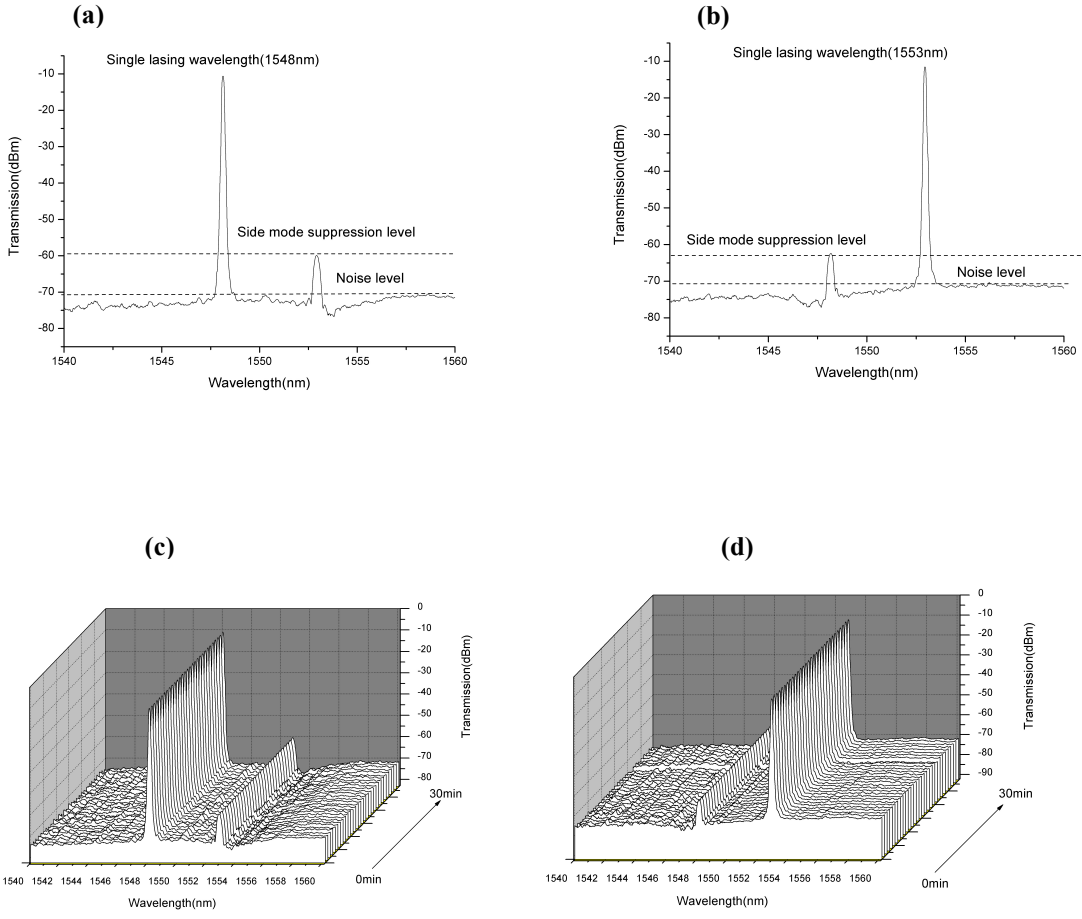


Figure 6.5. Single-wavelength lasing oscillation of the proposed fibre ring laser using 45° -TFG and 77° -TFG lasing at two the seeding wavelengths (a) 1548 nm and (b) 1553.nm; (c) and (d) show the stable laser outputs at these two wavelengths for a 30 min period.

The amplitude variations of the laser output were measured to be less than 0.5 dB within 30 mins at the laboratory conditions and the spectrum was recorded every single minute and is plotted in Figures.6.5 (c, d). From Figures 6.5 (a, b) we can see that the OSNR is more than 60 dB and the SMSR is larger than 50 dB for both laser lines. Owing to the especial functionality of the 45° -TFG and the low reflectivity of the two seeding FBGs, these two values are higher than that of the reported EDFLs [90, 133-135].

As it is depicted in Figure 6.6 (a), by changing the polarisation direction of the light launching at 45° between the equivalent fast- and slow-axis of the 77° - TFG, dual

wavelength output of two orthogonal polarisations was achieved. We have continuously monitored the dual wavelength operation of the proposed laser for 30 mins under the laboratory condition, and no noticeable changes were observed for a fixed position of PC (Figure 6.6 (b)).

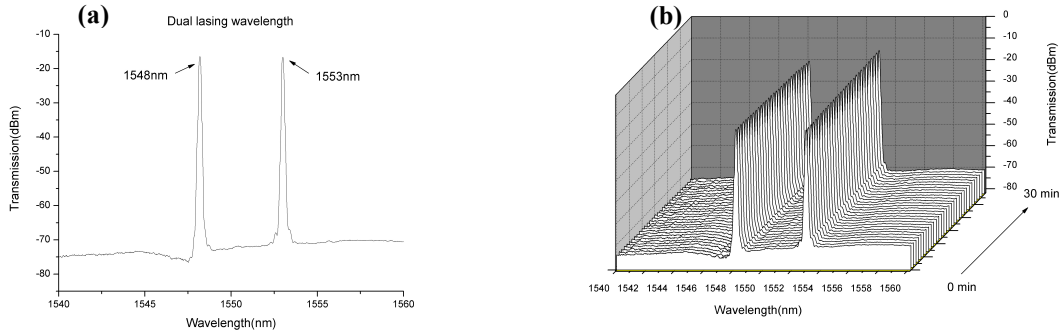


Figure 6.6. (a) Dual-wavelength lasing oscillation of the proposed fibre ring laser, (b) Stability of dual-wavelength oscillation (30 times repeated scan).

The values of signal to noise ratio for both lasing wavelength were more than 60 dB whereas the values of SMSR for 1548 nm & 1553 nm oscillations were about 47 dB & 51 dB, respectively. The line widths of both single- and dual-wavelength laser oscillations were measured to be less than 0.01 nm limited by the resolution of the available OSA (ANDO 76317B).

DOP measurement of the output of the proposed fibre laser was conducted by the setup shown in the dotted line box in Figure 6.1.

$$\text{DOP} = \text{P pol} / (\text{P pol} + \text{P unpol}) \times 100 \%$$

Where P_{pol} and P_{unpol} indicate the power of the polarised and un-polarised parts of the light respectively. Therefore, 100% DOP represents a single polarisation output.

Based on our group's previous investigation of the characteristic of a 45°-TFG as an in-fibre polariser [90] the output of the laser cavity without employing the 45°-TFG is showing the DOP value of ~ 2 dB equivalent to 22.48% in percentage term, indicating an almost unpolarised laser output. In this configuration, the DOP value of the laser output was measured similar to the PDL measurement such that by adjusting the polarisation controller, the maximum ($P_{pol} + P_{unpol}$) and the minimum ($1/2 P_{unpol}$) value of the laser output were measured. By subtracting the minimum value from the maximum value, the DOP about 35 dB was measured for the proposed ring cavity. This value corresponds to 99.94% in percentage term and clearly indicates a highly polarised output of the laser.

We have also characterised the pumping efficiency of the EDF system just for the lasing at ~ 1553 nm. For this experiment, first the output of the ring cavity was connected to an OSA, then the driven current to the 1480 nm pump diode was increased gradually. When the current was below the threshold, we only saw the ASE broadened spectrum on the OSA and, as soon as the current reached the threshold, a narrow lasing peak at ~ 1553 nm appeared on the screen of the OSA. At this point, the output terminal of the ring laser was disconnected from the OSA and attached to a power meter via a pigtail fibre. The output power of the laser for each driving current was recorded. Figure 6.7 plots the laser output against pumping current for the lasing wavelength at ~ 1553 nm. From the figure one can estimate that the apparent pumping efficiency is about $1.54 \mu\text{W}/\text{mA}$.

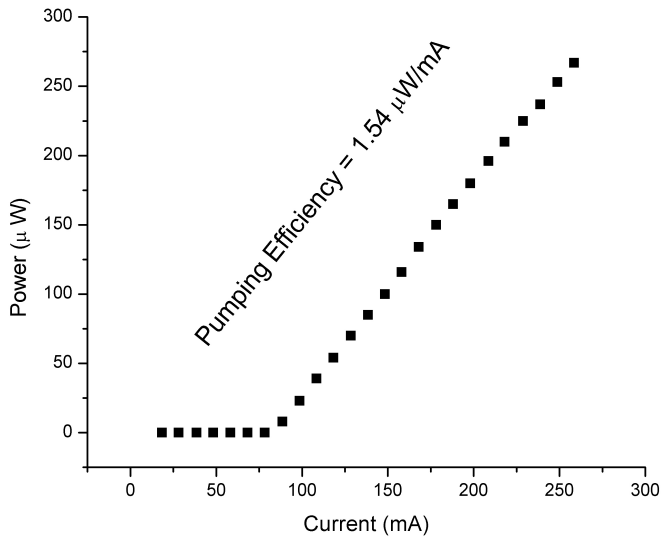


Figure 6. 7. Output power vs pump diode current for lasing at 1553 nm.

6.2.2. *Triple and Quadruple Wavelength Oscillation Laser Cavity [P3]*

In this part, the above work has been developed and modified by employing few more components in the structure of the ring laser resulting in a switchable triple and quadruple wavelength output. The schematic diagram of the proposed laser cavity is shown in Figure 6.8. As one may notice that the structure of this new cavity is different from the previous system only by employing an additional large angle TFG (79° -TFG) and one extra PC situated between 77° -TFG and 79° -TFGs. In the triple and quadruple wavelength operation, we used one and two more seeding FBGs, respectively, to match with the polarisation loss bands of 79° -TFG. Also due to the availability of the laboratory facilities at the time of this experiment, a 975 nm pump laser was used to pump the fibre laser cavity through a 980/1550 WDM. The operation principle for triple and quadruple oscillation is basically the same as what has been explained for the dual-wavelength operation in the last section; in this

system, selection of lasing wavelength is achieved by controlling the polarisation states of the light using two PCs.

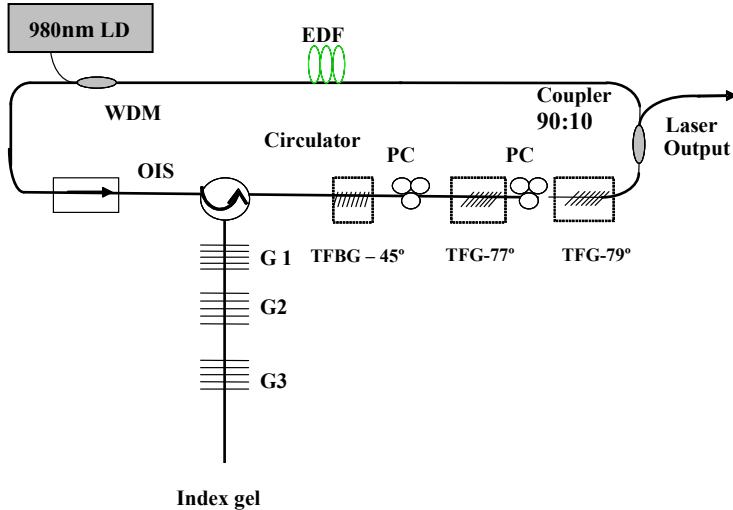


Figure 6. 8. Schematic diagram of the tripe and quadruple wavelength fibre ring laser cavity.

The 79°- TFG was also UV inscribed in the hydrogen loaded SMF-28 fibre with a paired polarisation loss peaks matching the additional seeding FBGs.

Figure 6.9 (a) presents the full transmission spectrum of 79°-TFG in the wavelength range from 1200 nm to 1700 nm. As figure shows, it also exhibits multiple split polarisation peaks. Figure 6.9 (b) shows zoomed spectra for one pair of polarisation peaks of the 79°-TFG when the grating was excited with probing light at three polarisation states (0° , 45° and 90°), showing PDL response.

In the triple wavelength experiment, three seeding FBGs (G1, G2, and G3) were coupled into the laser cavity by a circulator. The Bragg wavelengths and reflectivities of these seeding FBGs are 1547 nm/ 2.5 dB, 1553 nm/ 2.2 dB and 1563 nm/ 2.1 dB, and their wavelengths were chosen to match the two pairs of loss bands of 77°-TFG and 79°-TFG.

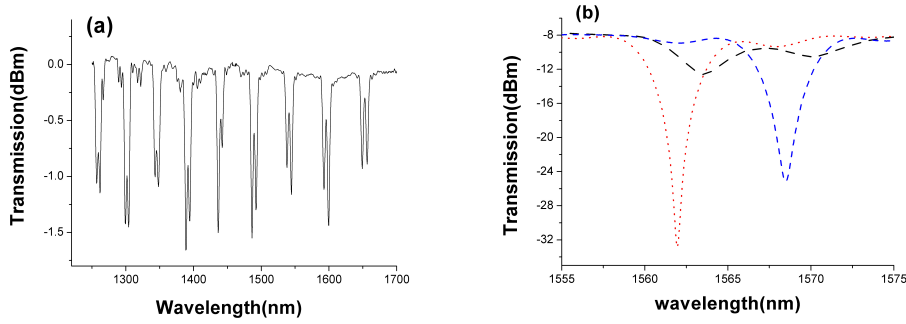


Figure 6.9. (a) Transmission spectrum of the 79° -TFG over wavelength range of 1200 nm – 1700 nm (b) Zoomed spectra of one paired polarisation loss peaks of 79° -TFG around 1550 nm measured with randomly (solid line) and fully polarised input lights (dashed lines).

By adjusting two PCs, one located between 45° -TFG and 77° -TFG and the other one between two 77° -TFG and 79° -TFG, the polarisation state of the light entering the two large angle TFGs (polarised in the equivalent fast- or slow-axis of the TFGs) can be controlled to excite different polarisation peaks at different wavelengths. Figures 6.10 (a-c) evidently demonstrate the single wavelength oscillation of the fibre ring laser at the three seeding wavelengths at 1547.05 nm, 1553.27 nm and 1563.05 nm, respectively.

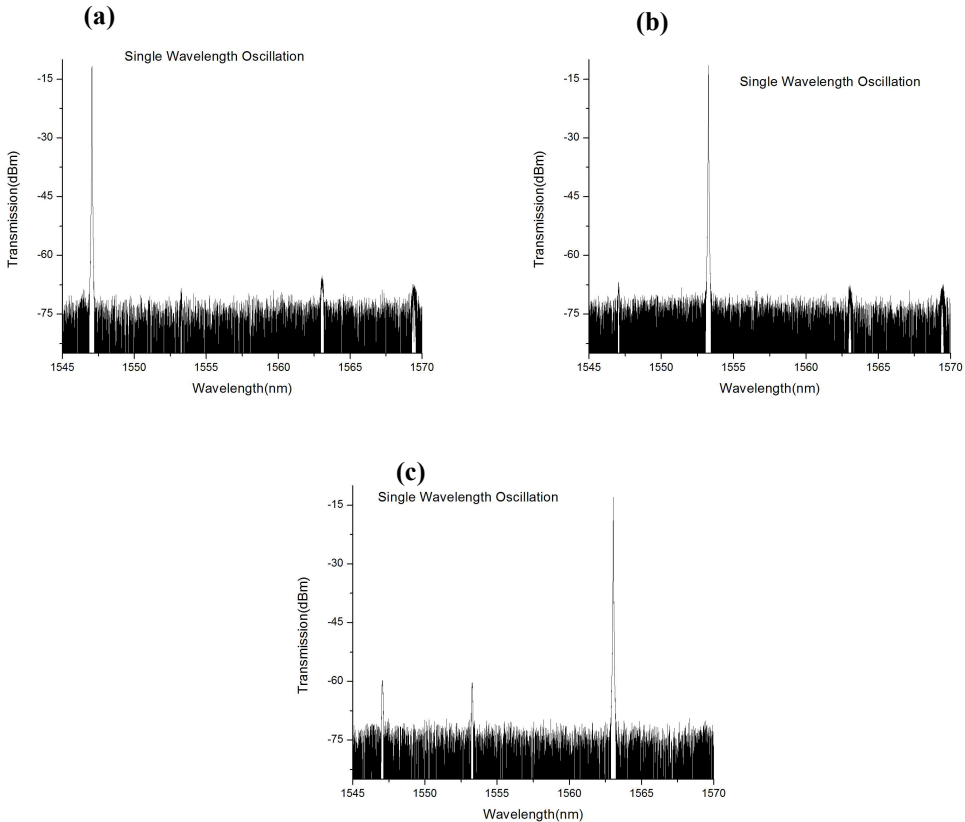


Figure 6.10. Single wavelength oscillation at (a) 1547.05 nm (b) 1553.27 nm and (c) 1563.07 nm.

Similarly, by adjusting the two PCs, dual- and triple-wavelength operation are achievable. Figures 6.11 (a-c) show three sets of dual-wavelength oscillations at 1547.06 nm /1553.27 nm, 1547.06 nm /1563.07 nm and 1553.27 nm /1563.07 nm, respectively. Figure 6.12 shows the spectrum for one triple-wavelength oscillations at 1546.94 nm / 1551.99 nm / 1562.63 nm.

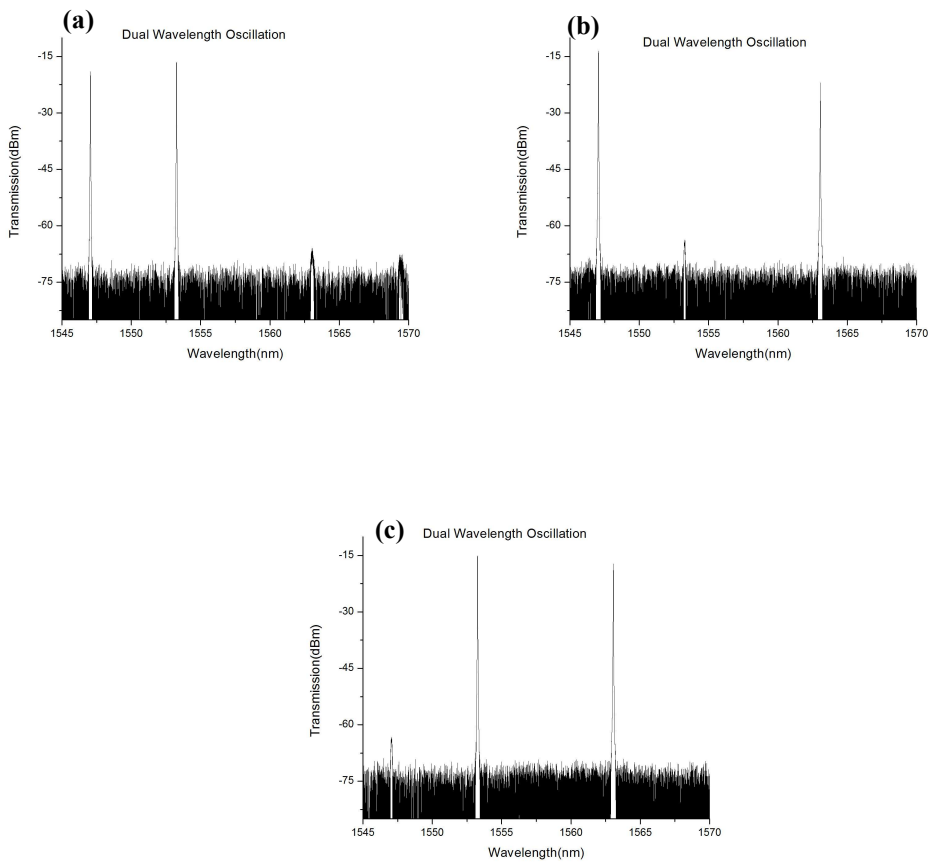


Figure 6.11. Demonstration of alternative dual wavelength lasing at (a) 1547.06 nm / 1553.27 nm (b) 1547.06 nm / 1563.07 nm and (c) 1553.27 nm / 1563.07 nm

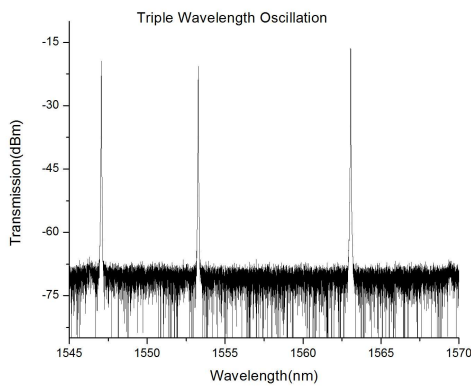


Figure 6.12. Triple wavelength oscillation for all three wavelengths.

By adding one more seeding FBG at 1569 nm/5.6 dB to match the second polarisation loss peak of 79°-TFG, we further investigated quadruple wavelength operation of the system incorporating one in-fibre polariser based on the 45°-TFG and two PDL filters

based on 77°-TFG and 79°-TFG. As 1569 nm is very close to the edge of the gain window of EDF, the seeding FBG at this wavelength was fabricated almost twice stronger than other three seeding FBGs in order to achieve the laser oscillation at 1569 nm. In fact the gain equalisation of EDF spectrum was achieved by adjusting the different reflectivity values for seeding FBGs. By adjusting the PCs to control the polarisation state of the light entering the 77°-TFG and 79°-TFG, single-wavelength lasing at either the four seeding wavelengths has been demonstrated. Figures 6.13 (a-d) evidently show the single wavelength oscillation of the fibre ring laser at the four seeding wavelengths at 1547.05 nm, 1553.27 nm, 1563.05 nm and 1568.97 nm respectively.

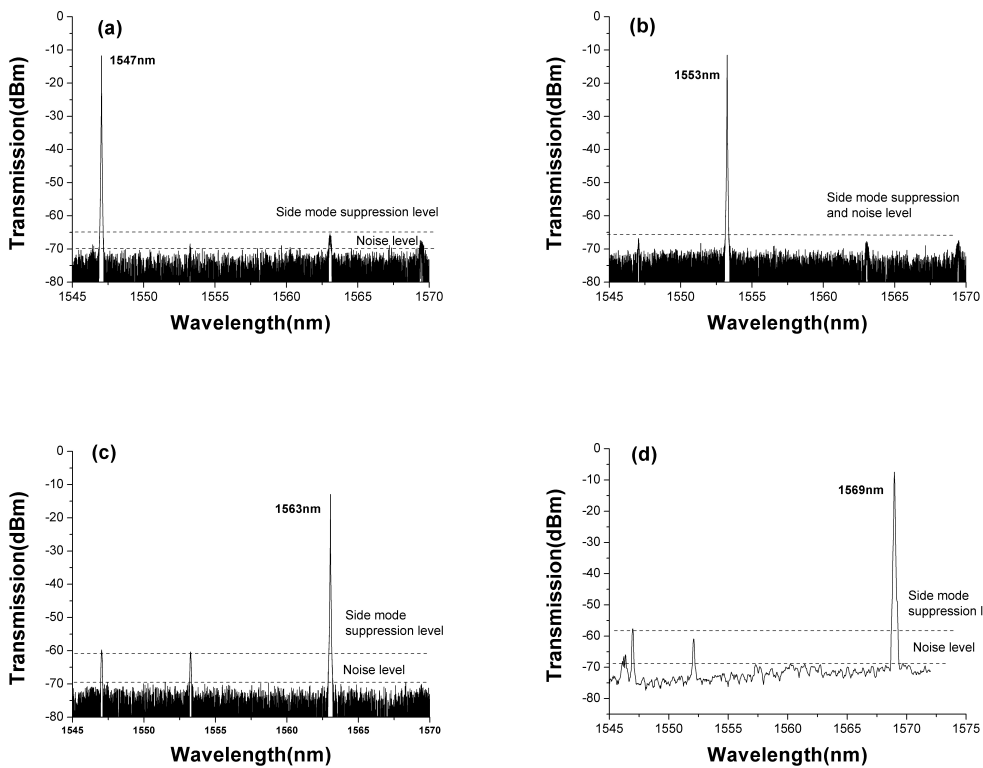


Figure 6. 13. Single wavelength lasing at (a) 1547 nm, (b) 1553 nm, (c) 1563 nm and (d) 1569 nm.

We have also investigated the pumping efficiency for the EDL system while operating at the single lasing oscillation of ~1553 nm. To ensure a systematic study

of the laser's characteristic, the same measurement of pumping efficiency was carried out for the single laser oscillation at ~ 1569 nm.

For this experiment while laser was oscillating at 1553 nm, first, the output of the ring cavity was connected to an OSA. Then the driven current to the 975 nm pump diode was gradually increased. When the current was below the threshold, we only saw the ASE broadened spectrum on the OSA and, as soon as the current reached the threshold, a narrow lasing peak at ~ 1553 nm occurring on the OSA was observed. At this point, the output terminal of the ring laser was disconnected from the OSA and attached to a power-meter via a pigtail fibre.

We then recorded the output power of the laser for each driving current. Figure 6.14 plots the laser output against pumping current for the lasing wavelength at ~ 1553 nm. From the figure that the apparent pumping efficiency is about $1.95 \mu\text{W}/\text{mA}$ is estimated. The same procedure was done for the proposed system while it was operating at 1569 nm. The result is demonstrated in Figure 6.15 and presenting a different pumping efficiency of about $3.75 \mu\text{W}/\text{mA}$ for the laser oscillation at 1569 nm. The increased value of pumping efficiency for this laser output can be explained by considering the fact that the corresponding seeding FBG at 1569 nm is almost twice stronger than the one relevant to 1553 nm oscillation of the laser output.

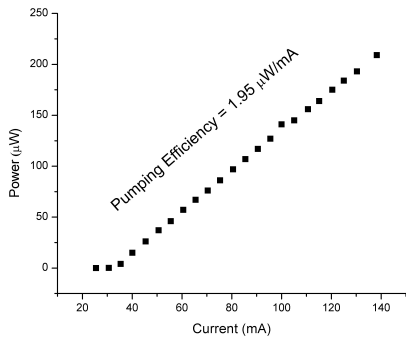


Figure 6. 14. Output power against pump diode current for lasing at 1553 nm.

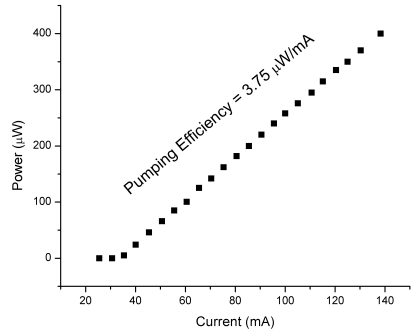


Figure 6. 15. Output power against pump diode current for lasing at 1569 nm.

The single polarisation state of the outputs for this fibre ring laser system has also been verified by connecting the laser output to a PC followed by a commercial polariser and a power-meter. The measured DOP was in the range of 30 dB (99.80%) to 35 dB (99.94%) for the lasing oscillation at four different wavelengths, indicating a very high degree of single polarisation operation of the laser system.

Similarly, by adjusting the two PCs to change the PHB profile so the laser cavity, oscillation at double, triple and quadruple wavelengths can be achieved in this system. Three sets of dual-wavelength oscillations at 1547.06 nm/1553.27 nm, 1547.06 nm/1563.07 nm and 1553.27 nm/1563.07 nm, are presented in Figures 6.16 (a-c) respectively

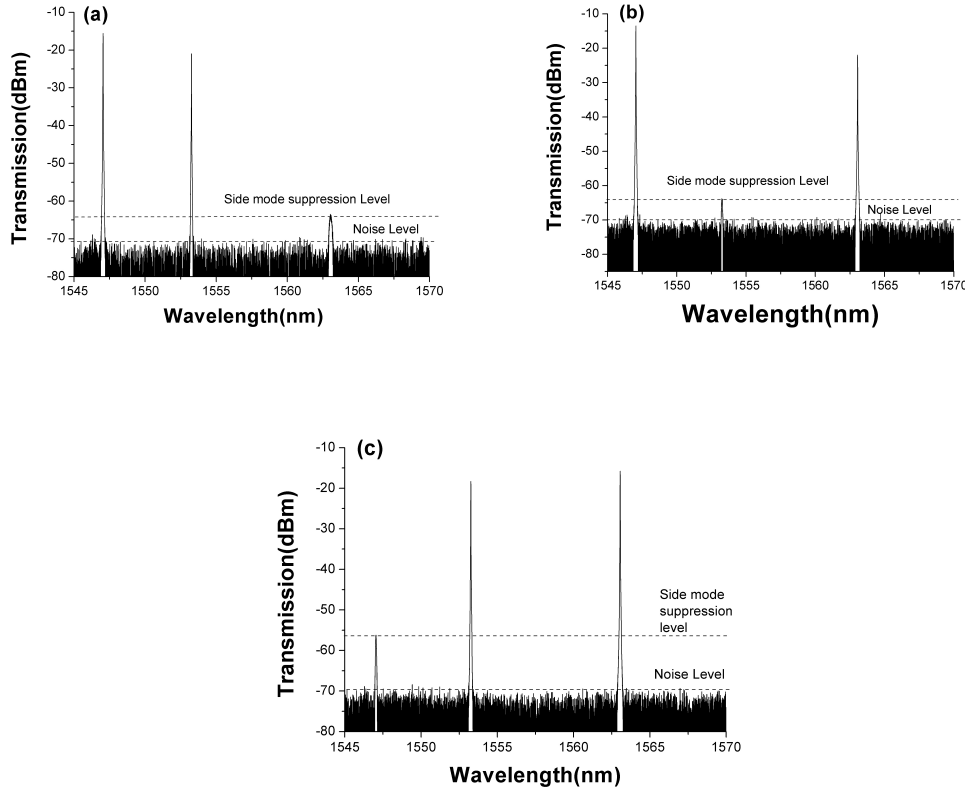


Figure 6.16. Demonstration of alternative dual-wavelength lasing at (a) 1547.06 nm/1553.27 nm (b) 1547.06 nm/1563.07 nm and (c) 1553.27nm/1563.07nm.

Figure 6.17 (a-c) show three sets of spectra for triple-wavelength oscillations at 1546.94 nm/1551.99 nm/1562.63 nm, 1546.94 nm/1551.99 nm/1568.89 nm and 1551.99 nm/1562.63 nm/1568.89 nm.

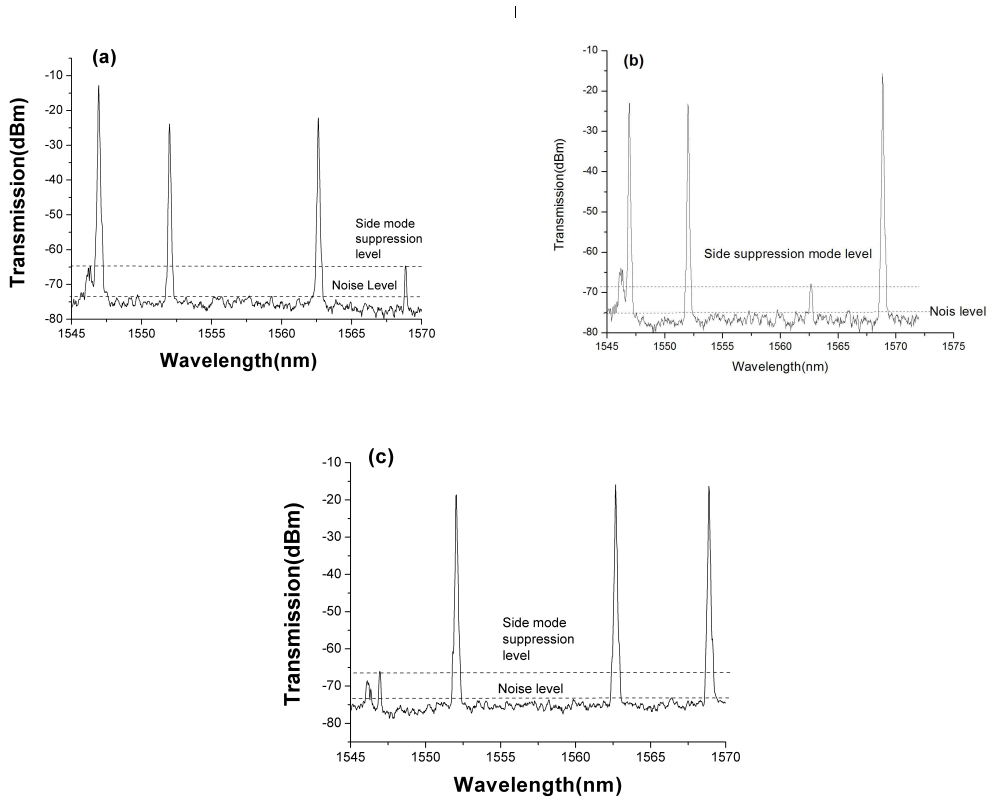


Figure 6.17. Triple wavelength oscillations at (a) 1546.94 nm/1551.99 nm/1562.63 nm (b) 1546.94 nm/1551.99 nm/1568.89 nm (c) 1551.99 nm/1562.63 nm/1568.89 nm.

By carefully adjusting two PCs the ring cavity will oscillate at quadruple lasing wavelength. Figure 6.18 indicates the spectrum for a quadruple laser oscillation at 1546.94 nm/1551.99 nm/1562.63 nm and 1568.89nm.

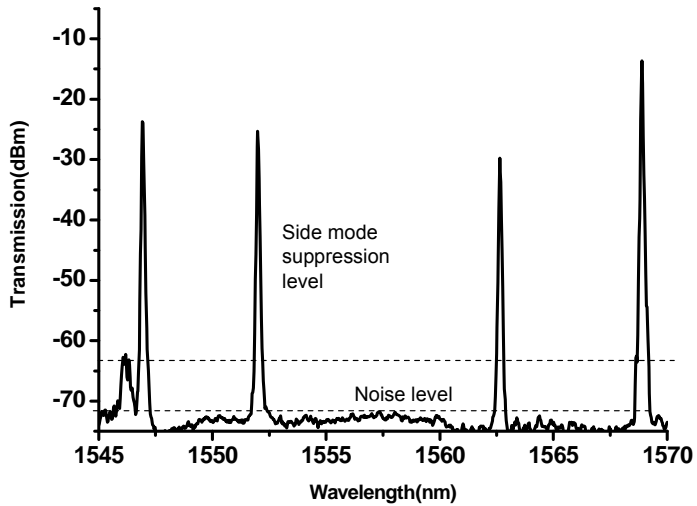


Figure 6. 18. The quadruple wavelength lasing of the proposed system.

All sets of single- and multi-wavelength lasing oscillations have been continuously monitored for 30 mins at the laboratory condition and room temperature for stability assessment. No noticeable amplitude fluctuation was observed for the laser operating at single- and multi-wavelengths when the PCs were fixed at their positions during the experiment. Figures 6.19 (a-d) are examples of the continuously monitored lasing profiles on the OSA for single and multi-wavelength lasing oscillations, showing no degrading of output amplitude.

From these figures, the output amplitude variation for all different lasing oscillation sets: single, dual, triple and quadruple were measured to be less than 0.5dB within 30 mins. The line-widths of single and multi-wavelength laser output were measured to be less than 0.01 nm. This value would be even smaller, if the employed OSA (ANDO 6317B) had a higher resolution.

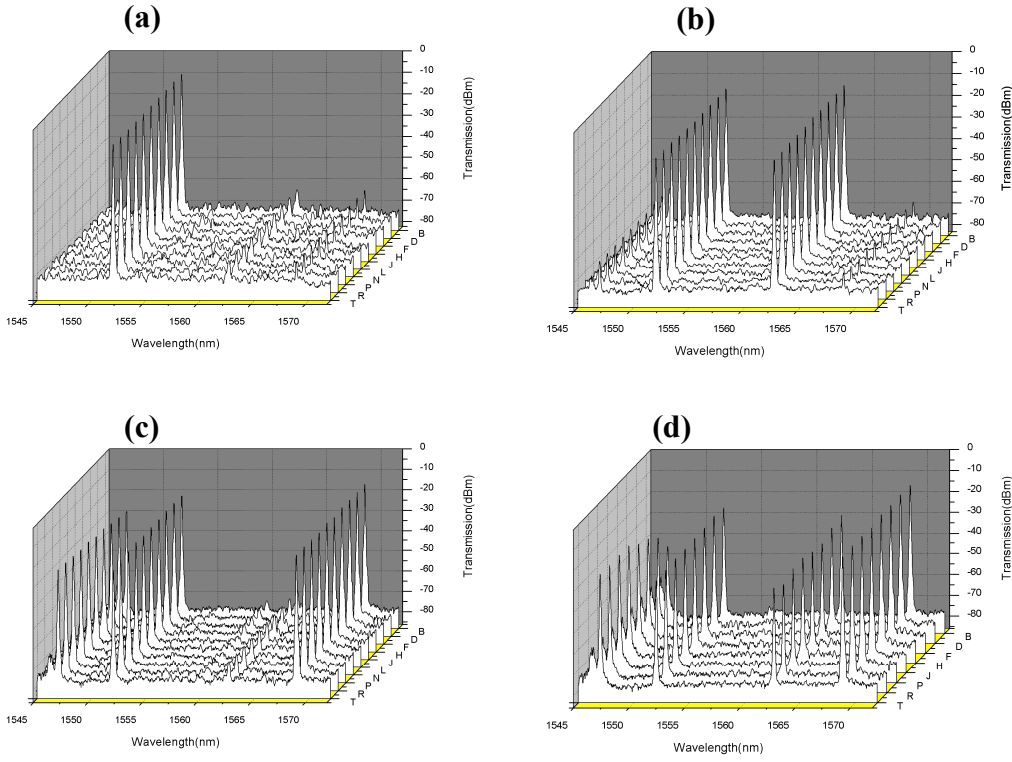


Figure 6.19. Stability measurement of (a) Single (b) Double, (c) Triple and (d) Quadruple lasing oscillations under the laboratory conditions & room temperature over 30 mins.

The measurement shows that values of OSNR for single, dual, triple and quadruple lasing wavelength in our proposed system are about 63 dB, 54 dB, 53 dB and 50 dB respectively. Also the SMSR value was more than 55 dB for single oscillation lasing wavelength and was measured to be about 50 dB, 48 dB and 40 dB for dual, triple and quadruple lasing oscillations respectively. Table 6.1 summarises these results.

Oscillation wavelength	Stability time	SMSR	OSNR
Single	30 min	55 dB	63 dB
Dual	30 min	50 dB	54 dB
Triple	30 min	48 dB	53 dB
Quadruple	30 min	40 dB	50 dB

Table 6.1. Summary of the measured technical values of the proposed TFG based fibre ring laser cavity.

6.2.3. Tuning and Sensing Capability of Proposed Laser Cavities

So far we have only demonstrated single- and multi-wavelength operations at fixed wavelengths. However, as the reflection bands of the seeding FBGs are much narrower than the loss peaks of the large angle TFGs, 77°-TFG and 79°-TFG, the proposed systems have the capability of wavelength tuning by tuning the Bragg wavelengths of the seeding gratings within the loss bands of the TFGs. If the seeding FBGs are subjected to the temperature and strain variations, their wavelengths will shift accordingly, thus the laser line can be varied. This shows the tuneability of the proposed laser system and also its capability for sensing the temperature and strain changes imposed on the seeding FBG. Because the laser line is much narrower than FBG bandwidth, the laser sensing system should be capable of measurement of much higher resolution than directly using FBGs as sensors.

Considering the above fact, sensing capability of our proposed dual and quadruple wavelength laser ring cavities were investigated for the temperature and strain sensing. To demonstrate this concept the dual wavelength laser system was made to lase at the single oscillation around 1548 nm and the seeding FBG with Bragg wavelength at 1548 nm was then heated up from 10 ° C to 90 ° C using a temperature controlled heater plate. The red shifting of the laser output was clearly observed with increasing temperature. Figure 6.20 (a) shows the temperature rising induced laser spectrum evolution while Figure 6.20 (b) indicates the laser output wavelength shift against the temperature. A temperature sensitivity of 11.6 pm/ ° C was estimated based on Figure 6.20 (b).

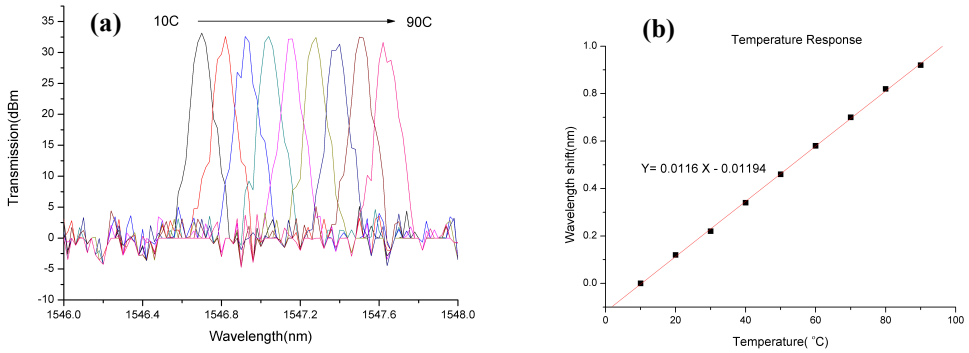


Figure 6.20. (a) Increasing temperature induced laser spectral evolution and (b) wavelength shift against temperature.

The seeding FBG was also subjected to the strain variation using a micrometer fibre stretcher. The applied strain was in a range from $0 \mu\epsilon$ to $8000 \mu\epsilon$. Figures 6.21 (a, b) present the results for the strain induced laser spectral evolution and the wavelength shift of the laser output against the applied strain, respectively. From the plot in Figure 6.21 (b), the strain sensitivity of the device is estimated to be about $0.9 \text{ pm}/\mu\epsilon$.

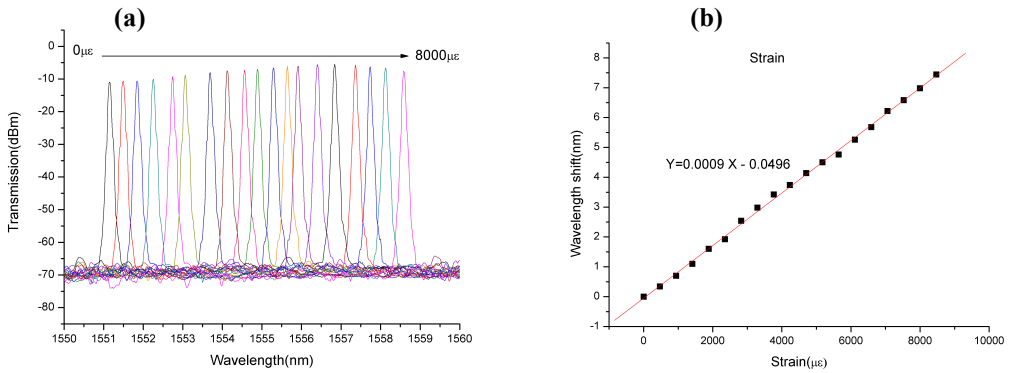


Figure 6.21. (a) Strain induced laser spectral evolution and (b) wavelength shift against strain.

A similar experimental procedure was made for the quadruple wavelength ring laser cavity. The system was made lasing at single wavelength at 1562.27 nm and the seeding FBG with central wavelength at about 1562 nm was subjected to rising temperatures from 0° C to 102° C using a temperature controlled heater and we

clearly observed that the output of the fibre ring laser system shifted towards the longer wavelength side. Figure 6.22 (a) shows the temperature rising induced laser spectrum evolution and Figure 6.22 (b) plots the laser output wavelength shift against the temperature.

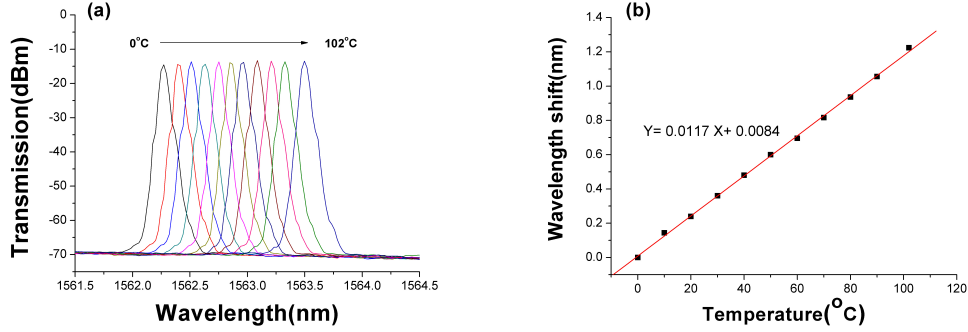


Figure 6.22. (a) Increasing temperature induced laser spectral evolution and (b) wavelength shift against temperature.

From Figure 6.22 (b) the temperature sensitivity of $11.7 \text{ pm/}^{\circ}\text{C}$ was estimated. This value is pretty similar to the temperature sensitivity of the dual wavelength ring laser cavity and also to the typical temperature sensitivity of FBG in this wavelength range.

The selected seeding FBG was also subjected to the strain variations using a micrometer fibre stretcher. The strain applied to the seeding grating was from $0 \mu\epsilon$ to $2324 \mu\epsilon$. Figures 6.23 (a, b) give the results for the strain induced laser spectral evolution and the wavelength shift against the applied strain, respectively. From the slope of the plot in Figure 6.23 (b), we estimate the strain sensitivity of $0.85 \text{ pm}/\mu\text{m}$ for the system.

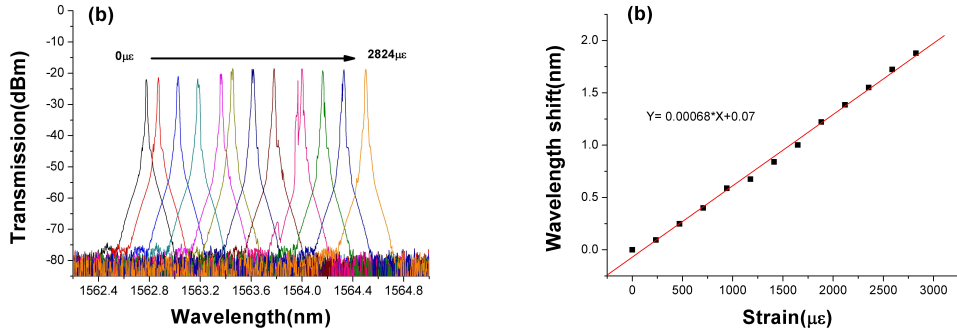


Figure 6.23. (a) Strain induced laser spectral evolution and (b) wavelength shift against strain.

6.3. Single Polarisation Fibre Ring Laser Using TFGs with small tilted structure [P1, P11]

In this section, we demonstrate an optical fibre laser capable of emitting highly polarised light by using a slightly tilted (only by 9.3°) fibre grating structure as the intra-cavity polariser. In comparison with the laser system using 45°-TFG, this configuration benefits from high efficiency, simple structure, and easy and low cost fabrication process.

6.3.1. *Polarisation characteristics of 9.3°-TFG*

The non-isotropic nature of the optical fibre and the environmental perturbations enable the SMF-28 fibre to support two different polarisation modes. As optical signals propagate through the fibre, their states of polarisation will evolve rapidly as one polarisation mode couples into the other. Depending on their tilting angles, TFGs can be employed for the light coupling from the guided modes into the radiation modes which are polarisation sensitive.

By optimising the TFG structure for a desired phase matching condition, the resonance of the radiation mode profile can cover the erbium fibre gain window (1500

nm-1580 nm). Because the mode coupling efficiency depends on the polarisation, TFGs with small tilted structures also exhibit significant PDL which may be used to discriminate lights with different polarisation states. Although the P-polarised light in small angle TFG will suffer larger loss in comparison with 45°-TFG, it should provide partial polariser function which may be utilised to realise single polarisation output for a fibre laser system. For this experiment, a small angle TFG was UV inscribed in H₂ loaded B/Ge fibre using scanning phase mask technique and 244 nm CW frequency doubled Ar+ laser. For the fabrication of this TFG, a phase mask with a pitch of 1083 nm was rotated about 6.5° respecting to the fibre axis to produce a tilted structure of the grating at ~9.3° in the fibre core. This 9.3°-TFG gives a broad radiation spectrum centred around 1535 nm. The transmission spectra of this fabricated 9.3°-TFG are shown in Figure 6.24 and one may see the microscope image of the TFG from the inset in this figure.

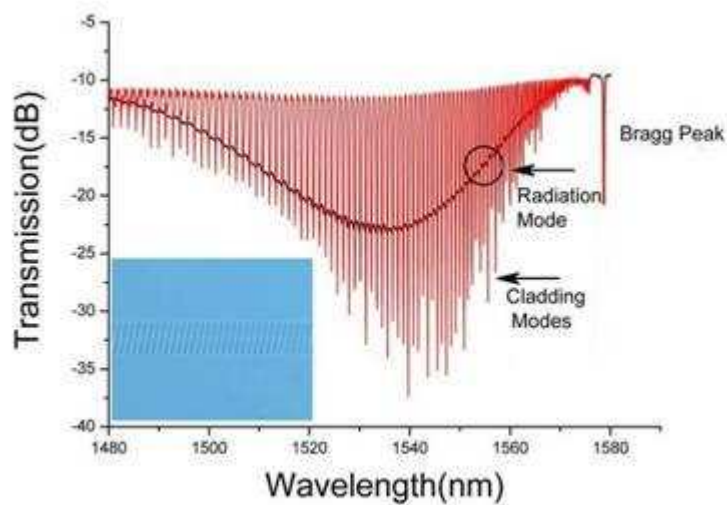


Figure 6. 24. The transmission spectra of the 9.3°-TFG in air (multi-resonance) and immersed in index matching gel (solid line) and the inset shows the microscope image of 9.3°-TFG.

The multi-resonance profile in Figure 6.24 is the coupling of core mode to the backward propagating cladding modes, observed when the grating was measured in

air, while the smooth profile is the coupling to the radiation modes obtained when the grating was immersed in the index matching gel. Furthermore, the 9.3° -TFG was characterised for its PDL value by employing a polariser and a PC between the BBS and the TFG itself, a similar setup as shown in Figure 6.2.

By adjusting the PC, we induced the variations in the polarisation status of the launching light and the PDL of the 9.3° -TFG for two orthogonally polarised lights (P_1 and P_2) were measured. As it presents in Figures 6.25 and 6.26 (a-c), a maximum value of PDL difference of ~ 10 dB can be achieved in the range of 1480 nm - 1560 nm for this 9.3° -TFG.

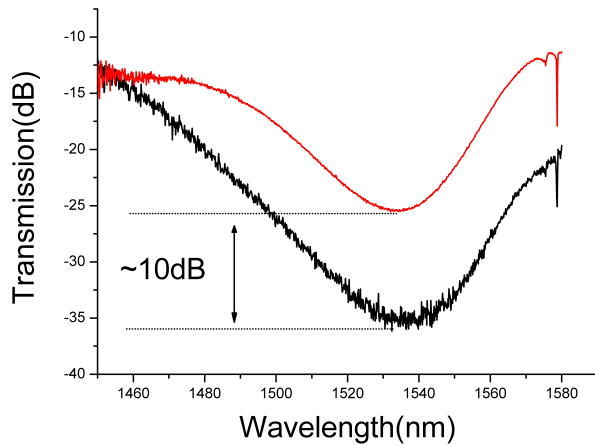


Figure 6. 25. PDL measurement for the 9.3° TFG while it was immersed in the index matching gel.

We also examined the PDL response of this grating in a much broader wavelength range. Figures 6.26 (a-c) show the PDL profiles (maximum and minimum for two different polarisations) when the grating was surrounded by air for zoomed short (1483 nm-1488 nm), medium (1537 nm-1543 nm) and long (1557 nm-1563 nm) wavelength ranges. Although the PDL profiles are in multi-peak form, the PDL value (difference between maximum and minimum) is all about 10 dB, which agrees well with the measurement performed when the grating was immersed in index gel.

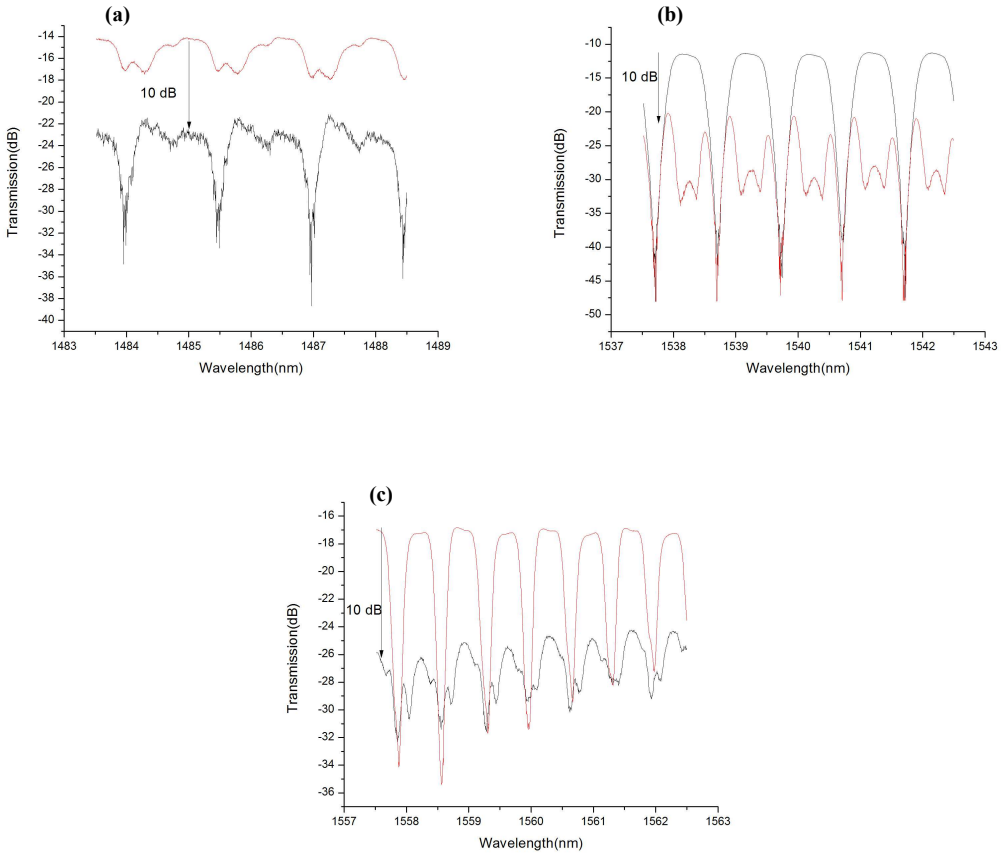


Figure 6.26. PDL measurement for the 9.3° -TFG while it was surrounded by air in (a) short-wavelength range, (b) medium wavelength range and (c) long wavelength range.

It is worth to notice that, although this 9.3° -TFG will provide a significantly high PER, there is still ~ 12 dB radiation (or transmission) loss for P-polarised light (P_1), whereas this loss for P-light is almost zero in a 45° -TFG structure [136].

6.3.2. Single polarisation output of fibre ring laser by using 9.3° -TFG

The 9.3° -TFG was inserted into a ring laser cavity similar to the previous experiments using large angle TFGs. The cavity contains a 10 m section of EDF, one OIS, one 1480/1550 nm WDM to pump the ring laser with a 1480 nm diode and a 30:70 coupler for the laser output. A FBG with Bragg reflection at 1535 nm was fed to the

cavity via a circulator as a seeding component to force the system lasing at 1535 nm.

The schematic diagram of the proposed system is shown in Figure 6.27.

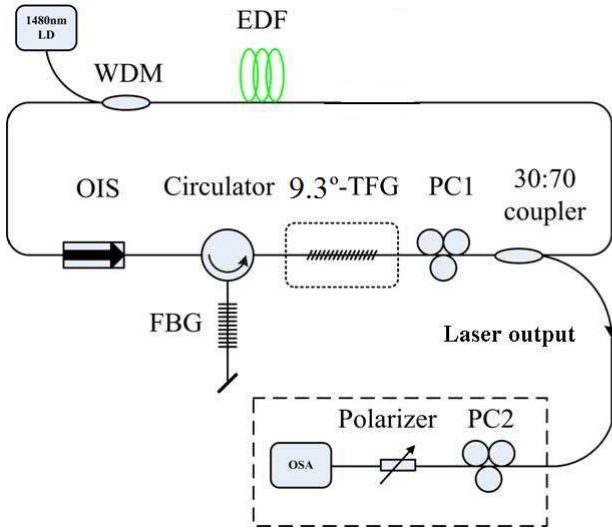


Figure 6. 27. Schematic diagram of the single polarisation fibre ring laser system.

By increasing the pump diode current to a threshold 80.5 mA, we started to see the lasing output on an OSA. In order to evaluate the polarisation state of the laser output, the maximum and minimum output on the OSA without incorporating 9.3°-TFG into the cavity was first examined using the setup shown in dotted box in Figure 6.27. The result showed the PER of only about 2 dB for the ring cavity indicating a randomly polarised output of the system.

We then inserted the 9.3°-TFG into the cavity and performed the same measurement. As shown in Figure 6.28 a PER value of 31.62 dB was achieved from such a laser system. This value indicates that the laser output is almost in single polarisation state, which gives an apparent DOP in percentage term as high as 99.86%.

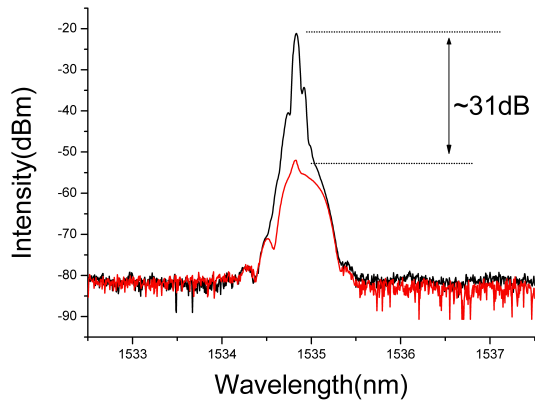


Figure 6. 28. Measured PER of the laser output oscillation at 1535 nm.

Similar to the previous investigation on different ring laser cavities which have been mentioned in this chapter, the pumping efficiency for this system was also investigated while it was operating at the single lasing oscillation at \sim 1535 nm.

For this experiment while laser was oscillating, the output of the ring cavity was connected to an OSA. Then the driven current to the 1480 nm pump diode was gradually increased.

For the current below the threshold level, only the ASE broadened spectrum was observed on the OSA and, as soon as the current reached the threshold, a narrow lasing peak at \sim 1535 nm occurring on the OSA was seen. At this point, the output terminal of the ring laser was disconnected from the OSA and attached to a power-meter so the output power of the laser for each driving current was recorded. Figure 6.29 plots the laser output against pumping current for the lasing wavelength at \sim 1535 nm.

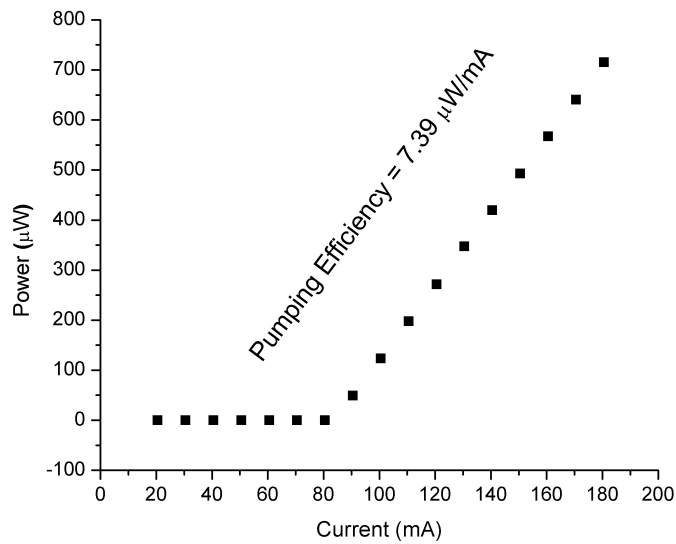


Figure 6. 29. Pumping efficiency of the proposed ring laser cavity.

From the figure we can estimate that the apparent pumping efficiency is $7.39 \mu\text{W}/\text{mA}$. This value is almost 7 times bigger than the pumping efficiency of the cavities based on large angle TFGs using the same laser diode, indicating higher efficiency of this system. The higher pumping efficiency may be explained based on the fact that in this system, the cavity contains fewer components so will benefit from less insertion and splicing loss comparing with the earlier discussed ring cavities.

The stability of the proposed system was also measured under lab condition and at room temperature for 30 mins. As shown in Figure 6.30 the single polarisation laser output was very stable as there was almost no noticed drop or changes over this examining period.

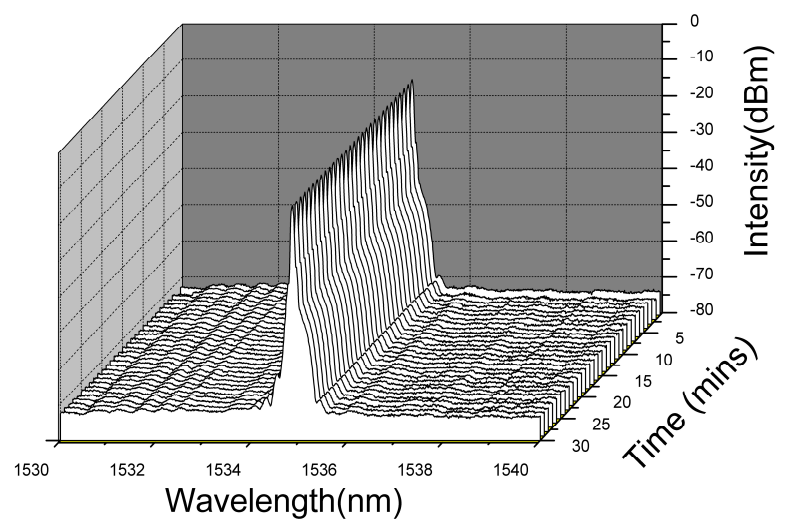


Figure 6. 30. Stability measurement of the single polarised laser output.

6.4. Chapter Conclusion

In this chapter, several novel techniques in realisation of single polarisation output switchable at single and multi wavelengths by using small, 45° and large TFGs as intra-cavity polariser and PDL filters are presented.

The proposed and demonstrated laser systems were all made of single mode fibre so benefit from advantages of low splicing and insertion loss and due to the same reason they can be considered as low cost systems comparing with the other reported single polarisation ring lasers in which special types of fibre, like PM and multimode fibres, are used to maintain the single polarisation operation.

The key fact of enabling single polarisation and wavelength switchable is the utilisation of unique polarisation properties of TFGs. We have demonstrated that a 45° -TFG can act as an ideal in-fibre polariser with PER as high as 30 dB and it does not impose any loss to the P-polarised light. A small angle TFG, 9.3° -TFG, can also provide some DOP function. In our case, it preformed a 10 dB PER. However, in comparison with 45° -TFGs, the small angle TFGs will also induce significant transmission loss to the P-polarised light. Both 45° -TFG and 9.3° -TFG have been inserted into the fibre laser cavities as an intra-cavity polariser, resulting in single polarisation output with DOPs as high as 30 dB (>99% in percentage term). The single and multi wavelength switchable function was realised by further incorporating TFGs with large tilted structures as PDL filters. When one such a grating, 77° -TFG, was used, single- and dual-wavelength operations were demonstrated. By inserting another large angle TFG, 79° -TFG, which provides two more polarisation loss peaks

at longer wavelength side, single, dual, triple and quadruple wavelength operations were demonstrated, showing impressive and versatile function. All single and multi wavelength outputs were monitored for stability at laboratory condition and no noticeable fluctuation was detected.

Furthermore to evaluate the functionality of TFG based fibre laser systems, we investigated their tuning and sensing capability. As the seeding FBGs have narrower reflection peaks than the loss bands of TFG PDL filter, as we demonstrated, each operation wavelength can be tuned within the bandwidth of the TFG loss band. The system can also be used as sensing system as the laser output shifts with the temperature/strain induced wavelength change of the seeding grating. In comparison with the case of directly using FBG as sensor, the laser detection system should give high resolution measurement.

Chapter 7

Conclusions and Future Works

7.1. Conclusions

This thesis was started with the review of the historical prospective of the photosensitivity mechanisms in optical fibres and a brief discussion on the reported photosensitisation techniques. An overview of mode coupling theory and phase match conditions for fibre gratings of different structures was also included in this study.

The thesis has performed a systematic investigation on design, fabrication and characterisation of novel structure fibre grating devices including chirped, type I, type IA, TFGs, TCFGs, MCFBGs and microslot FBG in different types of fibre, and their applications in optical sensing and laser systems.

Three UV inscription techniques – two-beam holographic, scanning phase mask and blank beam exposure phase mask scanning- and fs assisted chemical etching fabrication technique have been employed to write the advanced grating devices and sensitise their property to a wide range of physical and chemical measurands, including strain, temperature, bending and RI.

The two-beam holographic method was introduced as a low-cost and flexible inscription system permitting grating fabrication with arbitrary wavelengths. Several FBGs with central wavelengths in the range of 1400 nm have been fabricated using the two-beam holographic method for telecommunication applications, which were supplied to internal collaboration projects. The scanning phase mask technique has been employed to produce the majority of high quality and complex grating structures in this thesis. The most significant novel and complex grating devices fabricated by this technique are the tilted structured normal and chirped FBGs. The tilted structures from a few degrees up to 81° have been realised with distinctive spectral properties, which have been utilised to realise in-fibre polarisers and PDL filters in the body of different fibre laser ring cavities. The blank beam exposure phase mask scanning

method, in which a section of highly hydrogenated fibre is pre-exposed to UV radiation, has been proposed as an ideal inscription technique to fabricate type IA gratings in different types of fibre. The technique benefits from achieving uniform high quality gratings with the least demand for highly stable apparatus over the prolonged exposure. This thesis has presented the detailed fabrication and characterisation process of type I-IA gratings formed in three different types of optical fibre - PS 1250/1500, B/Ge and SM 1500. A strong OH absorption band at 1400 nm region, which forms simultaneously with IA gratings, was shown for all three fibre types. The presented different strengths of absorption profiles for the three fibres indicated that the final shape is a combination effect of the fibre core dopants and the existing hydrogen level in the fibre. Thermal characteristics of the sensor comprising a standard Type I grating fabricated directly adjacent to a Type IA grating show a lower temperature coefficient by 1 pm/°C. Novel work was presented by investigation of the hydrogen diffusion effect in different samples; the experimental data show a larger wavelength shift for Type I than Type IA grating written in the same fibre and kept under the same conditions over the same period of time.

The in-fibre nature and high sensitivity of fibre grating devices make them as attractive and ideal optical sensors for structure health monitoring applications in airspace, maritime, civil and transportation engineering research. Part of this thesis has presented the first time embedding of FBG arrays in Al matrix alloy composite by ultrasonic consolidation technique. These samples have been investigated for their thermal, loading and bending responses. The obtained results have clearly demonstrated the self-sensing capability of the embedded FBGs which would be

beneficial to a range of applications such as monitoring the operation and health condition of engineering structures.

Another particular interest is to employ FBGs as bio/chemical sensors while chemical composition variations in the surrounding medium will result in the Bragg wavelength shift. However, since to measure small changes in chemical/biological solution, it is necessary for the optical mode to penetrate evanescently into the surrounding medium solution, but the normal FBGs are intrinsically insensitive to RI measurement due to the mode coupling between well bounded core modes in this class of gratings. As a solution, novel work has been demonstrated to sensitising fibre gratings by inducing microstructure. Fabrication of different size MCFBGs and a liquid core microslot-FBG employing the fs inscription aided chemical etching technique has been implemented. Characterisation of the proposed microstructured fibre grating devices presented not only the enhanced RI sensitivity but also the feasibility of simultaneous RI and temperature measurements. As such devices exhibited a better mechanical strength than other reported approaches; they represent a more ideal structure for implementation of in-fiber bio-chemical sensors.

Among all discussed grating devices in this thesis, those with tilted structures (TFGs and TCFGs) are counted as the most complicated elements which needed to be carefully studied. The experimental investigation on the structures, inscription methods and spectral, PDL and thermal characteristics of small angel TCFGs and TFGs with small, large and 45° tilted structures were demonstrated in this thesis. The phase matching conditions and associated coupling regimes for TFGs in single mode fibres were also examined.

Corresponding to the size of the tilt angles, three mode coupling regimes – backward cladding mode coupling, radiation out coupling and forward cladding mode coupling – have been clearly identified. The comparative investigation of UV written TFGs and TCFGs with small tilt angles (up to 10°) was proposed utilising phase mask fabrication technique and hydrogen loaded single mode optical fibres. Spectral, thermal and polarisation properties of these gratings were systematically characterised and exhibited.

We have developed and discovered novel applications for TFGs in realisation of single polarisation laser output operating with switchable single and multi wavelengths in which the combination of small-, 45° and large- angle TFGs as intra-cavity polariser and PDL filters was employed.

It has been experimentally performed that due to the unique polarisation property, 45°-TFG can perform as an ideal in-fibre polariser with PER value as high as 30 dB. The experimental data also showed the PER value of 10 dB for a 9.3°-TFG indicating the capability of providing polariser function to some extent. Both, 45°- and 9.3°-TFGs were employed as in-fibre polariser in the body of a ring laser cavity leading to a single polarisation laser output. It has been exhibited that further incorporation of large angle TFGs as PDL filters in the ring laser cavity results in realisation of the single and multi wavelength switchable function.

The functionality of TFG based fibre laser systems has further evaluated in terms of the stability, tuning and sensing feasibilities. There was no major fluctuation noticed for single- and multi-wavelength laser operations at laboratory condition over the period of 30 mins. Also owing to the relatively narrow reflection peak of seeding FBGs, it has been exhibited that each operation wavelength can be tuned within the bandwidth of the loss bands of TFG PDL filter. Hence by subjecting the seeding

FBGs to the external changes such as temperature or strain, the laser output wavelength can be shifted and tuned.

7.2. Suggestion For Future Research

7.2.1. Further Investigation On Small Angle TCFGs

7.2.1.1. Small Angle TCFGs For Strain and RI Sensing

There is a wide range of reports in which FBG based sensors have been used for temperature, strain and micro-bending measurements. Regardless of numerous advantages of FBGs over traditional optical sensors, temperature cross sensitivity error is a major issue when temperature and strain simultaneously affect an FBG.

As it was discussed in section 3.4.3, TCFGs follow similar coupling mechanism to TFGs and the mode coupling occurs between the core and the radiation mode field in a contra-propagating direction. If the tilt angle is small enough, the light will be coupled in to both backward core and cladding modes and one can see both Bragg peak and radiation resonance profile in the transmission spectrum of TCFGs. It is predicted that the radiation resonances are sensitive to the external perturbations. This can introduce a solution for temperature cross sensitivity problem as when the Bragg resonance is only sensitive to axial strain and temperature and the cladding mode resonances are sensitive to the external perturbations such as strain, temperature, bending, and RI measurands [139, 140].

7.2.1.2. Single Polarisation Fibre Ring Laser Based on Small Angle TCFGs

Referring to section 3.4.4, TCFGs with the external tilt angles $\geq 6^\circ$ are polarisation dependent. Our experimental investigation indicates the higher PDL value for small angle TCFGs than TFGs with the same tilt angle. Also, stronger PDL is associated with grating having fringes more tilted. So it might be worth to investigate the characteristics of TCFGs with larger tilt angles.

Similar to what has performed in section 6.3 employing small angle TFG, it might be possible to incorporate the small angle TCFG as in fibre polariser into the body of the laser ring cavity. Due to the relatively higher PDL value of TCFGs, a bigger DOP is predicted to be achieved for the laser output in such a configuration.

7.2.1.3. Small Angle TCFG Based Side Detection Spectrometer

TFGs are capable of coupling the light out of fibre core and based on this feasibility, small angle TFGs have been employed to realise the side detection spectrometers in several approaches [141]. In such an application, the detection dynamic range is limited to the radiation profile of TFGs and also the fibre should be immersed in index matching gel to achieve a smooth profile and tap the light out of the fibre. In the case of small angle TCFGs, as it was explained in chapter 3, the loss peaks induced from the radiation mode out-coupling for different wavelengths are spectrally superimposed, resulting in one broad and almost smooth transmission loss peak and this radiation loss band becomes even broader with increasing tilt angle. This broad radiation profile can provide the spectrometer a wider detection dynamic range and also as there is no need for gel immersion of the grating, so the proposed TCFG based spectrometer would benefit from a simpler and compact configuration.

7.2.2. Modified FBG Based Devices By Femtosecond Assisted Chemical Etching Technique

7.2.2.1. Microslot Fabry Perot Cavity For RI Sensing

Following our discussion in chapter 5 regarding the recent scientific attentions on the advanced micro-photonic structures employed for modern biomedical, chemistry and sensing applications and also the importance of the RI measurements, our proposed microstructuring technique based on fs laser inscription aided chemical etching has a huge potential for further development. As an example, in-fibre Fabry Perot cavity can be simply formed by employing a pair of FBGs with different wavelengths which are written in the same piece of fibre and slightly apart from each other. The created Fabry Perot resonances are intrinsically insensitive to RI of surrounding medium as the light is only confined in the core and there is no interaction between the evanescent field with the surrounding medium. Inducing a small microslot in the Fabry Perot cavity may help these resonances to access to the RI solution making the proposed device a desirable and robust candidate for RI sensing in a range of applications. A systematic study including fabrication and characterisation of such devices having different size microslot is worth to be explored in future.

7.2.2.2. Temperature-Strain Duality FBG Sensor

As it was discussed in 7.2.1.1, the spectral response of FBGs to strain and temperature are usually mixed, and this cross-sensitivity error is a certain technical concern demanding for practical solutions. A range of solutions have been reported in which FBGs with different characteristics were employed to offer different ratios of the

strain/temperature responses of each FBG [142, 143], but these ratio differences are generally low, providing a poor discrimination resolution. LPGs are another solution as they are highly sensitive to temperature but not to strain [144], however their relatively large size makes them unsuitable for situations where miniature device is desirable.

Also FBGs written in polymer optical fibres present a large thermal sensitivity [145]. Recently, Zhou *et.al* [146] have combined the FBGs in polymer and silica fibers for stain sensing with temperature discrimination capability by a large ratio. That work can be further developed by making few samples of pair-FBGs in the same fibre and inducing microchannels of different sizes in one of the grating using the proposed fs inscription and chemical etching technique. The microchannel then will be filled with polymer showing much higher temperature sensitivity than the normal FBG but still with similar strain response. So, the normal FBG can be used as a temperature reference sensor and such devices can provide a high resolution distinguish between temperature and strain sensing responses. A comparative investigation on such samples made of different size microchannels sizes and filled with various types of polymer is suggested to achieve the optimum results.

Chapter 8

Publications & References

8.1. Publications:

- P1. **P. Saffari**, C. Mou, L. Zhang and I. Bennion “Single polarisation output of erbium-doped fibre ring laser utilising a small tilted fibre grating structure,” *international conference on Bragg Gratings Photosensitivity and Poling in Glass Waveguides (BGPP 2010)*, Karlsruhe, Germany, 21-24 June 2010.
- P2. **P. Saffari**, H. Fu, K. Zhou, L. Zhang and I. Bennion, “Microchanneled Chirped Fibre Bragg Grating For Simultaneous measurement of Temperature and Refractive Index,” *Oral Presentation, SPIE Europe: Optics and Optoelectronics*, Prague, Czech Republic, 2009.
- P3. **P. Saffari**, C. Mou, H. Fu, L. Zhang and I. Bennion, “Multiple-Wavelength Switchable Fibre Ring Laser Based on Polarisation Selective Tilted Fibre Bragg Grating Capable for Strain and Temperature Sensing,” *Poster Presentation, SPIE Europe: Optics and Optoelectronics*, Prague, Czech Republic, 2009.
- P4. C. Mou, **P. Saffari**, H. Fu, K. Zhou, L. Zhang and I. Bennion, “Single- and dual-wavelength switchable erbium-doped fiber ring laser based on intracavity polarization selective tilted fiber gratings,” *Appl. Opt.*, **48**, 2009.
- P5. C. Mou, **P. Saffari**, D. Li, K. Zhou, L. Zhang, R. Soar and I. Bennion , “Smart structure sensors based on embedded fibre Bragg garting arrays in aluminum alloy matrix by ultrasonic consolidation,” *Meas. Sci. Technol.*, **20**, 2009.
- P6. E. M. Davies, **P. Saffari**, C. Mou, K. Zou, L. Zhang and I. Bennion, “Refractive index sensitivity enhancement of 81° tilted Bragg gratings by cladding etching,” poster presentation, *the 20th International Conference on Optical Fiber Sensor(OFS-20)*, Edinburgh, Scotland, 2009.
- P7. C. Mou, **P. Saffari**, D. Li, K. Zhou, L. Zhang, R. Soar and I. Bennion, “Embedded Fibre Bragg Grating Array Sensors in Aluminium Alloy Matrix by Ultrasonic Consolidation,” poster presentation, *the 19th International Conference on Optical Fiber Sensors(OFS-19)*, Perth, Australia, 2008.
- P8. H. Fu, K. Zhou, **P. Saffari**, C. Mou, L. Zhang, S. He and I. Bennion, “Microchanneled Chirped Fiber Bragg Grating Formed by Femto-Second Laser Aided Chemical Etching for Refractive Index and Temperature Measurements,” *IEEE Photon. Technol. Lett.*, **20**, 1609-1611, 2008.
- P9. H. Fu, K. Zhou, **P. Saffari**, C. Mou, L. Zhang, S. He and I. Bennion, “Microchannelled Chirped Fibre Bragg Grating Based Refractive Index Sensor Formed by Femto-second Laser Processing and HF-etching,” Oral Presentation, *34th Conference on Optical Communication, ECOC2008*, Brussels, Belgium, 21-25 September 2008.

Accepted:

- P10. **Pouneh Saffari**, ZjinYan , Kaiming Zhou, Lin Zhang and Ian Bennion, “Liquid core fibre Bragg grating based refractive index sensor formed by femtosecond assisted chemical etching technique,” *international conference on Optical Fibre Sensor(OFS-2)1*, Ottawa, Canada, 2011.

Submitted:

- P11. **P. Saffari**, C. Mou, L. Zhang and I. Bennion, “Single polarisation state of erbium doped fibre ring alser employing small angle tilted grating,” *IEEE Photon. Technol. Lett.*, 2011
- P12. **Pouneh Saffari**, ZjinYan , Kaiming Zhou, Lin Zhang and Ian Bennion “Liquid core refractometer based on micro-slot fibre Bragg using femtosecond assisted chemical etching technique,” *Opt. Express.*, 2011.

8.2. References:

1. Bates, Regis J. Optical Switching and Networking Handbook. New York: McGraw-Hill, 2001.
2. K. O. Hill, Y. Fujii, D. C. Johnson, and B. S. Kawasaki, “Photosensitivity on optical fibre waveguides: application to reflection filter fabrication,” *Appl. Phys.*, **32**, 647-649, 1978.
3. T. Erdogan, “Fiber grating spectra,” *Lightwave. Technol.*, **15**, 1277-1294, 1997.
4. J. Stone, “Photorefractivity in GeO₂-doped silica fibers,” *Appl. Phys.*, **62**, 4371-4374, 1987.
5. K. O. Hill, B. Malo, F. Bilodeau, D. C. Johnson, J. F. Morse, A. Kilian, L. Reinhart, and K. Oh, “Proceedings of the Conference on Optical Fiber Communication,” *Opt. Soc. Am.*, **14**, 14, 1991.
6. M. M. Broer, R. L. Cone, and J. R. Simpson, “Ultraviolet-induced distributed-feedback gratings in Ce³⁺ -doped silica optical fibers,” *Opt. Lett.*, **16**, 1391, 1991.
7. F. Bilodeau, D. C. Johnson, B. Malo, K. A. Vineberg, K. O. Hill, T. F. Morse, A. Kilian, and L. Reinhart, “Ultraviolet-Light Photosensitivity in Er-3+-Ge-Doped Optical Fibre,” *Opt. Lett.*, **15**, 1138-1140, 1990.

8. D. P. Hand and J. S. Russell, "Photoinduced refractive index changes in fibre Bragg gratings," *Appl. Phys. Lett.*, **15**, 102-104, 1990.
9. C. Fiori and R. Devine, "Evidence for a wide continuum of polymorphs in a-SiO₂," *Physical Review B*, **33**, 2972-2974, 1986.
10. D. Wong, S. B. Poole, and M. G. Sceats, "Stress-birefringence reduction in elliptical-core fibers under ultraviolet irradiation," *Opt. Lett.*, **17**, 1773-1775, 1992.
11. A. Attard, "Fermi level shift in Bi₁₂SiO₂₀ via photon-induced trap level occupation," *Appl. Phys.*, **71**, 933-937, 1992.
12. D. L. Williams, "Photosensitive index changes in germania doped silica fibres and waveguides," *Photosensitivity and Self-Organisation in Optical Fibers and Waveguides*, Quebec, Canada, Proceedings SPIE, **2044**, 55-68, 1993.
13. N. Lawandy, "Light induced transport and delocalisation in transparent amorphous systems," *Opt. Commun.*, **74**, 180-184, 1989.
14. A. Miotello and R. Kelly, "Laser irradiation effects in Si+-implanted SiO₂," *Nucl. Instrum. Methods. Phys. Res., Sect. B* **65**, 217-222, 1992.
15. E. J. Friebele, C. G. Askins, M. E. Gingerich, and K. J. Long, *Nucl. Instrum. Methods. Phys. Res., Sect. B* **1**, 355, 1984.
16. P. Kaiser, "Drawing-induced coloration in vitreous silica fibers," *Opt. Soc. Am.* **64**, 475, 1974.
17. A. Othonos and K. Kalli, *Fibre Bragg gratings: Fundamental and applications in telecommunications and sensing*, Artech House Publishers, ISBN 0890063443, 1st Edition, 1999.
18. P. St. J. Russell, D. P. Hand, and Y. T. Chow, "Optically-induced creation, transformation and organisation of defects and colour-centres in optical fibres," *International Workshop on Photoinduced Self-Organization Effects in Optical Fibre*, Quebec City, Quebec, Proceedings SPIE, **1516**, 47-54, 1991.
19. R. M. Atkins, V. Mizrahi, and T. Erdogan, "248-nm induced vacuum UV spectral changes in optical fibre perform cores: Support for a colour centre model of photosensitivity," *Electron. Lett.*, **29**, 385-387, 1993.
20. D. A. Parthenopolous and P. M. Rentzepis, "Three-dimensional optical storage memory," *Meas. Sci. Technol.*, **245**, 843-845, 1989.

21. D. P. Hand and P. S. Russell, "Photoinduced Refractive-Index Changes in Germanosilicate Fibres," *Opt. Lett.*, **15**, 102-104, 1990.
22. B. Malo, K. A. Vineberg, F. Bilodeau, J. Albert, D. C. Johnson, and K. O. Hill, "Ultraviolet-Light Photosensitivity in Ge-Doped Silica Fibres - Wavelength Dependence of the Light-Induced Index Change," *Opt. Lett.*, **15**, 953-955, 1990.
23. K. D. Simmons, S. LaRochelle, V. Mizrahi, G. I. Stegeman and D. L. Griscom, "Correlation of defect centers with wavelength-dependent photosensitive response in germania-doped silica optical fibers," *Opt. Lett.*, **16**, 141-143, 1991.
24. T. E. Tsai, E. J. Friebel, and d. L. Griscom, "Thermal stability of photoinduced gratings and paramagnetic centers in Ge- and Ge/P-doped silica optical fibres," *Opt. Lett.*, **18**, 935-937, 1993.
25. T. Tsai, G. M. Williams, and E. J. Friebel, "Index structure of fiber Bragg gratings in Ge-SiO₂ fibers," *Opt. Lett.*, **22**, 224-226, 1997.
26. B. Leconte, W. Xie, M. Douay, P. Bernage, P. Niay, J. F. Bayon, E. Delevaque, and H. Poignant, "Analysis of color-center-related contribution to Bragg grating formation in Ge:SiO₂ fiber based on a local Kramers-Kronig transformation of excess loss spectra," *Appl. Opt.*, **36**, 5923-5930, 1997.
27. W. X. Xie, P. Niay, P. Bernage, M. Douay, J. F. Bayon, T. Georges, M. Monerie and B. Poumellec, "Experimental-Evidence of 2 Types of Photorefractive Effects Occurring During Photo inscriptions of Bragg Gratings Within Germanosilicate Fibres," *Opt. Commun.*, **104**, 185-195, 1993.
28. P. Cordier, J. C. Doukhan, E. Fertein, P. Bernage, P. Niay, J. F. Bayon, and T. Georges, "TEM Characterization of Structural-Changes in Glass Associated to Bragg Grating Inscription in a Germanosilicate Optical-Fibre Preform," *Opt. Commun.*, **111**, 269-275, 1994.
29. P. Niay, P. Bernage, S. Legoubin, M. Douay, W. X. Xie, J. F. Bayon, T. Georges, M. Monerie, and B. Poumellec, "Behaviour of Spectral Transmissions of Bragg Gratings Written in Germania-Doped Fibres - Writing and Erasing Experiments Using Pulsed or CW UV Exposure," *Opt. Commun.*, **113**, 176-192, 1994.
30. A. Main, "Optical fibre sensors and their interrogation", Chapter 2 of PhD Thesis, Photonics Research Group, Aston University, Birmingham, 2008.
31. B. Malo, J. Albert, D. C. Johnson, F. Bilodeau, and K. O. Hill, "Elimination of Photoinduced Absorption in Ge-Doped Silica Fibres By Annealing of Ultraviolet Color-Centers," *Electron. Lett.*, **28**, 1598-1599, 1992.

32. K. S. Chiang, M. G. Sceats, and D. Wong, "Ultraviolet Photolytic-Induced Changes in Optical Fibres - the Thermal-Expansion Coefficient," *Opt. Lett.*, **18**, 965-967, 1993.
33. D. Wong, S. B. Poole, and M. G. Sceats, "Stress-birefringence reduction in elliptical-core fibers under ultraviolet irradiation," *Opt. Lett.*, **17**, 1773-1775, 1992.
34. P. W. Levy, "Reactor and gamma-ray induced coloring in crystalline quartz and Corning fused silica," *J. C. P.*, **23**, 764-765, 1955.
35. D. L. Williams, B. J. Ainslie, J. R. Armitage, R. Kashyap, and R. Campbell, "Enhanced UV photosensitivity in boron codoped germanosilicate fibres," *Electron. Lett.*, **29**, 45-47, 1993.
36. P. J. Lemaire, "High-pressure H₂ loading as a technique for achieving ultrahigh UV photosensitivity and thermal sensitivity in GeO₂ doped optical fibres," *Electron. Lett.*, **29**, 1191-1193, 1993.
37. F. Bilodeau, "Photosensitization of optical fiber and silica-on-silicon/silica waveguides," *Opt. Lett.*, **18**, 953-955, 1993.
38. L. Dong, J. L. Cruz, L. Reekie, M. G. Xu, and D. Payne, "Enhanced photosensitivity in tin-co doped germanosilicate optical fibres," *IEEE Photon. Technol. Lett.*, **7**, 1048-1050, 1995.
39. L. Dong, J. L. Cruz, J. A. Tucknott, L. Reekie, and D. N. Payne, "Strong photosensitive gratings in tin-doped phosphosilicate optical fibers," *Opt. Lett.*, **20**, 1982-1984, 1995.
40. D. L. Williams and R. P. Smith, "Accelerated Lifetime Tests On UV Written Intra-core Gratings in Boron Germania Co doped Silica Fibre," *Electron. Lett.*, **31**, 2120-2121, 1995.
41. J. Canning, M. Aslund, and P. Hu., "Ultraviolet-induced absorption losses in hydrogen-loaded optical fibres and in presensitized optical fibres," *Opt. Lett.*, **25**, 1621-1623, 2000.
42. G. Simpson, "Optical fibre sensors and their interrogation", Chapter 2 of PhD Thesis, Photonics Research Group, Aston University, Birmingham, 2005.
43. F. Blodeau, B. Malo, J. Albert, DC. Johnson, KO. Hill, Y. Hibino, Y. Abe, and M. Kawachi, "Photosensitisation of optical fibre and silica-on-silicon/silica waveguides," *Opt. Lett.*, **18**, 953-955, 1993.

44. R. M. Atkins, P. J. Lemaire, T. Erdogan, and V. Mizrahi, "Mechanisms of Enhanced UV Photosensitivity Via Hydrogen Loading in Germanosilicate Glasses," *Electron. Lett.*, **29**, 1234-1235, 1993.
45. S. Kannan, J. Z. Y. Guo, and P. J. Lemaire, "Thermal stability analysis of UV-induced fibre Bragg gratings," *Lightwave. Technol.*, **15**, 1478-1483, 1997.
46. S. Ishikawa, A. Inoue, M. Harumoto, T. Enomoto, and H. Kanamori, "Adequate aging condition for fibre Bragg grating based on simple power law model," presented at *Optical Fibre Sensors (OFS1998)*, 183-184, 1998.
47. H. Patrick, S. L. Gilbert, A. Lidgard, and M. D. Gallagher, "Annealing of Bragg Gratings in Hydrogen-Loaded Optical-Fibre," *Appl. Phys.*, **78**, 2940-2945, 1995.
48. T. Erdogan, V. Mirrahi, P. Lemaire, and D. Monroe, "Decay of ultraviolet-induced fibre Bragg gratings," *Appl. Phys.*, **76**, 73-80, 1994.
49. S. R. Baker, H. N. Rourke, V. Baker, and D. Goodchild, "Thermal decay of fibre Bragg gratings written in boron and germanium co doped silica fibre," *Lightwave. Technol.*, **15**, 1470-1477, 1997.
50. S. Pal, J. Mandal, T. Sun, and K. T. V. Grattan, "Analysis of thermal decay and prediction of operational lifetime for a type I boron-germanium co doped Fibre Bragg grating," *Appl. Opt.*, **42**, 2188-2197, 2003.
51. G. Brambilla and H. Rutt, "Fiber Bragg gratings with enhanced thermal stability," *Appl. Phys. Lett.*, **80**, 3259-3261, 2002.
52. M. Fokine, "Formation of thermally stable chemical composition gratings in optical fibers," *Opt. Soc. Am. B* **19**, 1759-1765, 2002.
53. M. Aslund and J. Canning, "Annealing properties of gratings written into UV-presensitized hydrogen-out diffused optical fibre," *Opt. Lett.*, **25**, 692-694, 2000.
54. A. Miotello, and R. Kelly, "Laser irradiation effects in Si+-implanted SiO₂," *Nucl. Instrum. Methods. Phys. Res., Sect. B* **65**, 217-222, 1992.
55. B. Malo, J. Albert, K. O. Hill, F. Bilodeau, and D. C. Johnson, "Effective index drift from molecular hydrogen diffusion in hydrogen-loaded optical fibres and its effect on Bragg grating fabrication," *Electron. Lett.*, **30**, 442-444, 1994.
56. A. Yariv, "Coupled-mode theory for guided-wave optics," *IEEE Quantum. Electron.*, **9**, 919-933, 1973.

57. H. Kogelnik, and C. W. Shank, "Coupled wave theory of distributed feedback lasers," *Appl. Phys.*, **43**, 2327-2335, 1972.
58. T. Erdogan, "Cladding-mode resonances in short- and long- period fiber grating filters," *Opt. Soc. Am. A***14**, 1760-1773, 1997.
59. A. M. Vengsarkar, P. Lemaire, J. Judkins, V. Bhatia, T. Erdogan, and J. Sipe, "Long-period fiber gratings as band-rejection filters," *Lightwave Technol.*, **14**, 58-65, 1996.
60. V. Bhatai and A. M. Vengsarkar, "Optical fiber long-period grating sensors," *Opt. Lett.*, **21**, 692-694, 1996.
61. T. Erdogan, and J. E. Sipe, "Tilted fiber phase gratings," *Opt. Soc. Am. A***13**, 296-313, 1996.
62. D. K. W. Lam, and B. K. Garside, "Characterization of single-mode optical fiber filter," *Appl. Opt.*, **20**, 440-445, 1981.
63. G. Meltz, W. W. Morey, and W. H. Glenn, "Formation of Bragg gratings in optical fibers by transverse holographic method," *Opt. Lett.*, **14**, 823-825, 1989.
64. R. Kashyap, J. R. Armitage, R. Wyatt, S. T. Davey, D. L. Williams, "All-fibre narrowband reflection gratings at 1500nm," *Electron. Lett.*, **26**, 730-732, 1990.
65. R. Kashyap, J. R. Armitage, R. J. Campbell, D. L. Williams, G. D. Maxwell, B. J. Ainslie, and C. A. Millar, "Light-sensitive optical fibers and planar waveguides," *B. T. Technol.*, **11**, 150-154, 1993.
66. H. Patrick and S. L. Gilbert, "Growth of Bragg gratings produced by continuous-wave ultraviolet light in optical fiber," *Opt. Lett.*, **18**, 1484-1486, 1993.
67. B. J. Eggleton, P. A. Krug, and L. Poladian, "Experimental demonstration of compression of dispersed optical pulses by reflection from self-chirped optical fiber Bragg gratings," *Opt. Lett.*, **19**, 877-880, 1994.
68. Q. Zhang, D. A. Brown, L. Reinhart, T. F. Morse, "Tuning Bragg wavelength by writing gratings on prestrained fibers," *IEEE Photon. Technol. Lett.*, **6**, 839-842, 1994.
69. K. O. Hill, B. Malo, F. Bilodeau, D. C. Johnson, and J. Albert, "Bragg gratings fabricated in monomode photosensitive optical fiber by UV exposure through a phase mask," *Appl. Phys. Lett.*, **62**, 1035-1037, 1993.

70. Y. Kondo, K. Nouchi, T. Mitsuyu, M. Watanabe, P. G. Kazansky, and K. Hirao, "Fabrication of long-period fiber gratings by focused irradiation of infrared femtosecond laser pulses," *Opt. Lett.*, **24**, 646-648, 1999.
71. E. Fertein, C. Przygodzki, H. Delbarre, A. Hidayat, M. Douay, and P. Niay, "Refractive-Index Changes of Standard Telecommunication Fiber through Exposure to Femtosecond Laser Pulses at 810 cm," *Appl. Opt.*, **40**, 3506-3508, 2001.
72. F. Hindle, E. Fertein, C. Przygodzki, F. Dürr, L. Paccou, R. Bocquet, P. Niay, H. Georg Limberger, and M. Douay, "Inscription of Long-Period Gratings in Pure Silica and Germano-Silicate Fiber Cores by Femtosecond Laser Irradiation," *IEEE Photon. Technol. Lett.*, **16**, 1861-1863, 2004.
73. A. Martinez, M. Dubov, I. Khrushchev and I. Bennion, "Direct writing of fibre Bragg gratings by femtosecond laser," *Elec. Lett.*, **40**, 1170-1172, 2004.
74. Y. Lai, K. Zhou, K. Sugden, and I. Bennion, "Point-by-point inscription of first-order fiber Bragg grating for C-band applications," *Opt. Express.*, **15**, 18318-18325, 2007.
75. Y. Liu, "Advanced fibre gratings and their application," Chapter 4 of PhD Thesis, Photonics Research Group, Aston University, Birmingham, 2001.
76. H. G. Limberger, P. Y. Fonjallaz, P. Lambelet, R. P. Salathé, C. Zimmer, and H. H. Gilgen, "OLCR characterization of efficient Bragg gratings in optical fiber," *Photosensitivity and Self-Organization in Optical Fibers and Waveguides*, Quebec, Canada, Proceedings SPIE, **2044**, 272-283, 1993.
77. Othonos and X. Lee, "Novel and improved methods of writing Bragg gratings with phase masks," *IEEE Photon. Technol. Lett.*, **7**, 1183-1185, 1995.
78. J. D. Prohaska, E. Snitzer, S. Rishton, and V. Boegli, *Electron. Lett.*, **29**, 1614-1617, 1993.
79. Q. Zhang, D. A. Brown, L. Reinhart, T. F. Morse, J. Q. Wang, and G. Xiao, *IEEE Photon. Technol. Lett.*, **6**, 839-841, 1994.
80. P. S. Westbrook, K. S. Feder, P. I. Reyes, P. Steinurzel, B. J. Eggleton, R. G. Ernst, L. Reith and D. M. Gill, "Application of fiber Bragg grating filter/tap module to a wavelength-locked low-chirp directly-modulated 10Gb/s Rz transmitter," in *Optical Fiber Communication Conference*, Anaheim, California, 680-682, 2002.
81. G. Meltz, W. W. Morey, and W. Glenn, "In-Fibre Bragg grating tap," *Optical Fibre Communications*, San Francisco, California, USA, *1990 OSA Technical Digest Series 1*, TuG1, 1990.

82. K. S. Feder, P. S. Westbrook, J. Ging, P. I. Reyes, and G. E. Carver, “In-fiber spectrometer using tilted fiber gratings,” *IEEE Photon. Technol. Lett.*, **15**, 933-935, 2003.
83. R. Kashyap, R. Wyatt, and R. J. Campbell, “Wideband gain flattened erbium fibre amplifier using a photosensitive fibre blazed grating,” *Electron. Lett.*, **29**, 154-156, 1993.
84. E. Chehura, S. W. James, and R. P. Tatam, “Temperature and Strain discrimination using a single tilted fibre Bragg grating,” *Opt. commun.*, **275**, 344-347, 2007.
85. C. Jáuregui, A. Quintela, J. M. López-Higuera, “Interrogation unit for fiber Bragg grating sensors that uses a slanted fiber grating,” *Opt. Lett.*, **29**, 676-678, 2004.
86. G. Simpson, K. Zhou, L. Zhang, and I. Bennion, “Wide bandwidth, high resolution spectral interrogation using a BFBG-CCD array for optical sensing applications,” *16th International Conference on Optical Fibre Sensors (OFS-16)*, Japan, 2003.
87. P. S. Westbrook, T. A. Strasser, and T. Erdogan, “In-line polarimeter using blazed fiber gratings,” *IEEE Photon. Technol. Lett.*, **12**, 1352-1354, 2000.
88. J. Peupelmann, E. Krause, A. Bandemer, and C. Schäffer, “Fibre-polarimeter based on grating taps,” *Electron. Lett.*, **38**, 1248-1250, 2002.
89. K. Zhou, X. Chen, A. G. Simpson, L. Zhang, and I. Bennion, “High extinction ratio in-fiber polarizer based on a 45°-tilted fiber Bragg grating,” in *Optical Fiber Communication Conference*, Anaheim, California, paper OME22, 2005.
90. K. Zhou, G. Simpson, X. Chen, L. Zhang, and I. Bennion, “High extinction ratio in-fiber polarizers based on 45°-tilted fiber Bragg gratings,” *Opt. Lett.*, **30**, 1285-1287, 2005.
91. S. J. Mihailov, R. B. Walker, P. Lu, H. Ding, X. Dai, C. Smelser and L. Chen, 217 “UV-Induced polarisation-dependant loss (PDL) in tilted fibre Bragg gratings: application of a PDL equaliser,” *IEE Proc. Optoelectronics*, **149**, 211-216, 2002.
92. K. Zhou, L. Zhang, X. Chen, R. Suo, and I. Bennion, “Implementation of optical fibre sensors with low thermal cross-sensitivity utilising ex-45° tilting grating structures,” *18th International Conference on Optical Fibre Sensors (OFS-18)*, Cancun, Mexico, 2006.

93. X. Chen, K. Zhou, R. Suo, L. Zhang, and I. Bennion, "In-fibre twist sensor based on TFBG structures," *18th International Conference on Optical Fibre Sensors (OFS-18)*, Cancun, Mexico, 2006.
94. K. Zhou, L. Zhang, X. Chen, and I. Bennion, "Optic sensors of high refractive-index responsivity and low thermal cross sensitivity that use fiber Bragg gratings of $>80^\circ$ tilted structures," *Opt. Lett.*, **31**, 1193-1195, 2006.
95. Y. J. Rao, "In-Fibre Bragg grating sensors," *Meas. Sci. Technol.*, **8**, 355-375, 1997.
96. T. Poulsen, M. O. Berendt, A. Bjarklev, L. Gruner Nielsen and C. E. Soccilich. "Bragg grating induced cladding mode coupling caused by ultra-violet light absorption," *Electron. Lett.*, **34**. No. 10, 1998.
97. H. Patrick, and S. L. Gilbert, "Growth of Bragg gratings produced by continuous-wave ultraviolet light in optical fiber," *Opt. Lett.*, **18**, 1484-1486, 1993.
98. B. Poumellec, "UV induced densification during Bragg grating inscription in Ge: SiO₂ preforms," *Opt. Materials*, **4**, 441, 1995.
99. W. X. Xie, P. Niay, P. Bernage, M. Douay, J. F. Bayon, T. Georges, M. Monerie and B. Poumellec, "Experimental-evidence of 2 types of photorefractive effects occurring during photoinscriptions of Bragg gratings within germonasilicate fibers," *Opt. Commun.*, **104**, 185-195, 1993.
100. Y. Liu, J. A. R. Williams, L. Zhang, and I. Bennion, "Abnormal spectral evolution of fiber Bragg gratings in hydrogenated fibers," *Opt. Lett.*, **27**(8), 586-588, 2002.
101. G. Simpson, K. Kalli, K. Zhou, L. Zhang, and I. Bennion, "Blank beam fabrication of regenerated type IA gratings," *Meas. Sci. Technol.*, **15**, 1665-1669, 2004.
102. G. Simpson, L. Zhang, K. Zhou, and I. Bennion, "Abnormal photosensitivity effects and the formation of type IA FBGs," *Bragg Gratings, Poling and Photosensitivity (BGPP-2003)*, Monterey, USA, 2003.
103. G. Simpson, K. Kalli, K. Zhou, L. Zhang, and I. Bennion, "An ideal method for the fabrication of temperature compensating IA-I strain sensors," presented at *OFS16*, Nara, Japan, 2003.
104. D. R. White, "Ultrasonic consolidation of aluminium tooling" *Adv. Mater. Processes* **161**, **64** and **65**, 2003.

105. C. Y. Kong, R. C. Soar, and P. M. Dickens, "Characterisation of aluminium alloy 6061 for the ultrasonic consolidation process," *Mater. Sci. Eng.*, **A363**, 99-106, 2003.
106. C. Y. Kong, R.C. Soar, and P. M. Dickens, "Optimum process parameters for ultrasonic consolidation of 3003 aluminium," *Mater. Process. Technol.*, **146**, 181-187, 2004.
107. C.Y. Kong and R. C. Soar, "Fabrication of metal-matrix composites and adaptive composites using ultrasonic consolidation process," *Mater. Sci. Eng.*, **A 412**, 12- 18, 2005.
108. E. Crinon and J. T. Evans, "The effect of surface roughness, oxide film thickness and interfacial sliding on the electrical contact resistance of aluminium," *Mater. Sci. Eng.*, **A 242**, 121-128, 1998.
109. A. D. Kersey, M. A. Davis, H. J. Patrick, M. LeBlanc, K. P. Koo, C. G. Askins, M. A. Putnam, and E. J. Fribele, " Fibre Grating Sensors," Invited Paper.
110. Y. Liu, "Advanced Fibre Gratings and their Application," Chapter 7 of PhD Thesis, Photonics Research Group, Aston University, Birmingham, 2001.
111. A. Iadicicco, A. Cusano, A. Cutolo,R. Bernini, and M. Giordano, "Thinned fiber Bragg gratings as high sensitivity refractive index sensors," *IEEE Photon. Technol. Lett.*, **16**, 1149-1151, 2004.
112. A. Iadicicco, S. Campopiano, A. Cutolo, M. Giordano, and A. Cusano, "Refractive index sensor based on microstructured fiber Bragg grating," *IEEE Photon. Technol. Lett.*, **17**, 1250-1252, 2005.
113. A. Iadicicco, S. Campopiano, A. Cutolo, M. Giordano and A. Cusano, "Self temperature referenced refractive index sensor by non-uniform thinned fiber Bragg gratings," *Sens. Actuators, B***120**, 231-237, 2006.
114. Y. Lai, K. Zhou, L. Zhang, and I Bennion, "Mirochannels in conventional single-mode fibers," *Opt. Lett.*, **31**, 2559-2561, 2006.
115. K. Zhou, Y. Lai, X. Chen, K. Sugden, L. Zhang and I. Bennion, "A refractometer based on a micro-slot in a fiber Bragg grating formed by chemically assisted femtosecond laser processing," *Opt. Express*, **15**, 15848-15853, 2007.
116. X. Shu, L. Zhang, and I. Bennion, "Sensitivity characteristics of longperiod fiber gratings," *Lightwave. Technol.*, **20**, 255-266, 2002.

117. M. N. Ng, Z. Chen, and K. S. Chiang, "Temperature compensation of long-period fiber grating for refractive-index sensing with bending effect," *IEEE Photon. Technol. Lett.*, **14**, 361-362, 2002.
118. R. M. Measures, *Structural Monitoring with Fiber Optic Technology*, London, U.K.: Academic, 2001.
119. C. Hnatovsky, R. S. Taylor, E. Simova, V. R. Bhardwaj, D. M. Rayner, and P. B. Corkum, "Polarization-selective etching in femtosecond laser-assisted microfluidic channel fabrication in fused silica," *Opt. Lett.*, **30**, 1867-1869, 2005.
120. A. Cusano, A. Cutolo, M. Giordano, and L. Nicolais, "Optoelectronic refractive index measurements: Applications to smart polymer processing," *IEEE Sensors.*, **3**, 781-787, 2003.
121. R. Bernini, S. Camponiano, and L. Zeni, "Silicon micromachined hollow optical waveguides for sensing applications," *IEEE Select. Topics Quantum Electron.*, **8**, 106-110, 2002.
122. C. F. Chan, C. Chen, A. Jafari, A. Laronche, D. J. Thomson and J. Albert, "Optical fiber refractometer using narrowband cladding-mode resonance shifts," *Appl. Opt.*, **46**, 1142-1149, 2007.
123. M. Holtz, P. K. Dasgupta, G. Zhang, "Small-volume Raman spectroscopy with a liquid core waveguide," *Anal. Chem.*, **71**, 2934 -2938, 1999.
124. M. Brown, T. Vestad, J. Oakey and D. W. M. Mar, "Optical waveguides via viscosity-mismatched microfluidic flows," *Appl. Phys. Lett.*, **88**, 134-139, 2006.
125. S. Yamashita and K. Hotate, "Multiwavelength erbium-doped fiber laser using intracavity etalon and cooled by liquid nitrogen," *Electron. Lett.*, **32**, 1298-1299, 1996.
126. K. J. Zhou, D. Y. Zhou, F. Z. Dong, and N. Q. Ngo, "Room temperature multiwavelength erbium-doped fiber ring laser employing sinusoidal phase-modulation feedback," *Opt. Lett.*, **28**, 893-895, 2003.
127. S. Pan, X. Zhao, and C. Lou, "Switchable single-longitudinal mode dual-wavelength erbium-doped fiber ring laser incorporating a semiconductor optical amplifier," *Opt. Lett.*, **33**, 764-766, 2008.
128. Y. Yao, X. Chen, Y. Dai, and S. Xie, "Dual-wavelength erbium doped fibre laser with a simple linear cavity and its application in microwave generation," *IEEE Photon. Technol. Lett.*, **18**, 187-189, 2006.

129. X. Liu and C. Lu, "Self-stabilizing effect of four-wave mixing and its applications on multiwavelength erbium-doped fiber laser," *IEEE Photon. Technol. Lett.*, **17**, 2541-2543, 2005.
130. Y. G. Han, T. V. A. Tran, and S. B. Lee, "Wavelength-spacing tuneable multiwavelength erbium-doped fibre laser based on four-wave mixing of dispersion-shift fiber," *Opt. Lett.*, **31**, 697-699, 2006.
131. S. Pan, C. Lou, and Y. Gao, "Multiwavelength erbium-doped fibre laser based on inhomogeneous loss mechanism by use of a highly nonlinear fibre and a Fabry-Perot filter," *Opt. Express*, **14**, 1113-1118, 2006.
132. D. Liu, N. Q. Ngo, S. C. Tjin, and X. Dong, "A dual-wavelength fibre laser sensor system for measurement of temperature and strain," *IEEE Photon. Technol. Lett.*, **19**, 1148-1150, 2007.
133. Z. Liu, Y. Liu, J. Du, S. Yuan, and X. Dong "Switchable triple wavelength erbium-doped fiber laser using a single fiber Bragg grating in fiber-maintaining fiber," *Opt. Commun.*, **279**, 168-172, 2007.
134. L. Sun, X. Feng, W. Zhang, L. Xiong, Y. Liu, G. Kai, S. Yuan, and X. Dong, "Beating frequency tunable dual-wavelength erbium-doped fibre laser with one fibre Bragg grating," *IEEE Photon. Technol. Lett.*, **16**, 1453-1455, 2004.
135. C. Mou, X. Chen, K. Zhou, L. Zhang, I. Bennion, S. Fu, and X. Dong, "Realisation of single polarisation state of fiber ring laser by utilising intracavity 45°-tilted fiber Bragg grating," presented at the *International Topic Meeting on Bragg Gratings, Photosensitivity, and Poling in Glass Waveguides*, Quebec, Canada, 2007.
136. D. Liu, N. Q. Ngo, S. C. Tjin, and X. Dong, "A dual-wavelength fiber laser sensor system for measurement of temperature and strain," *IEEE Photon. Technol. Lett.*, **19**, 1148-1150, 2007.
137. Z. Liu, Y. Liu, J. Du, S. Yuan, and X. Dong "Switchable triple wavelength erbium-doped fiber laser using a single fiber Bragg grating in fiber-maintaining fiber," *Opt. Commun.*, **279**, 168-172, 2007.
138. L. Sun, X. Feng, W. Zhang, L. Xiong, Y. Liu, G. Kai, S. Yuan, and X. Dong, "Beating frequency tunable dual-wavelength erbium-doped fiber laser with one fiber Bragg grating," *IEEE Photon. Technol. Lett.*, **16**, 1453-1455, 2004.
139. G. Laffont, P. Ferdinand, "Tilted short-period fibre-Bragg-grating-induced coupling to cladding modes for accurate refractometer," *Meas. Sci. Technol.*, **12**, 765-770, 2001.

140. C. Caucheteur, P. Mégret, "Demodulation technique for weakly tilted fiber Bragg grating refractometer," *IEEE Photon. Technol. Lett.*, **17**, 2703-2705, 2005.
141. C. Chen, L. Xiong, A. Jafari, J. Albert, "Differential sensitivity characteristics of tilted fiber Bragg grating sensors," in *Proceedings of SPIE*, **6004**, paper 6004-13, 2005.
142. C. Caucheteur, K. Chah, F. Lhommé, M. Blondel, P. Mégret, "Simultaneous bend and temperature sensor using tilted FBG," in *Proceedings of SPIE*, **5855**, 707-710, 2005.
143. R. Sui, "Advanced fibre gratings in normal and infrared glass fibres by UV and near-infrared-femtosecond lasers, Chapter 5 of PhD Thesis, Photonics Research Group, Aston University, Birmingham, 2008.
144. M.G. Xu, J.-L. Archambault, L. Reekie and J.P. Dakin, "Discrimination between strain and temperature effects using dual-wavelength fibre grating sensors," *Electron. Lett.*, **30**, 1085-1087, 1994.
145. P. M. Cavaleiro, F. M. Araújo, L. A. Ferreira, J. L. Santos and F. Farahi, "Simultaneous measurement of strain and temperature using Bragg gratings written in germanosilicate and boron-Codoped germanosilicate fibres," *IEEE Photon. Technol. Lett.*, **12**, 1635-1637, 1999.
146. Frazao, R. Romero, F. M. Araujo, L. A. Ferreira, J. L. Santos, "Strain-temperature discrimination using a step spectrum profile fibre Bragg grating arrangement, Sensors and Actuators," *A: Physical*, **120**, 490-493, 2005.
147. H. J. Patrick; G. M. Williams; A. D. Kersey, J. R. Pedrazzani, A. M. Vengsarkar, "Hybrid fiber Bragg grating/long period fiber grating sensor for strain/temperature discrimination," *IEEE Photon. Technol. Lett.*, **8**, 1223-1225, 1996.
148. Z. Xiong, G. Peng, B. Wu, and P. Chu, "Highly tunable Bragg gratings in single-mode polymer optical fibers," *IEEE Photon. Technol. Lett.*, **11**, 352-354, 1999.
149. K. Zhou, X. Chen, D. Webb, L. Zhang and I. Bennion, "Simultaneous temperature and strain measurement with enhanced resolution up to 20 times by using a compact hybrid optical waveguide Bragg grating," *Asia Optical Fiber Communication and Optoelectronic Exposition and Conference (AOE)*, Shanghai (CN), 2008.